

Detection and Evaluation of Partial Discharges in Power Transformers with Special Sensors and Diagnostic Methods

Von der Fakultät für Elektrotechnik und Informatik
der Gottfried Wilhelm Leibniz Universität Hannover

zur Erlangung des akademischen Grades

Doktor-Ingenieur

(abgekürzt: Dr.-Ing.)

genehmigte Dissertation

von Herrn

M.Sc. Mohammad Esmaeil Akbari Azirani

geboren am 19.07.1989

in Esfahan

2023

1. Referent: Prof. Dr.-Ing. Peter Werle
2. Referent: Prof. Dr.-Ing. Heyno Garbe
3. Referent: Prof. Dr.-Ing. Michael Hartje

Tag der Promotion: 17.10.2023

Acknowledgements

I am profoundly grateful to my esteemed supervisor, Prof. Peter Werle, whose unwavering guidance, support, and encouragement have been the cornerstone of my PhD journey. His insightful feedback and constructive criticism have not only shaped my research but also fostered my growth as both a scientist and an individual. I consider myself incredibly fortunate to have had the privilege of working under his mentorship, and I will forever cherish the invaluable lessons he imparted.

I extend my heartfelt thanks to Prof. Asghar Akbari Azirani, whose invaluable advice streamlined my experiment procedures and illuminated my results. His contributions were pivotal to the successful completion of my thesis. I am also indebted to Prof. Ernst Gockenbach and Prof. Hossein Borsi for their mentorship and steadfast guidance throughout my academic odyssey.

The unwavering love, steadfast support, and enduring encouragement from my family have been my guiding lights. Their presence has been a constant source of strength and inspiration. Their belief in me, even during the most challenging times, fueled my determination and resilience, making the completion of my PhD possible. I am deeply moved by their unconditional love and unwavering faith in my abilities, and I will forever cherish their pivotal role in my achievements.

My sincere appreciation goes to the bachelor's and master's students whose active participation made my research possible. Their willingness to contribute their time and effort was instrumental, enhancing the validity and relevance of my findings.

To my friends, colleagues, and the institute's workshop, I extend my gratitude for their camaraderie and unwavering support, both in the lab and in social settings. Their companionship, feedback, and encouragement have been instrumental in my academic and personal development. I am also thankful for my close friends, whose constant presence provided a sense of

community and solace during my studies. Their unwavering support and understanding were invaluable.

I express my deepest gratitude to the wider scientific community for their groundbreaking contributions to the field. Countless researchers and scholars have paved the way for my research. The wealth of literature, data-sets, and collaborative platforms they provided has been instrumental in expanding my knowledge and advancing scientific progress.

I am deeply humbled and thankful for the collective efforts of all those mentioned above. Their contributions have played an indispensable role in shaping my academic journey and preparing me for the challenges and opportunities that lie ahead.

Dedicated to
my beloved wife,
my remarkable son,
my cherished parents,
and my wonderful brother.

Contents

List of Figures	xi
List of Tables	xvii
List of Abbreviations	xix
Abstract	xxi
Zusammenfassung	xxiii
Overview	1
Introduction	3
1 Theoretical Background	13
1.1 Partial Discharge	14
1.1.1 PD Phenomenon	14
1.1.2 Measurement of PD	18
1.1.2.1 Conventional Electrical PD Measurement Method	19
1.1.2.2 Unconventional Methods	22
1.2 Transformer Fault Diagnosis using DGA	25
1.2.1 Fault Gases in Transformers	25
1.2.2 Evaluation Methods of DGA Data	26
1.2.3 Online DGA Monitoring Systems	28
1.2.4 Fault Gas Monitoring System in the Gas Cushion . . .	30
1.3 UHF PD Measurement Technique	31
1.3.1 PD Detection via the UHF Technique	31
1.3.2 Principles of Localization via the UHF Technique . . .	36
1.3.2.1 Multilateration with Four Sensors	36
1.3.2.2 Methods for Determining the Arrival Times of UHF Signals	37

1.3.2.3	Measurement Uncertainties in the Determination of AT	41
1.3.3	UHF Probes	43
1.3.4	Employed UHF PD Measurement Setup	46
1.3.4.1	Transformer Tank Model	46
1.3.4.2	PD Fault Models	47
1.3.4.3	PD Measurement System	50
1.3.4.4	Analysis of the EM Waves Emitted by PD	52
2	Development of a Special Fault Gas Monitoring System	55
2.1	Preliminary Investigations on Commercially Available Sensors	57
2.1.1	Test Setup	58
2.1.2	Test Procedure	59
2.1.3	Effect of Temperature	60
2.1.4	Effect of Pressure	61
2.1.5	Effect of Oxygen Content	63
2.1.6	Long Term Application under Low Oxygen Level	65
2.2	Novel Online Monitoring System	67
2.2.1	Auxiliary Sensors	68
2.2.1.1	Behavior of the Sensors within the Intended Operation Range	71
2.2.2	Microcontroller Evaluation System	72
2.2.3	Investigations on the Lab Prototype	73
2.2.3.1	Fault Gas Generation by Hot-Spot in Insulating Liquid	73
2.2.3.2	Fault Gas Generation by PD in the Windings	77
2.3	The Monitoring System <i>TGM-101</i>	81
2.3.1	Control System	82
2.3.2	Sensor System	83
3	Optimal Parameter Settings for UHF PD Detection	87
3.1	Applicability of UHF PD Detection	87
3.2	UHF Frequency Selection	95
3.2.1	Influence of the DUT	95
3.2.2	Frequency Analysis of the EM Waves Emitted by PD	100
3.3	Proposed Algorithm for Frequency Selection	104
3.4	Practical Measurements Using Different Frequency Settings	107

4	Development of Methods for Enhanced PD Localization	115
4.1	Novel Localization Approach	115
4.1.1	Influence of Determined ATs on Localization Accuracy	115
4.1.2	Selection Criteria	119
4.2	Simulation of the Wave Propagation using the FDTD Method	124
4.2.1	Introduction to FDTD Method	124
4.3	Localization Algorithm	129
4.3.1	Overview of the Algorithm	129
4.3.2	Signal Processing Units	130
4.3.3	Calculation of PD Location	134
4.4	Arrival Time Determination of UHF Signals	135
4.4.1	Time Window Contrast Function Method (TWCF) . . .	136
4.4.2	Comparing AT Detection Methods	137
4.5	Determination of the Target Sequence	139
4.6	Wavelet Denoising	141
4.7	Preliminary Investigations on the Proposed Localization Algorithm	142
4.7.1	Case 1: Direct Line of Sight between the PD Source and the Probes	143
4.7.2	Case 2: Combined Metal Lattice Barrier with Press-board Barrier	143
4.7.2.1	Clustering the Candidate Coordinates	144
4.7.3	Case 3: Metal Barrier	147
4.8	Experimental Validation	149
4.8.1	Case Study: Transformer Tank Model	149
4.8.2	Case Study: Transformer Replica	155
4.9	Graphical User Interface and Features of the Localization Algorithm	163
	Conclusion	165
	Bibliography	169

List of Figures

1	The breakdown of failure causes in terms of the various constituents of a transformer according to [14]	7
2	Failure rate vs. lifetime of a transformer adapted from [15]	9
1.1	Dielectric with air-filled cavity adapted from [32]	15
1.2	Equivalent circuit diagram for a dielectric with air-filled cavity with a spark gap SG adapted from [32]	15
1.3	External voltage $v(t)$, and cavity voltage $v_1(t)$ with and without PD adapted from [32]	16
1.4	Transient currents passing through the PD equivalent circuit in case of breakdown adapted from [33]	17
1.5	Overview of a partial discharge test circuit adapted from [21]	20
1.6	Simplified circuit for PD measurements for power transformers adapted from [21]	21
1.7	Structural representation of a Duval triangle [73]	27
1.8	A four-port network	35
1.9	ATs of simultaneously captured signals by four UHF probes	37
1.10	Examples of commercially available monopole antennas for power transformers: (a) <i>Omicron UVS 610</i> [117], (b) <i>PDIX TVS 2</i> [118], and (c) <i>BSS UHF 50/80</i> [119]	45
1.11	Examples of commercially available UHF plate sensors for the dielectric window of power transformers: (a) <i>Omicron UHT 1</i> [121], (b) <i>Doble UHF PD Plate Sensor</i> [122], and (c) <i>BSS UHF-PS1</i> [123]	45
1.12	Transformer tank model with a 110 kV bushing and UHF sensors inserted through the oil drain valves [87, 133]	47
1.13	PD fault models for (a) surface discharge, (b) internal discharge, and (c) corona [133]	48

1.14	Utilized color code in this thesis to represent increasing charge density, with blue denoting fewer occurrences, and red highlighting a higher frequency of similar events at a given phase angle of a PRPD pattern	48
1.15	Electrical PRPD patterns associated with (a) surface discharge model, (b) internal discharge model, and (c) corona discharge model [133]	49
1.16	Specially designed PD fault model for localization measurements	50
1.17	<i>Omicron</i> PD measurement system (a) <i>MPD 600</i> with its battery pack <i>MPP 600</i> , (b) charge calibrator <i>CAL 542</i> , (c) UHF bandwidth converter <i>UHF 620</i> , (d) UHF pulse generator <i>UPG 620</i> , and (e) UHF probe <i>UVS 610</i> [134]	51
1.18	<i>Tektronix DPO7345C</i> digital storage oscilloscope [135]	52
1.19	<i>Rohde & Schwarz</i> vector network analyzer <i>ZVA8</i> [139]	53
2.1	Designed test vessel for conducting the preliminary investigations [143]	58
2.2	Test setup for determining the characteristics of the chosen fault gas sensors [143]	59
2.3	Behavior of sensors (a) SA and (b) SB at ambient pressure by increasing the hydrogen concentration at different temperature levels [143]	60
2.4	Behavior of sensors (a) SA and (b) SB at room temperature by increasing the hydrogen concentration at different pressure levels [143]	62
2.5	Overview of the test setup for varying the oxygen content of the test vessel [143]	63
2.6	Behavior of sensor SB by increasing the hydrogen concentration at (a) different temperature levels and ambient pressure, and (b) at different pressure levels and room temperature in an environment with an oxygen level below 3 % [143]	64
2.7	Long term measurement with sensor SB under an oxygen level below 3 % at room temperature and ambient pressure [143]	66
2.8	Behavior of the sensor SB in nitrogen by increasing the hydrogen concentration at room temperature and ambient pressure levels with run fifth to eighth via optimized method	67
2.9	Developed lab prototype with the sensor system, the evaluation board, and the universal power supply [144]	68

2.10 Behavior of the temperature sensor at different temperature levels	69
2.11 Behavior of the pressure sensor at different pressure levels	69
2.12 Behavior of the oxygen sensor at different oxygen levels	70
2.13 Behavior of the humidity sensor at different humidity levels	71
2.14 Arduino Mega 2560 used in the evaluation system of the lab prototype [145]	72
2.15 Test vessel with nitrogen cushion above the insulating liquid with a ceramic resistor for replication of hot-spot in insulating oil [144]	74
2.16 Test setup for fault gas generation and detection of hot-spot in insulating oil using a ceramic resistor [144]	75
2.17 Fault gases concentrations at room temperature and ambient pressure levels determined by gas chromatography and output voltages of the fault gas sensors [144]	76
2.18 Schematic of the installed prototype on the hermetic transformer [144]	77
2.19 Hermetically sealed railway transformer and its oil filling pipe	78
2.20 Electrical equivalent circuit of the test setup [144]	79
2.21 PRPD pattern of the generated PD fault [144]	79
2.22 The hermetically sealed transformer with the installed lab prototype on the oil filling pipe [144]	80
2.23 Output voltages of the fault gas sensors of the installed laboratory prototype on the hermetically sealed transformer for a long-term measurement [144]	81
2.24 Control system of <i>TGM-101</i>	82
2.25 Casing of the sensor board	83
2.26 Sensor board attached to the cover of the casing	84
2.27 Setup for determining a look-up table for the sensor system	84
3.1 Transformer tank model with numerated valves	88
3.2 Test circuit enabling simultaneous electrical and UHF PD measurements [133]	89
3.3 PRPD patterns corresponding with the surface discharge fault model [133]	91
3.4 PRPD patterns corresponding with the internal discharge fault model [133]	93
3.5 PRPD patterns corresponding with the corona discharge fault model [133]	94

3.6	Reflection coefficient of the UHF probes introduced into the transformer tank via oil valves 1 to 4 and in free space [133]	96
3.7	Transmission coefficient of the UHF probes introduced into the transformer tank with (a) S_{21} and S_{43} , and (b) S_{42} and S_{31} [133]	99
3.8	Test circuit for capturing UHF PD pulses [150]	101
3.9	Frequency spectrum of PD pulses of the internal discharge model received by two UHF probes [150]	102
3.10	Practical approach towards the selection of the optimal frequency range for performing UHF measurements in power transformers [133]	106
3.11	Wide-band measurement with a bandwidth of 1.9 GHz of PRPD patterns associated with internal discharge model at a center frequency of 1.05 GHz [133]	108
3.12	Medium-band measurement with a bandwidth of 70 MHz of PRPD patterns associated with the internal discharge model at a center frequency of 245 MHz	109
3.13	Medium-band measurement with a bandwidth of 70 MHz of PRPD patterns associated with the internal discharge model at a center frequency of 440 MHz	110
3.14	Medium-band measurement with a bandwidth of 70 MHz of PRPD patterns associated with the internal discharge model at a center frequency of 350 MHz	111
3.15	Medium-band measurement with a bandwidth of 70 MHz of PRPD patterns associated with the internal discharge model at a center frequency of 800 MHz	112
4.1	2D analogy model with three UHF probes	117
4.2	2D tank model with the obtained locations of PD in case of erroneous AT determination of the signal received by probe 2	118
4.3	2D tank model with the obtained locations of PD in case of applying selection criteria to erroneously determined AT of the signal received by (a) probe 1, and (b) probe 3	121
4.4	2D tank model with the obtained locations of PD in case of erroneous AT determination of all received signals (a) before, and (b) after applying the selection criteria	123
4.5	PD pulse used as excitation source	125
4.6	EM wave propagation due to PD at time step 2.36 ns	126
4.7	EM wave propagation due to PD at time step (a) 1.38 ns, and (b) 2.57 ns	128

4.8	Overview of the localization algorithm	130
4.9	(a) The wavelet function ψ , and (b) scaling function ϕ of <i>sym5</i> wavelet	132
4.10	Comparing the ATs detected by contrast function method and TWCF method for a set of data-sets captured by four UHF probes [163]	137
4.11	ATs of four simultaneously captured UHF signals; note that ATs are superimposed in some cases [163]	139
4.12	Cross correlation of two UHF signals; the vertical dotted line indicates the location of the maximum value [163]	141
4.13	Effect of wavelet denoising on a typical UHF signal [163]	142
4.14	Metal lattice barrier in combination with pressboard barrier	144
4.15	3D schematic of candidate PD coordinates and the barriers around the PD source [163]	146
4.16	Metal barrier	147
4.17	Frequency spectra of two signals captured by probe 1 [163]	148
4.18	Schematic view of the transformer tank model with four probes inserted through the two lowest and the two highest oil drain valves	150
4.19	View of the surface discharge model next to the active part model inside the tank from its opening	151
4.20	Test circuit for performing PD localization measurements using the UHF technique	152
4.21	Interior of the tank model with the locations considered for the PD fault model in regards to the active part model	153
4.22	Top view of the scaled-down transformer model with cover removed	156
4.23	Test circuit for performing PD localization measurements using the UHF technique	157
4.24	Schematic view of the transformer model with the selected positions for the PD model	158
4.25	Acquired locations and the final determined position for the PD fault in (a) absence, and (b) presence of the active part	160
4.26	Localization accuracy as a function of the number of data-sets considered in absence, and presence of the active part	161
4.27	Entering window of the coordinates of the sensors via the implemented graphical user interface of the PD localization algorithm	163

4.28 Visualized localization results via the implemented graphical user interface of the PD localization algorithm	164
--	-----

List of Tables

1	Failure rate change of transformers in substations and in power plants according to [10]	5
2	Failure rate change of transformers by condition of units according to [10]	6
4.1	Locations of the PD fault model and the UHF probes of the 2D analogy model	117
4.2	Results of analyzing 1000 signal sets for localizing the PD source [163]	138
4.3	Localization accuracy for case 1; direct line of sight between PD source and probes [163]	143
4.4	Localization accuracy for case 2; metal lattice with pressboard barriers; final point obtained by median of ATs [163]	144
4.5	Localization accuracy for case 2; metal lattice with pressboard barriers; final point obtained by clustering method [163]	146
4.6	Localization accuracy for case 3; metal barrier; final point obtained by clustering method [163]	147
4.7	Coordinates of the tip of the UHF probes inserted into the tank model	150
4.8	Existence of an uninterrupted path between PD fault locations and the probes	152
4.9	Coordinates of the considered locations for the PD fault model inside the tank	153
4.10	Localization results in absence of the active part model	154
4.11	Localization results in presence of active part model	154
4.12	Coordinates of the considered locations for the PD fault model inside the tank	157
4.13	Localization results in absence of the active part	159
4.14	Localization results in presence of the active part	159

List of Abbreviations

ABS	Acrylonitrile Butadiene Styrene
AC	Alternating Current
ADC	Analog to Digital Convertor
AF	Antenna Factor
AT	Arrival Time
ATWT	Arrival Time Window Threshold
CFM	Contrast Function Method
DCS	Dynamic Commulative Sum
DFT	Discrete Fourier Transform
DGA	Dissolved Gas Analysis
DSO	Digital Storage Oscilloscope
DUT	Device Under Test
EM	Electromagnetic
EMC	Electromagnetic Compatibility
ERC	Electromagnetic Reverberation Chamber
FAT	Factory Acceptance Test
FDS	Frequency Domain Spectroscopy
FDTD	Finite Difference Time Domain
FID	Flame Ionization Detector
FRA	Frequency Responce Analysis
FTIR	Fourier-Transform Infrared
GC	Gas Chromatography
GIL	Gas-Insulated Line
GIS	Gas-Insulated Switchgear
GSU	Generator Step-Up
GTEM	Gigahertz Transverse Electromagnetic
GUI	Graphical User Interface
HV	High Voltage
IEC	International Electrotechnical Comission

KF	Kleinflansch
LV	Low Voltage
MV	Medium Voltage
PC	Penalized Contrast
PD	Partial Discharge
PDC	Polarization and Depolarization Current
PDF	Probability Density Function
PEC	Perfect Electric Conductor
PRPD	Phase Resolved Partial Discharge
RF	Radio Frequency
RVM	Recovery Voltage Measurement
SNR	Signal to Noise Ratio
TCD	Thermal Conductivity Detector
TDOA	Time Difference Of Arrival
TE	Transverse Electric
TM	Transverse Magnetic
TW	Time Window
TWCF	Time Window Contrast Function
UHF	Ultra High Frequency
VHF	Very High Frequency
VNA	Vector Network Analyzer

Abstract

Transformers are key elements of the power grid. Due to their importance and high initial cost, asset managers utilize monitoring and diagnostic tools to optimize their operation and extend their service life. The main objective of this thesis is to develop new methods in the field of monitoring and diagnosis of transformers in order to reduce maintenance costs and decrease the frequency of forced outages. For this purpose, two concepts are proposed.

Small generator step-up transformers are essential in wind and photovoltaic parks. The first presented concept entails an online fault gas monitoring system for these transformers, specially hermetically-sealed transformers. The developed compact, maintenance-free and cost-effective monitoring system continuously tracks the level of the key leading indicators of transformer faults in the gas cushion.

The second presented concept revolves around partial discharge (PD) assessment by the UHF measurement technique, which is based on capturing the electromagnetic (EM) waves emitted in case of PD in the insulation of a transformer. In this context, the complex EM system established when probes are introduced into the tank of a transformer and with PD as the excitation source is analyzed. Drawing on this foundation, a practical approach to the detection and classification of PD with the focus on the selection of the optimal frequency range for performing UHF measurements depending on the device under test is presented. The UHF measurement technique also offers the possibility of PD localization. Here, the determined arrival time (AT) of the captured signals is critical. A PD localization algorithm, based on a multi-data-set approach with a novel AT determination method, is proposed. The methods and algorithms proposed for the detection, classification and localization of PD are validated by means of practical experiments.

Keywords:

Power Transformer, DGA, Partial Discharge, Condition Assessment, Monitoring, UHF Measurement Technique, PD Diagnosis, PD Localization

Zusammenfassung

Transformatoren sind Knotenpunkte des Energienetzes. Aufgrund der Bedeutung und der hohen Anschaffungskosten dieser Komponenten setzen die Betreiber Überwachungs- und Diagnosemethoden ein, um den Betrieb zu optimieren und die Lebensdauer zu erhöhen. Das Hauptziel dieser Dissertation besteht darin, neue Verfahren im Bereich der Überwachung und Diagnose von Transformatoren zu entwickeln, um die Wartungskosten zu senken und die Häufigkeit erzwungener Ausfälle zu reduzieren. Zu diesem Zweck werden zwei Konzepte vorgelegt.

Kleine Maschinentransformatoren sind in Wind- und Photovoltaikparks unverzichtbar. Das erste vorgestellte Konzept umfasst ein Online-Fehlgas-Überwachungssystem insbesondere für hermetisch verschlossene Transformatoren. Das entwickelte kompakte, wartungsfreie und kosteneffiziente Überwachungssystem verfolgt kontinuierlich den Fehlgasgehalt von Schlüsselgasen im Gaspolster.

Das zweite vorgestellte Konzept befasst sich mit der unkonventionellen UHF-Messtechnik für Teilentladung (TE). Hierbei wird das komplexe EM-System analysiert, welches durch die Einführung von Sensoren in den Transformatorrentank mit TE als Anregungsquelle entsteht. Auf dieser Grundlage wird ein praktischer Ansatz zur Erkennung und Klassifizierung von TE vorgestellt, wobei der Schwerpunkt auf der Auswahl des optimalen Frequenzbereichs für die Durchführung von UHF-Messungen in Abhängigkeit vom Prüfling liegt. Die UHF-Messtechnik bietet zudem die Möglichkeit der TE-Lokalisierung. Dabei ist die ermittelte Ankunftszeit der erfassten Signale entscheidend. Ein Algorithmus zur Lokalisierung von TE, der auf einem Multi-Datensatz-Ansatz mit einer neuartigen Ankunftszeit-Bestimmungsmethode basiert, wird vorgestellt. Die entwickelten Methoden und Algorithmen werden anhand von Experimenten validiert.

Stichwörter:

Leistungstransformator, DGA, Teilentladung, Zustandsbewertung, Überwachung, UHF-Messtechnik, TE-Diagnose, TE-Lokalisierung

Overview

This thesis aims to introduce and explore the application of various methods and techniques for monitoring and diagnosis of power transformers. The subsequent chapter provides an overview of the topics covered and outlines the objectives of the thesis.

Chapter 1 provides the theoretical background for the methods, measurements, and approaches utilized in this work. It covers the most common types of faults that can occur in transformers with focus on partial discharge. Subsequently, the fundamentals of various diagnostic techniques, in particular the gas-in-oil analysis and partial discharge assessment, are discussed. Furthermore, the methods and approaches in this work are described.

Chapter 2 presents the development of a fault gas online monitoring system for hermetically sealed power transformers with a gas cushion. This chapter discusses the design, implementation, and evaluation of a sensor system for tracking the fault gas level in the gas cushion of a transformer. The sensor system is capable of detecting potential faults before they become critical and issues an alarm signal based on the level of the fault gas detected. In addition, the chapter presents the integration of auxiliary sensors for monitoring environmental parameters and compensating the output voltages of the fault gas sensors from the effects of temperature and pressure.

Chapters 3 and 4 focus on the ultrahigh frequency (UHF) measurement technique for the detection and localization of partial discharge activity in power transformers. Chapter 3 presents a practical approach for selecting an optimal frequency range based on the properties of the device under test and discusses the application of the UHF technique in the detection and classification of partial discharge. Chapter 4 proposes a novel algorithm for the localization of partial discharge using the UHF technique by means of multilateration. The proposed algorithm is evaluated experimentally, and the results are presented and analyzed.

The final chapter of this thesis summarizes the approaches presented in

the previous chapters and provides a conclusion. It highlights the contributions of this work and discusses the potential of the proposed monitoring and diagnostic approaches for improving the reliability, safety, and performance of power transformers.

Introduction

The power grid is of paramount importance in every sector of society. Economic factors such as rising energy prices, environmental concerns such as greenhouse gas emissions, and technical issues with power device maintenance and operation as well as the increasing demand for energy from both households and industrial sectors lead to structural changes in power system configurations, as well as expansion and development of various new technologies for condition monitoring and assessment. The goal of these modifications and restructuring is to leverage new technologies to convert the power grid into one that is more dynamic, safe, efficient, and environmentally friendly. Moreover, the expansion of renewables is expected to be expedited by eliminating barriers and rationalizing planning and approval procedures. In such a competitive climate, transmission system and distribution network operators are striving to improve productivity and service quality while lowering the cost of equipment installation and maintenance, as well as the frequency of forced outages and shortage of electric energy.

Transformers, being one of the most expensive components of the electric power grid, account for a significant amount of the investment in electrical power transmission and distribution networks, and they contribute significantly to the continuity of energy supply in the long run. Power outages, poor service, and customer dissatisfaction result from transformer failures, which affect not only the reliability of the power grid but also the profitability of electric utilities. Since transformer replacement and maintenance are very costly, it is critical to monitor and evaluate the condition of transformers in order to determine suitable procedures to extend their life and manage the associated maintenance activities [1].

Several voltage transformations are required between the power generation source and the load. The power grid can be categorized into low voltage (LV), medium voltage (MV), and high voltage (HV). Power transformers manage all from stepping up the voltage level for transmission to stepping

down the voltage level for distribution to consumers. For this purpose, depending on the application, various transformer types are utilized. They are quite essential for the stability of the power grid. Taking into account step-up, step-down and distribution transformers, the total transformation capacity of all transformers in a power system can be estimated to be about four times the total installed capacity of the generating units [2].

Increased productivity and asset lifespan are a necessity in substantially restructured power systems owing to competition between institutions and power providers with restricted funds and resources. On the one hand, without a scheduled maintenance strategy, the likelihood of a power system failure increases; on the other hand, prolonging the service life of a crucial component such as a transformer increases the probability of a forced outage. As a result, new methods of monitoring, diagnosing, and maintaining equipment have recently been proposed in order to extend the equipment's lifetime and increase its reliability [3–5].

Condition monitoring, as well as preventive, predictive, and proactive maintenance procedures, are examples of general asset management actions that can be used on any valued asset, such as distribution and power transformers. Various criteria and status indicators may be used to maintain the lifetime of transformers. Temperature hot-spots, for example, can be used as a monitoring parameter for condition assessment, since they indicate an overload or a major issue within the transformer, and the progression over time of the same parameter can be used to estimate the transformer's remaining life. The higher the hot-spot temperature, the more decrease in the lifespan of the particular transformer is to be expected [6]. Transformer asset management is classified into three main categories [7]:

1. Procedures for condition monitoring and assessment
2. Maintenance and repair plans
3. Assessing aging process, health and remaining lifetime of the transformer

The performance and reliability of a power system mainly depend on the condition of its transformers. Maintenance or replacement expenses, threats to the environment, explosion and fire hazards, and a significant reduction in corporate profit are all potential outcomes of transformer failures. A transformer's replacement expenses may range from a few thousand to several million dollars [8]. Early failure detection and diagnosis may decrease repair expenses by up to 75 % and profit loss by up to 60 %, resulting in a

2 % yearly reduction on the price of a new transformer [9]. As shown in Table 1, the failure rate of a transformer rises considerably as it ages. The table presents the failure rate change of transformers in substations and power plants as a function of transformer age. It consists of three columns: the

Table 1: Failure rate change of transformers in substations and in power plants according to [10]

Transformer Age	Substation Units	Generator Units
< 16 years	0.5 %	0.8 %
16 - 24 years	1.0 %	1.5 %
25 - 34 years	1.5 %	2.0 %
35 - 50 years	2.0 %	2.5 %
> 50 years	3.0 %	3.5 %

first column lists the different age ranges of the transformers, and the second and third columns show the corresponding failure rates for transformers in substations and generator units, respectively. In the context of power transformers, a failure is defined as a condition in which the transformer is unable to perform its intended function. This can include a variety of reasons that prevent the transformer from operating properly, such as [11]:

1. Electrical failures:

These can include short circuits, open circuits, and insulation failures. Electrical failures are often the result of internal or external electrical stresses, such as overloading or lightning strikes.

2. Mechanical failures:

These issues can encompass winding deformation, core or coil displacement caused by significant forces, such as those experienced during short circuits, and mechanical damage resulting from external events like earthquakes or accidents.

3. Cooling system failures:

Cooling systems are critical for dissipating the heat generated by the transformer. Failures in the cooling system can cause overheating and damage to the transformer.

4. Accessories and components failures:

Transformers rely on a range of accessories and components, such as

bushings, tap changers, and control systems, to operate correctly. Failures in these components can also lead to transformer failures.

In Table 1, the failure rate is given as a percentage, and it increases with the age of the transformer. For example, for transformers that are less than 16 years old, the failure rate is 0.5 % and 0.8 % for substations and generator units, respectively. In contrast, for transformers that are more than 50 years old, the failure rate increases to 3.0 % and 3.5 % for substations and generator units, respectively.

The failure rate of different transformer types varies; for example, step up transformers in power plants have a higher failure risk than those in substations. The failure rate is strongly proportional to the transformer condition, as shown in Table 2, which presents different condition ratings of transformers and their corresponding failure rates. The condition rating indicates the overall health and performance of the transformer, with good representing the best condition and bad indicating the worst condition. According to

Table 2: Failure rate change of transformers by condition of units according to [10]

Condition Rating	Failure Rate
Good	0.6 %
Satisfactory	1.0 %
Fair	1.5 %
Poor	2.0 %
Bad	3.0 %

the data provided by Cigré, transformers with a good condition rating have a failure rate of 0.6 %, while transformers in satisfactory condition have a slightly higher failure rate of 1.0 %. As the condition of transformers deteriorates, the failure rates increase. The failure rate of transformers in poor condition is roughly three times than those in good condition [10]. This underscores the importance of regular maintenance based on monitoring and condition assessment to ensure the reliability and longevity of transformers in power systems.

Monitoring and assessment techniques, as well as new maintenance approaches, have become major challenges for the reliable operation of the power system due to the rising age of existing transformers [2]. The two processes of condition monitoring and condition assessment are intertwined. Transformer condition monitoring entails the development, implementation,

and evaluation of techniques and/or equipment to gather data and monitor certain parameters in order to prolong the asset's operational service life, while the condition assessment focuses on the development of new technologies to analyze data gathered in order to evaluate the transformer's present performance and forecast future operating trends [5].

A transformer may fail due to an electrical, electromagnetic, insulating, thermal, or chemical fault [12]. Between 1996 and 2010, a Cigré working group gathered 964 significant failures from a total of 167,459 transformers in 21 countries. Hereby, major failures were defined as those that result in a transformer outage lasting more than seven days [13]. Another investigation, which also included the cause of the fault, found 799 serious failures among the 22,181 transformers examined. According to this analysis, the transformer's winding, tap changer, and bushing have the highest failure rate, with the transformer's core, tank, cooling unit, and current transformer being the cause of a failure in only about 5 % of the cases [14], as illustrated in Figure 1.

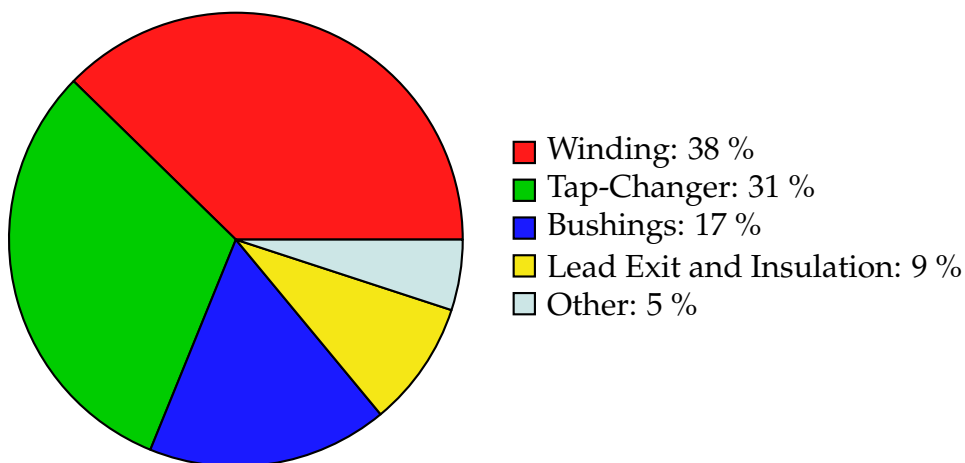


Figure 1: The breakdown of failure causes in terms of the various constituents of a transformer according to [14]

Various techniques have been utilized for condition monitoring and diagnosing the state of power transformers, with offline testing and time-based assessment being the prevailing methods. However, there has been a notable shift towards adopting online monitoring systems in recent years. This approach enables the collection of real-time data while the transformer is in operation, facilitating early detection of potential faults. Leveraging the capabilities of modern computers, processing data and managing a database has become readily feasible.

Condition assessment both in terms of monitoring and diagnosis is costly. When determining the budget for preventive measures, the decisive factor is one of economic nature. Two main aspects are hereby in focus; the first is the potential savings from avoiding forced outages. A forced outage caused by a failure not only compromises electrical grid reliability, but it is also accompanied with significant expenses for downtime and expensive steps to repair or replace the transformer. The second factor is the acquisition value of the asset. An asset's replacement value is among the deciding factors for determining the budget for installing monitoring devices and the general asset management strategy. Therefore, the monitoring approaches vary depending on the situation and on the transformer. Depending on the power rating and the corresponding size of the transformer, the asset manager decides on the appropriate measures for monitoring and diagnosis. Larger transformer units being utilized in crucial nodes of the grid demand a higher investment reflecting their value, both in financial and operational terms.

Among the different types of transformers as essential components of the power grid, generator step-up (GSU) transformers used in wind turbines and solar parks, are particularly critical. As these transformers are situated between the power network and a diverse range of generators, reliable monitoring and evaluation methods are necessary to ensure the continued and safe operation of the power grid. Due to factors such as their widespread geographic distribution, lack of monitoring, and greater susceptibility to unbalanced operation, GSU transformers are prone to faults and failures. Furthermore, owing to their variety and their application in numerous areas, it is challenging to undertake maintenance services at regular intervals due to the associated expense, and occasionally due to lack of simple access. As a result, these transformers are subjected to extreme loads, which could cause them to age prematurely. This could lead to excessive maintenance or replacement costs on the one hand, while the consumers experience power interruptions on the other hand, raising economic and social issues.

To minimize the risk of transformer failures and ensure their reliable operation, various monitoring equipment has been developed in recent years. These monitoring systems can be categorized into two main types: online monitoring and offline monitoring. Online monitoring systems are designed to continuously monitor the operational parameters of transformers in real-time. They use sensors and advanced data acquisition techniques to measure key parameters such as temperature, oil level, gas concentrations, and

electrical parameters. By analyzing the collected data, these systems can detect abnormalities or deviations from normal operating conditions, allowing for timely maintenance or corrective actions. Offline monitoring, on the other hand, involves periodic inspections and tests performed during planned maintenance outages or when the transformer is temporarily taken out of service. This includes visual inspections, oil sampling for laboratory analysis, and comprehensive diagnostic tests such as dissolved gas analysis (DGA), insulation and winding resistance measurements, and partial discharge (PD) testing. Offline monitoring provides valuable insights into the condition of the transformer and helps identify potential issues that may require maintenance or repairs. While both online and offline monitoring systems offer valuable information about transformer health, online monitoring systems are generally more advanced and provide continuous, real-time data.

The aging of components and the deterioration of the transformer's insulation system during its lifespan is an inevitable fact in the power system. As a component ages, it becomes increasingly degraded and requires more time to repair until it nears the end of its service life. The results presented in Table 1 also reflect this fact. Maintenance strategies may prolong the transformer's lifespan depending on the failure rate curve vs equipment lifetime, known as the bathtub curve as illustrated in Figure 2, however, the repair is more costly the closer the transformer gets to the end of its lifespan [15, 16].

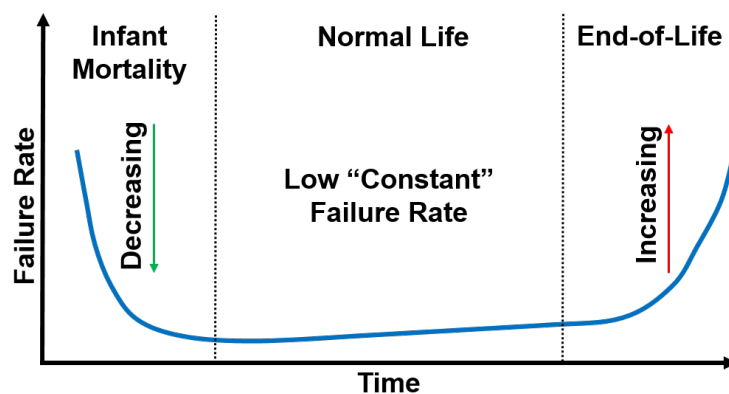


Figure 2: Failure rate vs. lifetime of a transformer adapted from [15]

Physical life, technical life, and economic life are three aspects of a transformer's lifespan. The physical life covers the lifespan of a transformer from the time it is first energized to the time it can no longer operate under normal circumstances and must be put out of service. Since the stress on different components of a transformer vary due to operational and environmental

reasons, certain components are more likely to reach the end of their service life, which reflects the technical lifespan. Furthermore, some equipment is no longer economically valuable, although it is still physically intact, meaning the component has reached the end of its economic lifespan. The asset's value declines gradually until it approaches zero, or until the equipment reaches the end of its economic life [16, 17].

The implementation of maintenance plans is the final step in transformer asset management. When a transformer is taken off the grid, it has an impact on the power system, however, a forced outage will be more costly. Maintenance, as a strategic tool, ensures that equipment and industrial processes run properly and reliably. Transformer maintenance should be scheduled ahead of time to avoid expensive interruptions.

Although monitoring is essential for asset management, supplementary diagnostic measurements are necessary to determine the optimal maintenance strategy based on the available data. In this regard, DGA is a technique used to monitor the condition of power transformers by analyzing the gases dissolved in transformer oil. The presence of certain gases in the transformer oil indicates the type of fault present in the transformer. The most common gases analyzed in DGA include hydrogen (H_2), methane (CH_4), ethylene (C_2H_4), acetylene (C_2H_2), and carbon monoxide (CO). These gases are produced by the decomposition of transformer oil and insulating material when a fault occurs in the transformer. DGA is a widely used and well-established method for monitoring and diagnosing power transformers. It is a non-invasive technique that can provide valuable information on the condition of the transformer. The results of DGA are used to identify the type and severity of the fault and to determine the appropriate maintenance or repair actions [18, 19].

For monitoring purposes, PD is a suitable target, since it is one of the early indicators of imperfections in the insulation system of a transformer [20]. Although the conventional electrical PD measurement method as described in *IEC 60270* [21], is well-established and widely used in the field of power transformer testing, it has certain limitations, especially for onsite measurements and online monitoring. Hence, alternative methods are investigated as complementary tools for PD diagnosis. One of these methods, which is based on the detection and evaluation of electromagnetic waves emitted in case of PD activity in the very high and ultrahigh frequency (VHF and UHF, from 100 MHz up to 3 GHz) is the UHF measurement technique.

In this thesis, the focus lies on the development of monitoring and diagnosis methods for liquid-filled transformers. In the monitoring and diagnosis of power transformers, two crucial and highly responsive techniques employed are DGA and PD measurements. The proposed approaches in this thesis are also build on these methods; firstly, a novel fault-gas-monitoring-system for smaller units, such as GSU Transformers in wind and photovoltaic farms is presented. Secondly, the application of the UHF measurement techniques for detection, classification, and localization of PD for larger units is proposed. These approaches can help to ensure the safe and efficient operation of power transformers and to prevent costly failures and downtime.

The proposed fault-gas-monitoring-system for hermetically sealed transformers offers a cost-effective and reliable approach to monitor and assess the condition of these critical components in the power grid. Unlike existing monitoring systems that analyze dissolved gases in the transformer oil, necessitating a gas extraction unit, this novel approach focuses on undissolved gases present in the gas cushion of the transformer. Among the common fault gases in transformers, hydrogen stands out with the lowest solubility due to its small, nonpolar nature, low molecular weight, and weak intermolecular forces, making it relatively insoluble compared to other gases [22]. Furthermore, hydrogen is particularly significant in DGA analysis as it is the most abundant gas produced during the early stages of a fault. Therefore, monitoring hydrogen concentrations in transformer oil is a common and effective method for detecting and diagnosing incipient faults in power transformers. Elevated levels of hydrogen in transformer oil can indicate the presence of PD, arcing, or overheating, which can lead to more serious faults if left unaddressed [23]. Hence, the focus of the proposed monitoring system will be on targeting hydrogen in the gas cushion.

The application of UHF technique in PD measurements is well established for gas-insulated switchgear (GIS) and gas-insulated transmission lines (GIL) [24–26]. In this thesis, the application of the UHF measurement technique in detection, classification, and localization of PD in larger transformer units is investigated. In this regard, suitable methods and algorithms are developed and verified experimentally. In the first step, a practical approach for the selection of the optimal frequency range for conducting UHF measurements aiming at detecting and categorizing PD is presented. Subsequently, the use of the UHF measurement technique in PD localization using multilateration is discussed. PD localization is an important aspect of PD diagnosis as it can provide valuable data, enabling informed maintenance

and repair decisions. Multilateration is a well-established technique for PD localization, which involves measuring the time delay between PD signals detected at multiple locations. However, the accuracy of UHF measurements for PD localization using multilateration may be affected by signal attenuation and reflection, which can present unique challenges. In this thesis, an effective localization algorithm with a novel approach for the determination of the arrival time of UHF signals is presented.

The efforts in this thesis aim at improving the condition assessment of oil-immersed transformers, allowing the transmission and distribution system operators to select the optimal maintenance plan for their assets, leading to an increase in operational reliability and an enhancement in the economic efficiency of these components.

Chapter 1:

Theoretical Background

The insulation system of a high voltage asset is the main focus of condition assessment methods both during the factory acceptance test (FAT) as well as after commissioning. In case of power transformers, chemical approaches along electrical fault diagnosis methods are among the most important techniques for monitoring their condition. Electrical methods can detect defects in the core, winding, bushing, and their insulation. Measurement of capacitance, loss factor, induced voltage test, insulation resistance, insulation withstand voltage at power frequency and at lightning or switching impulses, winding turn ratio and winding resistance are among the common tests. The advancements in the power industry have resulted in a demand for advanced electrical techniques and instruments to effectively assess and monitor the health of transformers. In recent years, complementary methods have been added to traditional electrical methods. These include frequency response analysis (FRA), frequency domain spectroscopy (FDS), recovery voltage measurement (RVM), and polarization and depolarization currents (PDC) techniques [27, 28].

Partial discharges (PD) are among the main indicators of a defect in the insulation system. In the context of power transformers, two commonly used PD detection techniques are dissolved gas analysis (DGA) and electrical PD measurement in accordance to *IEC 60270* [21].

DGA is a non-invasive diagnostic technique that analyzes the gases dissolved in transformer oil, which are produced as a result of a fault. The analysis of these gases can provide valuable information on the state of the transformer insulation system. DGA is a widely employed diagnostic technique for high voltage oil-filled equipment, making it one of the most prevalent methods. *IEC 60599* provides guidance on the interpretation of DGA results and the recommended actions to be taken based on those results [29].

Electrical PD measurement is another commonly used technique in

power transformers. *IEC 60270* covers the principles and techniques of conventional PD measurement, as well as the interpretation and evaluation of the measurement results [21]. The UHF measurement technique is among the non-conventional measurement methods that are applied as a complementary tool in PD diagnostics of power transformers. Although it is not separately standardized, the technical specification *IEC TS 62478* provides recommendations on conducting PD measurement with the UHF and acoustic methods [30].

In the following, the fundamentals of PD are outlined and different approaches on the topic of PD diagnosis are described. Subsequently, the principles of DGA in power transformers are discussed. Finally, the UHF measurement technique is addressed.

1.1 Partial Discharge

In the *IEC 60270* [21], PD is defined as "*a localized electrical discharge that only partially bridges the insulation between conductors and which can or cannot occur adjacent to a conductor*". Partial discharges are generally caused by local electrical stress concentrations in the insulation or on the insulation's surface. Such discharges occur as pulses with a length of considerably less than $1 \mu\text{s}$. PD is a phenomenon that takes place in dielectric materials when a high electric field is applied. It can lead to degradation and failure of the insulation system, which can be catastrophic in high voltage applications such as power transformers, cables, terminations, etc. In the following, the PD phenomenon is described using the Gemant and Philippoff capacitive model introduced in [31].

1.1.1 PD Phenomenon

One of the models used to describe the PD phenomenon is the dielectric with cavity model. This model assumes that the dielectric material contains a cavity or void, which creates a local electric field enhancement. The presence of the cavity changes the electric field distribution in the dielectric material, which affects the breakdown voltage of the insulation system. The model consisting of a dielectric with an air-filled cavity and an applied voltage $v(t)$ is shown in Figure 1.1.

The dielectric with cavity model can be represented by an equivalent circuit, as shown in Figure 1.2. The model consists of three capacitors, C_1 , C_2 ,

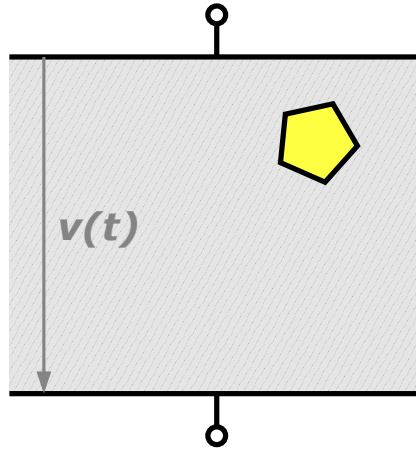


Figure 1.1: Dielectric with air-filled cavity adapted from [32]

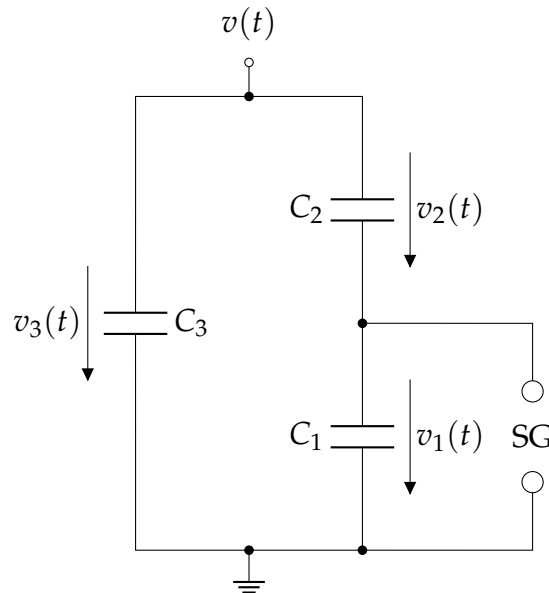


Figure 1.2: Equivalent circuit diagram for a dielectric with air-filled cavity with a spark gap SG adapted from [32]

and C_3 . C_1 represents the capacitance of the air-filled cavity, while C_2 represents the capacitance of the dielectric material in series with the cavity. C_3 represents the capacitance of the remaining dielectric material. A spark gap SG represents the breakdown in the cavity when the applied voltage $v(t)$ to the dielectric sample results in an higher voltage stress than the ignition voltage of the cavity [32].

When a high electric field is applied to the dielectric material, electrons are accelerated and collide with gas molecules in the cavity. This process ionizes the gas and creates a plasma, which conducts electricity. The spark gap in parallel with capacitor C_1 represents the discharge channel created by the plasma. The discharge channel creates a short circuit across capacitor C_1 ,

which changes the voltage drop across capacitor C_2 .

Figure 1.3 shows the applied voltage $v(t)$ and the voltage of the cavity $v_1(t)$ with and without PD. Without PD, the voltage of the cavity follows the

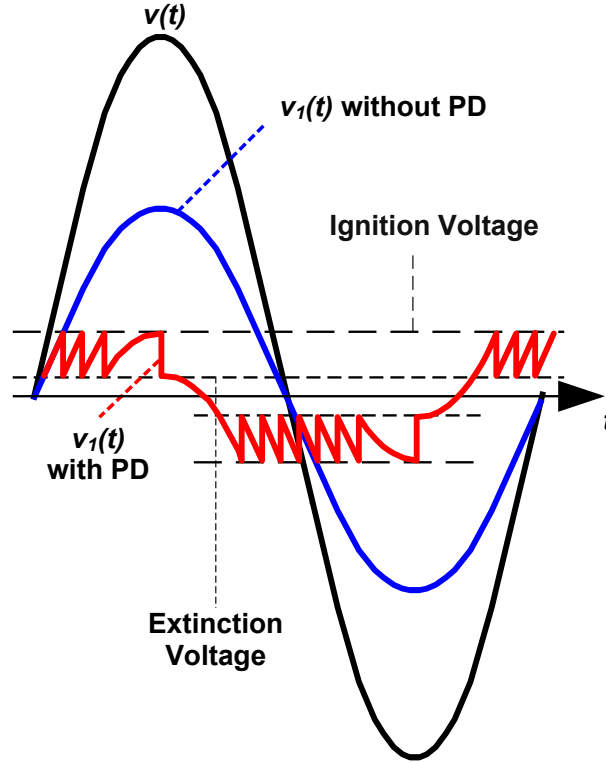


Figure 1.3: External voltage $v(t)$, and cavity voltage $v_1(t)$ with and without PD adapted from [32]

applied voltage. However, with PD, the voltage of the cavity drops abruptly when the discharge channel is created. When PD occurs, free electrons are accelerated in the electric field, leading to ionization and the creation of positive and negative ions. The electrons and ions can then recombine, leading to the emission of photons or acoustic waves.

If a breakdown occurs, the current flowing through the spark gap in the Gemant and Philippoff capacitive model (as shown in Figure 1.4) is the combination of two components: The current $i_1(t)$ that discharges the capacitance of the cavity C_1 , and the current $i_2(t)$ at the capacitance C_2 [31]. Moreover, the current $i_2(t)$ flowing through C_2 also flows through the capacitance C_3 . It is common practice to distinguish between the internal and external charges in the circuit. The internal charge, denoted as q_1 , is also known as the physical or true charge, and it is equal to the time integral of both transient currents, $i_1(t)$ and $i_2(t)$. This results in a voltage step, ΔV_1 , across the cavity capacitance C_1 [33]. It can be assumed, that $C_3 \gg C_1 \gg C_2$ [34]. Hence, the internal

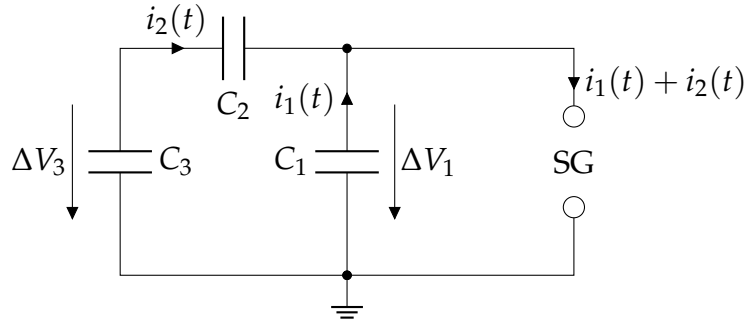


Figure 1.4: Transient currents passing through the PD equivalent circuit in case of breakdown adapted from [33]

charge q_1 can be calculated by:

$$q_1 \approx \Delta V_1 \cdot (C_1 + C_2) \quad (1.1)$$

When the transient current $i_2(t)$ flows through the series combination of capacitances C_2 and C_3 , the external charge q_3 is formed, which is equal to the time integral of $i_2(t)$. This charge causes a voltage step ΔV_3 to occur across C_3 . The magnitude of ΔV_3 is proportional to the capacitive divider ratio $\frac{C_2}{C_2 + C_3}$, which can be approximated as $\frac{C_2}{C_3}$. Thus, the external charge that can be detected at the terminals of the test object can be expressed as:

$$q_3 = \Delta V_3 \cdot C_3 \approx \Delta V_1 \cdot C_2 \quad (1.2)$$

Hence, ΔV_1 is calculated by:

$$\Delta V_1 = \frac{q_3}{C_2} \quad (1.3)$$

By substituting (1.3) in (1.1), q_3 equals to:

$$q_3 \approx q_1 \cdot \frac{C_2}{C_1 + C_2} \approx q_1 \cdot \frac{C_2}{C_1} \quad (1.4)$$

Considering the condition $C_1 \gg C_2$, the external charge q_3 that can be detected at the electrodes of the test object is significantly smaller than the internal charge q_1 . In other words, the voltage step ΔV_3 across the capacitance C_3 is much smaller than the voltage step ΔV_1 across the cavity capacitance C_1 .

In the context of PD, the terms "true charge" and "apparent charge" refer to internal and external charge, respectively. The apparent charge is the charge that can be measured by a PD detection system and is expressed in

coulombs, and is proportional to the amplitude of the PD signal [21]. The apparent charge is a useful parameter for detecting and monitoring PD events, as it can provide information about the severity of the PD activity. However, the apparent charge does not represent the total amount of charge generated by the PD events, as it only accounts for the charge that is detectable by the measurement system. The true charge, on the other hand, is the total amount of charge generated by the PD events, including the charge that is not detectable by the measurement system. The true charge is difficult to measure directly, as it is distributed over a large area and is often shielded by the surrounding insulation material. The difference between the apparent charge and the true charge can be attributed to several factors, such as the location and size of the PD cavity, the dielectric properties of the insulation material, and the frequency and duration of the applied voltage [35, 36].

In practice, the apparent charge is used as a proxy for the true charge, as it provides a convenient and measurable parameter for detecting and monitoring PD events. However, it is noteworthy that the apparent charge does not represent the total amount of charge generated by the PD events and may underestimate the severity and risk of insulation failure. Calibration is essential for accurate PD measurements because the apparent charge depends on the PD detection system and the measurement conditions. Calibration involves comparing the PD detection system with a reference system using a calibrated PD source. The calibration can be performed using a standard PD source, which can generate PD signals with various characteristics. The calibration process should consider the effects of the measurement system, such as the frequency response, the sensitivity, and the noise level. The calibration should also consider the effects of the ambient conditions, such as the temperature, the humidity, and the pressure. The calibration results should be traceable to a national or international standard to ensure the accuracy and reliability of the PD measurements [37–39]. In the following, the measurement of PD is discussed.

1.1.2 Measurement of PD

The measurement of PD is one of the most essential techniques for determining the condition of a high voltage asset's insulation. Since PD causes a progressive degradation of insulating materials, which finally leads to electrical failure, data collected via PD testing and monitoring provides valuable

information about the component. A total failure of the apparatus might result from such an electrical failure. The guidelines for measuring PD are described in *IEC 60270* [21]. Partial discharges are generated when the electrical stress within the insulation exceeds the local dielectric strength. This can occur in regions of the insulation where the electric field is particularly intense or inhomogeneous, leading to localized breakdown of the insulating material. The breakdown of the insulation can be caused by a variety of factors, including the presence of voids or cavities within the insulation, which can act as areas of increased electrical stress concentration. Other factors that can contribute to partial discharge include the presence of contaminants within the insulation, which can reduce its dielectric strength, and the effects of aging and degradation on the insulation material. Regarding PD in high voltage apparatus, the following factors are essential for PD-based diagnosis and subsequent condition assessment:

1. Type of PD
2. Severity of the damaging effect
3. Location of PD

The types of PD may be distinguished, i.e. a categorization of PD in discharges at sharp points or edges in a gaseous environment (so-called corona discharges), discharges at interfaces of different insulating materials (surface discharges), and discharges within insulation (internal discharges) is feasible based on the electrode configuration [40]. On the measurement front, regarding alternating current (AC), which is the subject of this thesis, parameters such as phase angle of the occurring PD pulse sequence in respect to the applied AC voltage, PD pulse intensity, and their polarity can be utilized to obtain a phase resolved partial discharge (PRPD) pattern. Each PD type is associated with a pattern image that has certain features. There is a large database, and this method is extensively used to evaluate conventionally obtained PD data and determine the type of PD [32].

1.1.2.1 Conventional Electrical PD Measurement Method

The intensity of PD, among other factors, is assessed in order to establish how severe the destructive impact of PD on the insulating material is. The International Electrotechnical Commission (IEC) has developed a standard for measuring PD activity in high-voltage equipment: *IEC 60270* [21]. This standard outlines the general principles of PD measurement and provides

guidance on the measurement procedures and interpretation of results. In this regards, a coupling capacitance (C_C) is usually connected in parallel to the device under test (DUT) for measuring the pulse amplitude with a high sensitivity. Both are connected to a test transformer with a current limiting resistor (R). A measuring impedance (MI) is put in series with either the DUT or the C_C . A typical PD test circuit is presented in Figure 1.5.

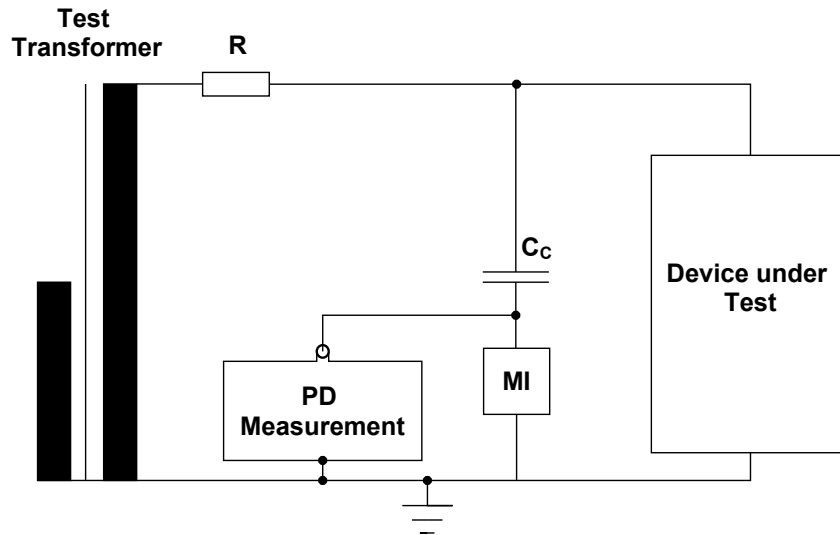


Figure 1.5: Overview of a partial discharge test circuit adapted from [21]

For measurements on power transformers, the bushing capacitance tap can be employed as C_C . The bushing tap is originally intended for capacitance and dissipation factor measurements [34]. For PD measurements, the high voltage bushing capacitance C_1 is used as the coupling capacitance C_C of the circuit shown in Figure 1.5. A simplified version of this test circuit is presented in Figure 1.6. Here, the transformer is fitted with a capacitance graded bushing. Hence, the bushing capacitance is employed as the coupling capacitance. The capacitance that appears across the input impedance of the coupling device when it is connected to a bushing tap can affect the sensitivity of the partial discharge measurement [21].

In case of PD, an electric discharge current flows through the circuit, as discussed in the previous section. It is not possible to measure the real charge turnover, since it is not directly accessible. However, the charge exchange between the coupling capacitor and the DUT can be measured and is described as the apparent charge. In reality, the apparent charge is much smaller than the real charge turnover, but has proven to be a suitable parameter for the quantification of the intensity of PD, as was discussed in the previous section. Moreover, since the apparent charge is considered for the evaluation,

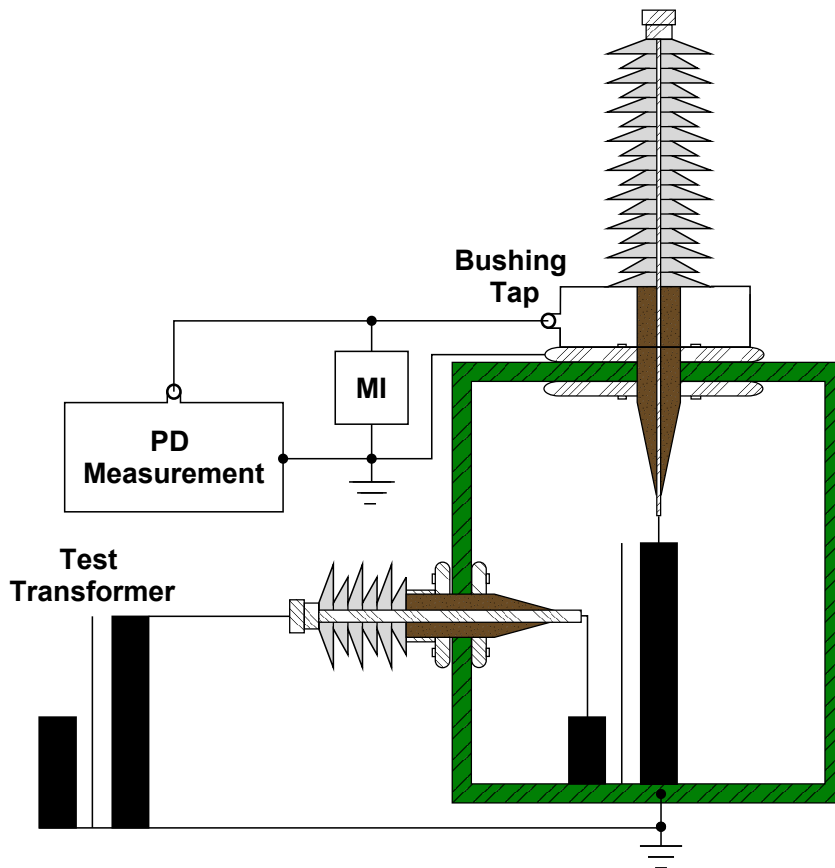


Figure 1.6: Simplified circuit for PD measurements for power transformers adapted from [21]

the electrical PD measurement can be calibrated by injecting a current impulse with a known charge quantity at the terminal of the DUT. This step is carried out when the measuring circuit is completely set up including the DUT but without applying high voltage. Hence, in the calibration, all stray capacitances are included, assuming that the pulse injection is carried out as close to the high voltage terminal of the DUT as possible. Up to this day, the only PD measuring method that offers the universal possibility of calibration, and therefore the determination of the apparent charge, is the electrical PD measurement method [32]. By measuring the intensity of the PD fault, the severity of the damaging effect can be addressed.

The conventional electrical PD measuring method is the standard approach in high voltage components. However, onsite measurements sometimes bear excessive interfering signals that cannot be suppressed by means of the methods applied during the FAT or in research facilities. Since the conventional method is susceptible to external disturbances, this is a major challenge, especially for on-site measurements. Another limitation of the conventional method is the aspect of PD localization. Electrical broadband

PD measurement methods utilize the characteristic distortion of a PD signal caused by its transmission through the winding to the decoupling point in order to determine the location of the PD fault. This method enables identification of all PD pulses originating from the same source, as they exhibit the same distortion, while PD signals from different origins exhibit distinct deformations and can be differentiated. However, this method is associated with high complexity and can only be applied, if the sectional transfer function of the winding is known prior to localization measurements [41–43]. Moreover, the localization of the PD fault is not satisfactory, since it only offers an approximate point along the winding in which PD occurred [44]. Hence, other non-electrical techniques have been developed in recent years.

Conventional PD measurement method, as standardized by *IEC 60270* [21], have been widely used in the industry for decades to assess the health of electrical insulation in high-voltage systems. However, this approach has limitations, as discussed in this section. To offer additional tools for PD assessment, researchers have developed unconventional PD measurement techniques that utilize various sensing technologies, such as optical, ultrasonic, chemical and radio frequency sensors. These new methods provide potential advantages over conventional PD measurements, and will be discussed in the subsequent section.

1.1.2.2 Unconventional Methods

Alternate aspects of PD, which can be used for its characterization, are its byproducts, such as heat or emitted light in the ultraviolet and/or infrared range, acoustic pressure waves in the ultrasonic range, chemical reactions and the formation of the associated key gases e.g. in oil-insulated transformers, and the emission of EM waves due to the high frequency pulses [34]. In the following, these aspects are outlined.

Thermal and Optical Techniques

Thermal techniques for transformer condition monitoring typically use infrared radiation in the far-infrared or thermal-infrared regions of the spectrum, which have frequencies between approximately 3×10^{11} Hz and 4×10^{14} Hz. These techniques may include the use of thermal imaging cameras or infrared sensors to detect hot spots or temperature variations in the transformer. Optical techniques for transformer condition monitoring typically use light in the visible and near-infrared regions of the spectrum, which have frequencies between approximately 4×10^{14} Hz and 8×10^{14} Hz. These

techniques may include the use of optical fibers, cameras, or laser-based sensors to measure parameters such as temperature, vibration, or color [45, 46]. The oil's optical and thermal characteristics, such as optical absorption coefficient, thermal conductivity, and thermal diffusion, vary as it ages, and these qualities may be employed as complimentary approaches for condition monitoring [47]. The heat generated by electrical losses in the winding and core is one of the key concerns with transformers. Since heat is among the main causes of transformer failures, temperature monitoring indicates the regions that are subjected to the highest thermal stress, the so-called hot-spots. By evaluating the oil temperature and environmental circumstances and using the thermal models developed for the transformer, the hot-spot may be determined indirectly. Temperature is measured using a variety of sensor approaches, including PT100 sensors, thermocouples, centralized and distributed optical fibers, and infrared or thermoplastic devices [28, 47, 48]. In regard to emitted light, sharp or pointed conductors or rough surfaces distort the electric field and tend to ionize the dielectric around them, usually air. This leads to corona discharges. The emission of light and also heat during this phenomena can be utilized to detect corona discharges by means of an ultraviolet or thermal camera.

Acoustic Approach

The acoustic PD measurement method involves detecting the pressure waves generated by the PD activity using a microphone or other acoustic sensors [49]. When a PD event occurs, it generates a burst of acoustic energy that propagates through the insulation material and into the surrounding air. This acoustic energy can be detected by a sensitive microphone placed near the equipment. The frequency range of the acoustic PD measurement method typically covers the range of audible sound, which is approximately 20 Hz to 20 kHz. However, PD activity can also generate ultrasonic frequencies, which are above the range of human hearing. These frequencies typically range from 20 kHz to 1 MHz. Acoustic PD measurement is a non-invasive and relatively simple technique that can be used to monitor PD activity in electrical equipment such as transformers, switchgears, and cables. It can be used to detect PD activity in real-time and can provide information on the location, magnitude, and frequency content of the PD events. However, it is important to note that the acoustic PD measurement method is not always effective in detecting PD activity in certain types of equipment

or under certain conditions, and it may need to be used in conjunction with other PD measurement techniques [50].

The main advantage of this approach is its immunity against electromagnetic noise. The acoustic method offers the possibility of PD localization using triangulation techniques. It has the advantage that the propagation velocity of acoustic waves is significantly lower than the EM waves, however, due to the thermosiphon effect, the velocity varies depending on the oil temperature [51]. Moreover, so-called silent PDs do not produce acoustic signals [52]. In such cases, the acoustic method is not applicable for PD localization.

Chemical Approach

The diagnosis methods based on the chemical reactions occurring inside a transformer due to the degradation of the insulation system in the event of a fault have grown more accessible and efficient as new instruments with increased sensitivity have been developed. The chemical methods of fault diagnosis can be divided into two main categories: those targeting the insulation oil, and those for the evaluation of oil-paper insulation. Techniques developed for the evaluation of a transformer's oil-paper insulation provide an accurate statement on the current status of the apparatus, however, they have the disadvantage that it is impossible to collect samples without disrupting the component's operation. The chemical technique of DGA is the most common method in this class for not only PD detection, but also identifying and categorizing electrical and thermal faults in liquid-filled power transformers. Local thermal abnormalities, so-called hot-spots in the event of a fault generate distinct patterns of gases that dissolve in the oil. Hydrogen, oxygen, nitrogen, carbon monoxide, carbon dioxide, methane, ethane, ethylene, acetylene, and other gases are examples of these gases, each of which has a distinct thermal stress profile. At temperatures of 800 to 1200 °C, an electrical discharge into the oil, for example, causes enormous quantities of hydrogen and acetylene. At temperatures exceeding 100 °C, faults in paper insulation also release carbon monoxide and carbon dioxide. Various methods have been proposed for the fault analysis using the absolute value or the ratios of these gases to each other [53–56].

The development of a cost-effective compact online monitoring system for hermetically sealed transformers with a gas cushion is presented in chapter 2 of this thesis. This approach is further discussed in section 1.2.

UHF Measurement Technique

The EM waves generated in case of PD activity can be utilized for PD diagnosis. The methodology for detection and classification, as well as for localization of PD by means of the UHF measurement technique are discussed in chapter 3 and chapter 4, respectively. In the following, an introduction is given.

Free electron charges that were previously at rest are accelerated and decelerated in the event of PD in the insulation of a transformer. These acceleration and deceleration generate a time-varying electromagnetic field that radiates outward from the PD source. By means of UHF probes, these EM waves can be decoupled from the device under test. The properties of the electromagnetic PD signal generated during the discharge phenomenon are determined by the following factors [57]:

- Number of electrical charges produced.
- The charge acceleration that is affected by the magnitude of the surrounding field force.
- The material properties of the insulation medium.
- The probe's position and angle as well as its surroundings in regards to the accelerating charge.

As the EM wave propagates through the surrounding medium, it undergoes attenuation due to various factors, such as absorption, reflection, and scattering. These factors are influenced by the properties of the medium, such as its conductivity, permittivity, and permeability [58].

The UHF measurement technique is the focus of this thesis, and a detailed discussion on its fundamentals is presented in section 1.3.

1.2 Transformer Fault Diagnosis using DGA

1.2.1 Fault Gases in Transformers

Transformer insulation liquids are primarily composed of hydrocarbons, which are organic compounds containing only carbon and hydrogen atoms, such as n-alkanes, iso-alkanes, and cyclic hydrocarbons, which have different boiling points and molecular weights [59, 60]. When energy is applied to these hydrocarbon chains, either thermally or electrically, the long chains

can split, resulting in the formation of various fault gases. These fault gases include hydrogen (H_2), methane (CH_4), ethane (C_2H_6), ethylene (C_2H_4), acetylene (C_2H_2), as well as higher-value hydrocarbons. Additionally, under the influence of paper insulation, fault gases such as carbon monoxide (CO) and carbon dioxide (CO_2) can also be produced during fault events [61–64].

Empirical studies have shown that similar faults lead to consistent fault gas quotients, which are evaluated according to the guidelines outlined in the *IEC 60599* [29]. The standard defines several categories for fault types. To determine the dissolved fault gases, oil samples from the transformer are collected, and the gases are extracted using various methods, such as vacuum extraction, membrane separation, or headspace analysis [65]. Vacuum extraction involves drawing a vacuum on the oil sample to induce the release of dissolved gases, which are then collected and delivered to the analytical equipment. Membrane separation uses a semi-permeable membrane to selectively filter and concentrate specific gases for analysis. On the other hand, headspace analysis involves heating the oil sample to release the dissolved gases into a headspace above the sample, which is then collected and analyzed [66].

The extracted gases are then analyzed using gas chromatography (GC). GC is a powerful analytical technique for DGA, as it allows for the separation and identification of individual fault gases dissolved in the transformer oil. By measuring the concentration of fault gases, valuable information about the transformer's condition and potential faults can be obtained [67–69].

Furthermore, gases that could not dissolve in the transformer oil, such as large amounts of free gas generated during severe faults, accumulate in the Buchholz relay. These gases can also be analyzed to provide insights into the transformer's condition. In this case, the gas collected in the Buchholz relay can be directly analyzed using GC [70].

1.2.2 Evaluation Methods of DGA Data

To evaluate DGA data for fault diagnosis, several methods have been developed over the years, each with its own advantages and limitations.

One of the most common methods for evaluating DGA data is the Duval triangle. The position of the plotted point within the triangle can indicate the type of fault that is present [67, 71, 72]. The conventional Duval triangle is depicted in Figure 1.7. It is divided into seven regions, labeled PD (partial discharge), D1 (discharges of low energy), D2 (discharges of high energy), T1 (overheating below 300 °C), T2 (overheating within 300 °C and 700 °C),

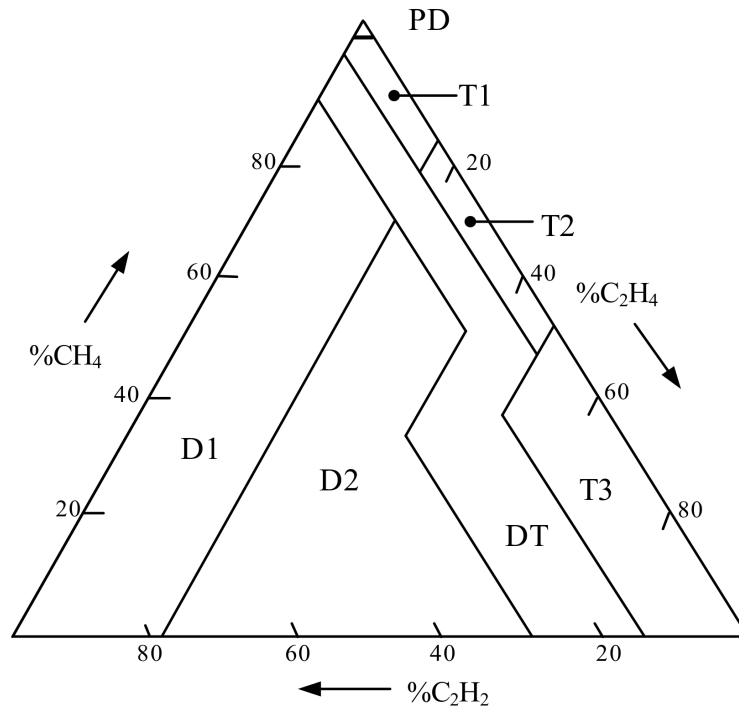


Figure 1.7: Structural representation of a Duval triangle [73]

T3 (overheating with temperatures above 700 °C), and DT (thermal faults and discharges at the same time), each of which corresponds to a different fault type or condition. The classifications are based on the relative concentrations of the three gases in the DGA data, as well as the total gas volume and the rate of gas generation [62, 63].

Other methods for evaluating DGA data include the Rogers ratio method, which compares the ratio of two different gas concentrations to a reference ratio, and the key gas method, which focuses on the concentrations of specific gases associated with different types of faults [74].

In addition to these methods, machine learning techniques, such as artificial neural networks and support vector machines, have also been applied to DGA data for fault diagnosis. These methods use statistical analysis and pattern recognition algorithms to identify patterns and trends in the data that may be indicative of specific faults [75]. Regardless of the method used, the interpretation of DGA data for fault diagnosis requires careful consideration of a number of factors, including the age and condition of the transformer, the operating history of the equipment, and any other relevant environmental or operational factors. Furthermore, it is important to validate any diagnostic conclusions drawn from DGA data with other complementary diagnostic techniques, such as insulation resistance measurements and visual inspections [76].

1.2.3 Online DGA Monitoring Systems

Online monitoring via DGA is a widely used technique for assessing the condition of power transformers. This method involves the detection and measurement of gases dissolved in transformer oil. By monitoring the levels of these gases over time, it is possible to detect any abnormal changes in the transformer's condition and take corrective and prophylactic action.

One major factor contributing to the cost of DGA monitoring systems is the need for specialized equipment to extract and analyze the gases dissolved in transformer oil. Oil sampling is typically performed using a dedicated sampling valve or port on the transformer, allowing for the collection of oil samples from the transformer tank. The oil sample is then delivered to the extraction unit, where gas extraction takes place. Gas extraction is typically accomplished using vacuum extraction or membrane separation.

Once the fault gases are extracted, they need to be analyzed. Sophisticated algorithms and statistical models are used to interpret the data and provide diagnostic information about the transformer's condition [77, 78]. There are several methods available for the analysis, each with its advantages and limitations. GC is a powerful and widely used technique for analyzing fault gases dissolved in transformer oil. It allows the separation and identification of individual gases based on their differential partitioning between a stationary phase and a mobile phase. However, GC is considered rare in monitoring systems because of its high cost and the requirement for consumable gases during the analysis process. Despite its accuracy, the expense and resource-intensive nature of GC limit its application in online monitoring systems. In recent years, sensors have gained popularity for fault gas analysis due to their cost-effectiveness and ease of implementation. Various types of sensors, such as semiconductor sensors and photo-acoustic sensors, are used for this purpose. Semiconductor sensors rely on changes in electrical properties when exposed to specific gases, while photo-acoustic sensors detect gases based on their absorption of modulated infrared radiation. These sensors offer real-time monitoring capabilities, making them valuable tools for continuous assessment of transformer health. Monitoring systems not only measure the concentrations of fault gases but also evaluate their occurrence rates over time. By continuously monitoring the rate of gas generation, it becomes possible to establish warning and alarm values for individual gas concentrations and their increases. These threshold values help identify abnormal conditions or potential faults in the transformer promptly.

Different fault gas analysis techniques offer varying levels of gas detection and quantification. Some methods allow the analysis of only specific gases, such as hydrogen (H_2), while others can detect a broader range of gases, including methane (CH_4), ethane (C_2H_6), ethylene (C_2H_4), acetylene (C_2H_2), carbon monoxide (CO), and carbon dioxide (CO_2). The comprehensiveness of gas analysis impacts the cost of monitoring systems, as more sophisticated techniques capable of detecting multiple gases tend to be more expensive.

The choice of fault gas analysis technique in monitoring systems depends on the specific requirements of the transformer application. While GC provides precise data, its higher costs may make it more suitable for periodic laboratory analysis rather than continuous monitoring. On the other hand, sensor-based systems offer a more cost-effective and real-time alternative, making them a popular choice for online monitoring. The data obtained from these monitoring systems, along with the evaluation of gas concentrations and occurrence rates, enable the setting of warning and alarm values, facilitating proactive maintenance and ensuring the reliable operation of transformers.

The cost of implementing an online DGA system depends on a variety of factors, including the size and complexity of the transformer, the level of monitoring required, and the specific equipment and software used. In general, the cost of DGA equipment ranges from several thousand to tens of thousands of euros, with additional costs for installation, maintenance, and ongoing monitoring [65].

Another factor contributing to the cost of DGA monitoring systems is the importance of ensuring that the data collected is accurate and reliable. This requires regular calibration and maintenance of the monitoring equipment, as well as ongoing training and expertise in order to interpret and analyze the data effectively.

Despite the initial cost, online DGA monitoring can provide significant benefits in terms of reducing downtime, extending the life of the transformer, and minimizing the risk of catastrophic failure. As such, it is a valuable tool for ensuring the reliability and safety of power distribution systems.

The decision to implement an online DGA monitoring system for a transformer typically involves a consideration of a number of factors, including the criticality of the transformer, its age and condition, the likelihood of failure, and the potential consequences of failure. Asset managers must carefully

evaluate these factors in order to determine whether the cost of implementing a DGA monitoring system is justified by the potential benefits in terms of improved reliability and reduced downtime [79]. Cost-effectiveness is also a key consideration in this decision-making process. By reducing the implementation costs, it may be ultimately cost-effective to equip also small GSUs with online monitoring systems.

1.2.4 Fault Gas Monitoring System in the Gas Cushion

Several failures of hermetically sealed power transformers with a gas cushion used in wind energy plants have been documented in recent years [80, 81]. Usually, fault gas analysis involves extracting gases from the transformer's oil and then subjecting them to analysis using various techniques, such as GC or sensors. However, by directly detecting the fault gases in the gas cushion, the resource-intensive gas extraction process can be bypassed. This not only streamlines the monitoring process but also reduces the operational costs associated with gas extraction. The elimination of the gas extraction step significantly simplifies the fault gas analysis setup, resulting in a more cost-effective monitoring system. The need for specialized equipment and consumables required for gas extraction is minimized, reducing both initial setup costs and ongoing maintenance expenses. Consequently, this approach enables utilities and industries to implement comprehensive monitoring systems for transformer health without incurring excessive financial burdens. The significance of detecting fault gases in the gas cushion becomes even more pronounced with the emergence of the new generation of small GSUs for wind and photovoltaic farms.

Hydrogen is one of the byproducts produced in this process, as are the majority of the other prevalent defects. Since hydrogen has the lowest Ostwald coefficient, it is an ideal choice to be the focus of a monitoring system installed in the gas cushion of a hermetically sealed transformer [72, 77, 82].

Based on the above premise, a semiconductor-based monitoring system is introduced in chapter 2, which is predicated on continuous tracking of the undissolved fault gases in the gas cushion and a set of environment sensors, to correct the fault sensors' output value for ambiance influences.

1.3 UHF PD Measurement Technique

The UHF PD measurement technique has been used for several decades to detect and localize PD in GIS and GIL. This method is based on detecting the electromagnetic waves that are emitted by PD during its propagation through the insulation material. UHF PD measurement can also be applied to power transformers. In this context, the UHF PD measurement technique is gaining increasing momentum in the industry as a valuable tool for the diagnosis and monitoring of high-voltage equipment [83, 84]. In this section, different aspects of this technique in regards to detection and localization of PD in transformers are discussed.

1.3.1 PD Detection via the UHF Technique

Among the many approaches for detection of PD in power transformers, the most frequent method is the phase resolved partial discharge (PRPD) pattern technique, in which all the PD pulses throughout a period of time are presented with regard to the phase of the power frequency of the AC cycle. This pattern may further be utilized to differentiate the types of PD [32, 85]. However, this approach is not always applicable, especially for on-site measurements when the noise level is especially high. Consequently, different approaches are being studied that provide a solution to this challenge, one of which is the UHF measurement technique. The fundamental advantage of this approach is, among other things, its resilience against external interference sources [86]. This may be leveraged in case of measurements with a high background noise. The transformer tank's metallic enclosure acts as a Faraday cage and provides a shielding effect that attenuates external EM interference signals [87, 88]. In this thesis, the relevance of the UHF measurement technique for the identification of various PD types is discussed. For this aim, the tank of the power transformer is investigated from an EM point of view, which has been of less interest in the literature. Various aspects, e.g. the transformer tank's geometry, that effect EM wave propagation are addressed in the following.

PD as Excitation Source

When PD is triggered in the insulation system of a HV apparatus, high frequency transient current pulses are generated. These current pulses regularly vanish and then resurface, as the applied voltage is commonly a sinusoidal wave. In respect to the EM wave propagation, only accelerated motion of electric charges leads to creation of both an electric and a magnetic field, which is the essential requirement for the radiation of EM waves according to the Poynting's Theorem [89]. These two fields are being coupled together by Maxwell's equations. In general antenna theory, it is typically assumed that the source of excitation is an alternating current, resulting in a back and forth acceleration of the charge. In case of PD as the stimulation source, the charge experiences temporary acceleration instead of a back and forth, as the current pulse that triggers the movement is more of an impulsive nature. Therefore, the employed probes must have a broadband characteristic for the detection of the EM waves emitted by PD. There are many researches focusing on simulating different types of PD and the associated propagation of EM waves [90–92].

Near and Far Field Consideration

In antenna theory, a difference is drawn between the near field and the far field behavior of an antenna. Three separate regions are defined: reactive near field region, radiating near field region, and far field region. In the reactive near field region, which only occurs in the proximity of the source, the reactive fields prevail, implying that the energy is stored in this region. At contrast, the far field region is in such a distance from the antenna, that the stored energy is minimal compared to the radiating energy. Furthermore, the power density of EM radiation in this area decreases with the inverse square of distance from the source. The transition zone between the reactive near field and the far field is termed the radiating near field region. According to theory, in this area, the reactive field is not dominating and the radiating field begins to emerge [93]. For antennas in most circumstances, the defining parameter is the far field, as the radiation pattern is set for that area, nevertheless, in the targeted application of an antenna for PD measurement in power transformers, the reactive near field and the radiating near field regions are in focus. In both, the radiation pattern greatly relies on characteristics such as the distance from the source, the surrounding of the source, and the type of the source itself. In several recent studies, e.g. in [94, 95], a calibration

approach for the UHF measurement technique in power transformers based on the antenna factor (AF) is presented. The AF indicates the needed electric field strength that generates 1 V at the terminal of a receiving antenna with a 50Ω impedance and typically permits an accurate far field calibration [93]. The suggested process to utilize the AF as a measure to counteract the impact of the UHF probe's sensitivity with the purpose of calibrating the UHF method appears inadequate. The absorption of emitted radiation by a probe in a gigahertz transverse electromagnetic (GTEM) cell filled with insulation liquid is simulated by the absorbent load located at the end of the cell, which replicates a far field scenario, thereby providing a reliable measure of the antenna factor (AF) of the probe. This is by no means the case, once the probe is inserted into a transformer tank [96, 97]. The complex inner structure, in presence of the active part, the tap-changer, etc. as well as the restricted size of the transformer tank, even for larger units, leads to significant reflections and therefore, mutual impedance and reactance effects [98, 99]. When evaluating and adjusting radiated emissions in the near field, using a simplified AF as a correction factor, which is computed for the far field, can result in measuring inaccuracies because the AF is a frequency-dependent component [100]. In addition, the transformer tank acts as a cavity resonator, which further complicates the possibility of calibration.

Transformer Tank as a Resonator

The tank of a transformer is a metallic enclosure that behaves as an EM cavity or resonator with its walls acting as a perfect electric conductor (PEC). The tank can be described as a rectangular waveguide that is electrically shorted at both ends. If the cavity, here the tank, is stimulated by a source in its interior, e.g., PD that arise owing to a failure in the insulation system of the transformer, the ensuing EM waves are contained inside its walls and therefore generate standing waves. In order to explain the propagation of the EM waves, the EM wave equation that is a shortened version of the Maxwell's equations is considered:

$$\nabla^2 \vec{E} - \mu\epsilon \frac{\partial^2}{\partial t^2} \vec{E} = 0 \quad (1.5)$$

where ∇^2 is the Laplace operator, μ is the permeability and ϵ is the permittivity of the medium within the cavity [101]. The boundary conditions of the cavity are required to be fulfilled to solve this equation for rectangular cavities. These equations have many solutions (the so-called modes) that are eigen-functions of the equation system. These modes are a function of the

form, size, and medium in which the EM waves propagate. Each mode has a cut-off frequency, below which that specific mode is not excited [102]. The modes in a cavity may be divided into two categories:

1. Transverse electric (TE) modes that have no electric field component in the propagation direction.
2. Transverse magnetic (TM) modes that have no magnetic field component in the propagation direction.

The boundary conditions of the cavity with PEC boundaries that have to be met are as follows:

- The component of the electric field that is tangential to the wall equals null ($E_t = 0$).
- The magnetic flux density component that is normal to the wall equals null ($B_n = 0$).

When energy is supplied into a cavity, standing waves are formed inside its walls with particular peaks and minima, generating patterns that are characterized by the resonance frequencies and modes. The resonance frequencies f_r for a rectangular cavity with the dimensions $l \times w \times h$ are obtained from the solution of the wave equation and are computed by [101]:

$$(f_r)_{mnp} = \frac{c_0}{2\sqrt{\mu_r \epsilon_r}} \cdot \sqrt{\left(\frac{m}{l}\right)^2 + \left(\frac{n}{w}\right)^2 + \left(\frac{p}{h}\right)^2} \quad (1.6)$$

where m , n , and p are the mode numbers and underscore the dependency on the coordinates, c_0 is the speed of light in vacuum, and μ_r and ϵ_r are the relative permeability, and the relative permittivity of the propagation medium within the cavity, respectively. The parameters l , w , and h are the length, width, and height of the cavity, respectively. It is noteworthy that the mode numbers can only take integers and at least two of them have to be non-zero in order for the EM waves to occur. For the analysis of the received UHF pulses, the s-parameters of the tank as a multi-port EM system needs to be studied. The notation s , which stands for scattering, hints to a commonly used parameter in radio frequency (RF), microwave, and antenna engineering [103]. For high frequencies, a given network, in this case the transformer tank, is preferably characterized in terms of EM waves instead of voltages or currents. The description is based on the ratio between the in- and outgoing waves due to practical considerations.

The s-parameters of a four-port network describe the relationship between incident waves a_i and reflected waves b_i at each port i . In this context, a port refers to a terminal or connection point, e.g. an antenna, through which electromagnetic waves can enter or exit the network. Figure 1.8 illustrates a four-port network. For the i^{th} port, the s-parameters are denoted as s_{ii} for reflection and s_{ij} for transmission.

A four-port network is shown in Figure 1.8. The notions a_i and b_i denote

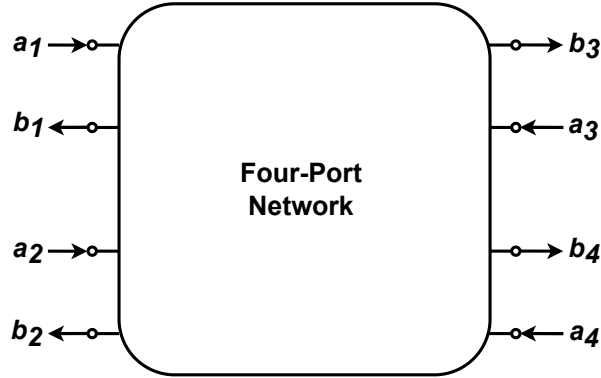


Figure 1.8: A four-port network

the incident wave, and the reflected wave from the i^{th} port, respectively. In terms of the s-parameters, the reflection coefficient s_{ii} , also known as return loss, is the most cited characteristic of an antenna and quantifies the portion of the incident wave a_i that is reflected back as the wave b_i at the same port. It is a measure of how well the port is matched to its characteristic impedance. A lower s_{ii} value indicates better impedance matching and less reflection. The transmission coefficient s_{ij} describes the portion of the incident wave a_i at the i^{th} port that is transmitted to the j^{th} port as the wave b_j . This parameter provides information about the coupling between the ports and indicates the amount of power transferred from one port to another. The relationship between the incident wave a_i and the reflected wave b_i at each port of the four-port network can be described using s-parameters as follows:

$$\begin{bmatrix} b_1 \\ b_2 \\ b_3 \\ b_4 \end{bmatrix} = \begin{bmatrix} s_{11} & s_{12} & s_{13} & s_{14} \\ s_{21} & s_{22} & s_{23} & s_{24} \\ s_{31} & s_{32} & s_{33} & s_{34} \\ s_{41} & s_{42} & s_{43} & s_{44} \end{bmatrix} \begin{bmatrix} a_1 \\ a_2 \\ a_3 \\ a_4 \end{bmatrix} \quad (1.7)$$

where s_{ij} represents the s-parameter relating the reflected wave at port i to the incident wave at port j . Each s-parameter is a complex number, and its magnitude and phase describe the amplitude and phase shift of the reflected

wave with respect to the incident wave. These parameters provide valuable information about the network's impedance matching, power transfer, and signal propagation characteristics. The s-parameter will be further addressed in chapter 3.

1.3.2 Principles of Localization via the UHF Technique

The localization of PD in a power transformer via the UHF measurement technique is based on multilateration, which is a common technique in radio navigation and surveillance systems. Here, the location of an unknown source is determined based on measuring the arrival time (AT) of energy waves with known propagation velocity. In telecommunication, the term arrival time of a signal refers to the instance, where the said signal is received by the receiver. In this section, a short overview is given on the topic of localization of PD faults in power transformers based on the Time-Difference-of-Arrival (TDOA) method.

1.3.2.1 Multilateration with Four Sensors

For applying the UHF technique for PD localization, UHF probes are inserted into the tank. These probes are then connected to an oscilloscope with high sampling rate and wide frequency range. While the test object is subjected to high voltage, the probes capture the signals emitted by the PD source. Using digital signal processing, the AT of each captured signal is determined. An example of a data-set consisting of four captured UHF signals with their determined ATs is given in Figure 1.9. To determine the location of PD in the tank of a power transformer via the UHF technique by multilateration, a minimum of four UHF probes and consequently four captured EM waves are necessary. The distance between the PD source and the respective UHF probe is correlated with the propagation velocity of the EM waves multiplied by their time of flight as follows:

$$(x_s - x_i)^2 + (y_s - y_i)^2 + (z_s - z_i)^2 = \frac{c_0^2}{\epsilon_r} \cdot (AT_i)^2 \quad (1.8)$$

where x_s , y_s , and z_s are the coordinates of the PD source, x_i , y_i , and z_i are the coordinates of each of the probe tips with i being the index relating to the probes, c_0 is the speed of light, and ϵ_r is the relative permittivity of the propagation medium. If it is assumed that the time axis starts at the PD inception time, as in Figure 1.9, the AT of each signal corresponds to the time

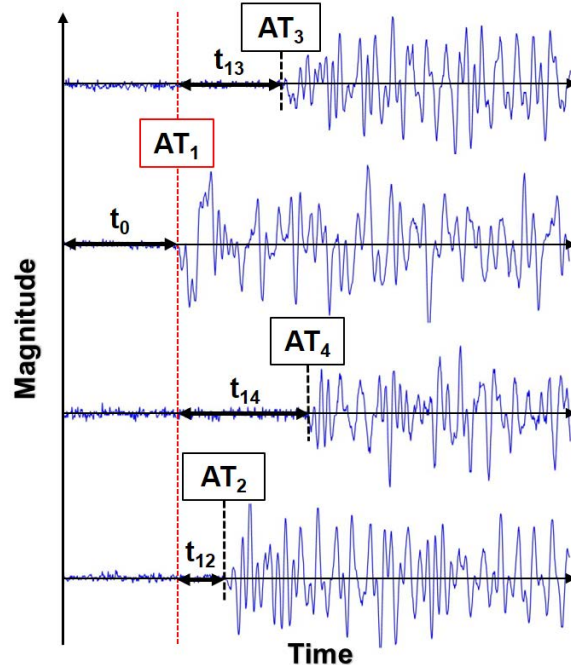


Figure 1.9: ATs of simultaneously captured signals by four UHF probes

of flight from the origin, in this context the PD fault, to the probe. Hence, the following applies:

$$\begin{cases} AT_1 = t_0, \\ AT_2 = t_0 + t_{12}, \\ AT_3 = t_0 + t_{13}, \\ AT_4 = t_0 + t_{14}. \end{cases} \quad (1.9)$$

The location of the PD source as well as t_0 , the time difference between the PD inception time and the AT of the trigger signal (AT_1), are the unknowns. The location of each of the four probes (x_i , y_i , and z_i) along with the AT differences between the trigger signal and the remaining three signals, i.e. t_{12} , t_{13} , and t_{14} , are known. Regarding the propagation velocity of the EM waves, if the medium is air ($\epsilon_r = 1$), the propagation velocity equals the speed of light c_0 . Otherwise, the relative permittivity ϵ_r of the medium, in which the electromagnetic (EM) waves propagate, needs to be taken into account. The solution of the system of non-linear equations resulting from substituting (1.9) in (1.8) delivers the location of the PD fault.

1.3.2.2 Methods for Determining the Arrival Times of UHF Signals

The multilateration technique necessitates the use of four signals. However, not all power transformers have enough valves to allow four monopole

probes to be inserted. Other sensor types, such as UHF plate sensors for placement on dielectric windows, may be used when fewer than four valves are available [104]. Moreover, it is also feasible to use one UHF probe in conjunction with acoustic sensors positioned on the transformer tank. The UHF probe provides the trigger signal in this manner [2]. Acoustic sensors are susceptible to surrounding disturbances, which is a flaw with this approach. When four UHF probes are employed, however, the best accuracy in localization is expected [105].

Throughout a UHF PD pulse, AT is the exact moment when the received signal emerges from the background noise. The difference in ATs, as well as the position of the UHF probes, are used to determine the position of the PD source in a Cartesian coordinate system as the algorithm's output. An incorrect determination of the ATs has a substantial impact on the accuracy of the localization. As a result, several AT detection techniques are provided in this section.

Determining sudden variations in the power of a signal is a straightforward way for AT detection [104, 106]. The cumulative sum of the energy of the original signal is employed to generate a new signal in this approach. The AT is yielded by this new signal's knee point, which has an incremental trend. Markalous *et al.* introduced a modified version of this approach in which the new signal is formed by removing a trend from the cumulative total of the energy in [107]. The AT is obtained by taking the minimum of the new signal in this modified technique. In [108], the disadvantages of these two approaches are discussed and an example is presented of when these two algorithms fail to discover the correct AT.

Another approach is to target the first peak of a signal to provide the AT [109]. Moreover, this approach can be combined with a wavelet transform to denoise the signals prior to the AT detection [110]. However, compared to the peak detection approach, AT detection based on the energy criteria has been shown to produce a more promising outcome [109]. Furthermore, depending on the noise intensity, the wavelet denoising creates a divergence in the detected AT. Hence, in this thesis, more modern approaches are considered. In recent studies, three promising AT detection approaches have been presented, and their efficiency in comparison to previous methods is reviewed. In the following, these three methods are described.

Average Time Window Threshold Method

Let X be a signal comprised of samples x_1, x_2, \dots, x_N . A time frame is specified and an average of the samples is determined over the window in the average time window threshold (ATWT) approach, as shown below [108]:

$$S(n) = \frac{1}{w} \sum_{k=n-w+1}^n |x_k|, n \geq w \quad (1.10)$$

The width of the time window w , can be calculated by the following equations:

$$w = \frac{1}{2 \cdot f_d} \quad (1.11)$$

$$f_d = \frac{\sum_{k=1}^N f_k \cdot Y(f_k)}{\sum_{k=1}^N Y(f_k)} \quad (1.12)$$

where Y denotes the amplitude of frequency components of the signal X with f_d being the average frequency of the signal calculated using its frequency spectrum $Y(f)$. Note that length of the time window w is a constant value. The window is shifted through the signal, and the average of samples in each window is determined. The computed mean values form a new signal, and its knee point provides the AT.

Dynamic Cumulative Sum

Dynamic cumulative sum (DCS) method is introduced in [111] to detect the AT of simulated UHF signals. A time frame is specified in the first stage of the DCS technique, which is identical to the ATWT approach. The window width is calculated as follows:

$$w = \text{Floor} \left(\frac{1}{2} \cdot \text{Length} \left(\frac{M_3}{\max(|M_3|)} \geq T \right) \right) \quad (1.13)$$

where the function *Floor* represents rounding down to the nearest integer, the function *Length* represents the number of elements in a given signal, T is a heuristically selected threshold of 0.1, and M_3 is the signal X 's third central moment, which has been separated into several sections [111]. The number of samples in each segment is determined by the following:

$$L = \text{Floor} (f_s \cdot t_w) \quad (1.14)$$

where f_s denotes the sampling frequency, and t_w denotes the length of a PD pulse within a transformer tank before being reflected by the tank's walls, which is set to 2 ns. The samples in section s will be represented by X_s . In section s , the third central moment M_3 may be determined as follows:

$$M_3(s) = E \left[(X_s - \mu(s))^3 \right] \quad (1.15)$$

where E stands for expected value operator and μ stands for arithmetic mean of samples in section s of length L .

A sample of the signal X at time t is regarded for the window length, and a DCS function is generated across a window before and after the sample as follows:

$$\text{DCS}(t) = \sum_{k=1}^w \log \frac{f_a^t(x_k)}{f_b^t(x_k)} \quad (1.16)$$

where f_a^t and f_b^t are the lag and lead windows' probability density functions (PDFs), respectively. The PDFs were established using a Gaussian distribution. The signal's AT is defined as the moment when DCS achieves its global maximum.

Contrast Function Method

This method's premise is based on the minimizing of a contrast function at the moment of the AT. At the midpoints, the signal X is split into two parts, and the contrast function for each breakpoint is determined as follows:

$$C(b) = \sum_{k=1}^{b-1} (x_k - \bar{X}_{1:b-1})^2 - \sum_{k=b}^N (x_k - \bar{X}_{b:N})^2 \quad (1.17)$$

where C is the contrast function, b is the signal's breakpoint and \bar{X} is the signal's empirical rms over the relevant segment. The AT of the signal is the breakpoint at which the contrast function hits the global minimum [112].

In the contrast function method (CFM), several statistical parameters such as mean and variance may be utilized instead of rms. Nonetheless, testing this approach on a variety of signal sets indicated that, when compared to the other statistical characteristics, the rms criteria results in the most accurate AT.

In chapter 4, the performance of the three presented methods in this subsection is compared.

1.3.2.3 Measurement Uncertainties in the Determination of AT

This subsection substantiates some of the challenges of PD localization via the UHF method.

Measurement Equipment

As with any other application, the measurement equipment has a major impact on the quality of the results. These includes the digital storage oscilloscope (DSO), the probes, and the communication coaxial cables used for connecting these two. In the following, the uncertainties associated with the utilized measurement equipment are discussed.

- **Thermal noise:**

Thermal noise, also known as Johnson noise or Nyquist noise, is an unavoidable source of error, since it is incoherent. Thermal noise is a product of the surrounding temperature, the resistance of the measurement setup, and the measurement bandwidth [113].

- **Quantization noise:**

Quantization noise is the inaccuracy generated by quantization in an oscilloscope's analog-to-digital converter (ADC). The quantization noise is also random and depends on the sample depth or bit depth. The amount of bits of information in each sample is known as bit depth, and it directly corresponds to the sample's resolution. It also corresponds with the system's dynamic range, meaning the maximum and minimum amplitude of the signals to be digitized by the oscilloscope. These are determined by the measurement settings and have an impact on the precision and accuracy of voltage measurements conducted with an oscilloscope. They also include a certain error [114].

- **Limited sampling rate:**

High-speed time domain measurements are required to detect the EM waves generated by the PD, which necessitates the use of an oscilloscope with a high sampling rate and appropriate bandwidth. However, a certain error is unavoidable, since the sampling rate of even modern oscilloscopes are limited. Although there is the option of digitally increasing the sampling rate by means of interpolating the data, this is not applicable for the challenging localization measurements in power transformers.

- **Run-time variations due to the length of the coaxial cables:**

The connection between the UHF probes and the DSO is realized via coaxial cables. Hence, the run-time of the signals is prolonged by $t_{cable,i}$, which describes the time it takes to travel through the i^{th} cable and reach the DSO. Since the localization is based on the time-difference-of-arrival of the UHF signals, if this value is identical for all four cables, it is not critical. However, a slight difference in the length of the four cables could result to an error, which is to be compensated by determining the exact length of all four cables and hence the $t_{cable,i}$. Depending on the ϵ_r of the material, the resulting difference due the length of the cables is to be considered.

- **Minimization of uncertainties due to measurement equipment:**

Different measurement parameters must be swept based on the received signals in order to reach the achieve possible measurement settings. Measurements should be performed with the DSO's maximum measurement bandwidth initially. Fine-tuning of the measurement parameters by examining the measurement results based on the signal-to-noise ratios and signal frequencies of the received signals will result in the reduction of the overall measurement uncertainty. However, since the PD signals of different sensors often indicate different values for the signal-to-noise ratios, a compromise must be established.

Method Limitations

In addition to the measurement uncertainties, there are a number of factors that limit the effectiveness of PD localization via the UHF measurement technique. A short overview is given in the following.

- **Missing line of sight between the fault location and the probes:**

One of the main challenges in localization of PD via the UHF measurement technique is that the determined AT of the signals has a lead or lag. A main contributing factor to this challenge is the complex interior of the transformer. When there is an incident between the EM waves emitted by PD and metallic parts inside the power transformer, e.g. the windings or the walls, or with dielectric materials, such as the paper insulation, the wave propagation is impacted, which in turn leads to an error. This topic is discussed further in chapter 4.

- **Limited insertion depth of the probes:**

Due to the prevailing electrical field in a power transformer, only a limited insertion depth of the probe is allowed. The UHF probes must be kept at a safe distance from the transformer windings to avoid the risk of short circuit or electrical discharge [115]. This impacts the probe sensitivity, since the insertion depth of the probe has a direct correlation with its sensitivity [116].

- **Effect of high-voltage bushings:**

Although the metallic enclosure of the tank is grounded and acts as a Faraday cage, resulting in a high robustness against external noise, the bushings as well as the bushing terminals allow a certain degree of external disturbances to impact the received signals by the probes. Furthermore, in case of PD, the bushings themselves act as antennas [87] and are stimulated by the PD currents.

- **Minimization of uncertainties due to method limitations:**

The listed factors in this section manifest themselves as leads or lags in the determined ATs of the UHF signals. This can have a huge impact on the localization accuracy. The presented approach in this thesis aims at minimizing their effect on the performance of PD localization via the UHF measurement technique.

In this section, a comprehensive overview of the measurement uncertainties and method limitations involved in PD detection and localization using the UHF measurement technique was presented, shedding light on the complexities and challenges of effectively applying this method in the diagnosis and assessment of power transformers.

1.3.3 UHF Probes

Available UHF Probe Technologies

For conducting UHF measurements in power transformers, various probe types are commercially available, which will be outlined in the following.

- **Monopole conical horn antenna:**

The monopole conical horn antenna is a widely used antenna design and the most common probe type for large power transformers. It is known for its broad bandwidth, high gain, and low sidelobe levels. The monopole conical horn antenna consists of a conical metallic horn

with a monopole antenna placed at its apex. The geometry of the horn is carefully designed to achieve desired radiation characteristics. The horn's flare angle, length, and aperture size play crucial roles in determining the antenna's performance. The flare angle of the conical horn affects the antenna's radiation pattern and directivity. A larger flare angle results in a wider beamwidth but lower directivity. Conversely, a smaller flare angle provides a narrower beamwidth and higher directivity. The length of the conical horn is an important parameter in achieving proper impedance matching and desired radiation characteristics. It is typically chosen based on the operating frequency to ensure that the horn supports the desired mode of propagation. The aperture size of the horn determines the antenna's gain. A larger aperture results in higher gain but also increases the size and complexity of the antenna. The aperture size is carefully determined to strike a balance between gain, size, and ease of fabrication. The performance of the monopole conical horn antenna is evaluated in terms of its radiation pattern, gain, impedance matching, and sidelobe levels. The conical horn's geometry ensures a well-defined and symmetric radiation pattern with low sidelobe levels. The monopole conical horn antenna exhibits high gain due to its efficient radiation mechanism and low losses. Impedance matching is crucial for efficient power transfer between the antenna and the feeding network. Various impedance matching techniques, such as using tapered transmission lines or impedance transformers, are employed to achieve a good match between the antenna and the feeding network. The conical horn design inherently provides low sidelobe levels, contributing to better signal reception and interference rejection [93].

As this type of sensor is intended for UHF measurements in power transformers, it can be inserted into the tank through the vent of an oil drain valve. Due to the fact that it is designed for DN 50 and DN 80 oil drain valves, it is also possible to use this type of sensor to retrofit transformers that are already in operation. Figure 1.10 shows a few examples of commercially available UHF monopole probes for measurements in power transformers.

The conical geometry is utilized to improve the probe's properties and obtain a broader bandwidth as compared to the short linear monopole antenna [120]. This probe type is suitable for measurements for a frequency range up to 3 GHz.

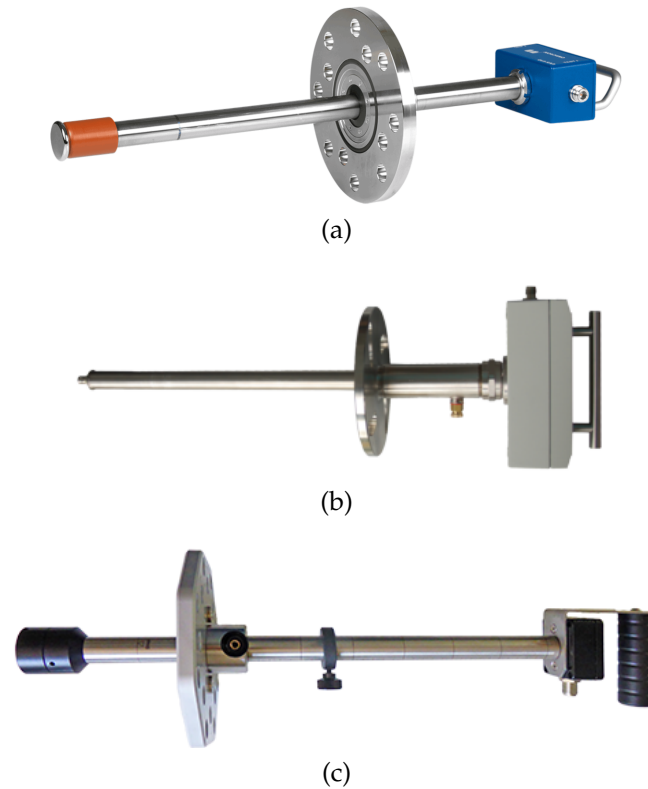


Figure 1.10: Examples of commercially available monopole antennas for power transformers: (a) *Omicron UVS 610* [117], (b) *PDIX TVS 2* [118], and (c) *BSS UHF 50/80* [119]

- **Plate sensor:**

UHF plate sensors are typically flat metallic plates or discs placed within the insulation system of a power transformer. These plates act as antennas to capture the UHF electromagnetic waves generated by PD events within the transformer. This probe type can either be integrated into the wall of new transformers, or be installed on a dielectric windows. There are also different plate sensors commercially available. A few examples are shown in Figure 1.11. The downside of

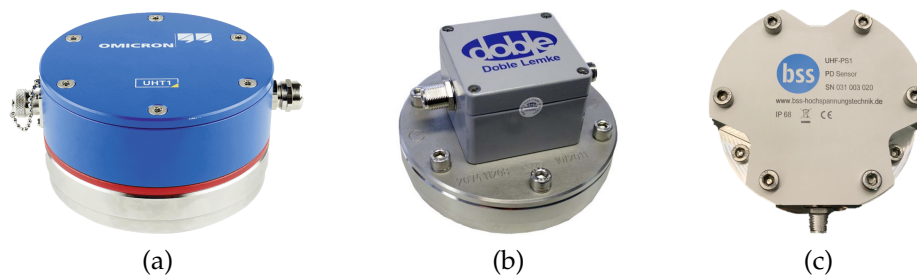


Figure 1.11: Examples of commercially available UHF plate sensors for the dielectric window of power transformers: (a) *Omicron UHT 1* [121], (b) *Doble UHF PD Plate Sensor* [122], and (c) *BSS UHF-PS1* [123]

this probe type is its lower sensitivity in comparison to the monopole probes [124]. Furthermore, the insertion depth is not adjustable.

- **Other probe designs:**

Aside from the two mentioned and more known sensor types, there are other probe types available that can be conducted for UHF measurements. Here, the turret-electrode antenna, the hilbert curve fractal antenna, and the archimedean two-wire spiral antenna are among the more prominent ones [125–128].

Probe Location

The probe location is an important factor in regards to the sensitivity of the receiving probe. A direct path between the PD source and the probe is ideal, but difficult to achieve. Many researches were conducted in this regard [129–132]. This topic is addressed in chapters 3 and 4 in the context of PD detection and localization.

1.3.4 Employed UHF PD Measurement Setup

Various measurements are carried out in this thesis to investigate and analyze the EM waves generated by PD activity in a power transformer. A general overview of the methodologies and measurement instruments utilized is provided in the following.

1.3.4.1 Transformer Tank Model

The UHF measurements conducted in this thesis are performed, among others, in an especially designed transformer tank model with six *DN 80* oil drain valves at different locations, which are employed for the insertion of the UHF probes into the tank. The tank has a length, width and height of 856 mm, 1236 mm and 1596 mm. The air-filled transformer tank model does not have an active part, and consequently permits the research of several aspects of EM wave propagation within power transformers generated by PD. The transformer tank model with two UHF sensors inserted via the lowest oil drain valves on two perpendicular sides of the tank is depicted in Figure 1.12.

The transformer tank model has a 110 kV bushing with a bushing tap on its top. The bushing protrudes into the tank and is connected to PD fault

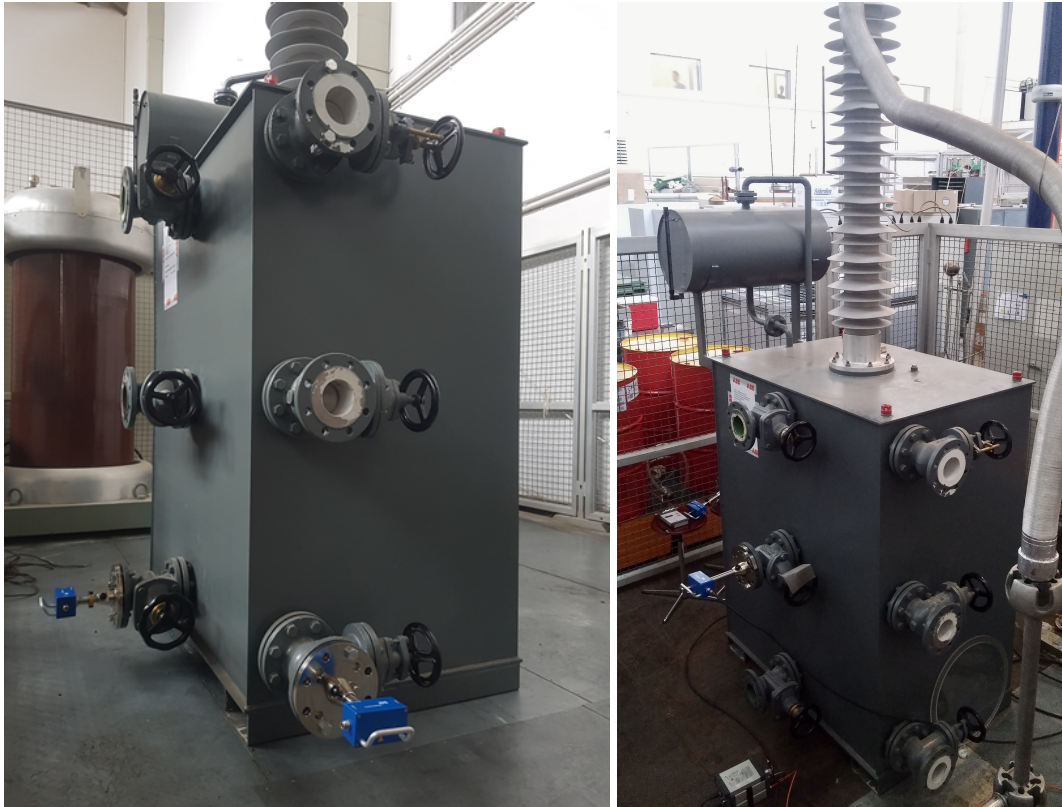


Figure 1.12: Transformer tank model with a 110 kV bushing and UHF sensors inserted through the oil drain valves [87, 133]

models. By applying high voltage via the bushing, PD can be generated artificially. Furthermore, the tank has a manhole with a lid on the front side, allowing the repositioning of the PD fault model with modest effort.

1.3.4.2 PD Fault Models

In order to analyze the EM wave propagation owing to PD, fault models are placed into the tank. For each of the common PD types, a fault model is implemented. In transformers, internal and surface discharges are among the most prevalent failures. A disc formed out of pressboard between two Rogowski electrodes is used to represent surface discharges (Figure 1.13a). The internal PD fault model consists of two electrodes with Rogowski profiles, each with a diameter of 2.75 cm, enclosed inside epoxide resin. The spacing between the electrodes measures 8 mm. In order to generate a void defect in the insulation, the solid insulation material is drilled through using a tiny round drill with a diameter of 0.8 mm until the mid-center of the electrodes. In Figure 1.13b, the employed PD fault model is depicted. For the purpose of completeness, corona discharge is also explored by adopting a needle-plane configuration, as illustrated in Figure 1.13c.

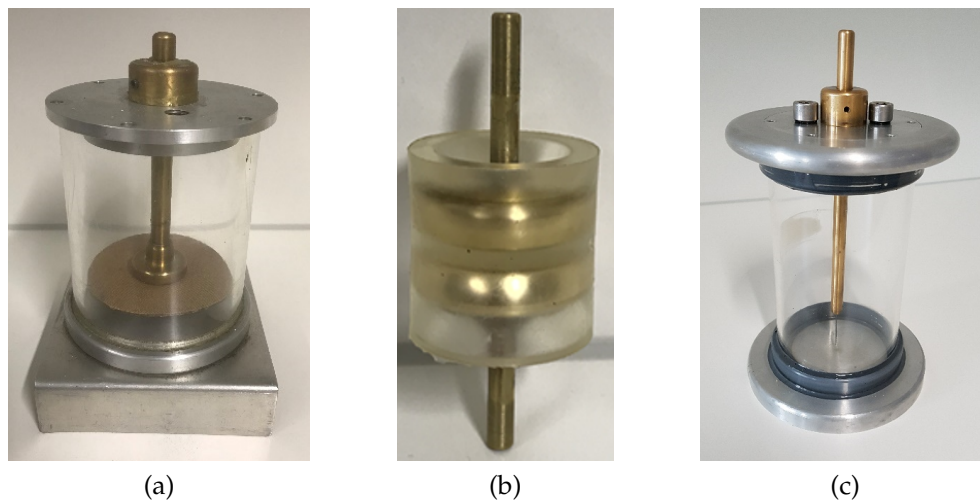


Figure 1.13: PD fault models for (a) surface discharge, (b) internal discharge, and (c) corona [133]

For these three PD fault models, an electrical measurement for determining the PRPD pattern is performed in compliance with *IEC 60270* [21]. The measurement frequency range is set from 100 kHz to 400 kHz. Figure 1.14 displays a color code utilized to represent multiple similar discharges, with red denoting numerous similar events and blue indicating a smaller number of similar events.

The findings for the surface fault model, the internal fault model, and the corona fault model are presented in Figure 1.15a, Figure 1.15b, and Figure 1.15c, respectively, using the color code illustrated in Figure 1.14. The three obtained electrical patterns correlate to the corresponding typical PD patterns in [85].

For the experiments concerning PD localization, a specific fault model is designed. This model, as illustrated in Figure 1.16, consists of two circular plastic discs with a diameter of 10 cm, a Rogowski electrode with a diameter of 2.94 cm, a brass rod with a needle at its tip and three plastic distance bars with a length of 30 cm each. The distance between the Rogowski electrode and the needle may be changed using a screw on the top support. Since this arrangement has no plastic sheath, the position of the needle tip, or the PD



Figure 1.14: Utilized color code in this thesis to represent increasing charge density, with blue denoting fewer occurrences, and red highlighting a higher frequency of similar events at a given phase angle of a PRPD pattern

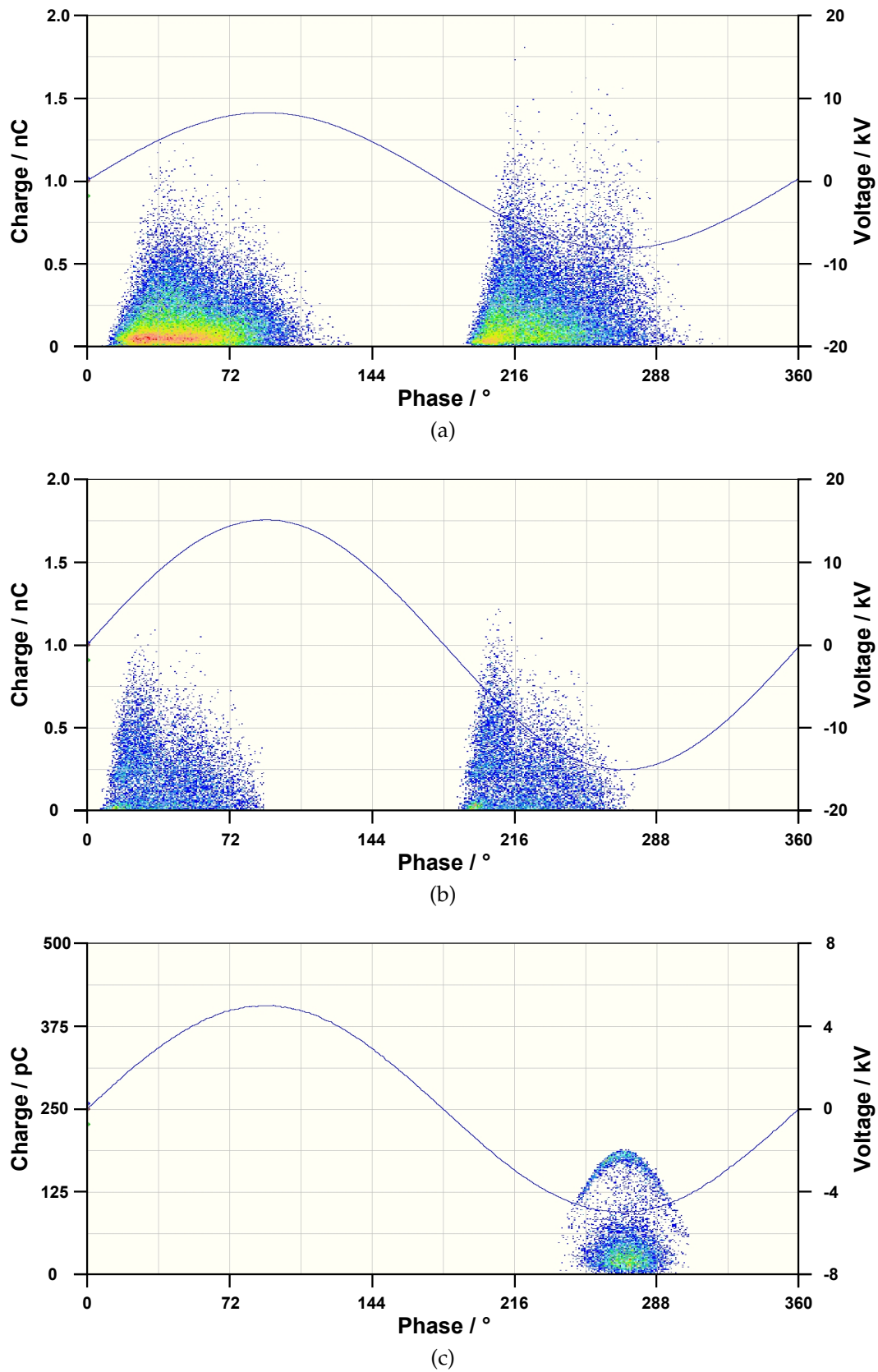


Figure 1.15: Electrical PRPD patterns associated with (a) surface discharge model, (b) internal discharge model, and (c) corona discharge model [133]

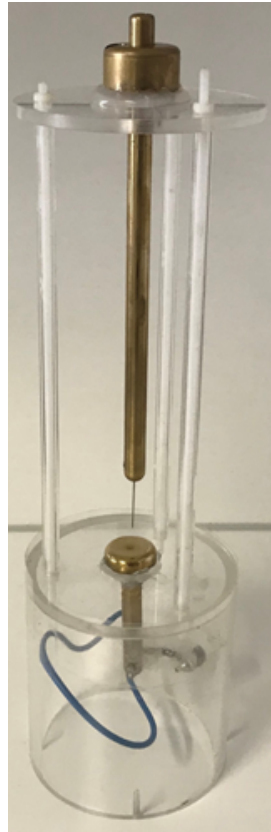


Figure 1.16: Specially designed PD fault model for localization measurements

location may be measured with a better precision. This fault model provides a straight line of sight between the PD site and the sensors, so the model itself causes no error in the duration of flight of the signals. Another variation of this PD fault model contains a disc made out of polyethylene between the needle and the Rogowski electrode, providing a surface discharge model with similar properties concerning the time of flight of the generated EM waves.

1.3.4.3 PD Measurement System

All PD measurements undertaken in this thesis are performed using the *Omicron* PD measuring system [134] shown in Figure 1.17, which permits with its current assessment features a high measurement accuracy. For the conventional PD measurement in accordance to *IEC 60270* [21], the *MPD 600* is connected to the PC unit *MCU 520* via fiber optic cables, resulting into a galvanic isolation between the measuring devices and the PC controller and hence, a significant reduction in the interference coupling. Furthermore, as the measurement system provides a modular construction, multi-channel

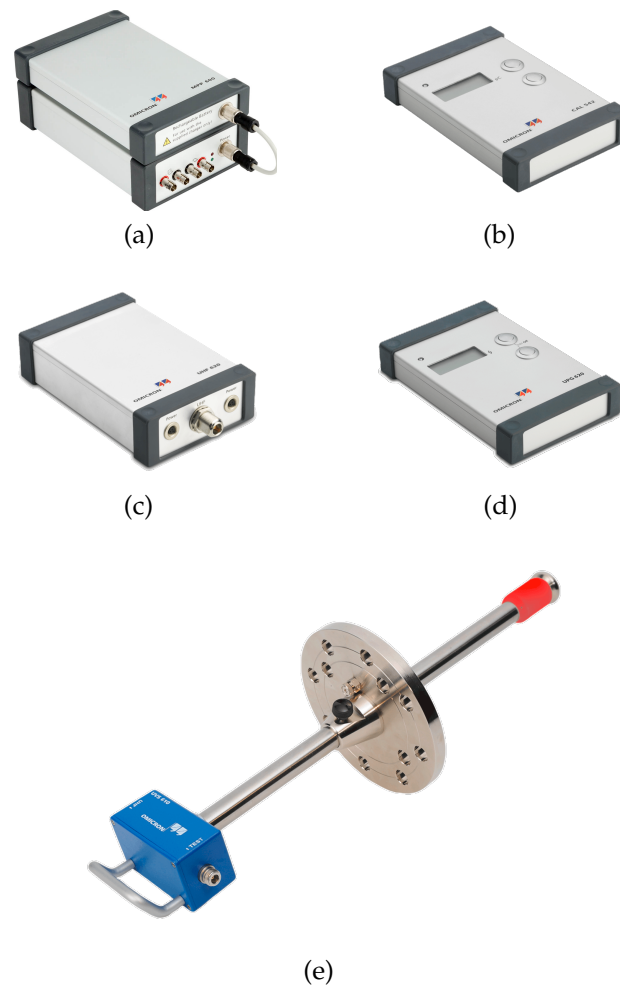


Figure 1.17: Omicron PD measurement system (a) *MPD 600* with its battery pack *MPP 600*, (b) charge calibrator *CAL 542*, (c) UHF bandwidth converter *UHF 620*, (d) UHF pulse generator *UPG 620*, and (e) UHF probe *UVS 610* [134]

measurements are enabled through its master-slave design, where the connection between the separate measurement units is likewise performed utilizing fiber optic cables permitting a perfect synchrony. Each measurement unit *MPD 600* is driven by a lithium-ion power pack (*MPP 600*) and is thus disconnected from the main power supply, consequently the measuring circuit is not impacted by external disturbances. The calibration in accordance to *IEC 60270* [21] is performed by injecting a calibration pulse with a calibrating charge of 100 pC via the calibrator *CAL 542*.

For performing UHF PD measurements, the conventional *Omicron* PD Measurement System can be expanded using the bandwidth converter *UHF 620* and the UHF probe *UVS 610*. For completing the sensitivity check as indicated in [30] prior to UHF measurements, the UHF pulse generator

UPG 620 may be deployed. In this thesis, the UHF Probe *Omicron UVS 610* depicted in Figure 1.17e is employed for performing UHF measurements. This sensor offers the possibility of adjusting the insertion depth of the probe between 5 cm and 45 cm, and it has a scale on the slide-rod. For the measurements in this thesis, the insertion depth varies between 5 cm and 7 cm. The insertion depth within each section is however fixed to ensure the comparability of the results. The probe is oil-resistant and thus can be employed for oil-filled transformer tanks. The insertion of the probe is realized via the oil drain valves on the transformer tank and it is compatible with both DN 50 and DN 80 valves. Hence, it can also be retrofitted to transformers in operation. It has a length and a diameter of 610 mm and 200 mm, respectively. It has a frequency range from 150 MHz up to 2 GHz, and a dynamic range of 70 dB [117].

1.3.4.4 Analysis of the EM Waves Emitted by PD

In the following, the equipment and methods for analyzing the EM waves emitted by PD in time and frequency domain are discussed.

For the acquisition and analysis of UHF signals, the DSO *Tektronix DPO7345C* is employed. With a Bandwidth of 3.5 GHz, a sampling rate of up to 40 GS/s, and its four channels, it allows in-depth measurements in time domain and satisfies the requirements for the experiments conducted in this thesis. The DSO is depicted in Figure 1.18.

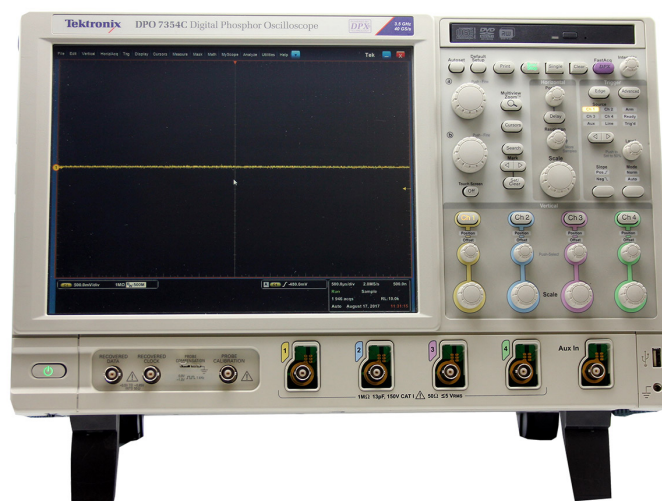


Figure 1.18: *Tektronix DPO7345C* digital storage oscilloscope [135]

The connection between the DSO and the probes is realized via low loss flexible communications coaxial cable *LMR-400-UF*. This coax cable has an impedance of 50Ω and suitable for both indoor and outdoor application. Furthermore, it is very flexible and easy to handle. Since it features a strong shielding effect, it is suitable for the measurements in this thesis. On both ends of the cable, N connectors with screw coupling is used. The N connector has also a defined characteristic impedance of 50Ω [136].

Recorded signals with the oscilloscope are voltage values on a preset time window. To analyze the results in frequency domain, the so-called Discrete Fast Fourier Transform (DFT) is used. This is an algorithm for decomposing discrete signals into their frequency components [137, 138]. In this thesis, the DFT method is deployed in *MATLAB* for the transformation of the signals from time domain into the frequency domain.

The *Rohde & Schwarz* vector network analyzer (VNA) *ZVA8* shown in Figure 1.19 is a high-end VNA with up to four ports for advanced measurements up to 8 GHz. Since it has four channels, it can determine the scattering pa-

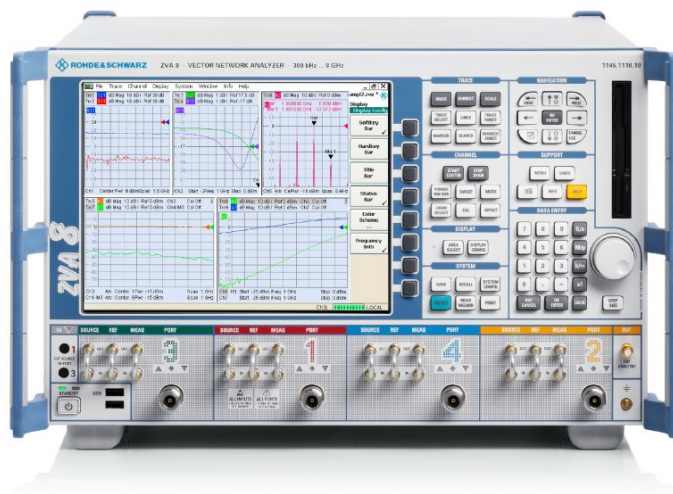


Figure 1.19: Rohde & Schwarz vector network analyzer ZVA8 [139]

rameters of a four-port network. Prior to performing measurements, a calibration is necessary. The VNA calibration is required to remove systematic errors at the relevant frequencies from the measurement instrument as well as any accessories employed to allow particular measurements, e.g. network analyzer test cables. For this purpose, the automatic calibration unit *ZN-Z5* with four ports is used. The VNA is connected to the calibrator and subsequently the device under test via *ZV-Z19* network analyzer test cables [139].

In this chapter, a comprehensive overview of PD and its measurement techniques was presented. The conventional electrical PD measurement

method, according to *IEC 60270* [21], was discussed, highlighting its significance in assessing insulation integrity and identifying faults in high-voltage systems. The concept of apparent charge, a vital parameter in PD quantification, was thoroughly analyzed. The chemical approach of DGA was addressed, focusing on its capability to detect and analyze PD events by monitoring specific gases dissolved in the insulating medium. The importance of DGA as a valuable complementary method to electrical PD measurement was emphasized. Subsequently, the UHF measurement technique was discussed, and its application in detecting and localizing PD was addressed. Finally, an overview of the measurement setup elements used in this thesis was provided, establishing the groundwork for the research findings and analysis in the subsequent chapters.

Chapter 2:

Development of a Special Fault Gas Monitoring System

Wind power generators, both on- and offshore, commonly use step-up power transformers to convert the turbine generator output voltage from a few hundred volts to the medium voltage levels of the collector system. Due to their frequent location within the tower or nacelle of a wind turbine or in a small utility near the tower, the size of transformers is a crucial factor to be considered. To meet space limitations, transformer manufacturers strive to make them as compact as possible. One of the most frequent variants are hermetically sealed liquid-filled transformers installed on the bottom of the tower. Since the temperature of these transformers fluctuates often in response to the wind situation, specific precautions are taken into consideration regarding the expansion of the insulating liquid. The sealed tank could be equipped with fins that expand owing to increased temperatures. However, due to the high number of load cycles occurring every day, this is not a preferred solution since the number of fin expansions is limited. Moreover, in order to avoid the insulating liquid to be exposed to ambient air and humidity, thus keeping its electrical qualities, the transformer is sealed by means of a gas cushion, commonly out of nitrogen or dry air [32].

In this chapter, the development process of a novel monitoring system for GSU transformers typically used in wind and photovoltaic farms is presented. The monitoring system should be able to detect and quantify the concentration of fault gases, especially hydrogen, and potentially methane and ethylene in the gas cushion of hermetically sealed transformers. The system should be reliable, easy to use, low-cost, and provide real-time data to the operators.

One possible approach is to use a gas chromatograph coupled with a thermal conductivity detector or flame ionization detector to analyze gas samples

extracted from the oil of the transformer. Currently available monitoring systems on the market apply this method. However, this approach is relatively expensive and requires skilled personnel to operate and maintain the system.

Existing DGA monitoring systems solely measure the dissolved fault gases in oil. When monitoring in the gas cushion, the dissolved gases are estimated based on their Ostwald solubility coefficients. However, it is important to note that hydrogen, in particular, is predominantly present in the gas phase rather than the oil. For a monitoring system's intended purpose as a fault or condition indicator without specifying the exact fault type, the detection of individual gases such as hydrogen, which are detectable in the gas, is sufficient.

Given hydrogen's low Ostwald coefficient and its generation through the decomposition of insulating material, its concentration can rapidly increase in the transformer's gas cushion. If the concentration reaches a critical level, it can lead to an explosion or fire, causing significant damage to the transformer and its surroundings. Therefore, it is of utmost importance to detect and monitor the concentration of hydrogen gas in the transformer's gas cushion and take corrective actions before it reaches a critical level. The maximum hydrogen concentration in the gas cushion of a hermetically sealed power transformer may vary depending on the transformer's operating conditions, design, and insulation materials [140–142]. Nevertheless, a hydrogen concentration in the range of up to 10000 ppm is absolutely sufficient for the intended monitoring system. Concentrations greater than this threshold will have triggered countermeasures from the operators. A maximum hydrogen concentration of 10000 ppm serves as a reasonable threshold for gas monitoring, as it can effectively indicate potential faults. By setting this threshold, the monitoring system can promptly provide early warnings to operators, enabling them to take appropriate actions to prevent failures.

A possible approach is to use semiconductor-based sensors, which is a low-cost and portable solution. These sensors can detect and quantify different gases simultaneously. The sensor system can be installed in such a way that it can analyze the fault gases in the gas cushion and evaluate the data using a microcontroller-based system. Hence, it can provide real-time data on the concentration of fault gases, which can be used to identify potential faults and take corrective actions before any failure occurs. It is noteworthy that the monitoring system for fault gases in the gas cushion of hermetically sealed transformers must be able to withstand a harsh environment. The system will be exposed to high temperatures, high pressure alternations, and

high levels of vibration, which can affect the performance and reliability of the sensors. Therefore, the sensors and other components of the monitoring system must be designed to withstand these harsh conditions. The sensors should be encapsulated in a protective housing that can withstand high temperatures and humidity, and the system should be designed to minimize the effects of vibration on the sensor readings. The proposed monitoring system must have a sensing range of up to 10000 ppm. The monitoring system for a hermetically sealed power transformer must adhere to specific boundary conditions for its operation. These include enduring an absolute pressure between 600-700 mbar and 1300 mbar, as well as a gas cushion temperature range between 10 °C and 60 °C during typical operation conditions. These values are commonly expected during normal transformer operation of such a transformer [140, 142].

As discussed in section 1.2 of the previous chapter, hydrogen is an ideal candidate to be targeted for monitoring in the transformer gas cushion since it is a reliable indicator of potential problems or faults in the transformer. Monitoring the hydrogen gas concentration can provide early warnings to the operators and enable them to take appropriate actions before any critical failures occur.

In the following, the preliminary investigations on semiconductor-based sensors suitable for the task at hand are discussed. Subsequently, the developed prototype and the investigations on the behavior of the monitoring system under various fault generation scenarios are addressed. Finally, the resulting monitoring system *TGM-101* is introduced and an overview is given on its components.

2.1 Preliminary Investigations on Commercially Available Sensors

There are numerous methods available to measure gaseous hydrogen. Following preliminary market research in the realm of available hydrogen sensors, two sensors were selected among a broader number of commercial semiconductor-based sensors. These two sensors, referred to as SA and SB hereafter, employ distinct functional concepts. Sensor SA employs a hydrogen sensitive Schottky diode, while sensor SB is a catalytic type gas sensor. The usability of both sensors in the harsh environment, often existent in the

gas cushion, which either consists of dry air or nitrogen with a very low oxygen content, is examined in the following. Furthermore, the influence of the broad range of operating temperature and pressure on the sensors is investigated.

2.1.1 Test Setup

In order to replicate transformer-like ambient conditions, the test vessel depicted in Figure 2.1 is used. It comprises of a glass cylinder fastened by two



Figure 2.1: Designed test vessel for conducting the preliminary investigations [143]

flanges. The bottom of the vessel is closed by an aluminum plate with one electrode connected to it. This electrode, which protrudes beyond the test vessel, finishes with a hose barb on the bottom and is linked via a silicone hose and a clamp to a two-way valve. Via this valve, gases can be introduced to the test vessel using a gas-tight syringe. In addition, it may be used to extract samples to determine the precise concentration of the component gases through gas chromatography. Furthermore, it acts as the way of altering the internal pressure of the vessel. The lid of the test vessel contains a recess used to place a gas-tight plug. This connector and its equivalent are the link between the sensors within the test vessel and the evaluation system reading the output signals. The voltage supply of the sensors is likewise accomplished via this socket. Moreover, a needle valve and an external pressure gauge are linked to the aperture of the test vessel's lid at its top. By closing both the valve at the end of the hose and the needle valve, the test vessel is sealed.

2.1.2 Test Procedure

Before sealing the lid and securing the screws, the vessel is filled with molecular sieve in order to maintain the humidity as low as feasible throughout the measurement by means of its water-absorbing characteristic. By closing the test vessel at this stage, there is about 20 % oxygen in the interior. In order to be able to alter the temperature, the vessel containing the sensors, is put within a climatic chamber.

Since the focus of the experiment centers on detecting hydrogen, the measurements are carried out by introducing pure dry hydrogen to the gas mixture within the test vessel. This is done by connecting a gas-tight vessel to the two-way valve at the end of the hose, which is linked to the test vessel. This provides the function of holding the hydrogen, while a set dosage may be given to the gas mixture within the test vessel with the gas-tight syringe serving the purpose of dosing. The test setup is depicted in Figure 2.2. The

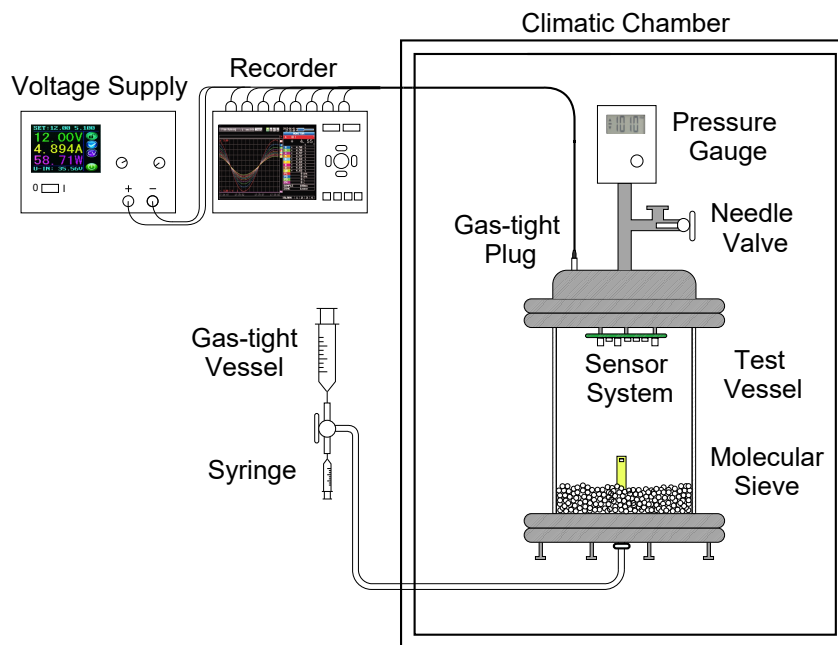


Figure 2.2: Test setup for determining the characteristics of the chosen fault gas sensors [143]

concentration ratio of gases is established by methods of the ideal gas law. For this reason, the number of particles at a certain pressure and temperature level is determined for the volume of the test vessel. The dosage of the additional hydrogen in all the subsequent measurements is constant, meaning the volume of hydrogen injected at every measurement point is identical. However, the conversion into ppm results in varied readings, owing to the

fluctuating amount of existing particles in the test vessel, which largely comprises of nitrogen, under different circumstances.

2.1.3 Effect of Temperature

The investigation of sensor performance at different temperatures is crucial to ensure that the sensor's response is stable and accurate over a wide range of temperatures. Figure 2.3 shows the results of this investigation. Tempera-

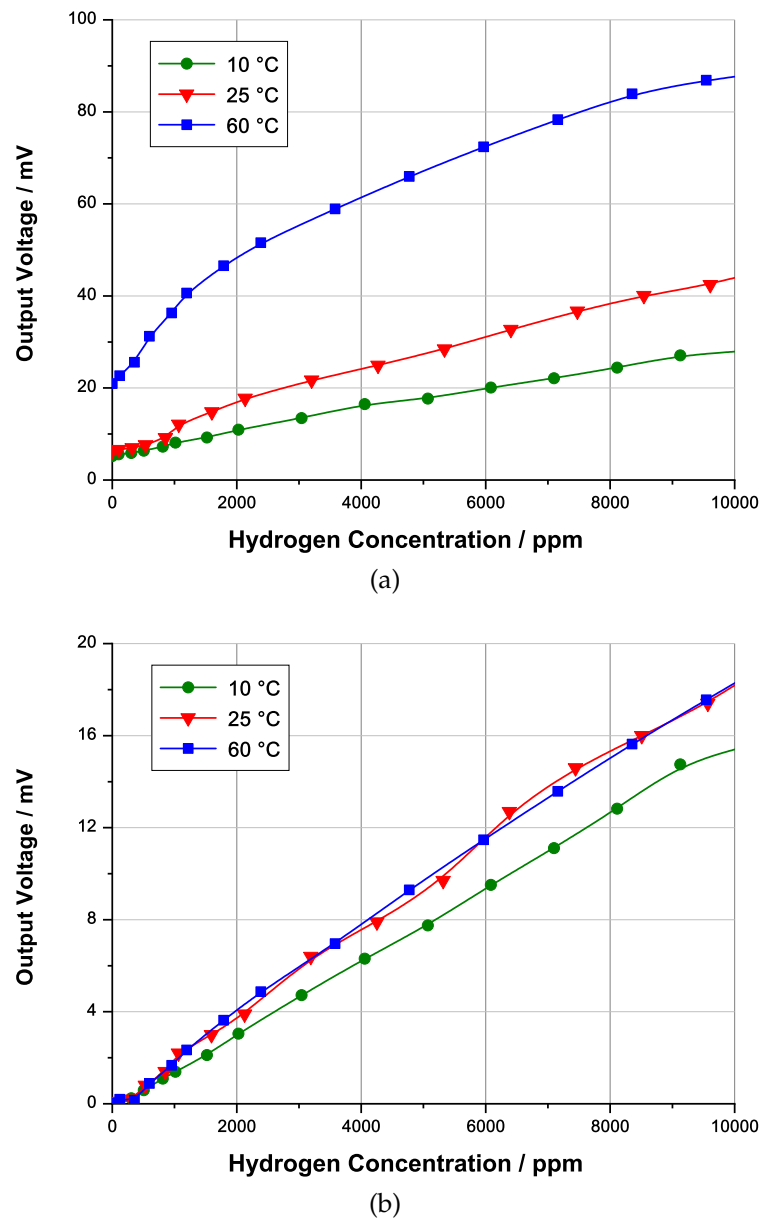


Figure 2.3: Behavior of sensors (a) SA and (b) SB at ambient pressure by increasing the hydrogen concentration at different temperature levels [143]

ture can affect the sensitivity, selectivity, and stability of gas sensors, and understanding the sensor's behavior at different temperatures is essential for

the development of a reliable monitoring system. In this regards, the temperatures 10 °C, 25 °C, and 60 °C are investigated. These temperatures are within the range that the monitoring system is likely to encounter in real-world operating conditions. A temperature of 25 °C is often used as a reference temperature for sensor testing because it is the standard temperature used for laboratory conditions. A temperature of 10 °C is used to represent low-temperature conditions that may occur when the transformer is not in operation or in regions with colder climates. A temperature of 60 °C represents high-temperature conditions that may occur during full-load operation [140].

For this investigation, the climatic chamber is adjusted at 10 °C, 25 °C and 60 °C to evaluate the sensors for their temperature profile. There is a waiting time for the conditions within the test vessel to stabilize before commencing to input hydrogen into the test vessel.

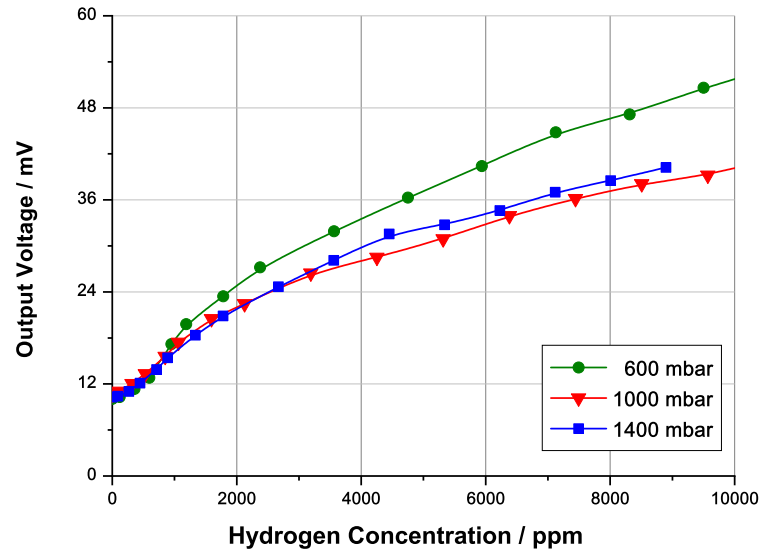
Figure 2.3 presents the outcomes for temperature variation under ambient pressure. The hydrogen concentration reporting range is at about 10000 ppm, which reflects the maximum hydrogen concentration that the sensors can report. Based on the findings, sensor SA's output voltage rises with temperature with a rather large reliance on the prevailing temperature in the climatic chamber. Sensor SB on the other hand exhibits a more steady output voltage under diverse temperature circumstances.

2.1.4 Effect of Pressure

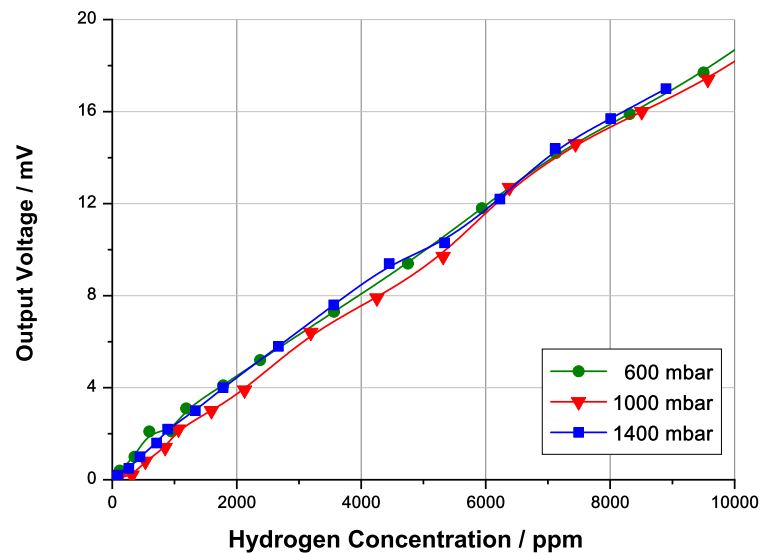
The pressure inside the transformer gas cushion can vary due to changes in temperature, load, or other operating conditions. The gas cushion pressure is usually maintained within a certain range to ensure that the transformer operates safely and efficiently. The pressure inside the transformer gas cushion can affect the performance of the gas sensors. Changes in pressure can cause changes in the gas flow rate and gas diffusion rate, which can affect the sensitivity and selectivity of the gas sensors. Therefore, it is essential to investigate the performance of gas sensors at different pressure levels to ensure that they provide accurate and reliable measurements under different operating conditions.

In order to cover the whole pressure range for the proposed application, air is supplied into the test vessel or steered out of it by means of a gas-tight syringe, depending on the required pressure level. For this reason, the pressure is adjusted in 400 mbar increments from 600 mbar to 1400 mbar, while maintaining room temperature in the climatic chamber. The findings

are presented in Figure 2.4. Both sensors are only slightly affected by the



(a)



(b)

Figure 2.4: Behavior of sensors (a) SA and (b) SB at room temperature by increasing the hydrogen concentration at different pressure levels [143]

different pressure levels in the test vessel, with sensor SB delivering a more consistent output voltage.

As the early experiments were concluded, it was established that sensor SB is more reliable than sensor SA. Additionally, the sensitivity of the sensor SA reduced with time and the measurement range dropped dramatically. As a result, sensor SA was deemed unsuitable for the intended application and was removed from the evaluation. As a result, sensor SB is the centerpiece of

the proposed monitoring system. Despite its minimal dependency on environmental circumstances, the proposed monitoring system is outfitted with environment sensors, allowing for output voltage compensation.

2.1.5 Effect of Oxygen Content

Since the monitoring system is targeting hermetically sealed transformers, operating under low oxygen level is a prerequisite. In the following, the parameters of pressure and temperature were modified in order to study their impact on the output signals of the sensors while in an atmosphere with a very low oxygen content. For this reason, the vessel is attached to a nitrogen container through a silicone hose, and the needle valve is slightly opened. By commencing the flow of nitrogen into the vessel, the air in its inside is progressively replaced with dry nitrogen. The suggested monitoring system is fitted with an oxygen sensor. The procedure continues until the oxygen concentration is below the sensitivity threshold of the oxygen sensor. Measurements using gas chromatography have showed that this occurs when the oxygen level is about below 3%. The suggested test setup is presented in Figure 2.5. Now the needle valve is closed again, so that no more exchange

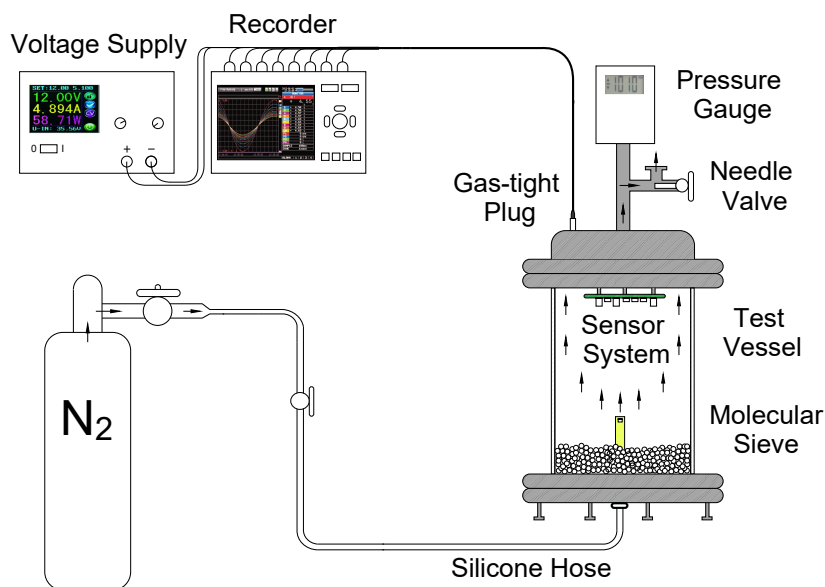


Figure 2.5: Overview of the test setup for varying the oxygen content of the test vessel [143]

may take place. The impact of low oxygen level on the output voltage of sensor SB is evaluated by repeating the experiment with pressure variation

under the new environment. The same steps are undertaken, with the distinction that nitrogen is now injected into the vessel or expelled from the vessel. When the necessary pressure is obtained, hydrogen is inserted into the vessel. The output voltage of sensor SB is measured at various hydrogen concentrations under change of temperature and pressure as shown in Figures 2.6a and 2.6b, respectively. The results indicate a distinct difference

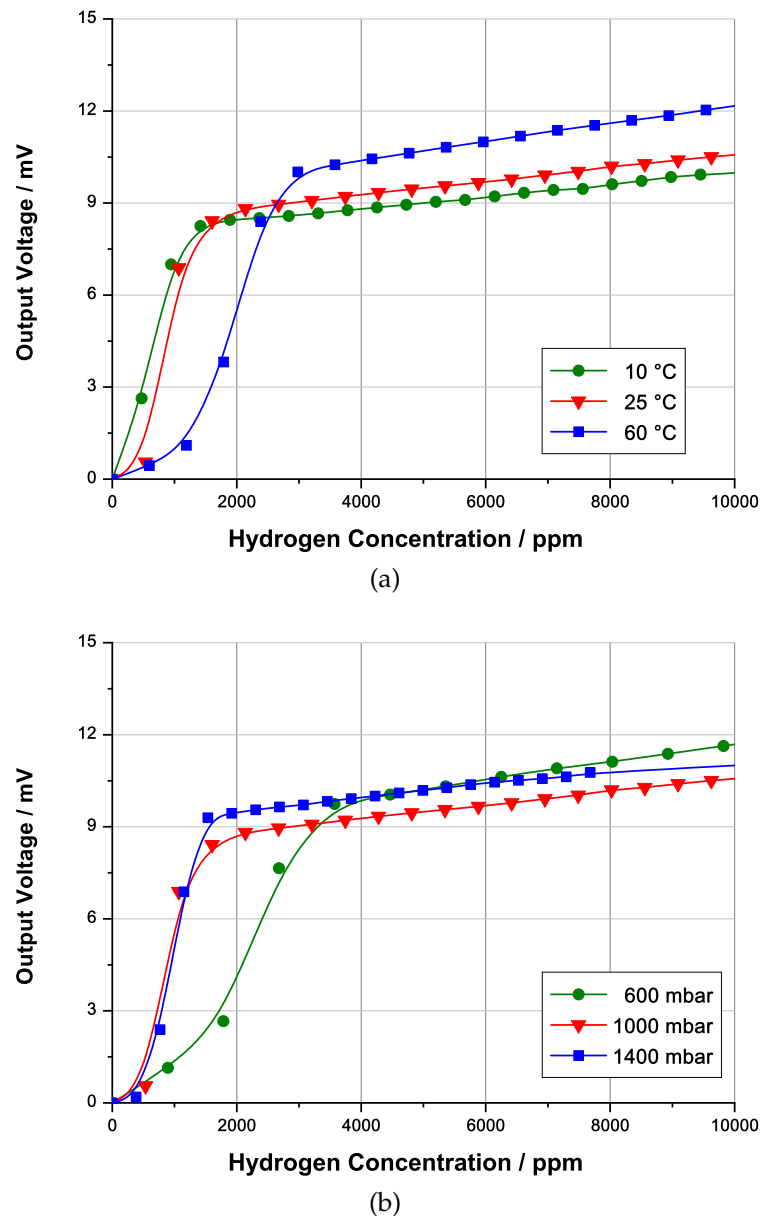


Figure 2.6: Behavior of sensor SB by increasing the hydrogen concentration at (a) different temperature levels and ambient pressure, and (b) at different pressure levels and room temperature in an environment with an oxygen level below 3 % [143]

in the behavior of sensor SB in nitrogen compared to its operation in atmospheric air. When around 20 % oxygen is present, the sensor demonstrates

a linear response at different hydrogen concentrations. Under low oxygen level on the other hand, it enters the saturation state at lower hydrogen concentrations, such that higher changes in the output voltage at low hydrogen concentrations are detected, which is exploitable in respect to the sensitivity of the sensor.

Sensor SB's curve may be separated into two segments. At lower hydrogen concentrations, the sensor is more sensitive and the rise in voltage is more substantial. At lower pressure levels and higher temperatures, this phenomena unfolds at a slower tempo. At higher hydrogen concentrations, the curves overlap, except at 60 °C, where the high temperature has a larger impact on the chemical processes within the sensor in the low oxygen environment, resulting in an increase in the output voltage.

2.1.6 Long Term Application under Low Oxygen Level

The question of long term usability of the sensor system in an inert and pseudo oxygen-free environment is another key concern. To analyze the behavior of the sensor system, the outlined actions in section 2.1.5 to replace the oxygen in the test vessel with nitrogen were carried out. For purposes of comparison, the pressure within the test vessel is equal to ambient pressure while preserving room temperature. Subsequently, 3000 ppm of hydrogen was added to the gas mixture in the test vessel, resulting in an increase in the output voltage of the sensors. The test vessel is resealed at this point and the measurement proceeded for 12 hours consecutively. The findings are presented in Figure 2.7. The red curve depicts the output voltage of the sensor SB with a dotted black trend line. The output voltage of the sensor SB declines with time at a ratio of 0.2 mV/h. The explanation is because the chemical processes within the sensor consume hydrogen and generate a little quantity of moisture, hence reducing the hydrogen concentration. In addition, the gas-tightness of the test vessel is not absolute and the hydrogen within may partly permeate into the ambient environment. To solve this difficulty, the usual approach was replaced with an optimized method for the operating of the sensor SB.

To increase the accuracy of the sensor system, an optimal driving approach was devised for the hydrogen sensor. The modified driving method aims to improve the long-term stability issue by adjusting the way the sensor is driven and read out, with the goal of mitigating potential sources of error.

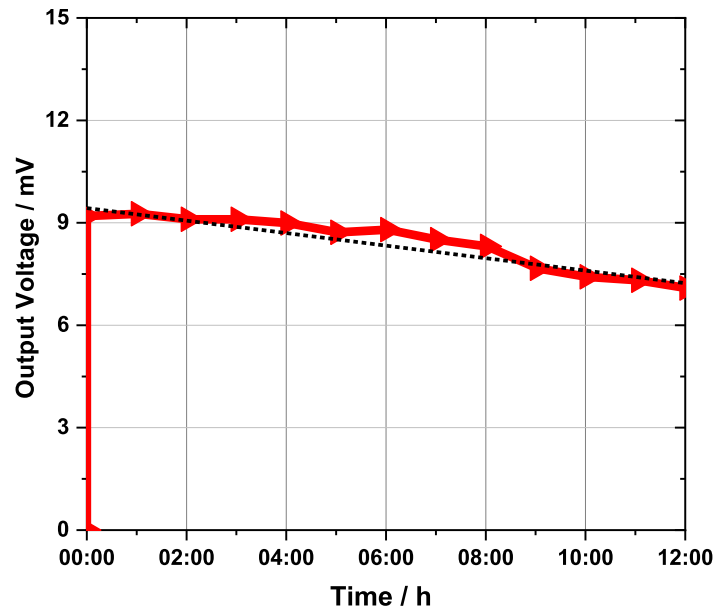


Figure 2.7: Long term measurement with sensor SB under an oxygen level below 3 % at room temperature and ambient pressure [143]

The efficacy of the optimized driving method was assessed through iterative measurements, which revealed the absence of the previously observed decrease in output voltage over time.

Ensuring the reproducibility of measurement outcomes is a critical concern, which prompted an investigation into the sensor's performance under conditions that closely emulate real-world scenarios. To this end, hydrogen was introduced in carefully controlled doses via a gas syringe into a vessel containing dry nitrogen, and the sensor's output voltage was measured. A total of eight iterations were conducted, with the initial four runs utilizing the standard measurement procedure, and the subsequent four runs implementing the optimized driving method. The findings are presented in Figure 2.8. In the course of the eight iterations, a sample scatter of roughly 0.62 was observed, reflecting the variation or discrepancy between the maximum and minimum values in the data-set. This observation implies the reproducibility of the outcomes using both methods.

In this section, the distinctive behaviors of two hydrogen sensors, which were selected after a comprehensive investigation on the available sensors on the market, were evaluated under change of temperature and pressure. The sensor with the most stable findings was selected for measurements under low oxygen level as necessary for installation in a monitoring system for hermetically sealed transformers and the results supported its applicability. The long term stability of the sensor was also studied and the findings were

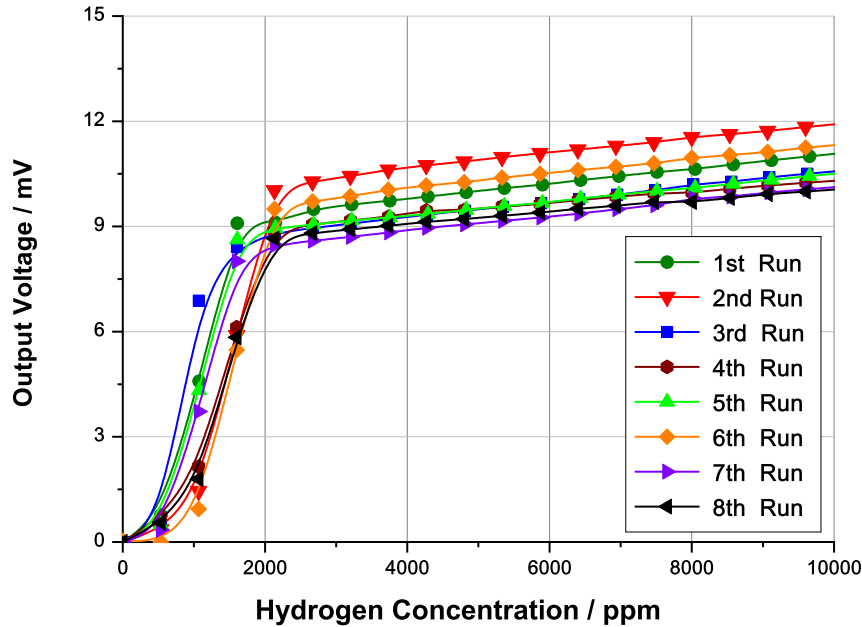


Figure 2.8: Behavior of the sensor SB in nitrogen by increasing the hydrogen concentration at room temperature and ambient pressure levels with run fifth to eighth via optimized method

given. Based on the performed research, it was determined that the sensor is appropriate for the construction of a cost-effective and compact failure gas monitoring system for power transformers sealed with gas cushion. A prototype is constructed based on the preliminary research, which will be detailed in the next section.

2.2 Novel Online Monitoring System

In order to compensate for the effects of environmental parameters such as temperature and pressure on the output voltages of the fault gas sensors, the sensor system is equipped with a set of auxiliary sensors in addition to the fault gas sensors. These auxiliary sensors also monitor environmental.

The lab prototype of the sensor system depicted in Figure 2.9 is developed to test its functionality. The lab prototype receives the output voltages of the sensors and transmits them to an evaluation unit where they are assessed. The sensor system continuously tracks the fault gas level and, based on the steepness of the increase and the amount of the fault gases, issues a warning or alarm signal. To ensure that the output signals of the sensors are accurately amplified, the evaluation unit comprises amplification circuits. In addition, the complete sensor system is enclosed in a die-cast aluminum casing that provides *IP66* protection, ensuring its durability and reliability.

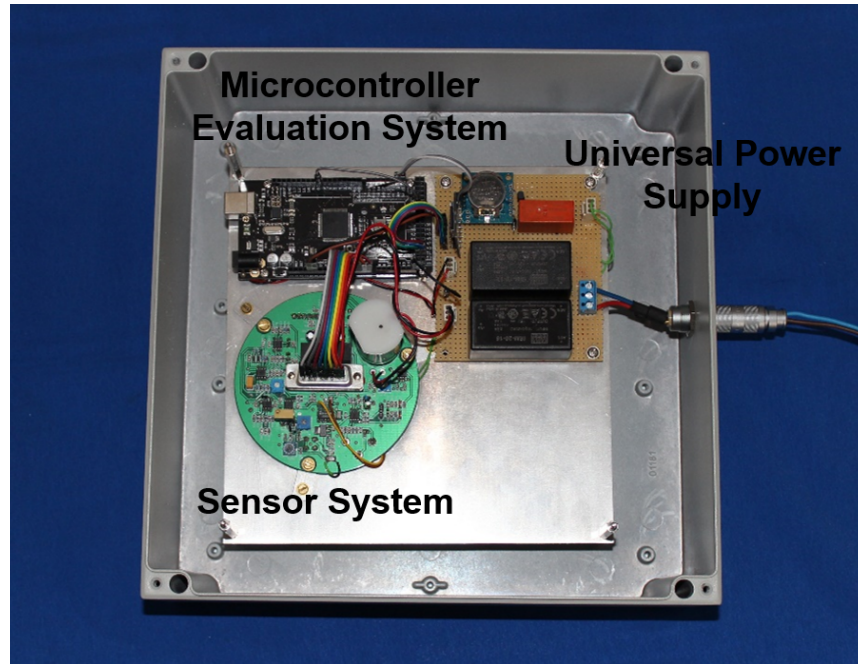


Figure 2.9: Developed lab prototype with the sensor system, the evaluation board, and the universal power supply [144]

Furthermore, a small flange adapter (KF) is placed on the housing, which provides a simple installation on the transformers. Figure 2.9 shows the lab prototype of the sensor system, including the auxiliary sensors, amplification circuits, and the die-cast aluminum casing with the flange adapter. This lab prototype is used to test the functionality and reliability of the sensor system before it is deployed in the field.

2.2.1 Auxiliary Sensors

In addition to the hydrogen sensors, the sensor system is equipped with auxiliary sensors to monitor the temperature, pressure, oxygen level, and the relative humidity. In the following, these sensors are discussed.

Temperature Sensor

This sensor is a thermocouple with built-in amplification and linearization in an integrated circuit. The temperature is determined via the thermoelectric effect, which is achieved by the connection of two different electrical conductors. Thereby one conductor is kept at the measurement temperature and the second serves as the reference. Through the difference, a thermo-voltage potential is created which is amplified. The sensor is applicable for temperatures from $-40\text{ }^{\circ}\text{C}$ to $+110\text{ }^{\circ}\text{C}$. The sensor has a guaranteed accuracy of $0.5\text{ }^{\circ}\text{C}$.

In order to investigate the behavior of the temperature sensor, it is installed into a closed vessel and placed inside a climatic chamber. The result is shown in Figure 2.10. The sensor has a nearly linear output.

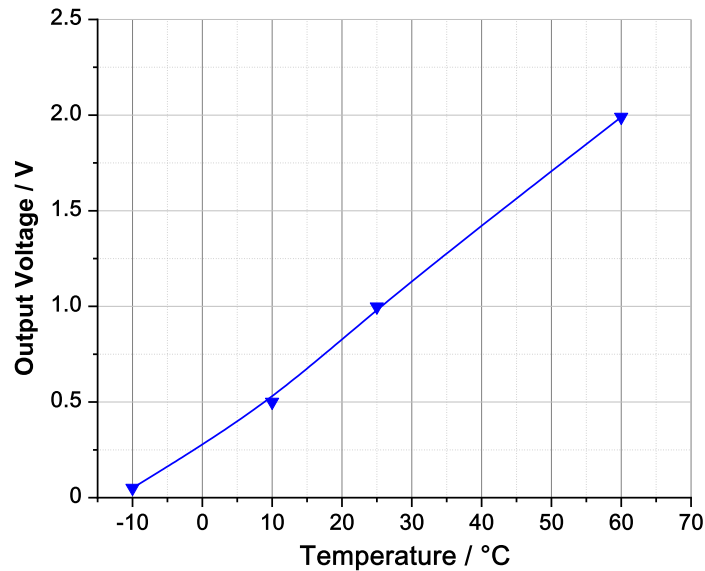


Figure 2.10: Behavior of the temperature sensor at different temperature levels

Pressure Sensor

The behavior of the pressure sensor is investigated by varying the pressure in the test vessel shown in Figure 2.1 and measuring the absolute pressure via an external pressure gauge. The result is shown in Figure 2.11.

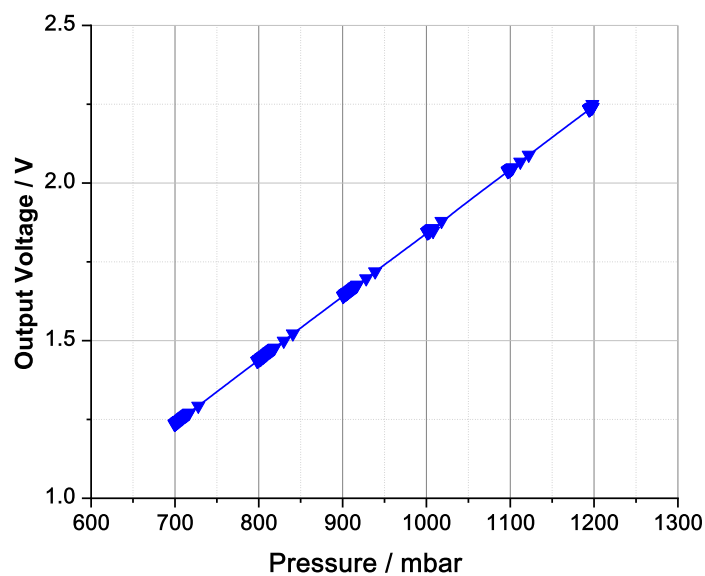


Figure 2.11: Behavior of the pressure sensor at different pressure levels

The utilized piezoresistive transducer is a state-of-the-art monolithic silicon pressure sensor designed for a wide range of applications. This transducer combines advanced micromachining techniques, thin film metallization, and bipolar processing to provide an accurate, highly analog output signal that is proportional to the applied pressure.

Oxygen Sensor

The electrochemical sensor for measuring oxygen concentration is basically a lead-oxygen battery with a lead anode, a gold oxygen cathode, and a weak acid electrolyte enclosed in an acrylonitrile butadiene styrene (ABS) housing. The oxygen molecules are reduced at the gold electrode after passing through a nonporous fluororesin membrane in the electrochemical cell. The amount of current flowing between the electrodes is proportional to the amount of oxygen in the gas mixture. When the oxygen concentration changes, the terminal voltages across the thermistor (for temperature compensation) and the resistor are read as the output signal. The oxygen sensor's functionality was examined in a closed vessel with ambient air. The oxygen concentration was gradually raised during the measurement. In addition, the percentage range of 0 to 15 % was examined. The vessel was filled with nitrogen for this purpose, and then oxygen was progressively introduced. Figure 2.12 depicts the results. The sensor's behavior is almost linear.

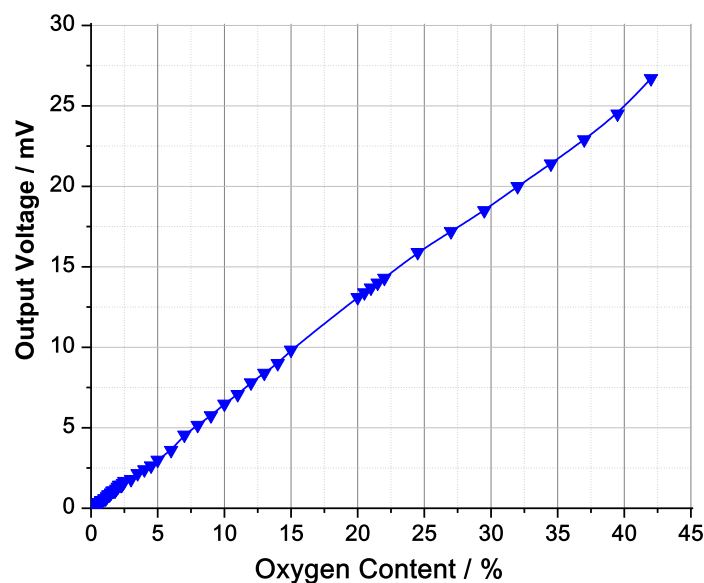


Figure 2.12: Behavior of the oxygen sensor at different oxygen levels

Humidity Sensor

The sensor consists of a laser-trimmed, thermoset, capacitive sensor element with a polymer material housing. It is based on the principle of a plate capacitor. A thin moisture-sensitive polymer layer is used as the dielectric. Absorbed moisture changes the dielectric constant, which is recorded as a measured variable. To investigate the behavior of the humidity sensor, it is placed inside a climatic chamber that offers the possibility to vary the humidity and measure it with a calibrated external sensor. The results are shown in Figure 2.13. This sensor also shows a linear behavior.

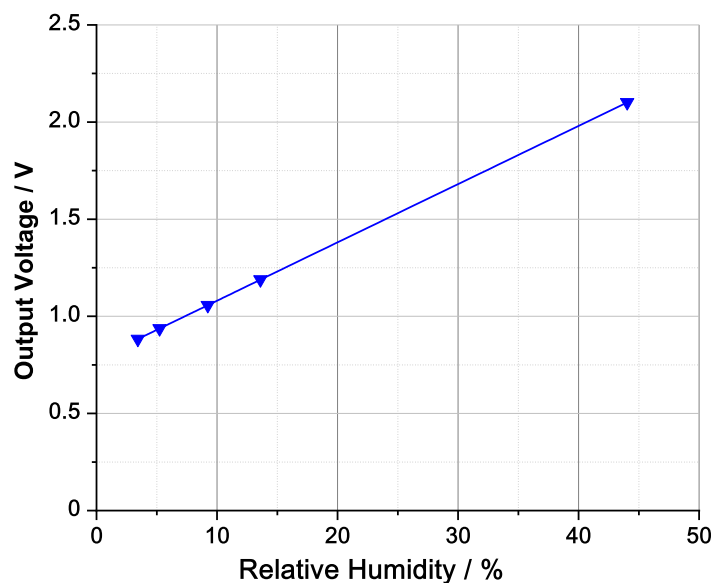


Figure 2.13: Behavior of the humidity sensor at different humidity levels

2.2.1.1 Behavior of the Sensors within the Intended Operation Range

In the course of the investigations carried, the auxiliary sensors were thoroughly studied, with a particular focus on assessing potential cross sensitivities. Linear behaviors were observed in all sensors during the experimental evaluations. However, despite comprehensive analyses, cross sensitivities were not detected in any of the sensors. Throughout the study, rigorous testing protocols were employed to scrutinize the sensors' responses to various stimuli and environmental conditions. The measurements were conducted under controlled settings, encompassing a wide range of operating parameters. Additionally, extensive data analysis was carried out, encompassing statistical methods and advanced signal processing techniques to discern any potential interference between the sensors.

The absence of such cross sensitivities underscores the robustness and reliability of the sensor design and manufacturing processes. These results reaffirm the suitability of the selected sensors for their intended applications and lay a solid foundation for their integration into the monitoring system, ensuring accurate and dependable data acquisition.

2.2.2 Microcontroller Evaluation System

The evaluation system of the monitoring system employs an Arduino Mega 2560 shown in Figure 2.14, which is a microcontroller board based on the ATmega2560 microcontroller. It has 54 digital input/output pins, 16 analog inputs, 4 hardware serial ports, a 16 MHz quartz crystal, a USB connection, a power jack, an ICSP header, and a reset button. It is powered using a univer-

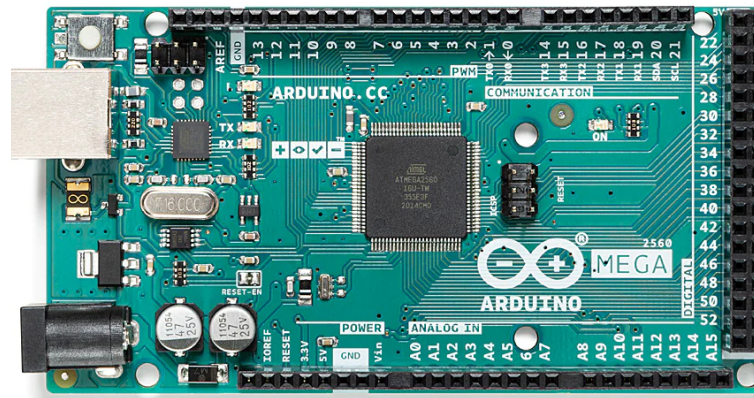


Figure 2.14: Arduino Mega 2560 used in the evaluation system of the lab prototype [145]

sal power supply, which can operate with different input voltages and frequencies, ranging from 100 V to 240 V and from 50 Hz to 60 Hz. The board has a 5 V regulator that supplies power to the microcontroller and other components. The ATmega2560 microcontroller has 256 KB of flash memory for storing code, 8 KB of SRAM, and 4 KB of EEPROM. It can operate at a clock frequency of up to 16 MHz and has 16 channels of 10-bit analog-to-digital conversion. The Arduino Mega 2560 was extended with the real time clock RTC DS3231 I2C module, which provides accurate timekeeping for a precise data logging. The DS3231 module communicates with the Arduino Mega 2560 using the I2C protocol, which allows multiple devices to share the same bus. It has a battery backup that keeps the clock running even when the main power is turned off, and it includes a temperature-compensated crystal oscillator that provides high accuracy and stability over a wide temperature

range. The Arduino Mega 2560 can be programmed using the Arduino software, which is an open-source programming environment based on the processing language. It includes a code editor, a compiler, and a bootloader that allows the code to be uploaded to the board using a USB connection. The programming language used by the Arduino is based on C and C++, with some additional libraries and functions specific to the Arduino platform [145]. The Arduino Mega 2560 with the Real Time Clock RTC DS3231 I2C module provides a powerful and flexible platform for testing the developed lab prototype.

2.2.3 Investigations on the Lab Prototype

2.2.3.1 Fault Gas Generation by Hot-Spot in Insulating Liquid

In order to recreate transformer-like ambient conditions, the test vessel depicted in Figure 2.15 was adopted. It consists of a double-walled glass cylinder that is securely fastened between two aluminum plates. On the bottom aluminum plate, three electrodes are connected. The center electrode, which protrudes beyond the test vessel, finishes with a hose barb on the bottom and is linked via a silicone tube and a clamp to a two-way valve. This two-way valve permits extracting gas samples to identify the precise concentration of the component gases by gas chromatography. The lid of the test vessel contains a recess used to insert a gas-tight connection. This connector, along with its corresponding socket, serves as the primary interface between the sensor system located inside the test vessel and the evaluation system responsible for logging and interpreting the sensor output voltages. The voltage supply of the sensors is likewise accomplished via this connection. Moreover, a needle valve and an external pressure measurement device are linked to the aperture of the test vessel's lid at its top. By closing both the valves at the end of the tube and the needle valve, the test vessel is sealed. Since the proposed monitoring system is intended to be mounted within hermetically sealed transformers, the ambient air inside of the test vessel needs to be replaced by nitrogen. For this purpose, analogous to the presented procedure in section 2.1.5, the test vessel is linked via the two-way valve and the center electrode to a nitrogen bottle using a silicone tube, and the needle valve on the lid of the test vessel is partly opened. By commencing the flow of nitrogen into the vessel, the air in its inside was progressively replaced with

dry nitrogen. The suggested monitoring system is fitted with an oxygen sensor. This procedure continues until the oxygen concentration falls below the sensitivity threshold of the oxygen sensor.

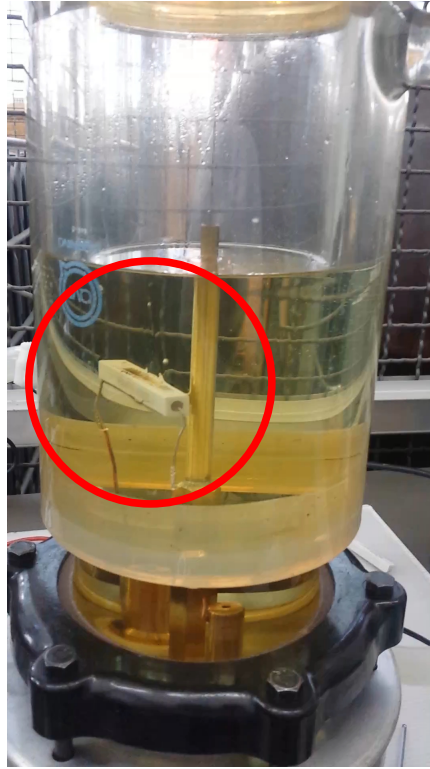


Figure 2.15: Test vessel with nitrogen cushion above the insulating liquid with a ceramic resistor for replication of hot-spot in insulating oil [144]

Two out of the three electrodes on the lower aluminum plate of the test vessel were utilized to simulate a thermal defect. Hereby, the vessel was filled to the top mouth of the middle electrode with insulating liquid. A $20\ \Omega$ ceramic resistor was placed between the two remaining electrodes and an AC voltage with a constant amplitude of approx. 20 V was applied. The current-carrying ceramic resistance was tempered owing to thermal losses. Thus, fault gases were produced via a simulated hot-spot fault at a temperature of around $250\ ^\circ\text{C}$ in the insulating liquid. The dissolved gases present in the oil within the test vessel gradually diffused into the gas cushion, where they were detected by the sensor system installed on the vessel's lid. In order to stabilize the total oil temperature during the measurement, the test setup was indirectly cooled using a circulator. The test setup is depicted in Figure 2.16.

After the test vessel was closed at room temperature and ambient pressure, and the air above the insulating liquid was replaced with nitrogen, a first gas sample was collected from the test vessel and analyzed via a GC.

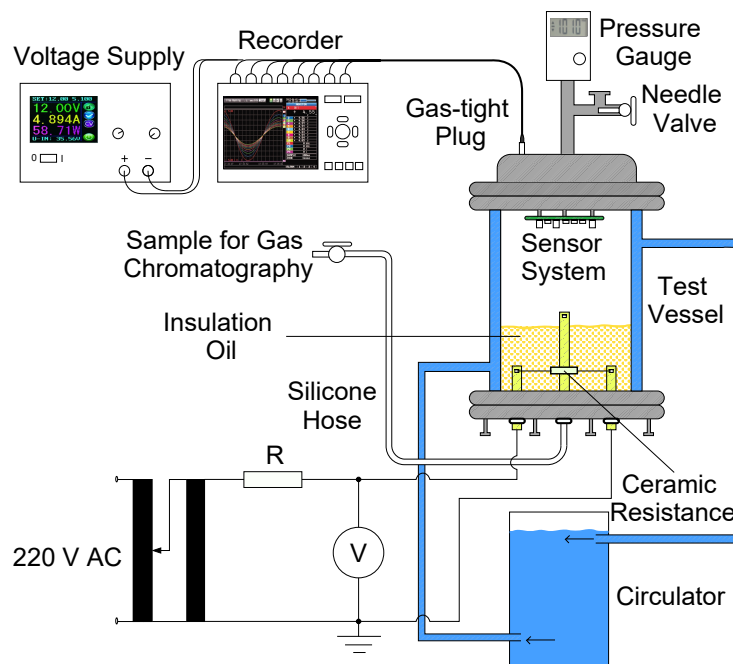


Figure 2.16: Test setup for fault gas generation and detection of hot-spot in insulating oil using a ceramic resistor [144]

The findings revealed that the gas combination in the vessel was 98.7 % nitrogen and 1.3 % oxygen. From this point on, a gas sample was collected hourly from the test vessel in order to identify the precise concentration of the fault gases, while voltage was delivered to the ceramic resistor. The findings of the gas chromatography are presented in Figure 2.17. The formation rate of the fault gases is practically consistent during the time length of the experiment.

To assess the accuracy of the fault gas sensors, the results are compared with the data obtained by gas chromatography. Two identical fault gas sensors were employed, with one sensor driven by standard method and the other with the optimized method. The output voltages of the fault gas sensors are displayed in Figure 2.17 alongside the fault gases concentrations determined using a GC.

The gas concentrations show a linear increase over time, with the rate of increase being constant for all the gases. The concentration of CH_4 was the highest among all the gases measured after 9 hours. The concentration of C_2H_4 and C_2H_2 were also relatively high compared to the other gases, while the concentration of C_3H_8 was the lowest. There is a consistent and homogeneous rise in the output voltages as well as a high correlation between the two traces observed. The trend-line of the traces are nearly linear with a 7 % deviation. Both driving methods have a similar response to each gas,

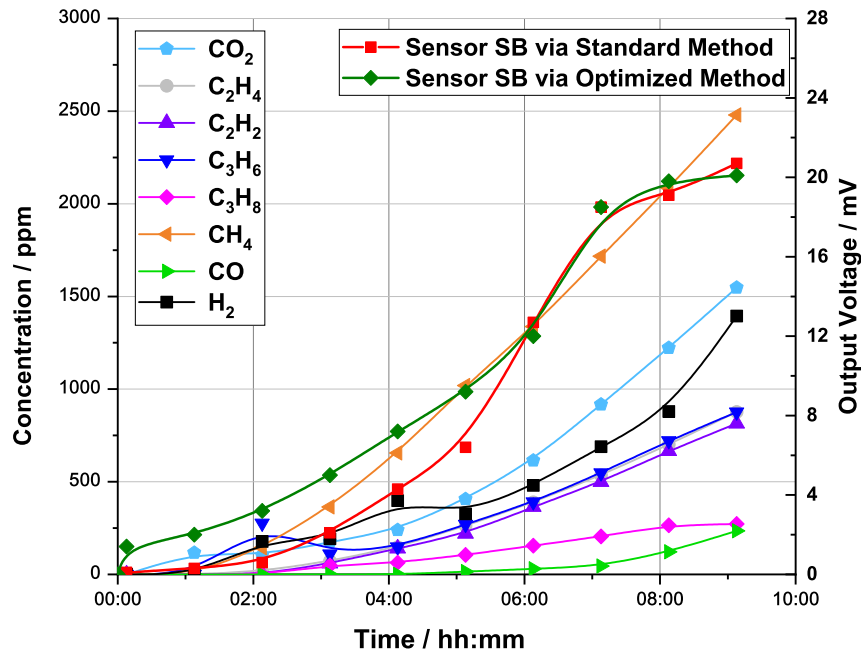


Figure 2.17: Fault gases concentrations at room temperature and ambient pressure levels determined by gas chromatography and output voltages of the fault gas sensors [144]

but the optimized method has a slightly higher sensitivity than the standard method. The sensor is intended to measure H_2 and CH_4 , but due to its measuring principle, it is also sensitive to other combustible gases.

Subsequent to this measurement, the fault gas sensors were subjected to an investigation, where they were employed in dry nitrogen and their sensitivity to individual gases including hydrogen as well as different hydrocarbons was studied by adding only one gas into a closed test vessel. The aim was to determine the concentration of each gas in a gas mixture based on the output of the fault gas sensors. Although the response of the sensors vary depending on the combustible gas in question with the highest sensitivity for hydrogen and methane, however, an exact determination of the gas concentrations in a gas mixture was not feasible. However, this is not a disadvantage, since the aim is to detect faults at an early stage. Since typical faults in transformers generate hydrocarbon gases, which are combustible, this is exploited for the task at hand. The developed online monitoring system tracks the rate of change of fault gases, which then used to issue early warning and alarm signals to the operator. This approach can contribute to preventing significant damage and ensure the long-term functionality of the transformers.

2.2.3.2 Fault Gas Generation by PD in the Windings

To test the lab prototype of the sensor system under genuine environmental circumstances, a hermetically sealed transformer was employed. The transformer tank was supplied with a nitrogen gas cushion. As depicted in Figure 2.18, the prototype was installed on the oil filling pipe of the transformer.

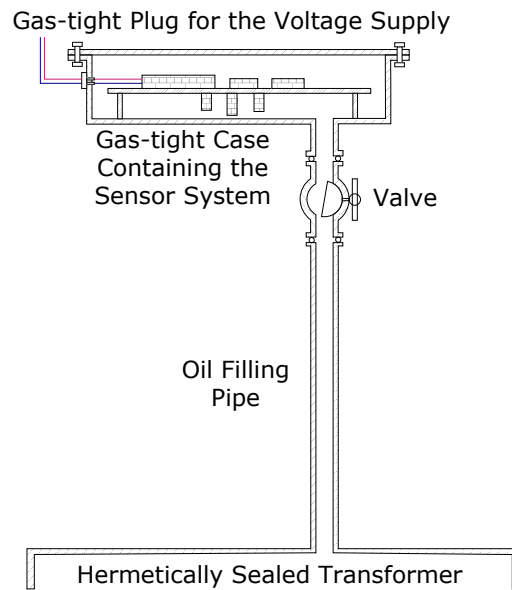


Figure 2.18: Schematic of the installed prototype on the hermetic transformer [144]

According to *IEC 60076-1*, a transformer shall have at least one plug for filling and one plug for draining the oil [146]. The oil filling pipe of hermetically sealed transformers is used to fill the transformer with oil during the manufacturing process and for maintenance purposes. The oil filling pipe is typically sealed after filling to prevent moisture from entering the transformer [147]. For the installation of the sensor system, the oil filling pipe is a suitable location, since the fault gases accumulate beneath it. Furthermore, this installation location results in a certain distance between the surface of the insulating liquid and the monitoring system, which leads to extra protection for the fault gas sensors. The undissolved fault gases rise along the oil filling pipe and are registered by the sensor system allowing a permanent monitoring of the transformer. If the output voltage of the sensor or the generation rate of the fault gases exceeds a specific threshold, a warning is initially delivered to the operator. If the situation deteriorate further, the sensor system will issue an alarm signal.

For the investigations conducted in this section, a single-phase 160 kVA hermetically sealed step-down railway transformer with a primary voltage

of 16 kV and a secondary voltage of 230 V or 460 V was used, as depicted in Figure 2.19.



Figure 2.19: Hermetically sealed railway transformer and its oil filling pipe

For the tests, the transformer was self-excited through its low-voltage terminals and regulated by an autotransformer. The accompanying electrical equivalent circuit expanded with a typical PD measurement circuit is depicted in Figure 2.20. Furthermore, the voltage on the high voltage side is monitored by a capacitive voltage divider.

Due to the fact that the filling procedure with insulating liquid did not take place under vacuum, the air bubbles in the oil cause PD when a strong electrical field is present. The PD intensity is controlled by means of voltage regulation. For the test of the whole system, the prototype was exposed to a long-term testing. The hermetic transformer was operated at high voltage for a period of around 22 days. The corresponding PRPD pattern of the generated fault is shown in Figure 2.21.

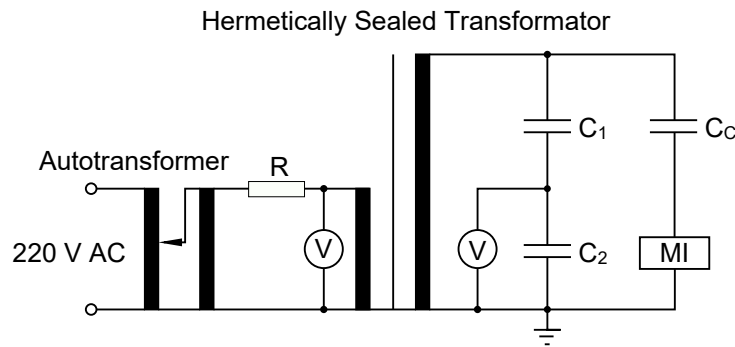


Figure 2.20: Electrical equivalent circuit of the test setup [144]

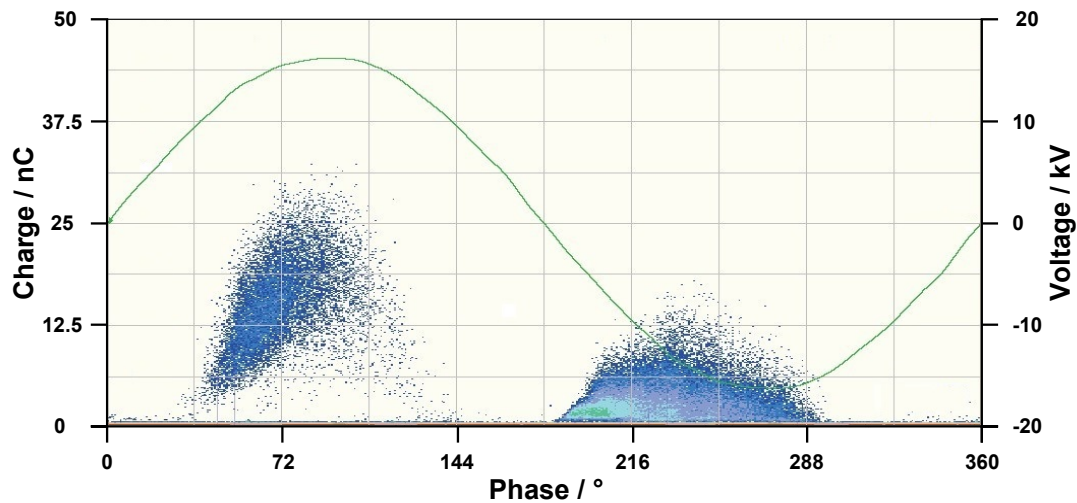


Figure 2.21: PRPD pattern of the generated PD fault [144]

The mounted laboratory prototype on the hermetic transformer is depicted in Figure 2.22. For the measurement, after determining the PDIV, the voltage was adjusted to 10 % above that value. During the testing period, there were samples taken from the gas cushion of the DUT at irregular intervals. These samples were extracted through a three-way valve underneath the monitoring system. Hereby, the voltage was terminated for a brief time period and a sample was obtained. Afterwards, high voltage was again applied. The samples were analyzed by means of a gas chromatograph. The results demonstrated that the generation rate of the fault gases were essentially maintained at a constant level for the whole period of the experiment.

The outcome of the performed measurement is illustrated in Figure 2.23. After the time period of 22 days, gas chromatography indicated a hydrogen concentration of 1500 ppm. Both fault gas sensors reveal a steady rise in the output voltage. The sensitivity of the sensors vary based on the driving method, however, a correlation between the two traces is seen. Figure 2.23 demonstrates that during the initial eight-day period of the experiment, the



Figure 2.22: The hermetically sealed transformer with the installed lab prototype on the oil filling pipe [144]

fault gas sensor driven by the standard method exhibited greater sensitivity, as indicated by the results. Afterwards, the improved procedure led into a greater output voltage. The cause for this behavior is that while the sensors are put near to each other, various fault gases have not the same influence on

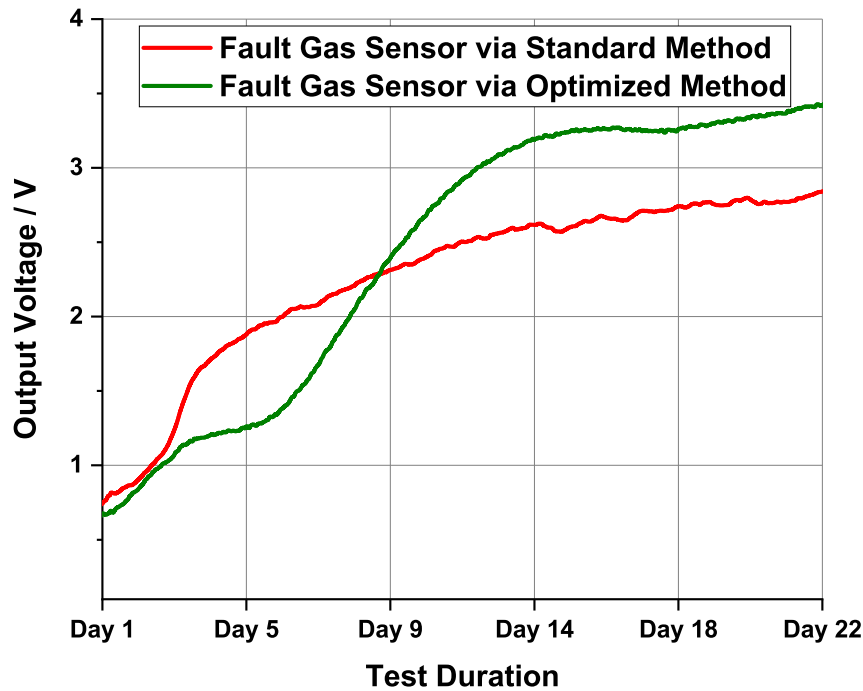


Figure 2.23: Output voltages of the fault gas sensors of the installed laboratory prototype on the hermetically sealed transformer for a long-term measurement [144]

the sensors. The output voltage rise relies on both the concentration of each fault gas as well as the applied driving technique. The experiment shows that any increase in the concentration of the fault gases is detected by the monitoring system, therefore in the event of major fault, the operator will be alerted, allowing for further measures.

The lab prototype resulting from the preliminary investigations was subjected to various measurement scenarios. The results were presented and discussed. Therefore, an industrial prototype is developed and initial field testing are being carried out. In the next section, the resulting monitoring system is presented.

2.3 The Monitoring System *TGM-101*

The laboratory prototype is industrialized after it passed the tests under different laboratory conditions. The resulting monitoring system is named *TGM-101*. In the following, an overview is given on its components.

2.3.1 Control System

The control system is housed in a *DIN* rail mount enclosure with a length, width and depth of 106.25 mm, 90.2 mm and 57.5 mm respectively. The housing is made of ABS. The control system and the sensor system communicate point-to-point via *RS-485*, so they can be up to 1200 m apart despite reliable data transmission. Data is transmitted utilizing a twisted cable and differential signals, which offer high noise immunity and long distance capabilities. This allows the operator to place the control system unrestricted depending on the circumstances, as the *RS-485* cable provides high resistance to environmental stress. In Figure 2.24, the control system is depicted.

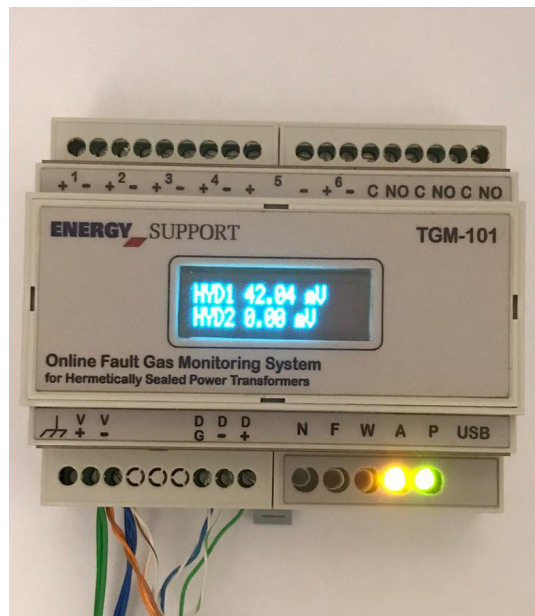


Figure 2.24: Control system of *TGM-101*

The control system collects the data and evaluates them. The raw sensor output is non-linear and can be affected by various environmental factors, as shown in previous sections. For compensating for these non-linearities and environmental effects is to use look-up tables. Look-up tables provide a way to pre-calculate the sensor output for different gas concentrations and environmental conditions, and then use this data to convert the sensor output to the corresponding gas concentration. This approach has several advantages, including accuracy, simplicity, and ease of implementation. The process of creating a look-up table involves first characterizing the sensor response to different gas concentrations and environmental conditions. This can be done by exposing the sensor to different known gas concentrations and measuring

the resulting sensor output. The environmental conditions, such as temperature, pressure, etc. will also be recorded during these measurements. Once this data is collected, it can be used to create a look-up table that maps sensor output to gas concentration for different environmental conditions. The look-up table can then be used in real-time gas concentration measurement applications. The sensor output is measured and then used to lookup the corresponding gas concentration in the pre-calculated table. The table can be interpolated to provide more precise values between the pre-calculated points. The resulting gas concentration will then be used by the control system. The developed sensor system has a warning and alarm function. If it detects an increase in the level of the fault gases, or the generation rate of the fault gases, a warning signal is triggered. If this pattern persists, an alarm signal will be activated. Both states are indicated by LEDs on the control system and by digital signals transmitted to the control room. Furthermore, the control system has a display on which all data can be called up. The data gathered by the sensors is both locally stored as well as transferred to the control room through digital and analog signals for asset management purposes. The warn and alarm flags are also transmitted to the control room.

2.3.2 Sensor System

The casing of the sensor system is a flameproof encapsulated aluminum housing with the protection class *IP 66*, meaning the sensor board is totally protected against dust as well as strong jets of water, with a length, width and depth of 150.25 mm, 150.2 mm and 99.1 mm respectively. In Figure 2.25, the casing is depicted. On its bottom, the casing has a *DN 25 ISO-KF*, which

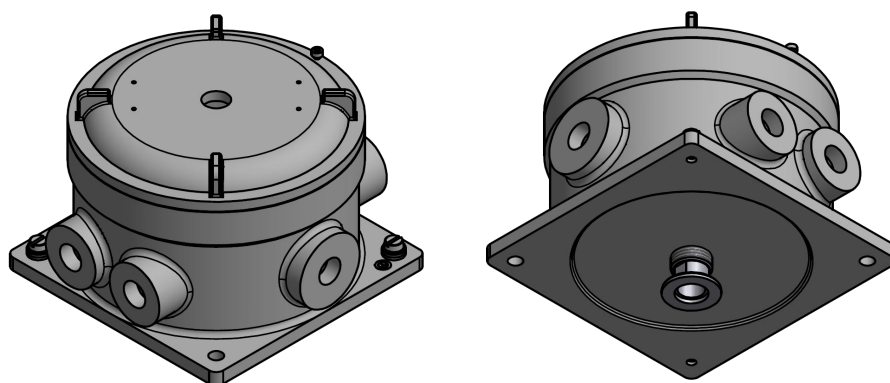


Figure 2.25: Casing of the sensor board

is a type of flange used for vacuum applications. This flange size is designed

to create a secure and tight connection between the casing and the transformer. The use of this flange ensures that there are no leaks between the sensor system and the transformer, which is essential. The sensor system is fastened on the cover of the housing. The electrical connection to the control board is via a vacuum-tight circular push pull connector on the cover. Figure 2.26 illustrates the sensor board attached to the cover of the casing. In the course of industrialization, all drive circuits of the sensors were redesigned and brought up to the latest state of the art. For the upgraded sensor sys-

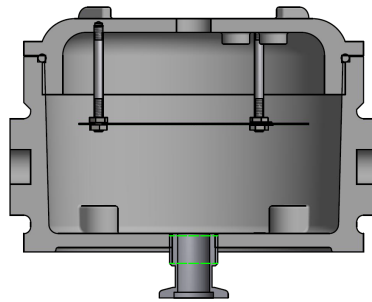


Figure 2.26: Sensor board attached to the cover of the casing

tem, a look-up table had to be determined for the fault gas sensors. For this purpose, a test setup was designed, which is shown in Figure 2.27. The test vessel contains a self-wound resistor required for the thermal decomposition of the transformer insulating oil to be tested. Constantan wire was used for

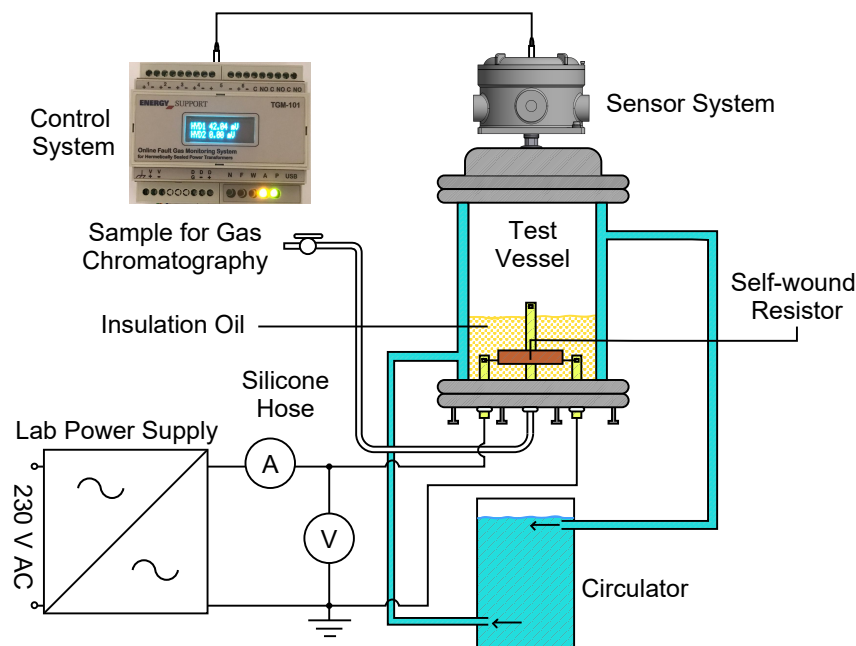


Figure 2.27: Setup for determining a look-up table for the sensor system

the winding. Constantan is an alloy consisting of 54 % copper, 45 % nickel and 1 % manganese. The great advantage of constantan is its constant resistance over a wide temperature range. The constantan wire was wound onto a ceramic tube and then a copper sleeve was placed over it. A temperature sensor is integrated into the wire, enabling an accurate temperature measurement. Various mixture combinations of fault gases were generated via this artificial hot-spot fault and a corresponding look-up table was established using DGA measurements of samples from both the oil and the overlying gas cushion. This serves the calibration of the sensor system.

The calibrated monitoring system *TGM-101* is currently undergoing trial tests on transformers in the field and completing the final steps to be available to operators.

The developed monitoring system is an innovative solution that enables the tracking of main leading indicators of faults in transformers in real-time. This system is designed to be maintenance-free, eliminating the need for additional operating materials. Furthermore, the system's compact design and cost-effectiveness make it an ideal choice for hermetically sealed transformers, whether located onshore or offshore. The system operates by utilizing algorithms to monitor the transformer's performance and detect any deviations from normal operating conditions. These deviations can be indicators of potential faults or failures, which, if left undetected, could lead to costly downtime or even catastrophic transformer failure. The monitoring system is designed to be easy to install and integrate seamlessly with existing transformer infrastructure. It is also designed to be highly customizable, with the ability to adjust the monitoring parameters to suit the specific needs of each asset.

The primary goal of *TGM-101* is to provide a reliable and cost-effective solution for monitoring the main leading indicators of faults in transformers, without sacrificing accuracy to a significant extent. This approach ensures that the system can be deployed widely, even in environments where the cost of traditional monitoring systems would be prohibitive.

Chapter 3:

Optimal Parameter Settings for UHF PD Detection

PD monitoring is a prophylactic measure in the assessment of HV equipment. The application of the UHF measurement technique in this regard is discussed in this chapter and a novel approach for selecting the optimal frequency range for conducting UHF measurements based on the device under test (DUT) is presented.

3.1 Applicability of UHF PD Detection

The analysis conducted in chapter 1 regarding the propagation of electromagnetic waves generated by PD in power transformers yielded the conclusion that the sensitivity of the UHF probe, which directly impacts the quality of PD detection using the UHF measurement technique, is influenced by two key factors: the placement of the UHF probe and the specific type of PD fault occurring in the transformer. In the case of an unfavorable sensor arrangement, it is conceivable that no signal is received by the antenna, even when the DUT features PD activity. In this section, measurement results are reported for the situation that the above indicated requirements are satisfied. PRPD pattern recognition is a well-known technique for the analysis of PD data as a first step. In the following, the possibility of applying the PRPD classification knowledge to patterns obtained through the UHF measurement technique is discussed by means of practical measurements in the transformer tank model introduced in chapter 1. A schematic overview of the tank is given in Figure 3.1.

The test circuit utilized for the measurements is depicted in Figure 3.2. The measurement is performed with the *OMICRON* measuring system as discussed in chapter 1. The electrical measurement for obtaining the PRPD

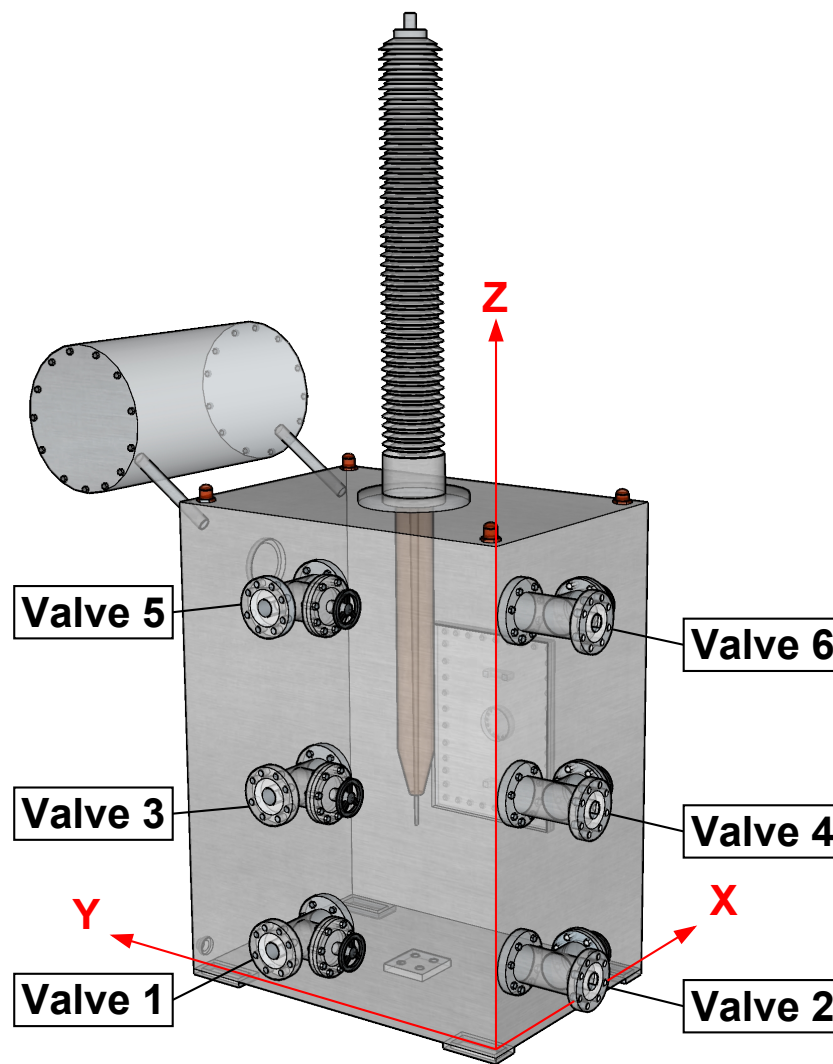


Figure 3.1: Transformer tank model with numerated valves

pattern is done in accordance with *IEC 60270* [21], while concurrently employing the UHF measurement technique with two identical *UVS 610* UHF probes. The detection frequency is set from 100 kHz to 400 kHz for the electrical measurement, while the UHF measurement includes the VHF and UHF bands. The topic of measurement bandwidth is discussed at length.

The UHF probes are inserted into the tank via valves 1 and 2 on two perpendicular sides of the transformer tank model. The sensitivity of the probes is highly influenced by their placement within the tank. To thoroughly explore this, the measurements are performed with both antennas concurrently. At this stage of the measurement, a sensitivity check is performed. According to *IEC TS 62478* [30], the sensitivity check for UHF measurements involves verifying the ability of the equipment to detect and measure weak signals. This is typically done by assessing the minimum signal level that

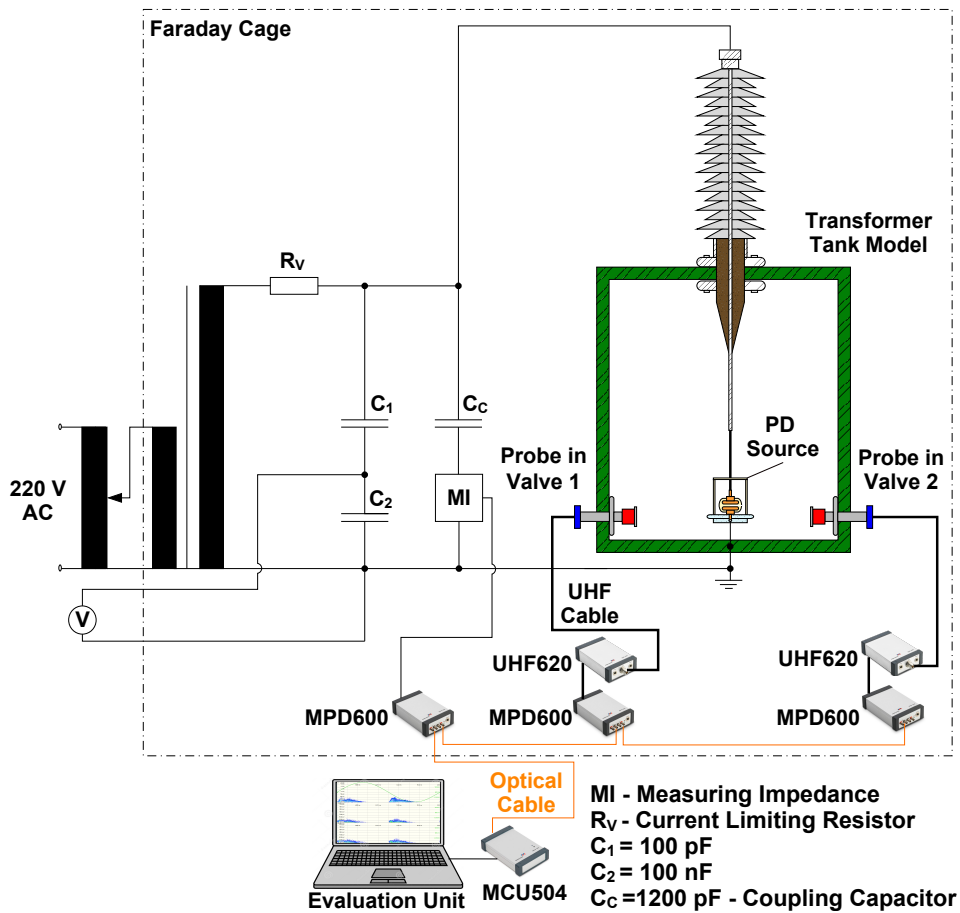


Figure 3.2: Test circuit enabling simultaneous electrical and UHF PD measurements [133]

can be reliably detected and distinguished from background noise, ensuring that the equipment meets the required sensitivity criteria specified in the technical specification. For this purpose, an artificial pulse is injected via the UHF pulse generator *UPG 620* to evaluate the detection sensitivity of the EM waves by the two sensors. Furthermore, this procedure establishes a reference signal to configure the measurement parameters of the two sensors, ensuring that the captured signals obtained from them can be effectively compared. Once the performance and sensitivity checks have been completed, the measurement system is ready to conduct UHF measurements.

For artificially generating PD pulses, the three PD fault models, namely the surface discharge model, internal discharge model, and corona discharge model, as introduced in chapter 1, are employed. Each fault model is positioned in the center of the transformer tank model and medium-band UHF

PRPD patterns are acquired by the test setup depicted in Figure 3.2. The detecting frequency is set from 100 kHz to 400 kHz for the electrical measurement. The UHF PRPD patterns were acquired with a measurement bandwidth of 70 MHz with a center frequency of 440 MHz. For each of the PD fault models, the resulting electrical and UHF PRPD patterns are presented in the following plots. Each plot consists of three rows:

- The first and third rows depict the UHF PRPD patterns acquired via a probe inserted through oil valves 1 and 2 of Figure 3.1, respectively.
- In the second row, the electrical PRPD pattern in accordance with *IEC 60270* [21] is shown and titled as IEC PRPD.

Each PRPD pattern represents a fixed time interval of 60 seconds, ensuring comparability across the results. It is noteworthy that in charge-based PD measurement as defined by *IEC 60270* [21], the y-axis represents the apparent charge of PD pulses in pC, while in UHF PRPD patterns, the y-axis reflects the magnitude of PD pulses received by the UHF probe in mV. However, a direct equalization of these values, a so-called calibration, is practically not possible as discussed in chapter 1. The x-axis in the presented PRPD patterns denotes the phase angle of the occurring PD pulse sequence in respect to the applied AC voltage.

First, the results of the surface discharge model shown in Figure 3.3 are analyzed.

A high correlation is observed regarding the phase of the captured PD pulses across all three PRPD patterns. The number of captured pulses varies, with the IEC PRPD displaying the highest density, and the UHF PRPD acquired with the probe inserted through valve 1 showing the lowest density. This has several reasons:

- **Detection range:**

The electric PD measurement method typically has a broader detection spectrum compared to the UHF method. It can capture a wide range of partial discharge activities, including both low-intensity and high-intensity discharges. This broader range allows the electric method to detect a larger number of pulses, including those with lower magnitudes that may not be detectable by the UHF method.

- **Essence of the methods:**

When comparing the electrical PRPD patterns with UHF PRPD patterns, it has to be noted that although the cause is the same, but different effects are being compared. In the electrical PD measurement

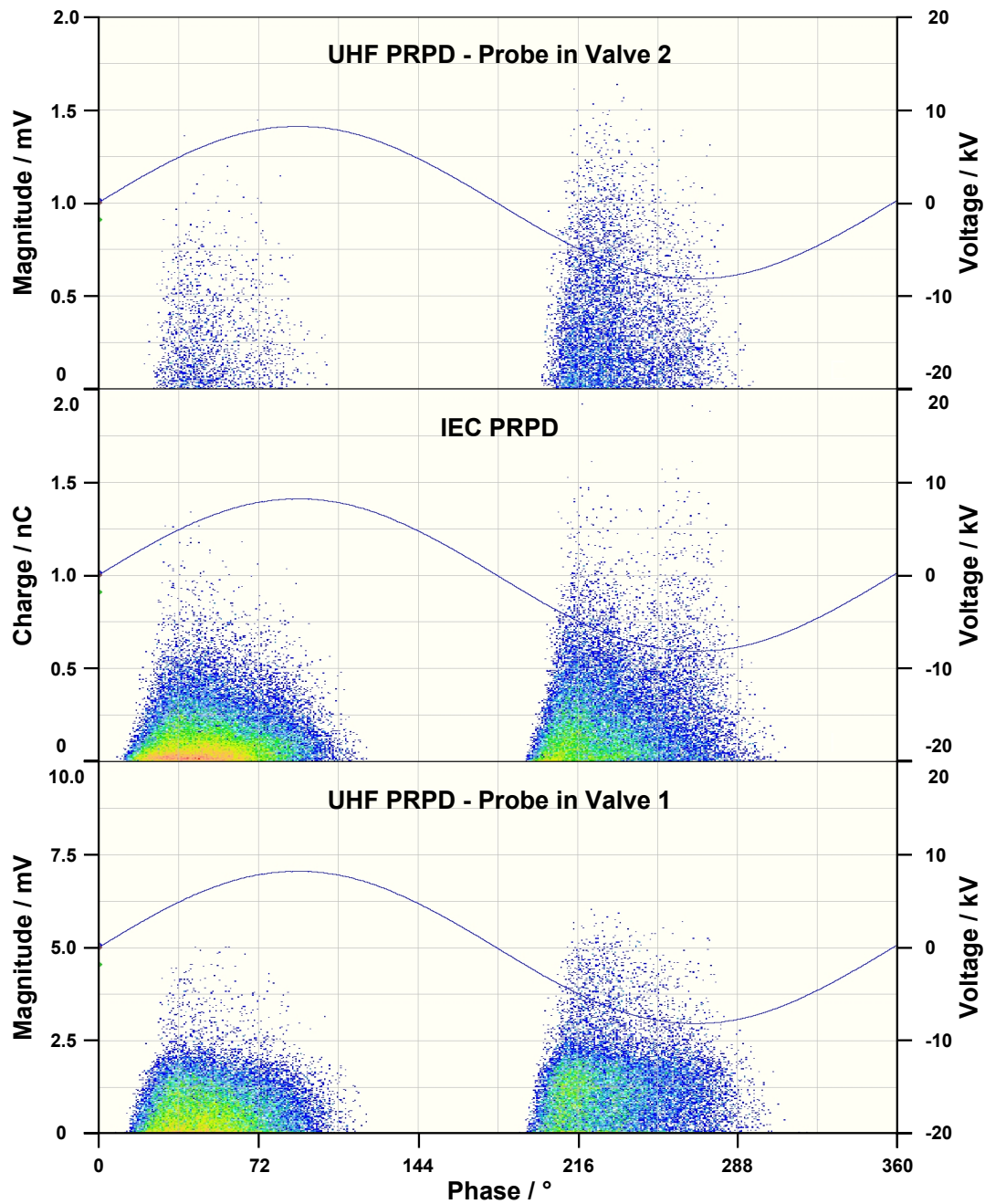


Figure 3.3: PRPD patterns corresponding with the surface discharge fault model [133]

method, the charge turn-over is the fundamental aspect that is taken into account. It involves the measurement of the electrical current associated with the PD pulses. In the UHF method on the other hand, the focus is primarily on capturing and analyzing the electromagnetic

emissions generated during PD events. Unlike the electrical PD measurement method that directly measures the electrical current associated with PD pulses, the UHF method detects the radiated electromagnetic signals in the ultra-high frequency range. Consequently, a direct pulse-to-pulse comparison between the two methods is not purposeful.

- **Sensitivity of the UHF method:**

The UHF method exhibits a notable discrepancy between the positive and negative half cycles, with a higher sensitivity observed during the negative half cycle compared to the positive half cycle [87]. The sensitivity discrepancy observed in the UHF method between the positive and negative half cycles is attributed to the distinct nature of the phenomenon that causes the propagation of electromagnetic waves in the event of PD. Moreover, the spatial surroundings inside the transformer enclosure can significantly impact the probe's sensitivity. The presence of conductive or insulating materials in close proximity to the probe may alter its electromagnetic environment, leading to signal reflections, interference, or attenuation. As a result, probes positioned in areas with complex electromagnetic interactions may display distinctive sensitivity characteristics compared to those located in less intricate regions.

The probe inserted through oil valve 1 demonstrates a discernibly superior sensitivity compared to the probe inserted through oil valve 2. This disparity in sensitivity can be attributed to the divergent positioning of the two oil valves within the tank. The probe inserted through oil valve 2, situated at the corner of the tank, inherently experiences a compromised sensitivity, while the probe inserted through oil valve 1, positioned at the central region of the wall, exhibits an enhanced sensitivity. The placement of the probe within the tank is a crucial factor in its ability to detect PD activity effectively.

Figure 3.4 depicts the PRPD patterns associated with the internal discharge model. As evident from the IEC PRPD pattern, the discharges in the positive and negative cycle are nearly identical. Both start shortly after the zero-crossing of the AC voltage cycle up to the maxima, which is typical for cavity discharges [32]. The same properties are observed for the UHF PRPD patterns. The noticed less number of pulses, and a higher sensitivity of the probe inserted through oil valve 1 in comparison to the probe placed on oil valve 2 are also observed in the UHF PRPD patterns acquired from the internal discharge model.

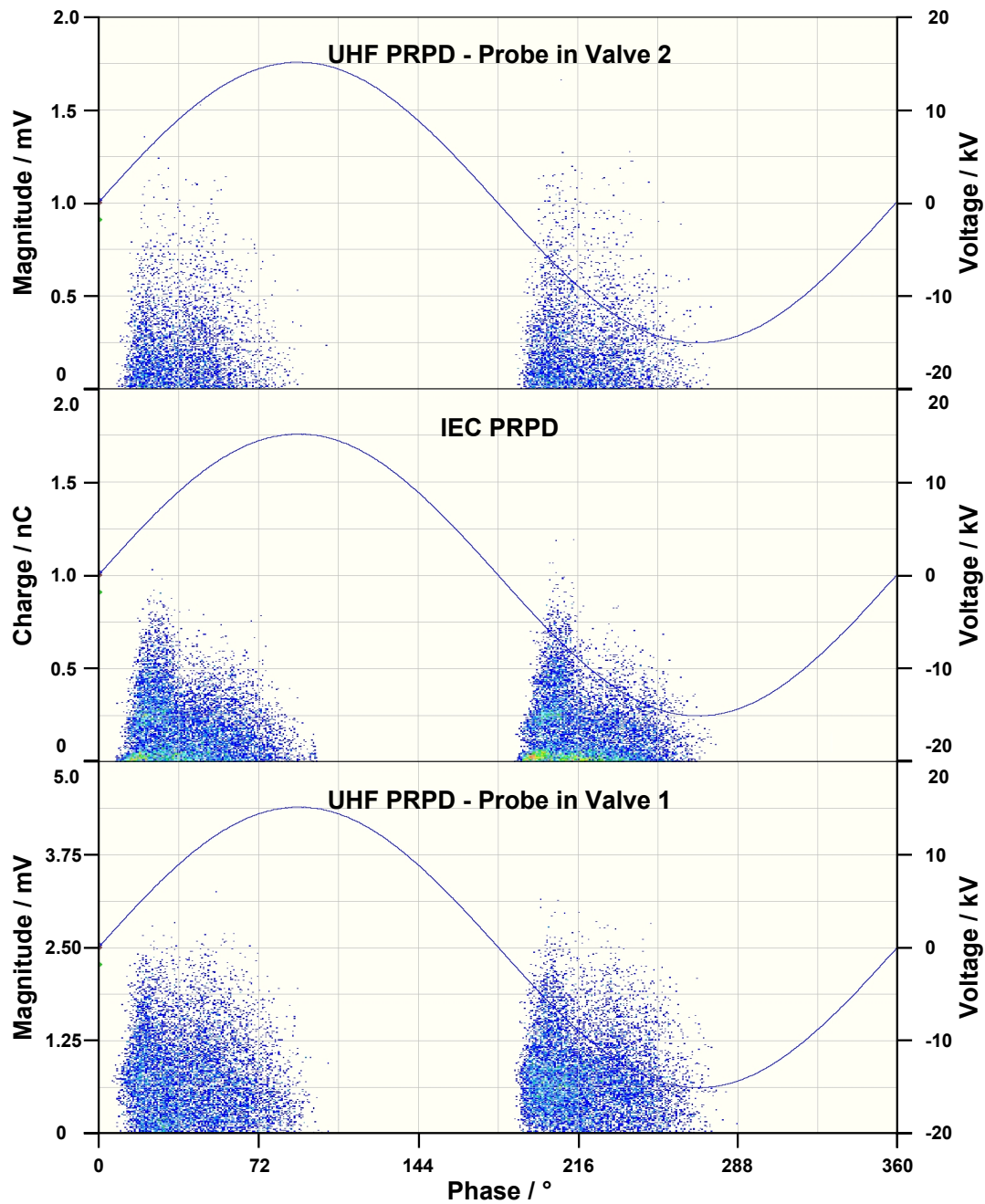


Figure 3.4: PRPD patterns corresponding with the internal discharge fault model [133]

Based on the results, in case of the surface and internal fault models, PD is identified by the patterns acquired via the probes. A good correlation between the IEC PRPD and the UHF PRPD patterns is observed. Finally, the results for the corona discharge fault model as shown in Figure 3.5 are studied.

For the corona discharge model, since the discharge magnitude in pC is lower in comparison to the other two fault models, the probe inserted

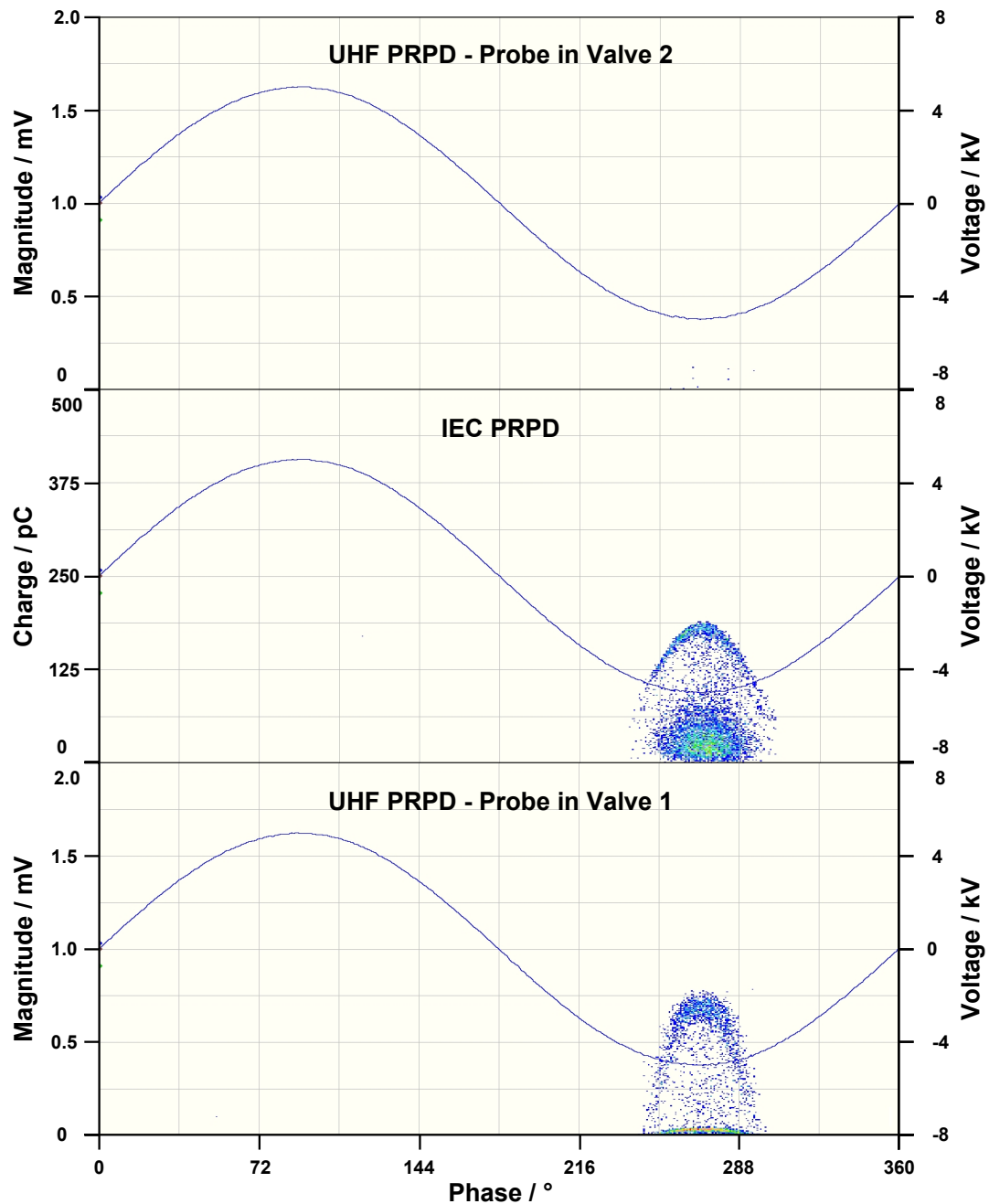


Figure 3.5: PRPD patterns corresponding with the corona discharge fault model [133]

through valve 1 has captured a pattern similar to the IEC pattern, however, the probe inserted via oil valve 2 has insufficient sensitivity, and therefore does not detect PD. This is related to the position and hence the sensitivity of the sensor and will be further addressed in the subsequent section.

In the UHF measurement method, the output signal is evidently influenced by the type of PD occurring. A notable disparity in the UHF signals is observed when comparing different PD types, which is particularly evident

in their amplitudes. For instance, in the case of surface discharge fault model, a PD event of approximately 0.5 nC resulted in an output signal of 2.5 mV at valve 1, and 0.5 mV at valve 2. When investigating internal PD events, even at the same 0.5 nC charge magnitude, the resulting output signals are significantly different. Specifically, valve 1 exhibits an amplitude of approximately 1.25 mV, while valve 2 displays the value of 0.5 mV. The evident dissimilarity between the two scenarios further underscores the challenges in calibrating the UHF measurement technique. The calibration process, which relies on establishing consistent relationships between charge magnitude via the *IEC 60270* [21], and the output signal amplitude of a probe, becomes intricate due to the variability introduced by diverse PD types and their associated EM waves. Consequently, it is evident that calibration poses inherent limitations in accurately quantifying the charge magnitude of different PD types using UHF signals.

In conclusion, the investigations in this section reveal that the sensitivity of the UHF technique is influenced by both the location of the probe as well as the PD type. Under favorable conditions, it is possible to achieve a similar PRPD pattern as, whereas under unfavorable circumstances, the detection of PD becomes unfeasible. Furthermore, the results demonstrate that the sensitivity is subject to the influence of numerous parameters, rendering calibration impracticable. This raises the question of whether the sensitivity can be enhanced by selecting more suitable settings, which will be examined in the subsequent sections.

3.2 UHF Frequency Selection

In this section, the focus lies on the influencing factors and how to select the proper frequency range depending on the DUT characteristics for conducting UHF PRPD measurements.

3.2.1 Influence of the DUT

To analyze how the position of the UHF probes and the design of the transformer tank as well as the antenna properties of the probes impact the captured EM signals, an investigation on the s-parameter is provided in this section. The s-parameter data for the UHF probes in relation to their reflection and transmission coefficients are evaluated in the following using the transformer tank model. For this reason, identical UHF probes are introduced

into the transformer tank via valves 1 to 4 according to Figure 3.1, and connected to port 1 to 4 of the Vector Network Analyzer (VNA) through 50 Ω UHF cables, respectively. The examinations conducted in this section utilized an automatic four-port calibration unit, in which all four channels of the VNA were connected to the calibration kit simultaneously via dedicated test cables. The calibration provides that the effects of the measurement accessories such as the cables, connectors, adapters, etc. are excluded from the s-parameter measurement of the equipment under test, in this instance the UHF probes. After calibrating the test setup, the connections are removed from the automated calibration kit and attached to the probes. Subsequently, the reflection and transmission coefficients of the four-port network are measured, and presented in Figure 3.6, and Figure 3.7, respectively. The subscript of the supplied s-parameter corresponds to the appropriate oil valve, via which the UHF probe is inserted into the tank.

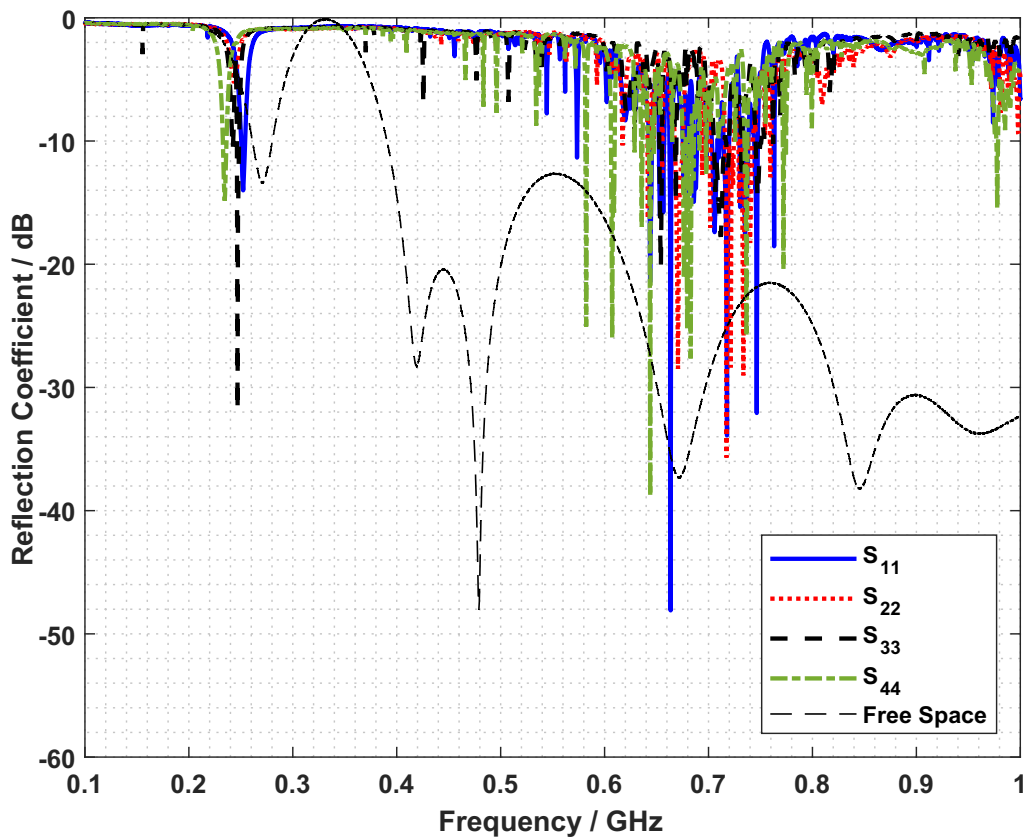


Figure 3.6: Reflection coefficient of the UHF probes introduced into the transformer tank via oil valves 1 to 4 and in free space [133]

As discussed in chapter 1, the transformer tank behaves as a resonator. In case of the transformer tank model in this thesis, it is reduced to a simple rectangular cavity with inner length, width and height of 816 mm, 1196 mm and 1556 mm, respectively. The resonance frequencies f_r of a rectangular

cavity are determined by:

$$(f_r)_{mnp} = \frac{c_0}{2\sqrt{\mu_r \epsilon_r}} \cdot \sqrt{\left(\frac{m}{l}\right)^2 + \left(\frac{n}{w}\right)^2 + \left(\frac{p}{h}\right)^2} \quad (3.1)$$

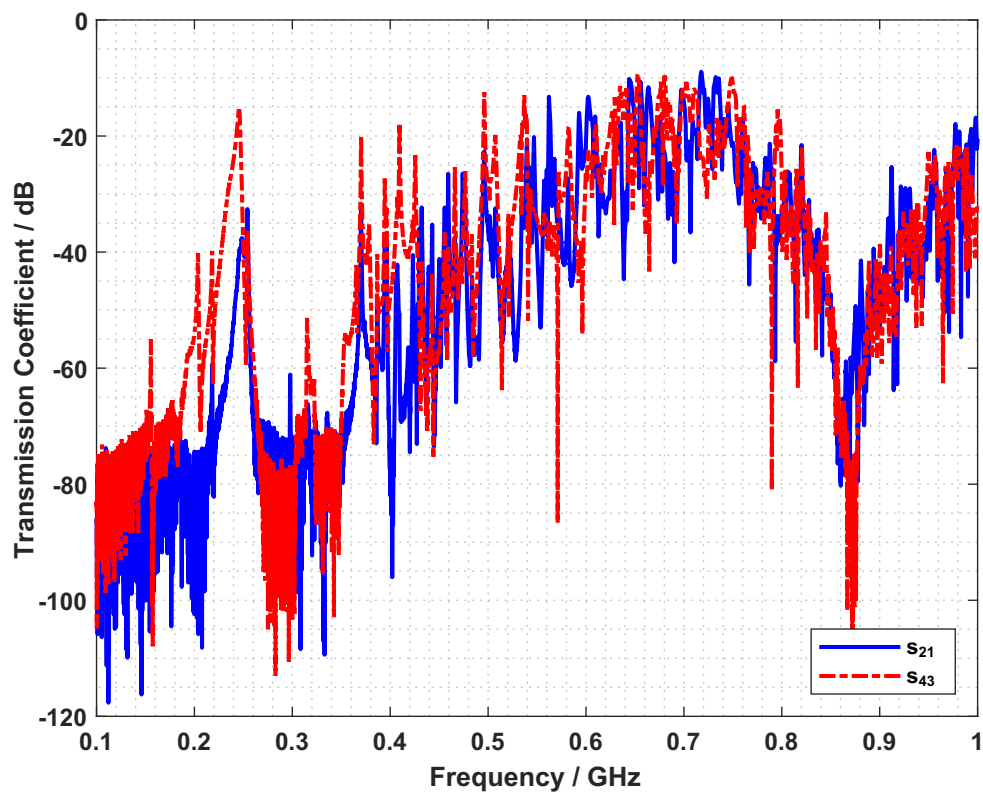
where m , n , and p are the mode numbers, c_0 is the speed of light in vacuum, and μ_r and ϵ_r are the relative permeability, and the relative permittivity of the propagation medium within the cavity, and the parameters l , w , and h are the length, width, and height of the cavity, respectively. Equation (3.1) illustrates that in a rectangular cavity, oscillation modes are only formed at a limited number of discrete frequencies [101]. For practical measurements, this is the first component that has to be taken into consideration while determining the optimal frequency range for UHF measurements.

The resulting lowest resonance frequency $(f_r)_{011}$ for the air-filled tank model considered in this work equates to 158 MHz. This is the first and dominating mode. The following six successive resonance frequencies are within the frequency range of 210 MHz to 280 MHz. The reflection coefficient of a probe reflects the quality of antenna matching between the probe and its environment. According to Jacobi's law, for optimum power transmission and also reception, the impedance of an antenna needs to match that of its surrounding [148]. This includes the medium in which the probe is inserted, but any metal or dielectric object in the immediate proximity of the probe directly influences the matching. The inside of the transformer tank comprises of several components that create inductors and capacitors associated with the probe. In addition, since the antenna is introduced via an oil drain valve, the valve itself also impacts the probe. The input reactance of each probe varies depending on which oil valve of the transformer tank is selected for insertion.

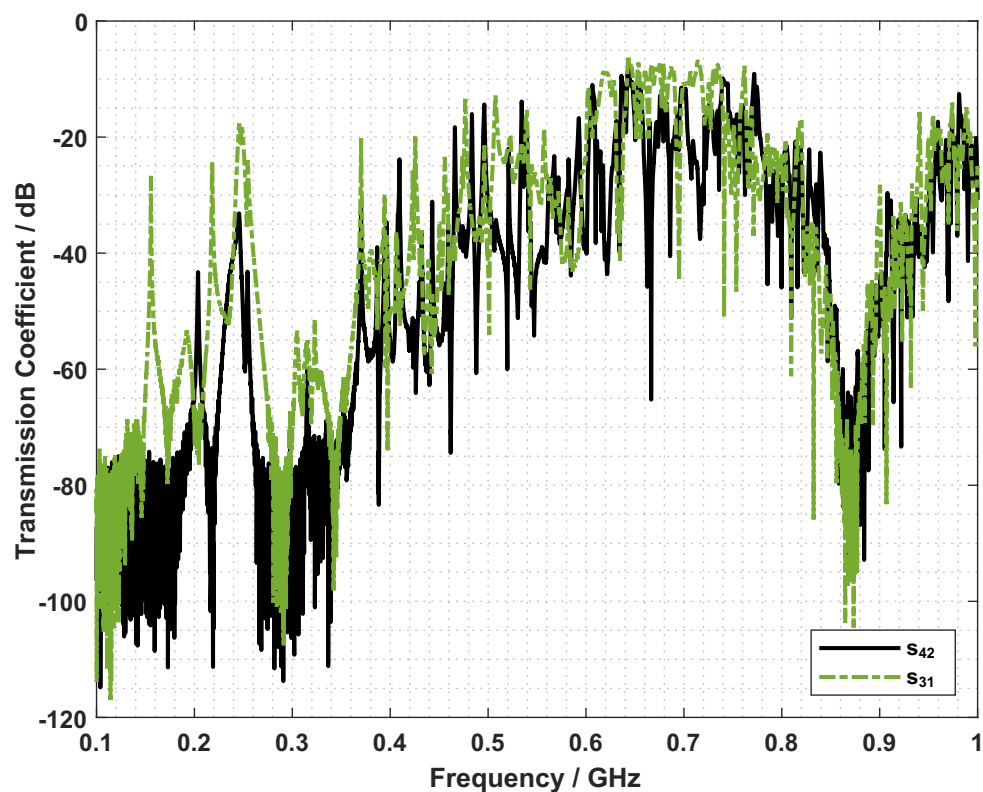
For comparison purposes, the reflection coefficient of the employed UHF probe is also measured in free space and presented in Figure 3.6. The minima in the reflection coefficient of an antenna indicate the frequencies at which the antenna exhibits good impedance matching and efficient power transfer, resulting in minimal power reflection and enhanced radiation or receiving performance. When an antenna is placed in free space, it is not influenced by any nearby structures or objects. When the same antenna is inserted into a rectangular cavity, several factors can affect the reflection coefficient. The presence of the cavity introduces new reflections, diffractions, and interference effects, which can alter the antenna's performance. These effects depend

on the size and shape of the cavity, as well as the antenna's position and orientation within it. In case of the presented results in Figure 3.6, a significant variation in the reflection coefficients is noted. Placing the probe into the transformer tank as a cavity results in the creation of a new electromagnetic system, where the resonance frequencies and influence of the cavity become predominant. In the new system, it is observed that the amplitude of the reflection coefficients in Figure 3.6 varies across the resonance frequencies of different probes in the tank. Concerning the probes inserted into the tank, a number of discrete frequencies are noticed, where the reflection coefficients are below -10 dB, which means that less than 10 % of the incident electromagnetic waves are being reflected back by the probes [149]. This suggests that the probes are efficient in capturing electromagnetic waves at those frequencies and converting them into electrical signals that can be measured via an oscilloscope. Small peaks are found in the frequency region below 200 MHz. At the computed dominant frequency of roughly 160 MHz, the probe inserted via oil valve 3 reveals a minor peak of -3 dB. The reflection coefficients of the probes put into oil valves 1, 2 and 4 reveal no peak at the lowest resonance frequency of 160 MHz. The initial resonance frequency that all the antennas exhibit is at roughly 245 MHz. The strongest and weakest peaks with -32 dB and -5 dB are associated with S_{33} , and S_{22} , respectively. This underlines a direct association between the vicinity to the walls and the sensitivity of the probe. Oil valve 2 is in the corner of the tank and hence from three sides in near vicinity to the tank walls or tank bottom. Oil valve 3 on the other hand is near the middle of the tank wall and consequently, in comparison to the other oil valves, the most distant from the tank walls. The probes in oil valves 1 and 3 exhibit a comparable result for their first respective peak with -14 dB. The sensitivity of the probes installed through the lowest oil drain valves (oil valves 1 and 2) is compared to the probes inserted through oil valves at the center of the two perpendicular transformer sides, i.e. oil valves 3 and 4, by means of considering their respective transmission coefficients S_{21} and S_{43} in Figure 3.7a. Furthermore, the transmission coefficients of a probe pair on the same wall, i.e. probes inserted through oil valves 2 and 4, and probes installed on oil valves 1 and 3 (S_{42} and S_{31}), are shown in Figure 3.7b.

By comparing the sensitivity of the probes inserted through the lowest oil drain valves (oil valves 1 and 2) to the probes inserted through oil valves in the center of the two perpendicular transformer sides (oil valves 3 and 4) in Figure 3.7a, the sensitivity of the probes inserted through the lowest oil drain



(a)



(b)

Figure 3.7: Transmission coefficient of the UHF probes introduced into the transformer tank with (a) S_{21} and S_{43} , and (b) S_{42} and S_{31} [133]

valves (oil valves 1 and 2) is determined. In addition, Figure 3.7b shows the transmission coefficients of a probe pair on the same wall, i.e. probes inserted via oil valves 2 and 4 and probes positioned on oil valves 1 and 3 (S_{42} and S_{31}).

A notable correlation between the measurement results of the reflection coefficient in Figure 3.6 and transmission coefficients in Figure 3.7 is observed. As anticipated, the transmission coefficients improve in the frequency ranges where the reflection coefficient is below -10 dB. The rationale is that a lower reflection coefficient indicates better matching, which leads to stronger radiation and, as a result, more of the injected power to the transmitting probe is transmitted to the receiver. At the tank's dominant frequency of 160 MHz, a peak is seen in S_{43} and S_{31} , whereas the peak in S_{31} with -27 dB is substantially greater. This is in turn related to the influence of the probe position and consequently its sensitivity. In both investigated scenarios of Figure 3.7, the initial joint resonance frequency occurs at roughly 245 MHz. Since the transmission coefficient contains both the effects of the propagation environment, in this case the transformer tank, as well as the antenna characteristics of the probe, it is concluded that the resonance frequencies of the tank as a cavity are aligned with those of the probe at some frequencies. Furthermore, the results of the investigation on the reflection and transmission coefficients underscore the fact that in this unique application of antennas, the near-field area of the antenna is in focus. This is in keeping with the notion of near and far field consideration of the EM waves discussed in chapter 1. As a result, the common assumptions associated with antenna theory in general are scarcely relevant in this particular application, since the issue is more complicated.

3.2.2 Frequency Analysis of the EM Waves Emitted by PD

In this section, a frequency analysis is performed on the UHF signals to examine the findings presented in the previous section through measurements conducted in the introduced transformer tank model.

For the measurements, UHF probes are inserted into the oil drain valves 1 and 2 according to Figure 3.1 with an insertion depth of 6 cm. The internal fault model introduced in chapter 1 is employed for generating PD pulses artificially. The UHF probes are connected to two channels of the 4-channel oscilloscope with a sampling frequency of 20 GS/s. The test setup of the conducted measurement is illustrated in Figure 3.8.

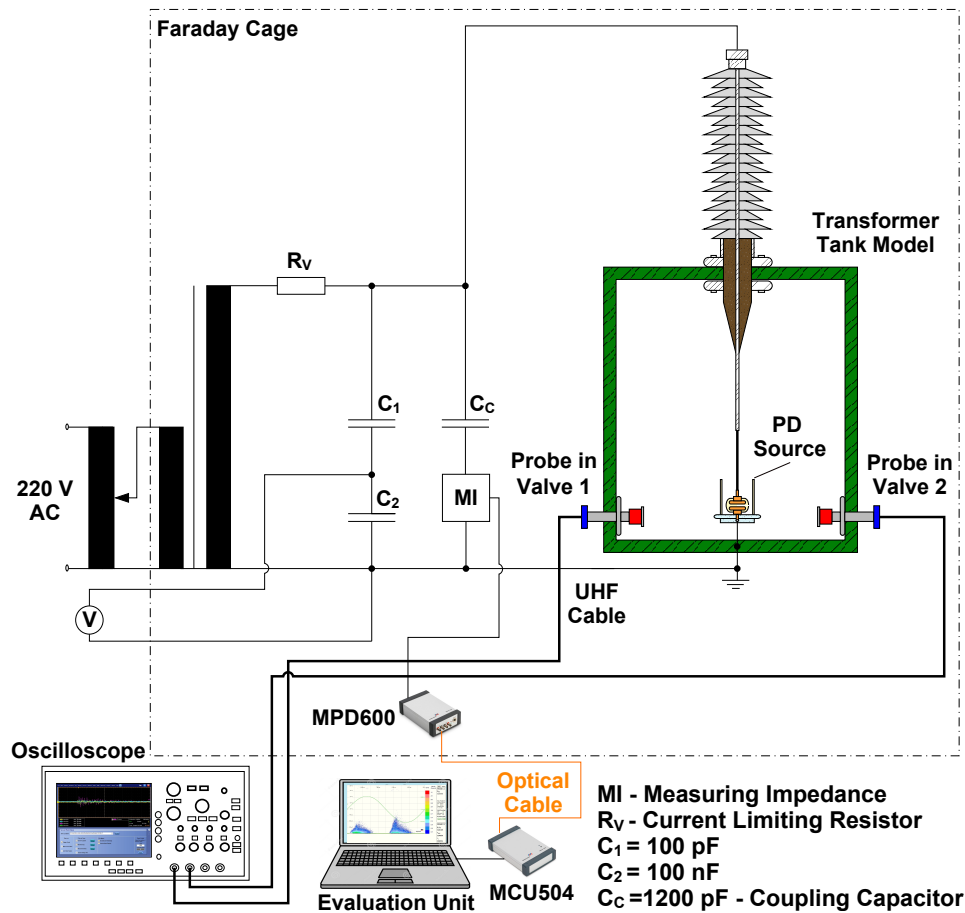


Figure 3.8: Test circuit for capturing UHF PD pulses [150]

Reflections might enhance or diminish particular frequency components of the received pulses owing to the relatively small size of the transformer tank. To focus on the initial part of the signal that contains the relevant information for this investigation, the arrival time, meaning the specific moment at which the signal is received by the probe, was determined. Subsequently, a time window with a width of 10 ns starting from the arrival time was selected and transformed into the frequency domain using discrete Fourier transform (DFT). This procedure was applied to 100 data-sets. This allows the effects of reflections or other interference that may occur to be mitigated. To combine the frequency spectra of 100 data-sets, the technique of averaging can be employed, which mathematically entails summing up the individual spectra and dividing the resultant by the total number of spectra. This statistical method yields an averaged frequency spectrum that represents the collective frequency characteristics of the signals analyzed within the chosen time frame. The resultant signal is presented in Figure 3.9.

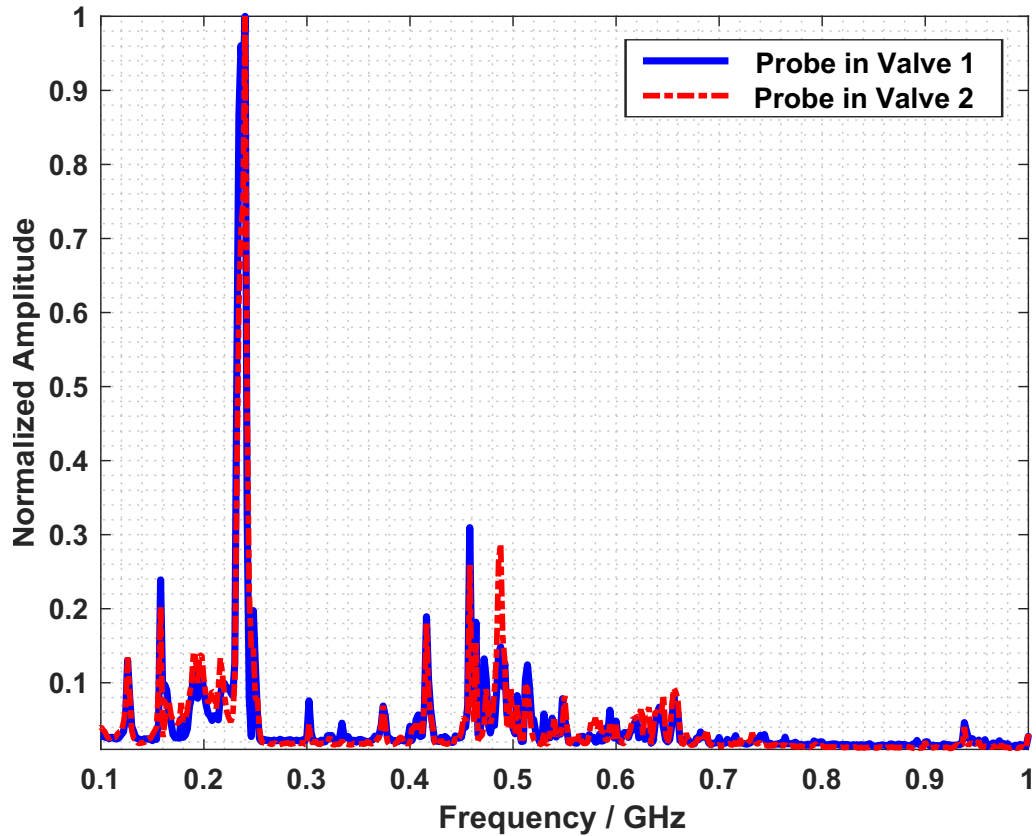


Figure 3.9: Frequency spectrum of PD pulses of the internal discharge model received by two UHF probes [150]

The results, as shown in Figure 3.9, may be interpreted by classifying the frequency range into 4 categories, as follows:

1. Below 160 MHz:

A transformer's tank is a rectangular cavity that is enclosed with metal. Each cavity has a dominant mode that is determined by its size, shape, and the medium used to fill it. Considering the transformer tank model in this thesis, the dominant frequency equals to 160 MHz. A signal with a frequency below this value will be significantly attenuated, according to theory [151]. A rectangular waveguide's dominant mode is derived by its dimensions and the medium in which EM waves travel. The bushing conductor that protrudes into the tank is accounting for the frequency components observed below 160 MHz. In this case, the PD fault model serves as the excitation source for the bushing conductor, which may be regarded as a monopole antenna in this context. This matter was addressed in section 1.3.2.3. The signals in this frequency range are captured by the probes before being attenuated due to the

tank's modest size. Conducting UHF measurements is not possible in this range.

2. Between 160 MHz and 300 MHz:

The electromagnetic waves produced by the PD fault model are responsible for the frequency components in this category. For both probes, the maximum is detected at a frequency of roughly 245 MHz. The frequency of the component with the greatest amplitude is dependent on a number of parameters, including the size of the transformer, the probe's location, the probe's antenna properties, the insulating medium, etc.; nonetheless, this range is recommended for UHF measurements.

3. Between 300 MHz and 700 MHz:

The main frequency content is concentrated in the preceding category. A cavity is predestined to resonate at specific frequencies, determined by its dimensions and geometry, and these frequencies correspond to the various resonant modes of the cavity. Hence, when a signal's frequency content is concentrated around a certain frequency range inside a cavity, the energy of the signal may spill over into neighboring frequency bins. Furthermore, the straight uninterrupted path between the PD fault model and the probe is the shortest. In reality, it is seldom the case that an uninterrupted path exists between the PD fault and the probe, since the active part of the transformer often disrupts the direct path resulting into reflections. Further UHF signal travel pathways may be determined by taking into account the tank's walls. This region is also appropriate for conducting UHF measurements for PD detection. At 440 MHz, the highest peak can be detected.

4. Above 700 MHz:

In this frequency range, there are hardly any frequency components to be observed. Only reflections could be seen in the higher frequency regions since the PD fault emits signals in the lower frequency bands; however, since each reflection loses a percentage of its energy, the signals are attenuated. As a result, this frequency range is incompatible with UHF measurements.

It is noteworthy, that the resonance frequencies of the antenna itself as a monopole with a length of 5 to 7 cm, depending on the insertion depth, have also to be considered. The first and lowest resonance frequency occurs at a length corresponding to one-quarter of the wavelength ($\lambda/4$). Hence,

the antenna resonance frequencies are above 700 MHz and thus outside the defined measurement frequency bands.

Based on the above frequency analysis of the UHF pulses for the transformer tank model, in the following section, guidelines are presented on how to determine the optimal frequency range for obtaining UHF PRPD patterns.

3.3 Proposed Algorithm for Frequency Selection

The measurement device *Omicron UHF 620*, as discussed in chapter 1, offers three bandwidth choices for performing UHF measurements: wide-band with 1.9 GHz, medium-band with 70 MHz, and narrow-band with 1.5 MHz. The wide-band measurement with a center frequency of 1.05 GHz does not provide reliable results, as a targeted measurement of the EM signals generated by PD is not achievable. The reason for this is that PD generates EM signals over a broad frequency range owing to the properties of the transformer tank as a cavity, and these signals can overlap with other signals in the frequency domain, making it difficult to distinguish between PD signals and background noise or interference. Furthermore, the broad measuring bandwidth leads to the receipt of signals with diverse amplitudes. For performing UHF PRPD measurements, an appropriate amplification factor has to be chosen, which, in case of a wide-band measurement, leads to the conundrum that the appropriate amplification factor of the measurement system is difficult to set, since either the gain factor is insufficient or the system is overdriven. By the latter, while UHF pulses are captured, suggesting PD may be identified, nevertheless, the resultant pattern exhibits a limited association with the electrical patterns. A narrow-band measurement option is also not recommended, as owing to the constrained bandwidth, even if signals are captured, the number of pulses is very limited and consequently, the obtained pattern is insufficient for interpretation. Therefore, a medium-band measurement is an appropriate compromise.

From a practical standpoint, the first factor to be considered is the dominant mode, which in case of a rectangular cavity is, as discussed in section 1.3.1, the TE_{011} mode. However, choosing the dominant frequency as the center frequency of the measurement is not advised. The optimal frequency range for performing UHF measurements is rather established by evaluating the mode density. This notion is known from electromagnetic reverberation chambers (ERC), where experiments for EM compatibility (EMC) are

carried out [102]. The dense mode environment within an ERC enables comprehensive characterization of device performance under challenging electromagnetic conditions. The objective is to evaluate the robustness, interference rejection capabilities, and overall reliability of wireless communication systems. Based on the concept of an ERC, the proposed approach for the selection of an optimal frequency range based on the properties of the DUT for conducting UHF measurements is to pick the lowest center frequency that contains the greatest number of resonance frequencies of the tank with regards to the measurement bandwidth. In case of the transformer tank model in this thesis, the resonance frequencies were determined using (3.1) and listed. The suitable choice is a center frequency of 245 MHz, which encompasses the six consecutive modes after the dominant mode. The studies on the s-parameter of the tank, where the first peak was observed at 245 MHz (Figure 3.7), are in accordance with the suggested approach of determining the optimal center frequency. A probable situation is that owing to external effects, a higher center frequency is to be chosen. In this scenario, a similar procedure is advised, where the center frequency with the most excited modes of the tank is selected. Applying this to the tank model in this thesis, the selection of a center frequency of 440 MHz is suitable, since it contains 13 resonance frequencies in the measurement bandwidth. Therefore, the following algorithm for the optimal frequency selection is proposed as shown in Figure 3.10.

The resonance frequencies of the tank must first be computed in order to identify the best frequency range for UHF measurements. The form and size of the DUT must be known for this purpose. In the case of a rectangular tank, the resonance frequencies may be calculated using (3.1). The target center frequency is the frequency with the maximum mode density, not the cut-off frequency as outlined in section 3.2. As a result, probable center frequencies are listed by the number of modes they include, depending on the measuring system's bandwidth.

The lowest center frequency is chosen for the measurement. Following that, the measuring system's gain level and amplification factor are adjusted. The instructions of the *IEC TS 62478* about the performance and sensitivity check are relevant for this step [30]. The background background noise is examined after choosing and adjusting the measurement parameters. If the background noise is acceptable, the UHF technique may be used to perform the measurement. Otherwise, fine-tuning of the chosen center frequency

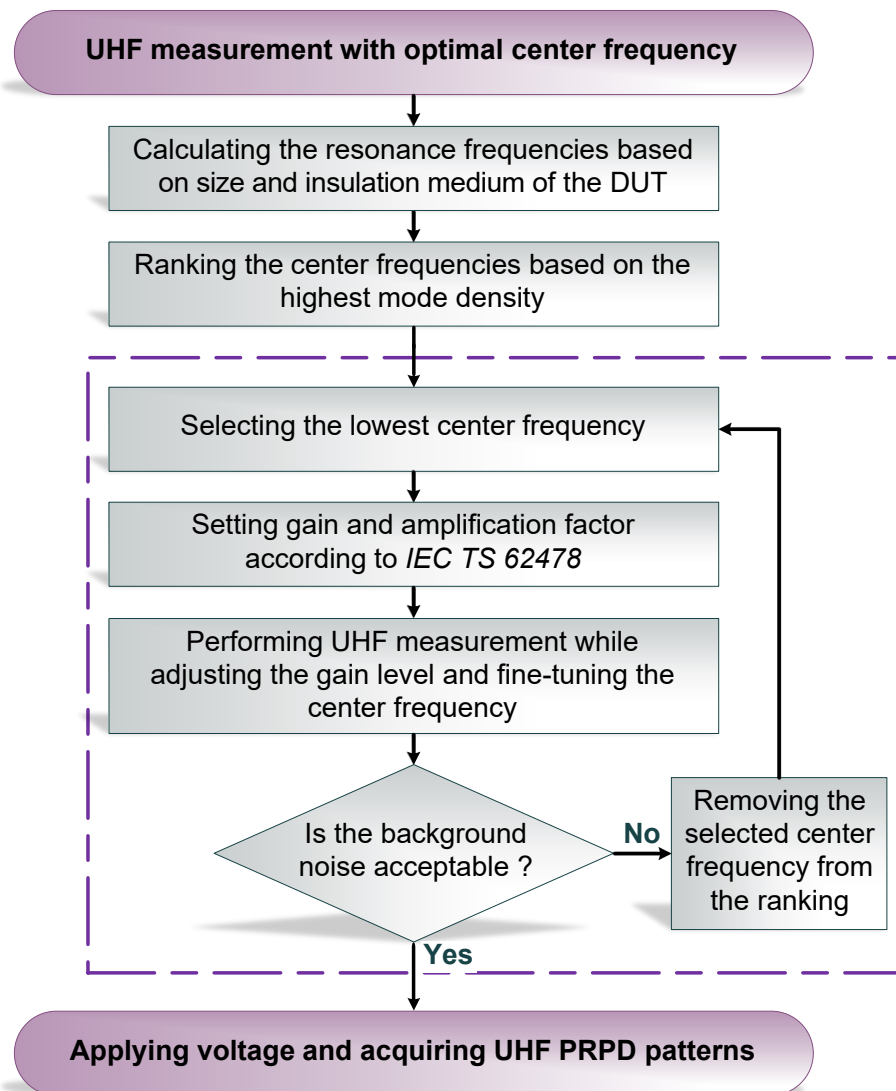


Figure 3.10: Practical approach towards the selection of the optimal frequency range for performing UHF measurements in power transformers [133]

might be undertaken first. If the background noise persists, the center frequency should be shifted to the next greatest frequency density position on the list of center frequencies, and the process repeated until the criteria are fulfilled. Figure 3.10 depicts the flowchart of the described approach to identifying an appropriate frequency range.

It is noteworthy that the active part within the transformer impacts the resonance frequencies. Moreover, the insulating oil will also impact the resonance frequencies of the tank, as the material in which the EM waves travel is represented in (3.1) by its permittivity and permeability. The oil valve, through which the probe is inserted is also an influencing element, as it acts as a semi-cylindrical cavity behind the antenna and consequently impacts

its antenna properties. The bushings and the bushing holes are the other components that determine the resonance frequencies. Equation (3.1) is recommended as a rule of thumb to find the optimum frequency range, but, similar to the electrical measurement, adjustments have to be made based on the individual conditions. In the following section, the proposed approach is validated by practical measurements.

3.4 Practical Measurements Using Different Frequency Settings

In the previous section, a thorough analysis on the frequency components of PD pulses was provided with the transformer tank model in focus. Furthermore, a practical approach on determining the most suitable frequency range for conducting UHF measurements based on the properties of the DUT was discussed. In the following, measurement results are presented. Here, the focus lies on wide-band and medium-band measurements. The former covers the complete spectrum from 100 MHz to 2 GHz. For the latter, the two center frequencies of 245 MHz and 440 MHz were deemed as suitable in the previous section. The frequency bandwidth for medium-band measurements is 70 MHz. For the UHF measurement, the test setup illustrated in Figure 3.2 is used. In terms of the fault model, the results for the surface PD model (Figure 1.13a) are exemplarily presented.

Wide-band Measurement

As previously mentioned in section 3.2.1, wide-band measurements seldom provide a pattern that is analogous to the electrical pattern. The outcome of a wide-band measurement is shown in Figure 3.11. Both probes detect signals, but the resulting patterns do not reveal the type of fault owing to challenges in regulating the amplification factor.

Medium-band Measurement

Two center frequencies, as discussed in section 3.2.1, were determined as suitable for performing UHF measurements in the transformer tank model: 245 MHz and 440 MHz. The results of UHF measurements for these two frequencies are presented in Figures 3.12 and 3.13, respectively.

The Figures 3.12 and 3.13 both indicate a high correlation between the UHF PRPD patterns and the electrical patterns. Based on the s-parameter

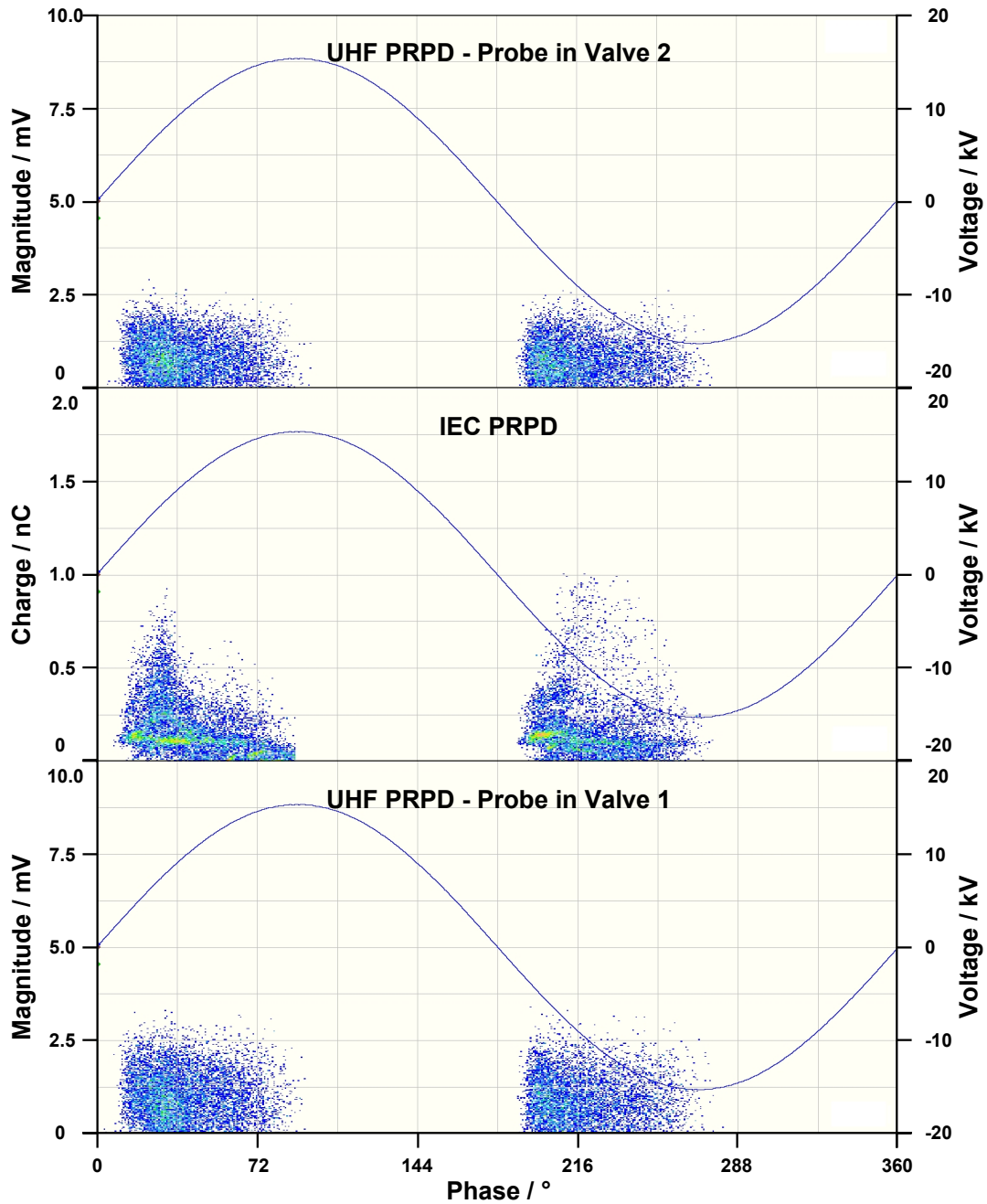


Figure 3.11: Wide-band measurement with a bandwidth of 1.9 GHz of PRPD patterns associated with internal discharge model at a center frequency of 1.05 GHz [133]

results in section 3.2.1, the probe inserted through oil valve 1 has a higher sensitivity than the probe inserted via oil valve 2. This is also reflected in the results. Furthermore, due to the number of excited modes in the tank, the number of recorded pulses at the center frequency of 440 MHz is significantly higher than that at the center frequency of 245 MHz.

While performing measurements using the UHF technique, if the frequency range of the measurement is not adjusted to the DUT, the possibility

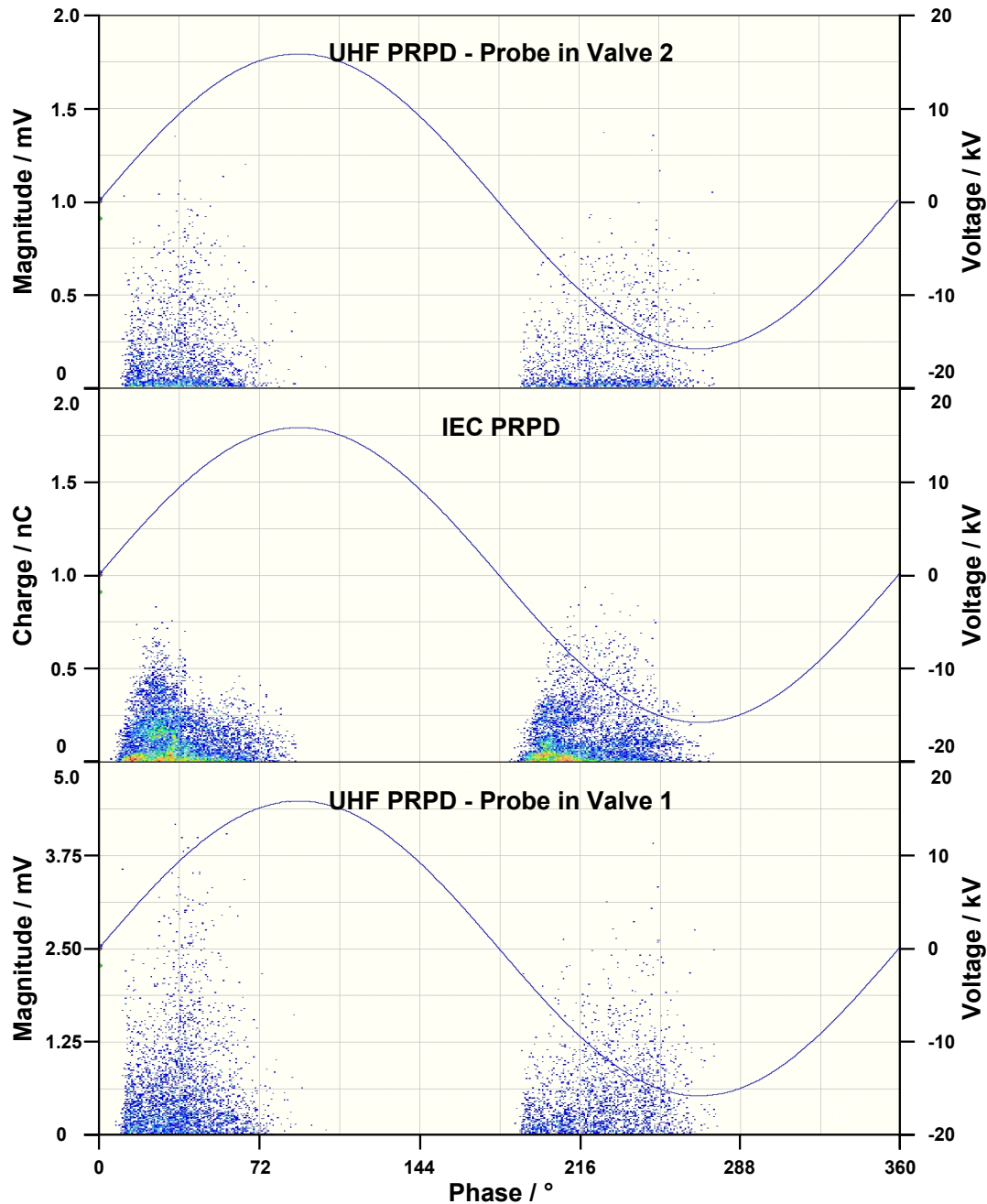


Figure 3.12: Medium-band measurement with a bandwidth of 70 MHz of PRPD patterns associated with the internal discharge model at a center frequency of 245 MHz

exists that even in case of PD activity, no EM radiation is detected. To demonstrate, UHF PRPD measurement was performed with the same arrangement at center frequencies 350 MHz and 800 MHz. The results are shown in Figures 3.14 and 3.15, respectively. The reason for this phenomenon is that these frequency components will not be able to propagate inside the tank since there are no modes that can sustain them. The attenuation of these frequency

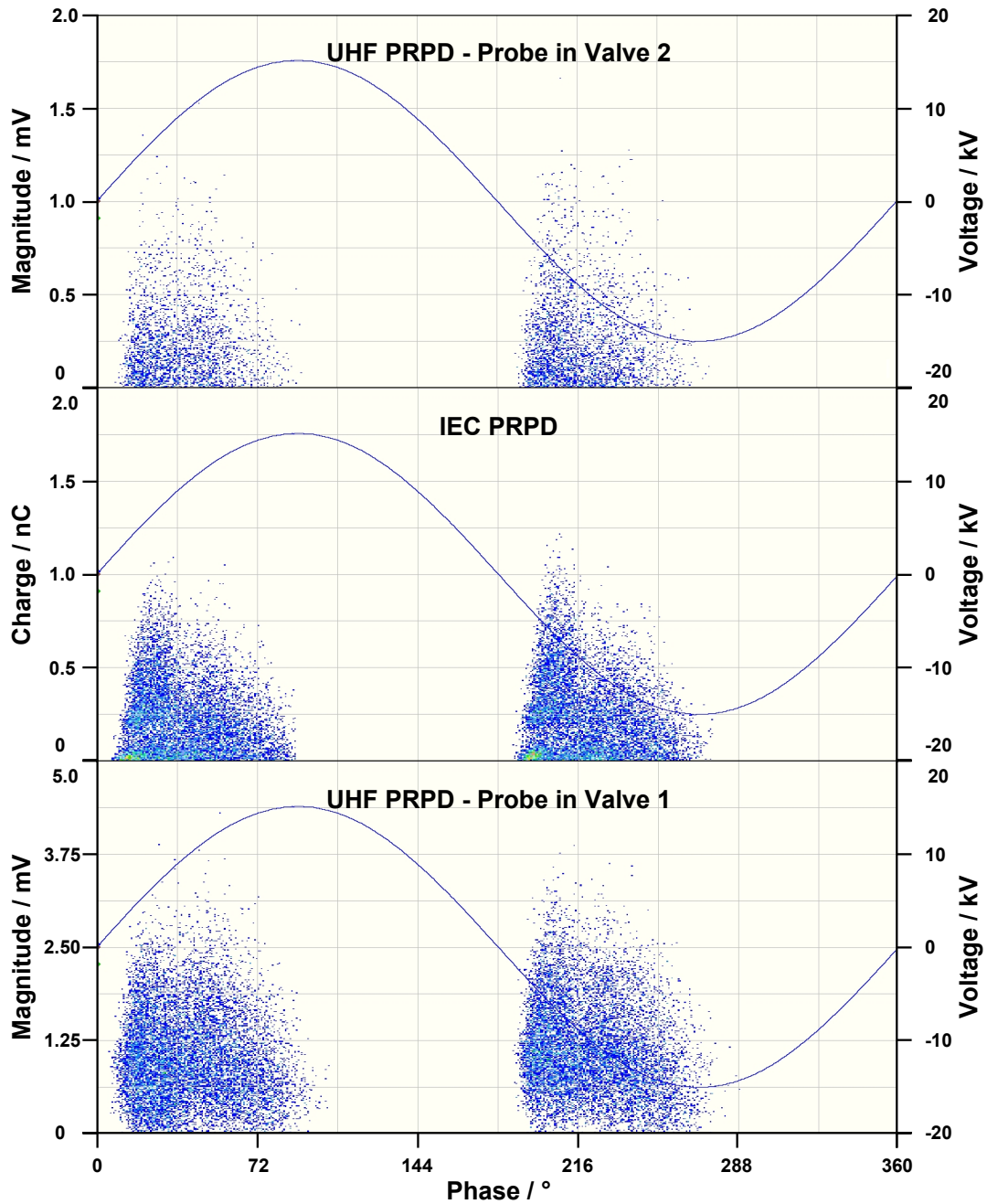


Figure 3.13: Medium-band measurement with a bandwidth of 70 MHz of PRPD patterns associated with the internal discharge model at a center frequency of 440 MHz

components inside the tank is very high, and the signal strength will be significantly reduced as it propagates along the cavity.

The PD fault models for surface and corona discharge were used to verify the observations provided in the subsection, with similar results. At a center frequency of 440 MHz, the PRPD patterns shown in Figures 3.3 and 3.5 were obtained. Although the frequency components of the signals and, as a result, the electrode layout of the PD source have an impact, however, the tank and

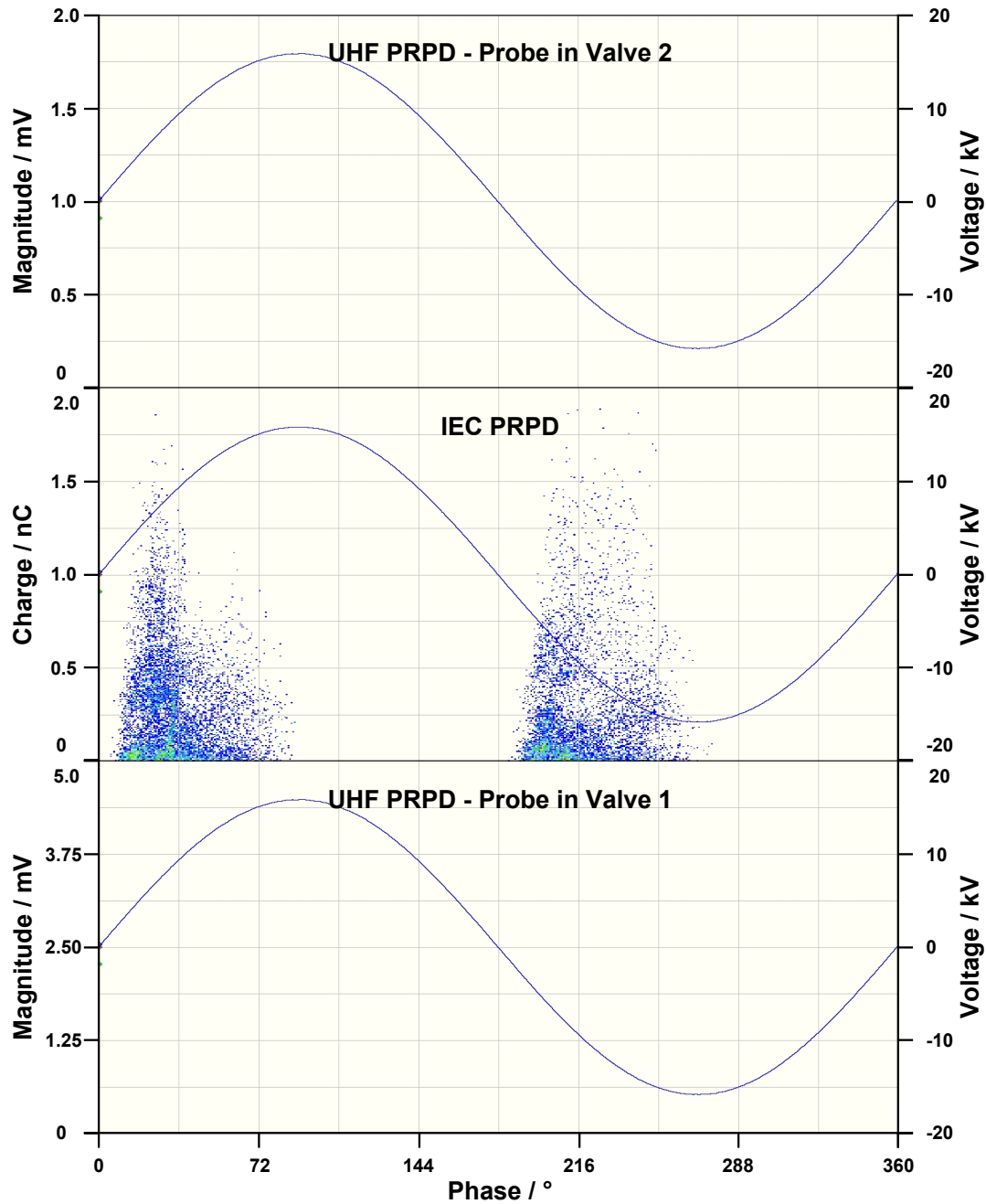


Figure 3.14: Medium-band measurement with a bandwidth of 70 MHz of PRPD patterns associated with the internal discharge model at a center frequency of 350 MHz

its electromagnetic characteristics are the crucial and deciding aspect.

Although the active part of a transformer exerts an influence on the propagation path of the EM waves emitted by PD, the impact on the displayed PRPD pattern, concerning the phase of the power frequency of the AC cycle, is found to be negligible. The EM waves generated during PD activities may encounter variations in the propagation path caused by the active

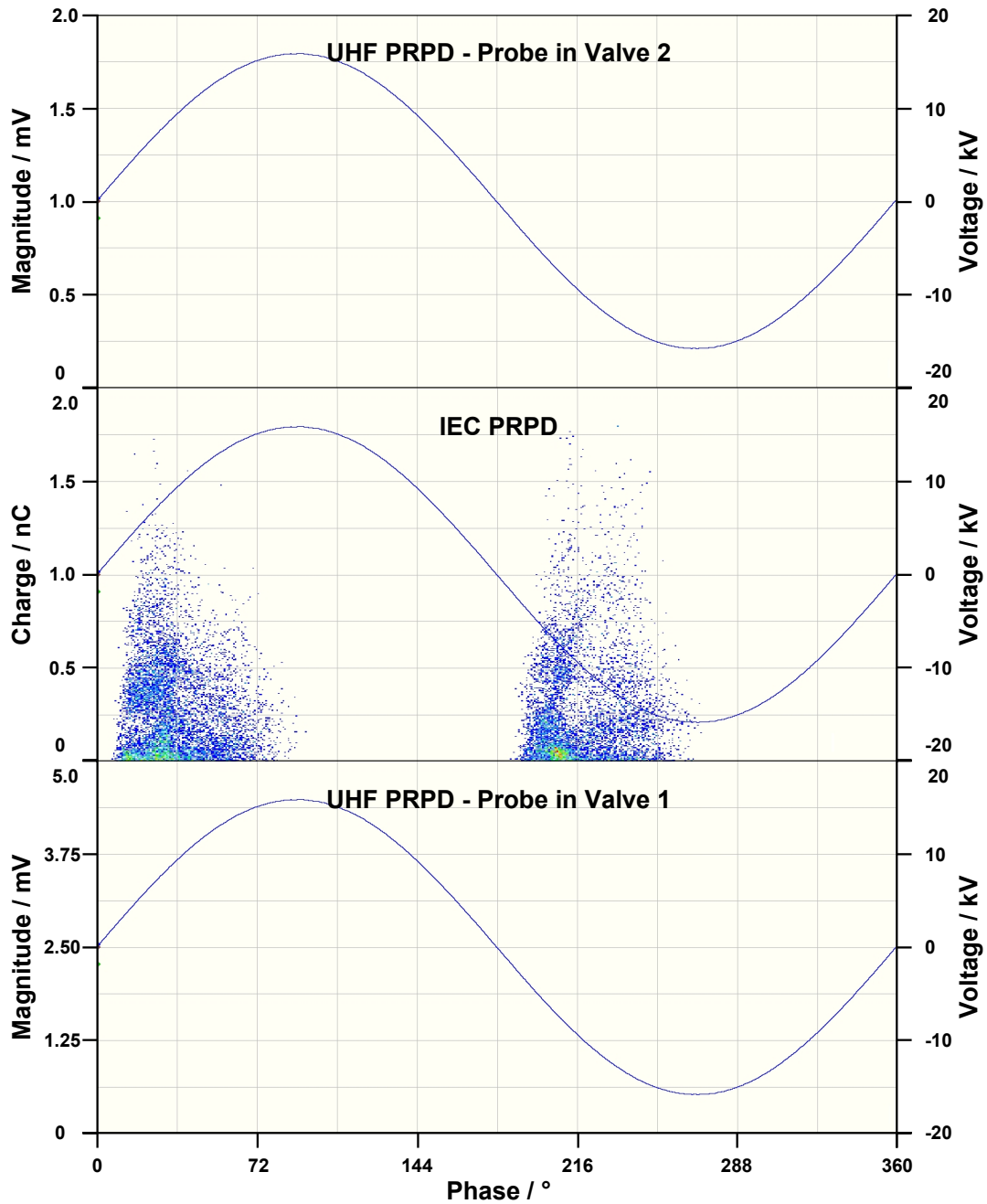


Figure 3.15: Medium-band measurement with a bandwidth of 70 MHz of PRPD patterns associated with the internal discharge model at a center frequency of 800 MHz

part within the transformer. These variations could potentially introduce delays or changes in the signals' travel times, affecting the phase relationship between the PD signals and the power frequency. However, since the EM waves propagate by the speed of light, the resulting delay caused by the active part of the transformer is minimal when compared to the power frequency's cycle time. As a consequence, any deviations in the propagation path are not significant enough to substantially alter the phase information

used to construct the UHF PRPD pattern [152].

In this chapter, the UHF PD measurement technique was studied from an EM standpoint. Individual key elements, such as PD as the excitation source, the UHF probe, and the transformer tank as a cavity, were explored in this regard. The effect of the transformer tank on the propagation of PD-generated EM waves was investigated by examining the measured *s*-parameter in a transformer tank model. It was demonstrated that, while the used UHF probe has broadband properties in free space, when inserted into the tank, a new EM system is established in which the tank's influence as a cavity resonator with specific resonance frequencies is dominant, as evidenced by the discrete profile of the reflection and transmission coefficients. These results led to the development of a practical method for determining the best frequency range for performing UHF measurements. The relevance of choosing an appropriate frequency range for utilizing the UHF approach was addressed by displaying measurement results from experiments done on a tank model. It was discovered that, in the presence of suitable measurement settings, there is a high correlation between conventionally obtained PRPD patterns and UHF PRPD patterns. Furthermore, it was demonstrated that under certain circumstances, the UHF measuring approach is incapable of detecting PD. This is due to factors such as the PD type and position, the characteristics of the used UHF probes and their placement, the active part, and the transformer tank all have an impact on the method's sensitivity. Because of these factors, a calibration that is equivalent to that of the *IEC 60270* [21] is not achievable. Finally, utilizing resonance frequencies and mode density, an effective methodology for choosing the most suitable frequency range based on the DUT was devised and presented.

Chapter 4:

Development of Methods for Enhanced PD Localization

The application of PD assessment in the condition monitoring of high voltage equipment entails three aspects: first, detection and PD type identification; second, determination of severity of the damaging effect; and lastly, PD localization in high voltage equipment. The focus of the last chapter was on the first two aspects, which were explored by comparing the UHF measurement technique to the conventional PD evaluation method. In this chapter, the determination of the PD fault location using the UHF measurement technique is presented.

4.1 Novel Localization Approach

In light of the presented measurement uncertainties in chapter 1, and to improve the localization accuracy with the UHF measurement technique, the proposed localization algorithm in this chapter applies a multi data-set approach, which is discussed in the following.

In this section, the influence of determined ATs on the resulting location for PD is analyzed by means of an analogy model. Subsequently, the approach of incorporating multiple data-sets facilitated by suitable selection criteria for computing the final coordinates of the PD fault is discussed.

4.1.1 Influence of Determined ATs on Localization Accuracy

The distance between the PD source and the corresponding UHF probe can be expressed in terms of the propagation velocity of the EM waves multiplied

by their time of flight as follows:

$$\begin{cases} (x_s - x_1)^2 + (y_s - y_1)^2 + (z_s - z_1)^2 = \frac{c_0^2}{\varepsilon_r} \cdot (t_0)^2, \\ (x_s - x_2)^2 + (y_s - y_2)^2 + (z_s - z_2)^2 = \frac{c_0^2}{\varepsilon_r} \cdot (t_0 + t_{12})^2, \\ (x_s - x_3)^2 + (y_s - y_3)^2 + (z_s - z_3)^2 = \frac{c_0^2}{\varepsilon_r} \cdot (t_0 + t_{13})^2, \\ (x_s - x_4)^2 + (y_s - y_4)^2 + (z_s - z_4)^2 = \frac{c_0^2}{\varepsilon_r} \cdot (t_0 + t_{14})^2. \end{cases} \quad (4.1)$$

where the coordinates of the PD source are denoted as x_s , y_s , and z_s , while the coordinates of each of the probe tips are represented as x_i , y_i , and z_i with i indicating the probe index. The parameter c_0 refers to the speed of light, and ε_r is the relative permittivity of the propagation medium. In this system of equations, the AT of each signal represents the duration taken by the signal to travel from the PD fault, considered as the source, to the probe. The time difference between the PD inception time and the AT of the trigger signal is denoted as t_0 , whereas t_{1i} indicates the time difference between the trigger signal and the AT of the signal captured by the i^{th} probe. The system comprises of four equations and four unknowns, namely the location of the PD fault and t_0 .

From a geometrical point of view, (4.1) describes a sphere with the tip of the corresponding probe as its origin and the radius defined by the propagation velocity times the time of flight. Since t_0 is unknown, the radii of all four spheres are dynamic values. Hence, the arrival time of each signal affects the radii of all four spheres and therefore has a significant influence on the localization accuracy. A sensitivity analysis on the ATs of the signals is presented in the following.

In order to investigate the influence of erroneously determined arrival times of the UHF signals on the calculated location of the PD, a 2D analogy model is considered. Here, the same localization principle is applied, however, due to the reduced dimensions, only three probes are required for the localization. A schematic overview of the model with the tank, the probes and the PD fault location is shown in Figure 4.1.

The considered tank in Figure 4.1 has a length and a width of 1000 mm, and 750 mm, respectively. A hypothetical Cartesian coordinate system with its origin at the bottom left corner of the tank is assumed. The coordinates of the tip of the three UHF probes and the location of the PD fault are listed in Table 4.1. The probes have each an insertion depth of 5 cm.

If the ATs are determined correctly, the system of equations in the 2D case results in three circles with their center at the probe tips and their point of

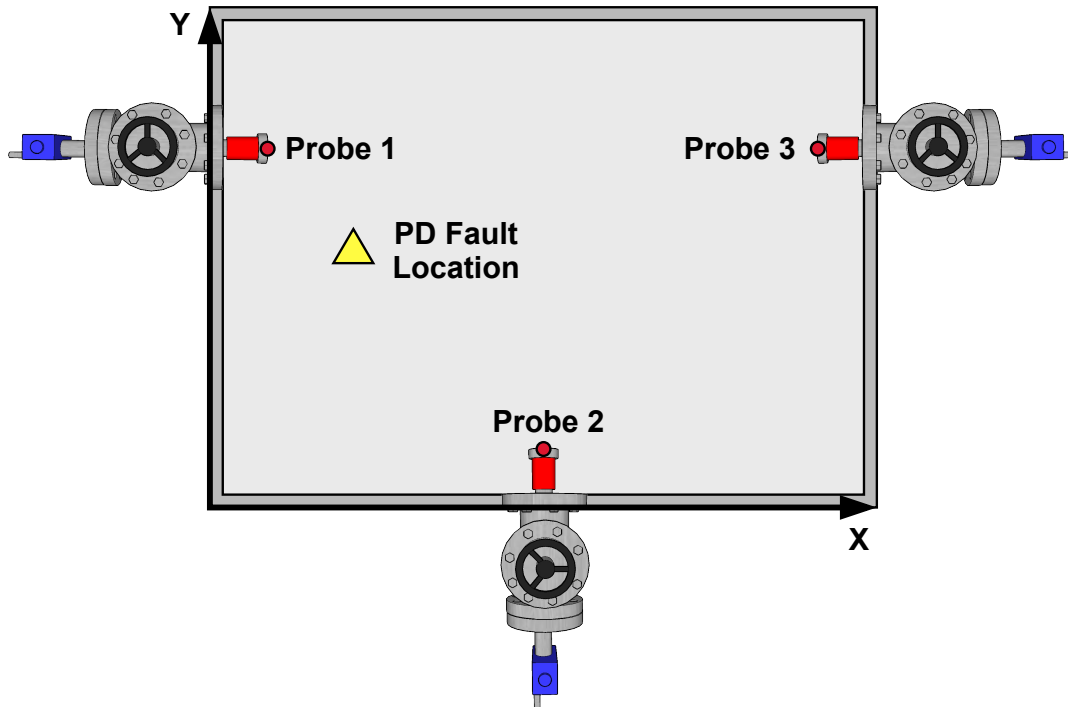


Figure 4.1: 2D analogy model with three UHF probes

intersection revealing the PD location. These circles are shown in Figure 4.2 alongside the probe tips and the PD fault location.

When performing localization measurements using the UHF technique, one of the main challenges is that the received signals are typically subjected to a lead or lag in their AT. This is the result of many influencing factors, such as reflections due to the transformer's walls, prolongations of the propagation path due to the active part, inadequacies of the AT determination method, varying propagation velocities depending on the materials etc. This has a significant impact on the resulting localization accuracy, as will be discussed in the following.

To assess how deviations in the determined ATs affect the accuracy of localization, an error in form of a lead or lag in the AT from its actual value

Table 4.1: Locations of the PD fault model and the UHF probes of the 2D analogy model

Element	X / mm	Y / mm
Probe 1	50	500
Probe 2	500	50
Probe 3	950	500
PD Fault	250	375

is assumed. This error is limited to ± 4 ns in 100 ps steps, corresponding to a sampling rate of 10 GS/s of an oscilloscope. The reduced version of the system of equations in (4.1) for the 2D case represents three circles with centers at the probe locations and radii proportional to the time difference between the PD fault and the probes, squared. If there were no errors in the ATs, the intersection of these circles would give the location of the PD fault. However, when there are errors in the ATs, the circles become distorted and the intersection points change.

To analyze the influence of errors in t_{12} on the obtained locations for PD, the system of equations (4.1) is solved for different values of t_{12} with a maximum error of ± 4 ns in 100 ps steps. This will result in a set of solutions (x_s, y_s) for each value of t_{12} as presented in Figure 4.2. It is noteworthy that

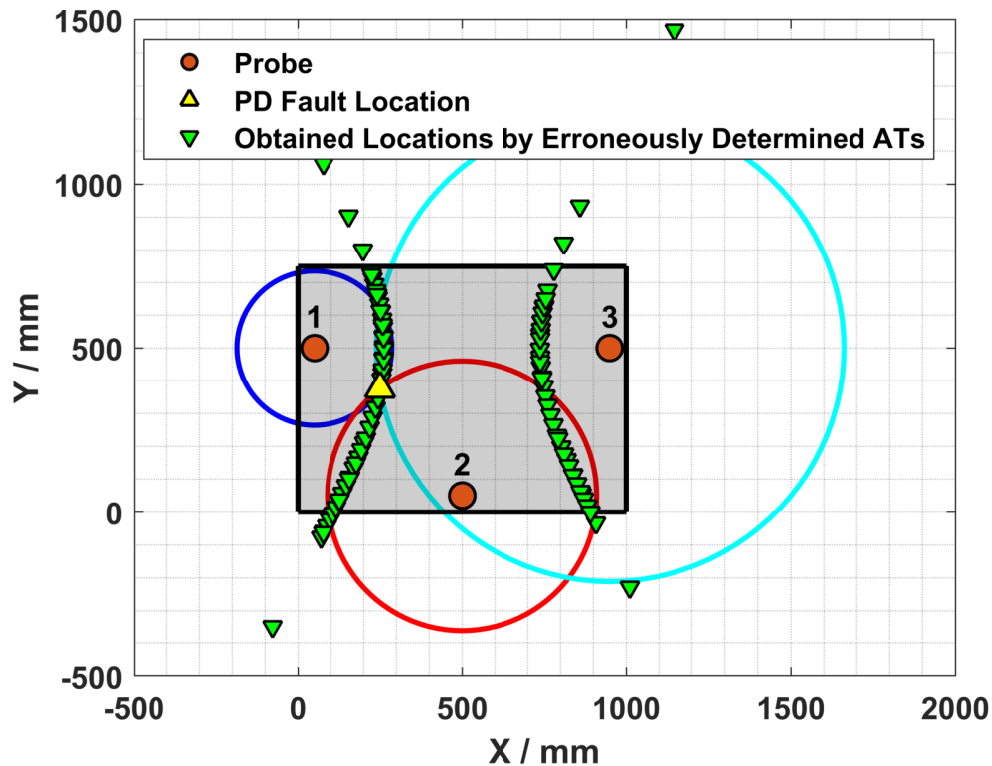


Figure 4.2: 2D tank model with the obtained locations of PD in case of erroneous AT determination of the signal received by probe 2

an error in t_{12} has a significant impact not only on the radius of the circle centered at the tip of probe 2 but also on all three radii. This is because an error in t_{12} causes a change in the calculated value for t_0 , which in turn affects the radii of all three circles in the system of equations.

Plotting all the obtained solutions for (x_s, y_s) will result in a shape known as a "locus of points" or "locus curve". This curve represents all the obtained locations of PD for different values of t_{12} , considering the defined error range.

Since there are three equations and three unknowns, each solution for (x_s, y_s) will correspond to a point in 3D space with t_{12} as the third dimension. Therefore, the locus of points will be a hyperbolic surface. The reason for this is that the circles resulting from the equations in (4.1) have different radii, and the distances between the centers of the circles are not equal. In other words, the system of equations does not describe the intersection of three spheres in a 3D space, which would result in an ellipsoid, but rather the intersection of three circles in the plane and a line. The shape of the locus curve depends on the specific values of the parameters in (4.1), however, since the analogy model is reduced to two dimensions, the locus curve will be a hyperbola. In this regard, the tips of the probes corresponding to the signals with correctly determined ATs are the focus of the hyperbola, and their midpoint is its center. The asymptote and eccentricity of the hyperbola depend on the spatial distribution of the probes with regards to the PD location. In case of PD localization in power transformers, i.e. in a 3D space, the same scenario results in a hyperboloid of two sheets.

To demonstrate the impact of an error in the AT on the resulting localization error, the introduced 2D model is considered again. An error of 500 ps in the AT of the trigger signal (received by probe 1) results in a localization error of around 8 cm. For probe 2 and probe 3, the resulting localization error is around 15 cm, and 17 cm, respectively. This indicates that the distance between the receiving probe correlates with the effect of its signal's AT on the accuracy of the localization. In the 2D analogy, the farther the PD location is from the probe, the larger the radius of the resulting circle. This in turn leads to a larger distance difference when the calculated location is considered in discrete steps. Hence, errors in the signal received by the probe farthest from the PD location result in the highest deviation in the obtained location for the PD. This presents a challenge because this signal is usually particularly attenuated due to reflections and possible obstacles.

4.1.2 Selection Criteria

As discussed in the previous section, the determined position for the PD is significantly affected by the precision of the AT determination. In this thesis, the proposed localization algorithm is based on processing multiple datasets. Hence, selection criteria are applied to increase the accuracy, which are addressed and discussed in this subsection using the introduced 2D analogy model. The first applied rule is the following:

- ▷ The value for t_0 has to be positive.

The system of equations resulting from correlating the distance between the PD source and the four UHF probes is non-linear. To address the problem, numerical methods are utilized as a common approach in solving complex equations. By employing numerical methods, the task of solving the equations is transformed into an optimization problem, where the primary objective is to minimize the sum of squares of the unknown parameters. To accomplish this optimization, certain constraints or restrictions must be imposed on the solution. One crucial limitation is related to the PD inception time t_0 concerning the AT of the trigger signal. It is essential to ensure that the PD inception time occurs before the arrival time, as a negative value for t_0 is physically infeasible and, therefore, not allowed in the context of this problem. Another vital constraint is related to the nature of the parameters involved in the equations. The parameters must take on real values only, and any complex or imaginary solutions are disregarded. This limitation arises due to the practical implications of the problem, as only real values make physical sense, which leads to the second rule:

- ▷ The obtained location for the fault must be feasible.

This rule removes some of the candidate locations by imposing strict requirements. By carefully assessing and utilizing crucial input data, including the precise dimensions of the tank and characteristics of its active part, this rule efficiently narrows down the pool of selected candidates for the PD fault location. The objective is to eliminate locations that have emerged in the process, but are implausible. These locations, often situated outside the confines of the tank, do not align with the physical constraints and practical considerations of the setup. Consequently, it is imperative to exclude such improbable positions from further consideration, as they can lead to misleading or erroneous results. By judiciously applying this rule, the analysis ensures that only relevant and feasible candidate coordinates of the PD source are taken into account. This enhances the accuracy and reliability of the subsequent evaluations and allows for a more precise localization of PD within the tank.

For demonstration purposes, the result of subjecting the obtained locations for the fault in case of a lead or lag in the AT of the signals received by probe 1, and probe 3, in 500 ps steps are depicted in Figure 4.3a, and Figure 4.3b, respectively. For each case, the result of solving the system of equations for the 2D model is shown as dashed circles indicating the obtained radii leading to the determined location.

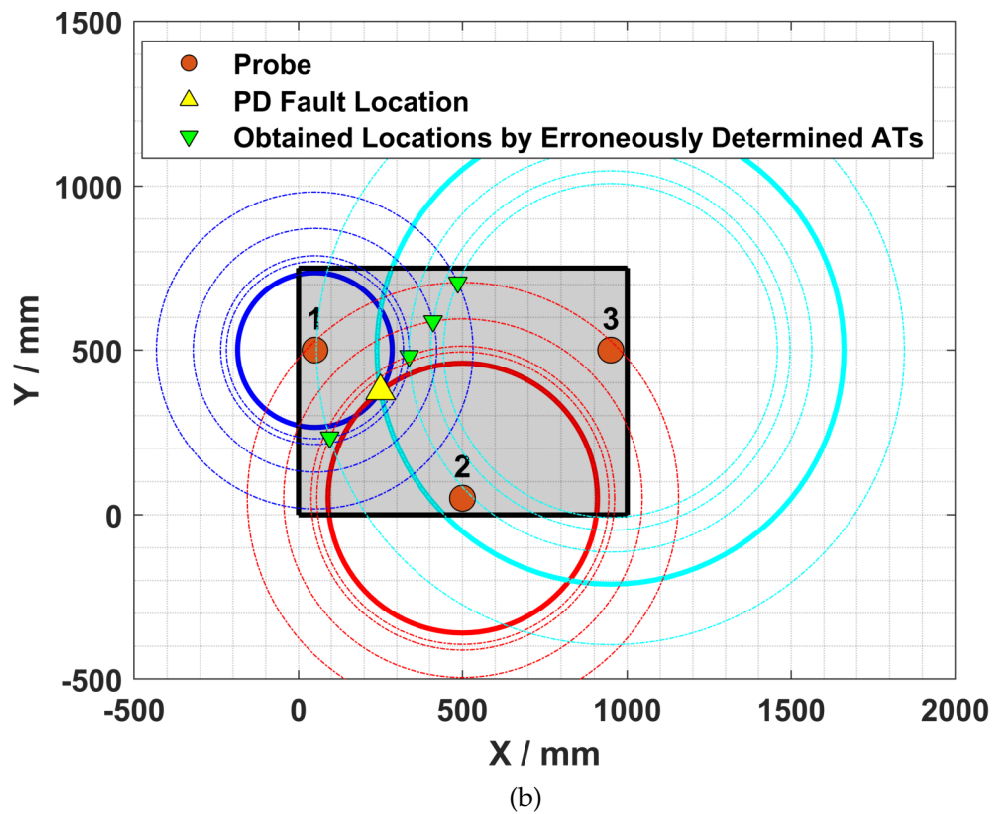
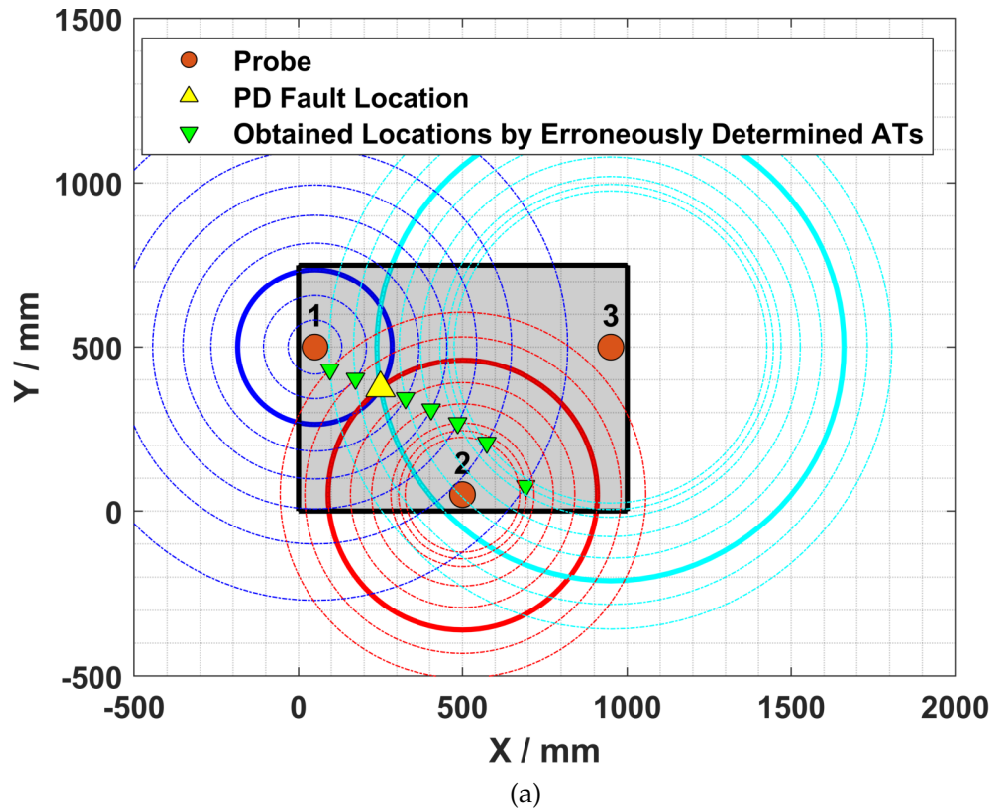


Figure 4.3: 2D tank model with the obtained locations of PD in case of applying selection criteria to erroneously determined AT of the signal received by (a) probe 1, and (b) probe 3

Regarding the results presented in Figure 4.3, it can be noted that for equal errors in ATs of the received signals by probe 1 and probe 3, the influence of the latter is more significant. Furthermore, by applying the selection criteria, only one of the curves of the hyperbola remains since the other curve is associated with negative values for t_0 .

In addition to the two aforementioned selection criteria, the following is also applied:

- ▷ The location of the fault has to correspond to the correct sequence of arrival.

It is assumed that the order of arrival of the signals from the PD source to the probes is known. This third rule significantly reduces the number of candidate data-sets that contribute to the computation of the final location for the PD. The method that is used to determine the arrival time of the signals and consequently the correct arrival sequence will be addressed in section 4.3.

In the cases considered so far, only the AT of one of the received signals was subjected to an error. This is rarely the case in practical measurements. In Figure 4.4a, the unprocessed obtained locations for the PD fault are illustrated, if the determined AT of the signals is subjected to a lead or lag between 1 to 5 samples. The sampling frequency is considered to be 10 GS/s, meaning a maximum error of 500 ps in the ATs. Figure 4.4b illustrates the result of subjecting the obtained locations shown in Figure 4.4a for the PD fault to the three selection criteria. The obtained locations surround the actual PD location.

A similar approach can be taken towards different constellations of the probes and the PD location with similar outcome. Lastly, a pattern can be obtained for each location inside the tank for the PD fault. This pattern represents possible erroneously obtained locations for PD that can be the outcome of a single data-set. This suggests that by increasing the number of considered data-sets in the evaluation, and therefore the obtained locations, a higher localization accuracy can be achieved. Moreover, clustering methods can be applied to determine the final location for the fault. In the presented results in this section, only a maximum deviation of 500 ps was considered. It is noteworthy that in practical measurements, the error in the AT determination could be well above this threshold. Hence, it is to be expected that even with a data-base consisting of several data-sets, only a small fraction are selected in the final stage of determining the PD location. An increased number of data-sets is however recommended to ensure the desired localization accuracy.

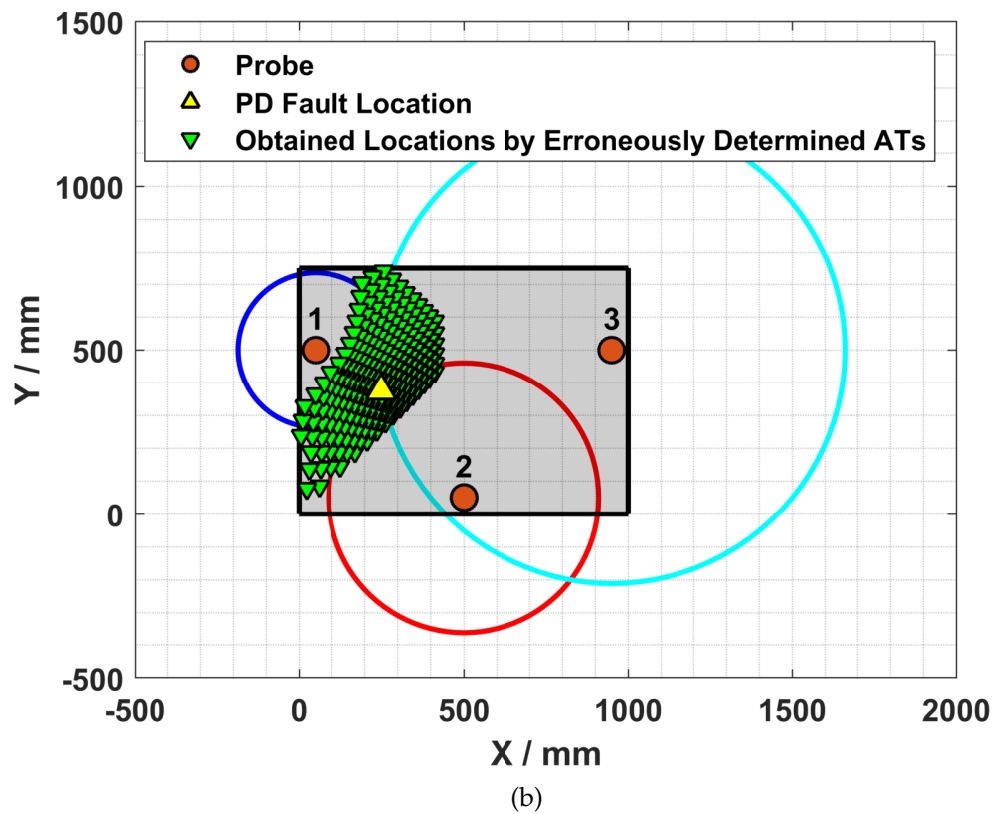
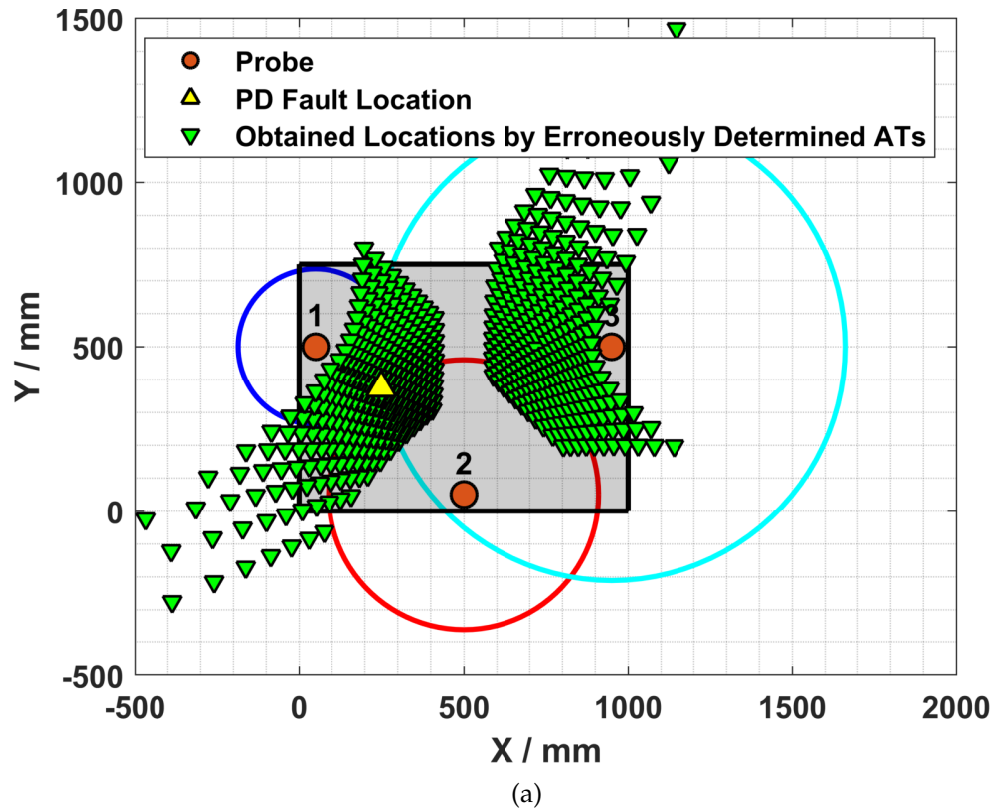


Figure 4.4: 2D tank model with the obtained locations of PD in case of erroneous AT determination of all received signals (a) before, and (b) after applying the selection criteria

4.2 Simulation of the Wave Propagation using the FDTD Method

The effect of deviation in the determined ATs of the signals on the obtained PD location was discussed in the previous section using a 2D-model. The method of digital signal processing applied to determine the AT is not the only factor affecting the localization accuracy. Since a transformer has a rather complicated inner structure, a direct line of sight between the PD location and the probes is seldom. The active part of the transformer causes reflections and thus extended propagation times. In this section, the effect of the active part is investigated. For this purpose, the Finite Difference Time Domain (FDTD) method, which is a numerical technique based on the finite difference concept, is used to solve Maxwell's equations for electric (E) and magnetic (H) field distributions [153].

4.2.1 Introduction to FDTD Method

The FDTD method replaces Maxwell's differential equations for E and H in time and spatial domain by finite difference equations and solves them numerically, enabling the simulation of electromagnetic wave propagation in complex geometries [154, 155].

For the simulation of the propagation of PD-generated EM waves, a representative PD current pulse is necessary. For this purpose, the Gaussian pulse in (4.2) is utilized [156]:

$$I(t) = I_0 \cdot \exp\left(\frac{-(t - t_0)^2}{2\sigma^2}\right) \quad (4.2)$$

where I_0 is the amplitude, t_0 is the initial time, and σ is the characteristic waveform parameter which describes the pulse width at half maximum value. In this thesis, the excitation source is based on a typical PD pulse within a transformer [157]. Furthermore, the signal is superimposed with white Gaussian noise. The result is shown in Figure 4.5.

A crucial matter in the FDTD technique is the approach towards the boundaries of the problem space. Since a numerical method is applied and the computational space is finite, appropriate boundary condition have to be implemented. In this work, the perfect electric conductor (PEC) boundary is utilized for metallic components. By enforcing this boundary condition, any arriving wave is entirely reflected as the tangential electric fields on the

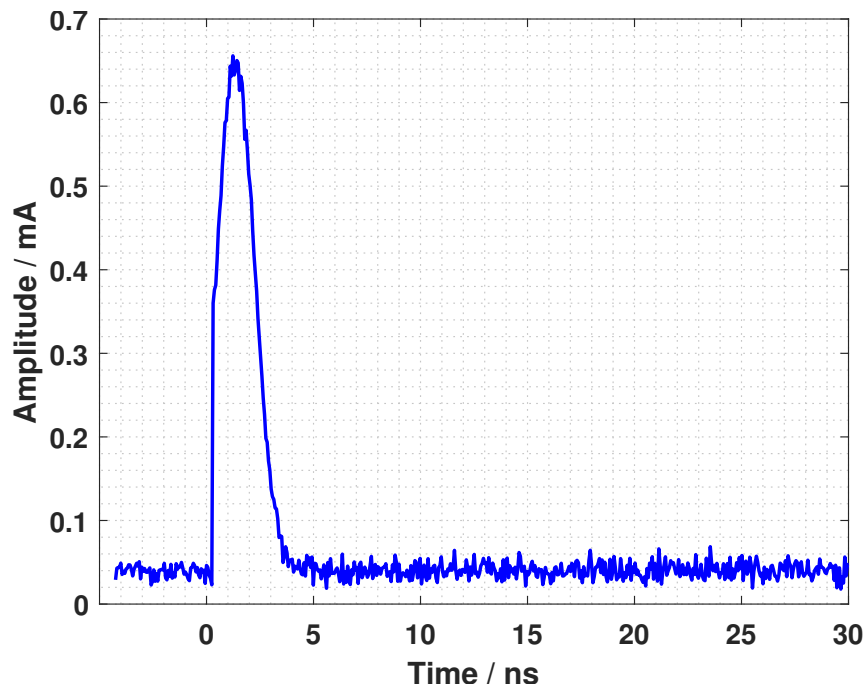


Figure 4.5: PD pulse used as excitation source

boundary of the domain are set to zero [154, 158]. The assumption of PEC boundary conditions is often used in simulations of electromagnetic waves in enclosed structures, including power transformers. This assumption is based on the following reasons [154]:

- **Conductivity of transformer walls:**

Transformer walls are usually made of metals such as steel, which have high electrical conductivity. This means that the walls can effectively reflect any incoming electromagnetic waves, as the free electrons in the metal can easily move and cancel out the electric field inside the metal.

- **High frequency range:**

PD in power transformers typically occurs at high frequencies in the range of several tens of MHz to several GHz. At these high frequencies, the skin depth of the electromagnetic waves is very small, typically in the order of micrometers or less. This means that the electromagnetic fields inside the transformer walls are negligible, and the walls can be treated as perfect electrical conductors.

- **Simplification of modeling:**

The use of PEC boundary conditions simplifies the modeling process, as it eliminates the need to model the electromagnetic fields inside the transformer walls. This can significantly reduce the computational cost and simulation time.

However, it is important to note that this assumption may not be completely accurate in some cases. Real-world transformers can have imperfections such as surface roughness, coatings, and other factors that can affect the reflection and absorption of electromagnetic waves. Additionally, the presence of insulation, winding structures, and other components can also affect the behavior of electromagnetic waves inside the transformer.

The FDTD method is used in the following to investigate the effect of the active part of a transformer on the propagation path of PD-emitted EM waves. For this purpose, the two-dimensional analogy model depicted in Figure 4.1 is again utilized.

Direct Path

In the arrangement shown in Figure 4.1, there is a direct path between the PD location and the three sensors. Hence, the EM waves generated by PD will travel the shortest path between their origin and the receiving probes, resulting in a direct line. Figure 4.6 shows the simulated EM wave at the moment it is received by probe 3, which is roughly 2.36 ns after PD inception. The color scheme used in the figures in this section includes turquoise for the

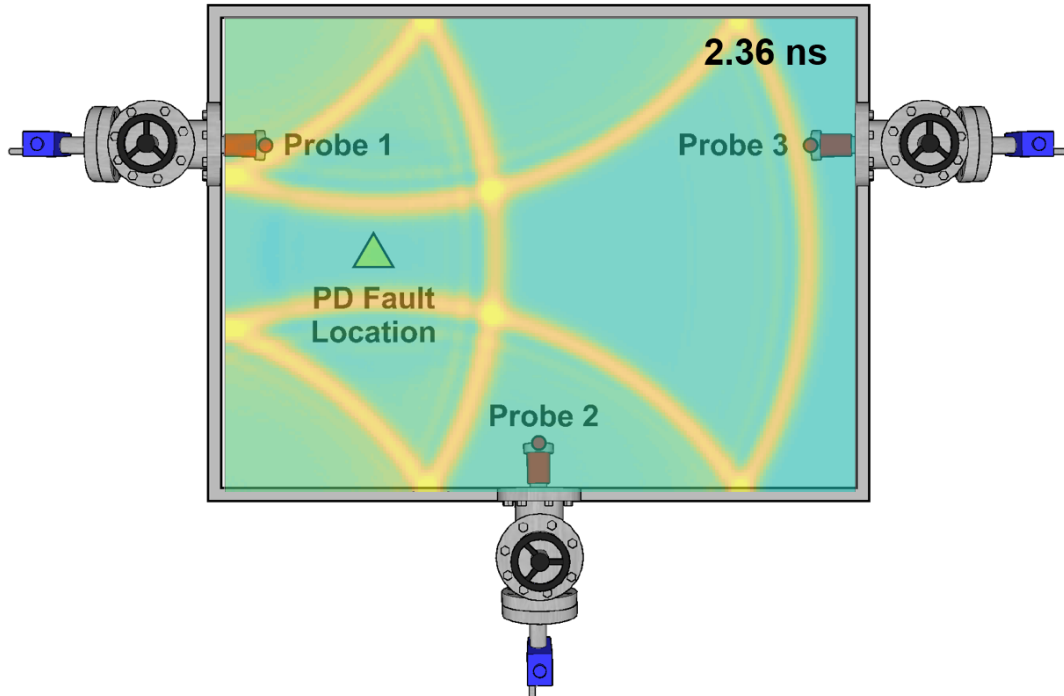


Figure 4.6: EM wave propagation due to PD at time step 2.36 ns

background, and yellow for the wavefront. Notable features such as reflections or interference patterns can be identified. Based on the observed wavefront spreading and amplitude decay, conclusions can be drawn regarding

the wave propagation behavior and the arrival time. Since the propagation medium in this case is assumed to be air, the EM waves propagate by the speed of light, meaning they have traveled 707.51 mm from the source to the probe. The Euclidean distance between the PD source and the tip of probe 3 is 711.07 mm. Since the FDTD method solves the Maxwell's equations numerically, a certain degree of error is to be expected. In this case, the resulting accumulated computational error is roughly 3.6 cm, which is 0.5 % of the total distance and therefore acceptable. It is noteworthy that the computational error depends on the number of iterations needed and consequently the computational time. Hence, the longer the travel distance between the source and the probe, the higher the computational error [154].

Disrupted Path

Due to the complex inner structure of a power transformer, it is unlikely that the path between the PD location and at least one of the probes is not disrupted. The possible obstacles in power transformers are either from conducting material, such as the windings, or insulating material, such as oil or paper insulation. EM waves travel through non-conductive materials with a certain degree of damping and also run-time prolongation. However, in comparison to the effect of conducting materials, their effect can be neglected. Since EM waves only minimally penetrate conductive material and are predominantly reflected, they have a significant effect on the run-times of the signals. In order to analyze this phenomenon, a full metallic circle with a diameter of 30 cm is assumed at the center of the two-dimensional analogy model. In this arrangement, the direct path between the PD source and the probes 1 and 2 is uninterrupted. This is not the case for probe 3, since the metallic obstacles disrupts the path. In order to analyze the effect of the barrier, two time instances are depicted in Figure 4.7.

Figure 4.7a and 4.7b show the EM waves at time instances 1.38 ns, and 2.57 ns after PD inception, respectively. The former is the time instance, at which the EM waves are captured by probe 2. Since the barrier does not interrupt the direct path between the source and the probe, this value remains unchanged. In case of the path to probe 3, this is not the case. Although the EM waves propagate at the speed of light, their behavior is quite different. Once light is generated, it will travel in a straight line. When it arrives at a surface, it is either absorbed, reflected, scattered, refracted, or it passes straight through. In either case, it still travels in a straight line. Would the EM waves behave similar to light, in the presented 2D model, the shortest path

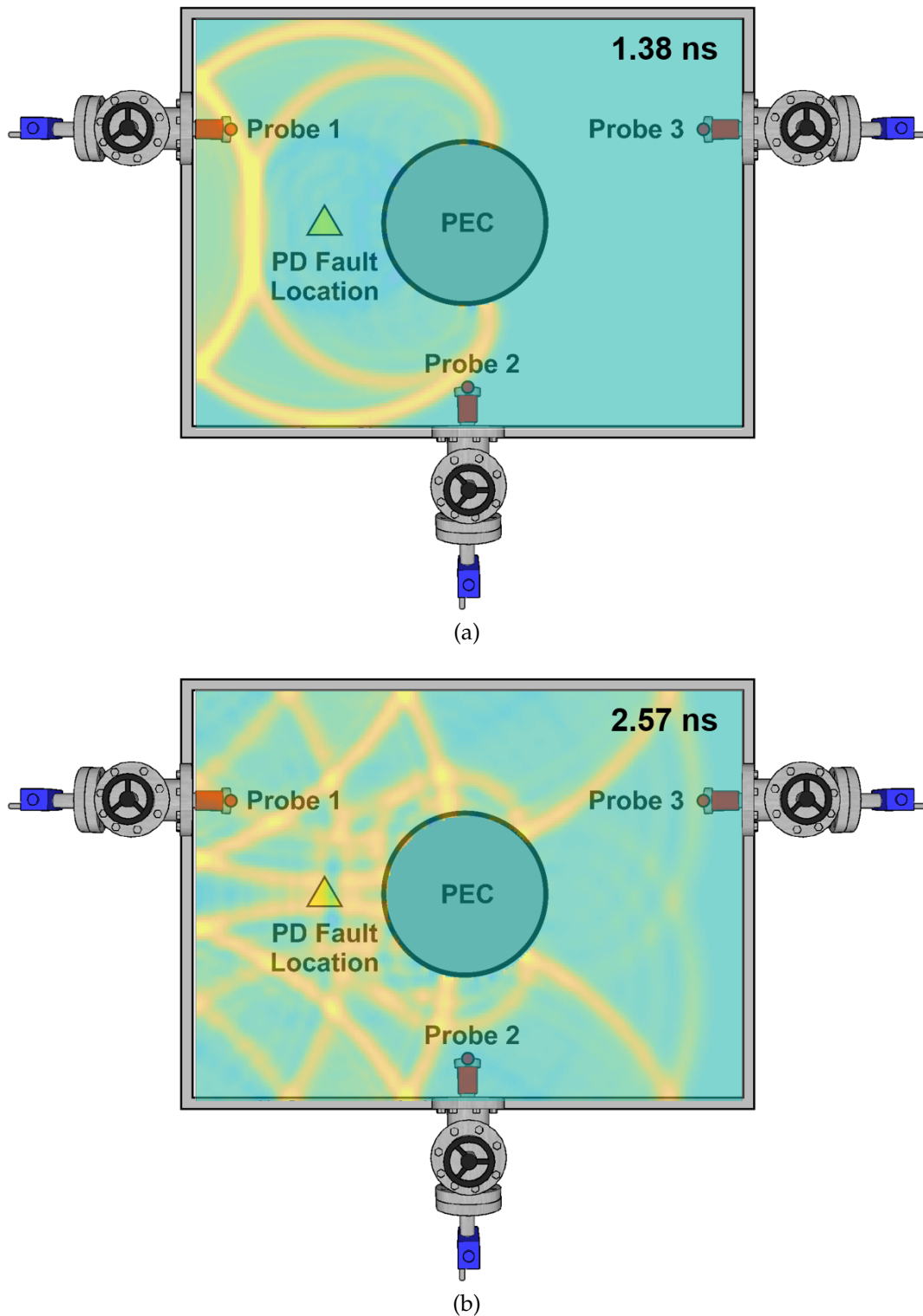


Figure 4.7: EM wave propagation due to PD at time step (a) 1.38 ns, and (b) 2.57 ns

would be the reflection from the upper wall of the tank. This is however not the case, since, as evident in Figure 4.7a, although the wave-front is partially reflected by the surface of the obstacle, a fraction of it moves around the obstacle and continues its path towards probe 3 and is received at the time

instance 2.57 ns after PD inception (Figure 4.7b). Hence, the AT of the signal received by probe 3 would be prolonged in this scenario by 0.21 ns, which is significant with regards to the sensitivity analysis of the ATs in section 4.1.

As demonstrated using the 2D analogy model, when the direct path between the PD fault location and the probe is disturbed by an obstacle out of conductive material, such as the active part of the transformer, the EM waves travel along the shortest possible path. The effect of non-conductive materials, such as the paper insulation system of the transformer, although prolonging the run-time of the waves, can be neglected in comparison to the effect of the active part.

4.3 Localization Algorithm

In the previous sections, the effect of inaccurate ATs in regards to the localization accuracy were investigated, therefore a novel PD localization approach is developed based on a practical perspective. In the following, the developed localization algorithm for PD is divided into blocks and a short description is given. The process of localization using UHF data-sets is addressed. It is noteworthy that the localization algorithm is implemented in *MATLAB*.

4.3.1 Overview of the Algorithm

The proposed algorithm, as shown in Figure 4.8, is divided into three main blocks: initial parameters, signal processing units, and finally the calculation of the PD location.

As stated in section 1.3.2, a minimum of four probes is necessary for performing UHF measurements aiming at localizing PD in a power transformer by multilateration. Furthermore, a high-sampling oscilloscope with a wide bandwidth is also required. The algorithm in this thesis processes several hundred data-sets (each consisting of four signals received by the four UHF probes), from which a fraction that satisfy the presented criteria is selected and used for determining the coordinates of the PD fault. Obtaining an adequately large database for a measurement is not a significant challenge, since modern oscilloscopes have an auto-trigger function. This allows the operator to specify the number of data-sets desired and, after optimizing the measurement parameters, to activate this function. The oscilloscope then triggers

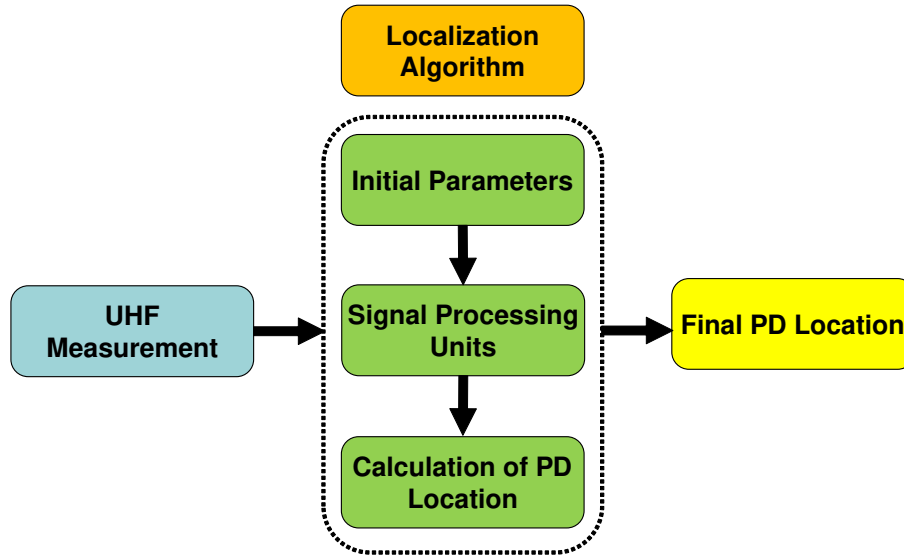


Figure 4.8: Overview of the localization algorithm

continuously until the preset number of data-sets is captured. PD is a recurring phenomenon. Depending on the sensitivity of the probes and their spatial proximity to the PD source, the duration of the localization measurement varies, but remains within reasonable time boundaries.

In the initialization step, general necessary parameters, such as the dimensions of the transformer tank, location and size of the active part and if existent the tap-changer, the coordinates of the tip of the probes, the relative permittivity ϵ_r of the propagation medium, etc., are provided to the algorithm. Furthermore, the number of data-sets to be processed by the algorithm is specified.

In the following, an overview on each of the remaining blocks of Figure 4.8 is presented.

4.3.2 Signal Processing Units

Certain pre-processing measures of the signals contribute to an increased localization accuracy. These measures as well as the AT determination method are described in the following.

Removing Linear Trends

In determining the AT of the signal, the aim is to pinpoint the precise moment at which the signal emerges from the background noise. Hence, in the first step, the trend of the data is removed, enabling to lie the focus on the fluctuations of the signal and consequently determining the AT accurately. This

is especially useful when the captured UHF signal includes a low-frequency component or a small deviation prior to the actual AT [159].

Noise Suppression

Wavelet denoising is a powerful technique for removing noise from signals while preserving important signal features. The localization algorithm employs a *sym5* wavelet and an automatic soft thresholding method at a decomposition level of 3 for wavelet denoising. The *sym5* wavelet is a symmetric wavelet that is commonly used in wavelet denoising. It has a high degree of smoothness and is well-suited for signals that have a smooth variation in their frequency content. The *sym5* wavelet is defined by a set of filter coefficients that are used in a multi-level decomposition of the signal. This decomposition separates the signal into different frequency bands, which can be thresholded to remove noise and then reconstructed to obtain a denoised signal.

In the context of wavelets, the wavelet function (ψ) and scaling function (ϕ) are used to describe its properties. These functions are shown in Figure 4.9 for the *sym5* wavelet and are expressed as discrete sequences of values. The x-axis is often divided into discrete points or intervals, and the wavelet and scaling functions are computed or sampled at these points. These points are essentially the "grid points" where the functions are evaluated, and the corresponding values of the functions at these points are plotted on the y-axis. The number of grid points or intervals on the x-axis is determined by the choice of the wavelet transform, the level of decomposition, and the desired resolution in the time or spatial domain. The wavelet function ψ is a fundamental component of the wavelet transform. It serves as a basis function that helps in the analysis of signals or images at various scales. The wavelet transform decomposes a signal into different frequency components and time-localized details using dilations and translations of the wavelet function. In simpler terms, the wavelet function is like a window that moves along the signal, capturing localized features at different scales. For the *sym5* wavelet, the specific shape and properties of ψ are designed to strike a balance between smoothness and localization, making it suitable for analyzing signals with both smooth and abrupt changes. The scaling function ϕ is another crucial element of wavelet analysis. It represents the coarse-scale features of a signal or image and is used alongside the wavelet function to form a multi-resolution analysis. The scaling function provides a way to analyze the low-frequency components of the data and understand its

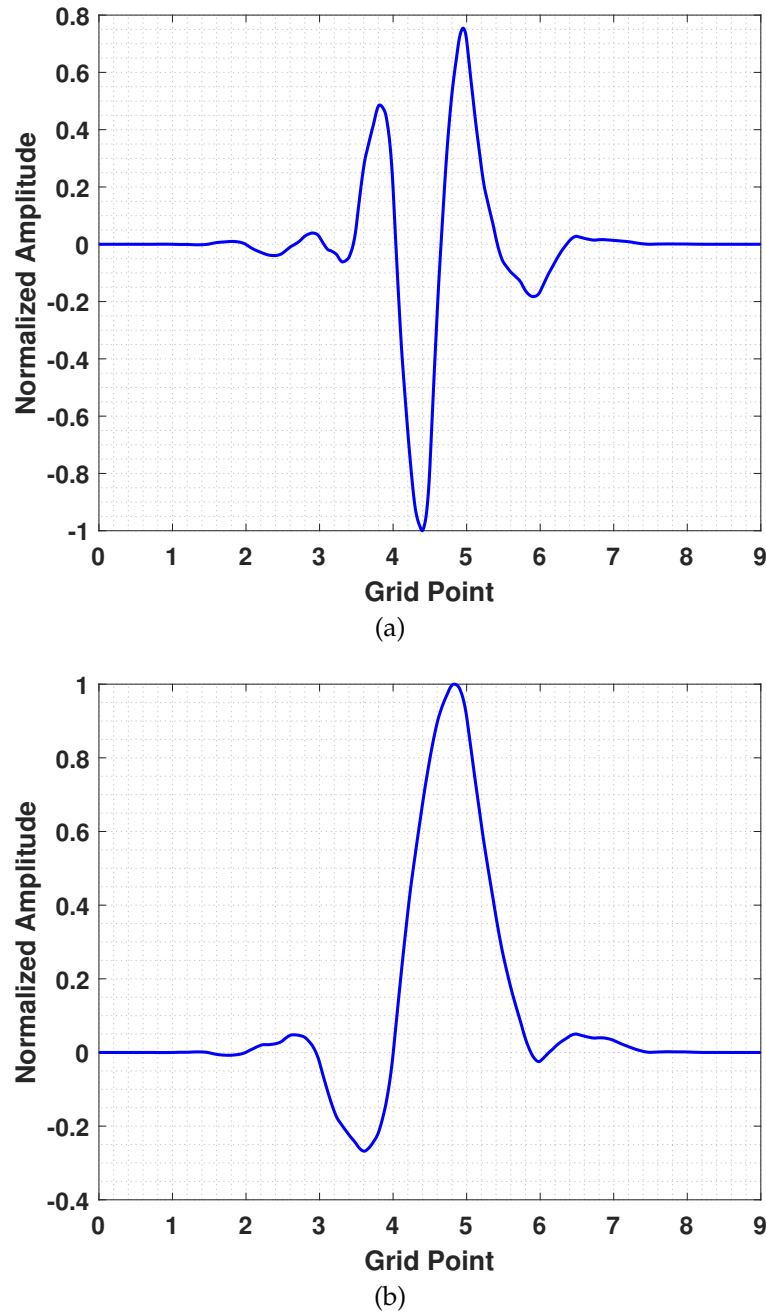


Figure 4.9: (a) The wavelet function ψ , and (b) scaling function ϕ of *sym5* wavelet

overall trends and behavior. In the wavelet transform, the scaling function captures the approximation or coarse-scale details of the input signal. The scaling function complements the wavelet function and together they form a basis for the wavelet transform.

Both the wavelet function and the scaling function have specific mathematical properties that are crucial for their effective use in wavelet analysis. The *sym5* wavelet and scaling functions are part of the Symlets family, which are symmetric wavelets with a finite number of vanishing moments. The

number of vanishing moments determines the degree to which the wavelet can accurately represent polynomial trends in the data.

The *sym5* wavelet has been shown to perform well in various applications, such as speech denoising and image denoising [160]. The automatic soft thresholding method is a popular thresholding approach for wavelet denoising. It is based on the concept of thresholding the wavelet coefficients to remove noise while preserving signal features. The soft thresholding method sets coefficients that are below a certain threshold to zero and shrinks coefficients that are above the threshold towards zero. The threshold is typically determined automatically based on the statistical properties of the wavelet coefficients. In this thesis, an automatic soft thresholding method at a decomposition level of 3 is applied, meaning that the signal will be decomposed into three levels of detail coefficients, and each level will be thresholded separately before reconstruction. This approach has been shown to be effective in denoising various types of signals, including biomedical signals and audio signals [161]. The application of a *sym5* wavelet by an automatic soft thresholding method at a decomposition level of 3 has empirically been proven effective in UHF PD localization, since the denoising method should neither introduce a time shift nor any alterations in the behavior of the signal.

Arrival Time Determination

The AT determination is the most important and challenging step in the localization. There have been several approaches proposed for this purpose. Among the most recent and effective are the Average Time Window Threshold method introduced by Mirzaei *et al.* in [108], and the Dynamic Cumulative Sum of Likelihood Ratio method by Jahangir *et al.* in [111]. For the algorithm proposed in this thesis, the novel Time Window Contrast Function (TWCF) method is utilized for obtaining the ATs. This approach is based on the Penalized Contrast method introduced by Lavielle in [112] with modifications to optimize for the task at hand. Here, the signal is divided into two partitions by a break-point. For each of those partitions, every point in that same partition is compared to a certain statistical parameter. The difference of the two partitions is added together. By shifting the break-point over the signal and obtaining the said difference, a contrast function is achieved. At the precise moment, where on the left side of the break-point is pure noise and on its right side is the UHF signal, the penalized contrast of the two partitions is at its minimum [162]. Hence, the AT of the signal complies with the break-point, at which the contrast function has its global minimum.

4.3.3 Calculation of PD Location

In order to calculate the coordinates of the PD fault, the corresponding location of each data-set is calculated before and after applying the signal processing units. The criteria, by which a fraction of the data-sets are selected for the final evaluation were discussed in section 4.1.2, and are as follows:

- The value for t_0 has to be positive.
- The location determined for the fault must be within the tank enclosure.
- The location of the fault has to correspond to the correct sequence of arrival.

In the following, the process to determine the target sequence as well as the method for calculating the final PD location from the obtained candidate locations are described.

Sequence of Arrival Times

As discussed in section 4.1.2, the sequence of arrival of the signals is a suitable parameter to remove outlier data from the captured signals. To determine the target sequence, the sequence of arrival of all data-sets are determined, both prior and after applying the aforementioned signal processing units. Data-sets where the sequence of arrival changes after applying the signal processing units are excluded from further consideration. These data-sets are likely to result into a false location for PD, since a change in the determined sequence of arrival after applying the processing units indicates a low signal to noise ratio (SNR). For the remaining data-sets, the corresponding PD location to each of them is calculated and those data-sets resulting in locations outside the tank are eliminated. Furthermore, only data-sets with a positive value for t_0 are considered. In the final act, the data-sets that remain are categorized based on their number of repetition in different AT sequences. The sequence which frequents the most is declared as the target sequence, if the difference with the second most frequent sequence is significant. Should that not be the case, i.e. the PD fault is located roughly in the middle of two probes, the corresponding signals to those probes of all data-sets are cross correlated to determine the target sequence [163]. Finally, only the obtained PD locations that correspond to the data-sets subjected to the presented selection criteria are considered and passed to the next step towards computing the PD location.

Determination of the Final Algorithm Output

The algorithm's final stage is to arrive at a definitive location for the PD based on the singled out candidate coordinates. Different approaches, such as the arithmetic average of the x, y, and z component of the candidate locations or mean value of the ATs of the candidate coordinates were investigated for this purpose [164]. In the following, the two more promising methods among the studied approaches for this purpose are presented:

- **Median of the ATs of the candidate coordinates:**

In this approach, the median of the ATs of the acquired candidate coordinates for the PD source are determined, and the resulting location declared as the final output.

- **Clustering:**

The final PD location is determined by dividing the candidate locations into two clusters using the soft clustering method *fuzzy c-means* [165]. In order to choose between the two obtained cluster centers, it is assumed that the one situated at a location with a higher electric field strength is more likely to be the PD location and is therefore, the final outcome of the algorithm.

In recent years, significant advancements in computational tools and simulation techniques have revolutionized the determination of electrical field strength inside power transformers. Through the use of exact simulation tools, engineers can now gain unprecedented insights into the intricate electric field distribution, enabling them to design, optimize, and assess transformer insulation systems with unparalleled accuracy and efficiency. These data can also be consulted for the purpose of diagnosis by the test engineer.

For the evaluation of the measurement results in the subsequent section, since PD is generated artificially by means of a PD fault model, its actual location is known. Hence, the accuracy of the algorithm, also called the localization error, is defined as the distance between the calculated and the actual location of PD and is used as the evaluation criterion.

4.4 Arrival Time Determination of UHF Signals

In Section 1.3.2, three AT determination methods were presented, namely the average time window threshold method (ATWT), dynamic cumulative sum

method (DCS), and the contrast function method. For the proposed algorithm, the AT detection method used is based on a modified version of the contrast function method, which will be addressed in the following. Subsequently, the presented AT determination methods will be compared to assess their effectiveness.

4.4.1 Time Window Contrast Function Method (TWCF)

If the signal has an offset or minor deviations prior to the actual AT, the contrast function approach produces an inaccurate AT. To address these issues, a modified version of this approach, namely the TWCF is developed. The signal's mean is subtracted from the samples in this technique. Furthermore, the AT's search range is narrowed from the whole duration of the signal to a specific time window (TW). The longest direct path that an EM wave may travel within the transformer tank is used to compute the TW's width. When the rectangularity of a transformer's tank is taken into account, the diagonal of the transformer meets this requirement. The time needed for the signals to transit the diagonal and hence the width of the TW is determined using the speed of the EM waves in oil or air.

The TW is moved across the signal until it meets the following criteria:

$$\frac{MAV_n}{MAV_{n-1}} \geq m \quad (4.3)$$

where MAV is the mean of absolute values of samples inside a TW, n is the TW's number, and m is a specified threshold. This threshold must be set high enough to prevent the white noise in the signals from being mistaken for the actual PD signal. The value of m is empirically set to 2.5 regarding the measurements conducted in this section.

A marginal range equal to the TW length is added to both sides of the candidate TW as a safety factor given the candidate TW, i.e. TW number n . As a result, the new TW will be three times longer than the original TW. The signal within the acquired time period is then evaluated using the contrast function method to detect the AT.

Figure 4.10 compares the performance of the contrast function and TWCF methods in determining the AT of a signal set. Here, the corona fault model depicted in Figure 1.16 is positioned in the center of the bottom plane of the transformer tank model (Figure 1.12), and a signal set is acquired by the UHF probes by applying high voltage to the needle. As can be observed, using the TWCF approach allows the AT detection to disregard oscillations in the

signal captured by probe 3. Furthermore, removing the DC component of the signal yielded in a more accurate AT for the signal of probe 4. Although the ATs acquired using the contrast function method were unable to provide an acceptable location for the PD, the TWCF method yielded a 16 cm accurate PD allocation.

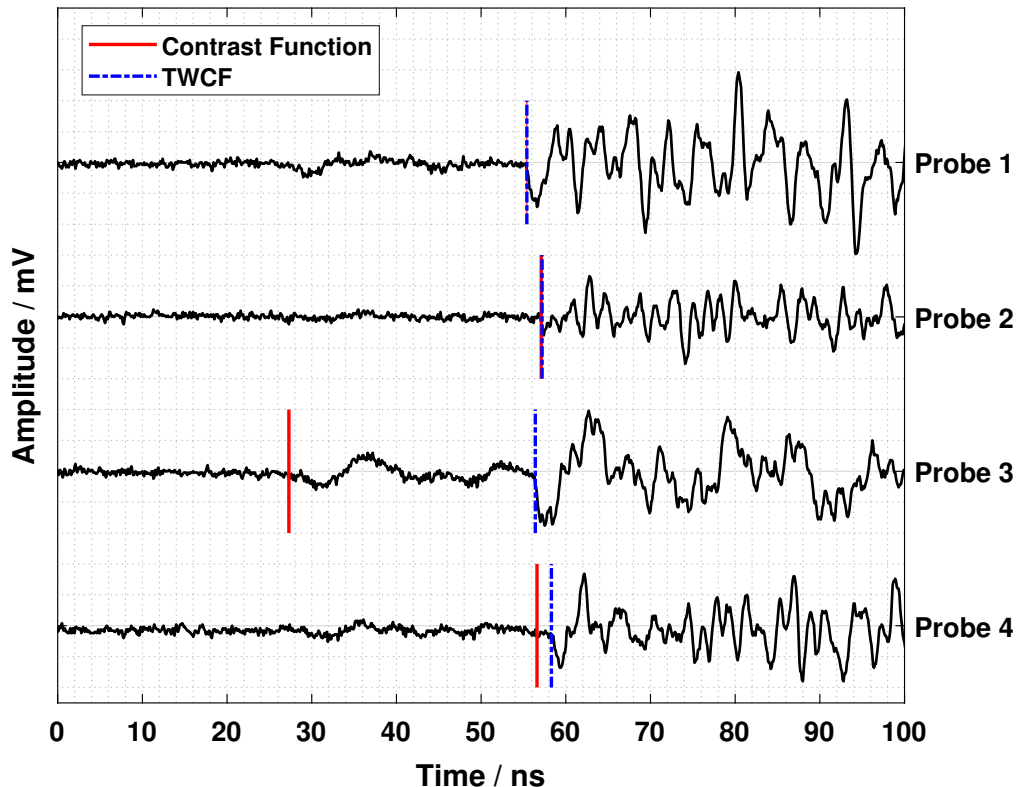


Figure 4.10: Comparing the ATs detected by contrast function method and TWCF method for a set of data-sets captured by four UHF probes [163]

4.4.2 Comparing AT Detection Methods

The three above-mentioned AT detection techniques, namely ATWT, DCS, and TWCF, are compared in the following. For this purpose, instead of just one signal set, several are recorded and evaluated for a more reliable and consistent comparison. The corona fault model depicted in Figure 1.16 is placed in the center of the transformer tank model's bottom plane, and 1000 signal sets are captured using four UHF probes. The voltage applied to the needle is adjusted to maintain the apparent charge of approximately 80 pC on the electrical PD measurement system. The signal sets' AT and the PD source's coordinates were computed.

Table 4.2 shows the number of obtained locations within the tank as well as the localization accuracies. The distance between the actual position of the

PD and the estimated location determined via the signal sets that delivered an acceptable location for the PD within the tank is characterized as localization accuracy.

Table 4.2: Results of analyzing 1000 signal sets for localizing the PD source [163]

AT Detection Method	Number of Valid Locations	Localization Accuracy / mm
ATWT	39	175
DCS	-	NA
TWCF	66	127
Modified DCS	34	158

When comparing rows 1 and 3 of Table 4.2, it is apparent that TWCF provides more PD locations and has a better localization accuracy. The DCS method did not provide any acceptable location for the PD source. The method's procedure was reviewed, and it was determined that a low value of the window width w obtained by (1.13) results in an inaccurate calculation of the AT. In this case, the window width must be adjusted in order to make a valid comparison between the three AT detection algorithms. Hence, the DCS method is modified to extend the window width by applying the same time window set in the TWCF method. With a larger number of samples, a more accurate fitting PDF is anticipated. It's worth noting that the AT detection threshold hasn't changed since it is obtained by (1.16). Table 4.2 also contains the results of applying the modified DCS method on the 1000 signal sets. The modified DCS method has a better localization accuracy than the ATWT method, but it offers fewer viable locations for the PD source. Nonetheless, the results in Table 4.2 show that the TWCF method is superior to the other AT detection methods.

Figure 4.11 shows an example signal presented to compare the ATs identified by ATWT, modified DCS, and TWCF methods. For the signal of probe 1, all methods provide the same AT. The AT identified by ATWT and modified DCS is one sample behind the AT detected by TWCF in the signal received by probe 3. For the signal captured by the second probe, modified DCS and TWCF techniques identify the same AT; however, there is a considerable lag for the AT detected by ATWT. The amplitude of the second probe's signal does not vary significantly in the area of the AT identified by TWCF, but there is a smooth transition. In other words, unlike energy-based AT detection techniques, PDF-based AT detection approaches are capable of

detecting minor changes in signal behavior. The AT displayed on the signal of the fourth probe demonstrates the advantage of TWCF over the modified DCS method. The improved DCS method has a downside of high sensitivity. ATWT and TWCF provide the same AT in this example. In conclusion, using the TWCF technique yielded a localization accuracy of 9.3 cm, while the other two methods delivered the PD's location outside the tank.

It's worth noting that different AT detection algorithms provide outcomes with different accuracies for a particular signal set; nevertheless, the robustness of a method can only be determined by applying it to a variety of randomly received signal sets. The reason for this is because the received signals in various transformers in practical applications are not of the same power and characteristics [163].

Based on the results presented in this section, the proposed AT detection method TWCF prevails and is used in the localization algorithm.

4.5 Determination of the Target Sequence

When applying a multi data-set approach, many possible locations for the position of the PD source within the tank emerge. To improve the accuracy

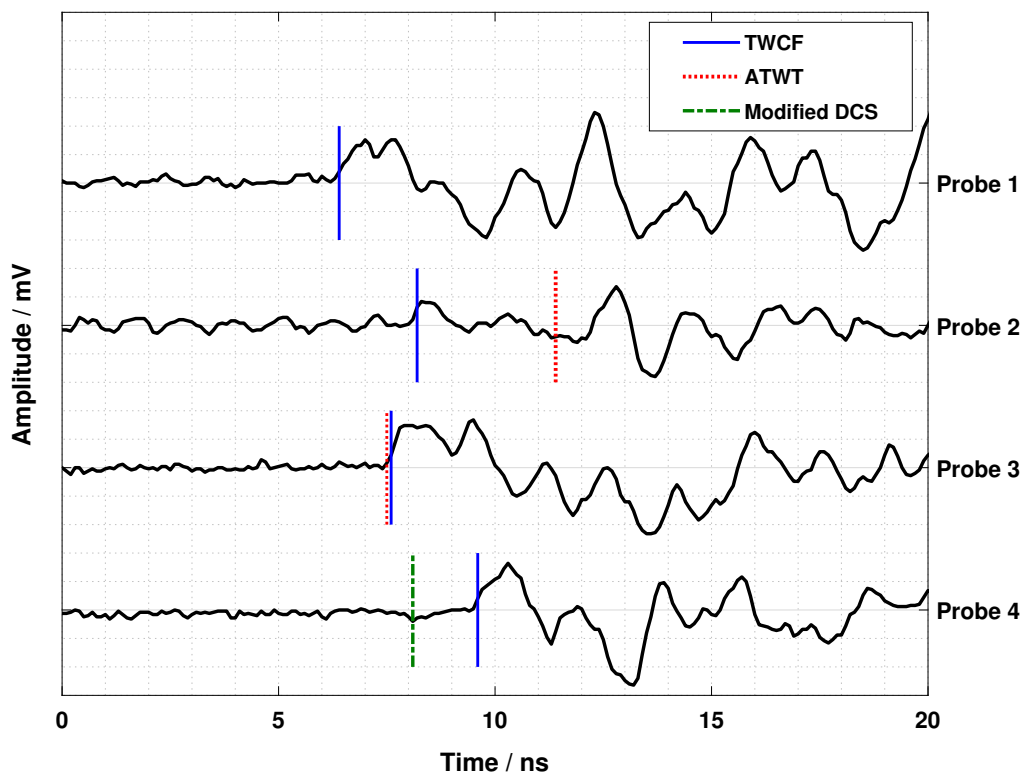


Figure 4.11: ATs of four simultaneously captured UHF signals; note that ATs are superimposed in some cases [163]

of the localization, signal processing methods are applied. This is discussed in the following section.

Each location inside the tank is linked to a unique set of AT differences in the recorded signals. With four UHF probes inside the tank, there are a total of 24 possible signal arrival sequences. Analyzing the 1000 signal sets provides multiple PD locations that correspond to a specific AT sequence number. As a result, the candidate locations for the PD source may be classified based on the ATs' sequence numbers, with locations that do not match the target sequence being disregarded. The process for determining the target sequence is detailed in the following.

Assume that 1000 signal sets are captured and processed in order to identify ATs and their sequences. The ATs are then used to determine the position of the PD source. The coordinates received outside of the tank are removed from the results. The remaining positions are divided into 24 categories resulting from the permutations of the four probes, each category corresponding to a unique AT sequence. The target sequence is determined from the two categories with the highest number of repetitions.

The two potential sequences are likely to exist in two states. Assume that the two most often occurring AT sequences are $seq_1=[1\ 2\ 3\ 4]$ and $seq_2=[2\ 1\ 4\ 3]$, respectively, for the first state. Note that the numbers correspond to the number of the UHF probe in the signal receiving sequence. Since all of the probes in seq_1 and seq_2 are in entirely different locations, the proposed algorithm acknowledges the target sequence as the one with the most repetitions.

If the two AT sequences are identical with only one probe pair swapped, such as $seq_1=[1\ 2\ 3\ 4]$ and $seq_3=[1\ 2\ 4\ 3]$, a complementary evaluation for the two probes with different positions in the sequences is necessary. This is likely when the distance between the PD source and two probes is almost equal, resulting in a slight discrepancy in the ATs of the signals received by the two probes. In this scenario, a cross correlation approach is applied. Cross correlation is a statistical method used to measure the similarity between two signals as a function of the time lag applied to one of them. It involves computing the convolution of one signal with a reversed version of the other signal. The resulting cross correlation function provides information about the time delay and the strength of the correlation between the two signals. Cross correlation is commonly used in signal processing, communication systems, and pattern recognition applications [166]. In the context of the proposed localization algorithm, the cross correlation of the two suspect signals is determined for each of the 1000 signal sets recorded. Figure 4.12

depicts cross correlation for two example signals, each of which has 5000 samples. The delay between the two signals is determined by the moment at

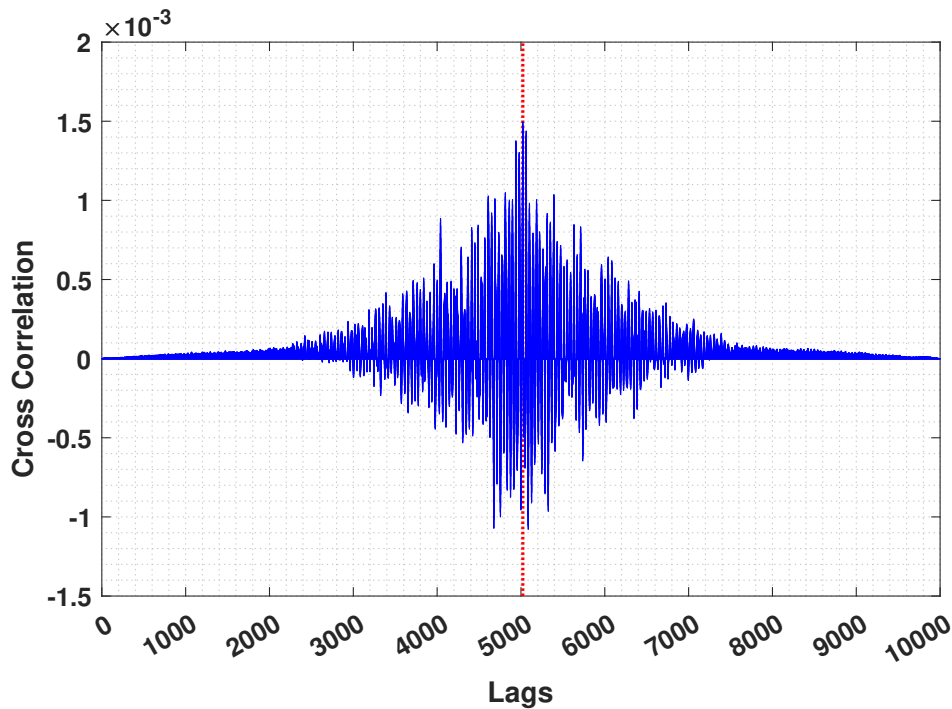


Figure 4.12: Cross correlation of two UHF signals; the vertical dotted line indicates the location of the maximum value [163]

which the cross correlation achieves its global maximum. In Figure 4.12, a red dotted line depicts this spot. As a result, the most frequent sequence is used to decide the precedence in receiving signals by the two dubious probes [163].

4.6 Wavelet Denoising

The degree to which a signal may be denoised without compromising the associated AT is critical. Various wavelets with different decomposition levels and thresholding characteristics have been suggested to identify PDs and ATs of PD signals [110, 167, 168]. However, the variety of new denoising techniques necessitates more research into the impact of wavelet denoising on AT determination.

The proposed algorithm in this thesis handles wavelet denoising as follows: if the ATs of a signal set offer an acceptable location but not the ATs of the denoised signals, this projected location is anticipated to be inaccurate and is removed from the PD candidate locations. The wavelet denoising is applied using *sym5*, a member of the symlet family. At a decomposition level of 3, an automated soft thresholding mechanism is used. These values were

arrived at using a heuristic approach. The performance of the implemented wavelet denoising function of the proposed localization algorithm for a typical UHF signal is shown in Figure 4.13. The signal is not subjected to a time shift or a change in behavior as a result of the denoising procedure [163].

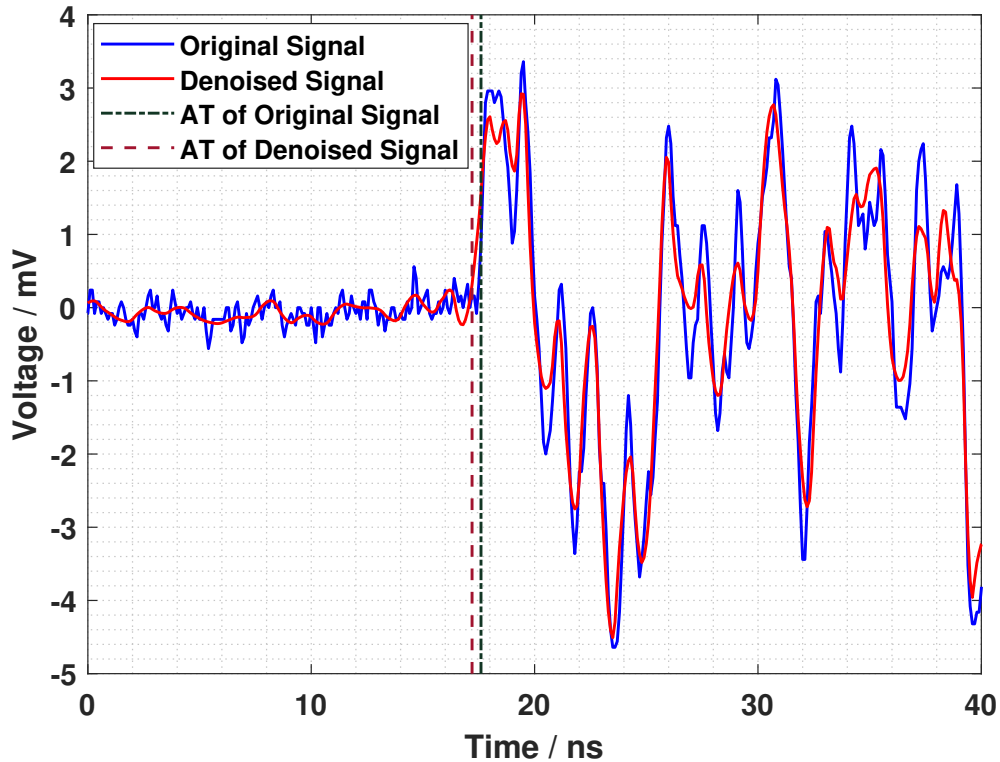


Figure 4.13: Effect of wavelet denoising on a typical UHF signal [163]

A few tenth of nanosecond deviation in the actual AT of a signal set results in an error in the localization accuracy in the order of a few centimeters. The localization accuracy decreases with increased deviation in the identified ATs from the correct ones, as discussed in section 4.1. This reduction in the accuracy continues until the determined PD location either lies outside the tank or includes imaginary coordinates. In these cases, the estimated PD location is considered as unacceptable and eliminated from further analysis.

4.7 Preliminary Investigations on the Proposed Localization Algorithm

In the previous sections, an overview of the novel localization algorithm was given and specific influencing factors were discussed in detail. In this section, the proposed localization algorithm is subjected to a preliminary investigation. For this purpose, three cases are studied to assess the effectiveness

of the localization algorithm. Different barriers are used to enclose the PD source in these scenarios. Each case consists of three coordinates for the PD source and 1000 signal sets are captured for the corresponding coordinates.

For all of the investigations in this section, the corona fault model depicted in Figure 1.16 is employed. The applied voltage to the needle plane structure of the PD source is around 2.5 kV. According to the *IEC 60270* [21], the associated apparent charge level was about 100 pC.

4.7.1 Case 1: Direct Line of Sight between the PD Source and the Probes

The PD source was positioned in three locations within the transformer tank model and a direct path to the PD source was ensured for all these locations. The median of the ATs of the determined candidate coordinates is considered and the resulting location declared as the output of the algorithm. Table 4.3 lists the coordinates of the PD source as well as the localization accuracy. In this scenario, the localization accuracy is less than 14 cm and typically below 10 cm. The best localization accuracy is anticipated in this case.

Table 4.3: Localization accuracy for case 1; direct line of sight between PD source and probes [163]

Location Number	PD Source Coordinates			Localization Accuracy / mm
	X / mm	Y / mm	Z / mm	
1	400	600	80	94
2	560	250	300	139
3	590	1000	300	77

4.7.2 Case 2: Combined Metal Lattice Barrier with Pressboard Barrier

This case is designed to replicate the path that EM waves take within a transformer with its active part. Figure 4.14 shows the test setup for this scenario, which displays the PD source surrounded by a metal lattice barrier encircled by a pressboard cylinder with height and diameter of 30.1 cm and 24.8 cm, respectively. The pressboard barrier represents the paper insulation, while the metal lattice barrier replicates a winding with its cooling channels. Table 4.4 reports the results of applying the localization algorithm at three distinct positions within the tank. As can be observed, the PD source is localized with

less precision than in case 1. As a result, a supplementary approach to the increase accuracy is proposed by means of clustering.

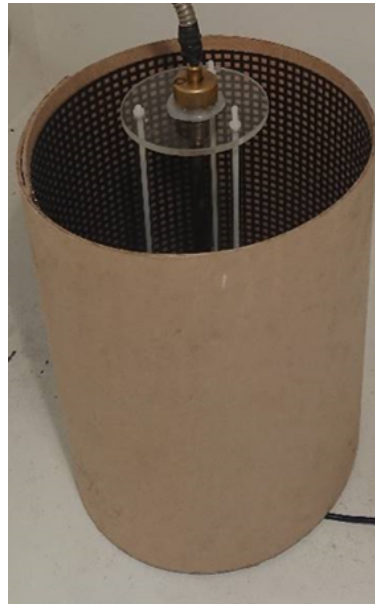


Figure 4.14: Metal lattice barrier in combination with pressboard barrier

Table 4.4: Localization accuracy for case 2; metal lattice with pressboard barriers; final point obtained by median of ATs [163]

Location Number	PD Source Coordinates			Localization Accuracy / mm
	X / mm	Y / mm	Z / mm	
1	400	600	80	241
2	570	250	280	207
3	580	980	280	312

4.7.2.1 Clustering the Candidate Coordinates

Multiple PD sources may be localized by classifying possible PD locations into several clusters. The measurements reported in [169] were conducted in an air-filled screened room with no barrier surrounding the PD source. Placing a barrier around the PD source, on the other hand, scatters the prospective PD locations across a vast region within the tank. As a result, rather than finding numerous PD sources, the goal of this subsection is to improve localization accuracy by using a clustering approach in the case of a single PD source.

The fuzzy c-means clustering approach is used in this case to segregate the candidate PD coordinates into two clusters [170]. Each candidate location's membership is established in a loop by minimizing a squared error objective function J_m as follows:

$$J_m = \sum_{k=1}^N \sum_{i=1}^C u_{ki}^m \cdot \|x_k - v_i\|^2 \quad (4.4)$$

where N and C denote the number of data points and clusters, u the degree of data point membership, m the weighting exponent, and v the clusters center, which may be determined as follows:

$$v_i = \frac{\sum_{k=1}^N u_{ki}^m \cdot x_k}{\sum_{k=1}^N u_{ki}^m} \quad (4.5)$$

This procedure is continued until the difference between two successive cycles falls below a certain threshold. Unlike case 1, where the definitive PD position was determined by the median of the ATs of the candidate coordinates, here the definite PD location is determined by a weighted average of the coordinates contained in a cluster.

To determine amongst the two resulting cluster center locations as which is the definitive PD position, a criteria is essential. For this, this electrical field distribution inside the transformer is taken into consideration. The PD is likely to occur in locations with a higher electrical stress, i.e. around a power transformer's windings. With the size and location of the windings, the distance between the center points and the windings is computed. The PD location is the center point of the cluster that is closest to the windings.

Figure 4.15 shows a 3D plot of the transformer tank model, along with a simplified schematic of the barrier. The PD source is located at position 1 in the first experiment, and the candidate coordinates for the PD location are divided into two clusters and their centers are correspondingly marked. The cluster center within the barrier satisfies the aforementioned criterion for the PD's location.

The localization results for the three defined cases with employing clustering for the determination of the PD location are reported in Table 4.5. When comparing Tables 4.4 and 4.5, it is clear that employing the suggested technique improves the localization accuracy significantly. Clustering the obtained locations into two clusters enables the consideration of additional factors, such as the electrical field distribution within the transformer, in the

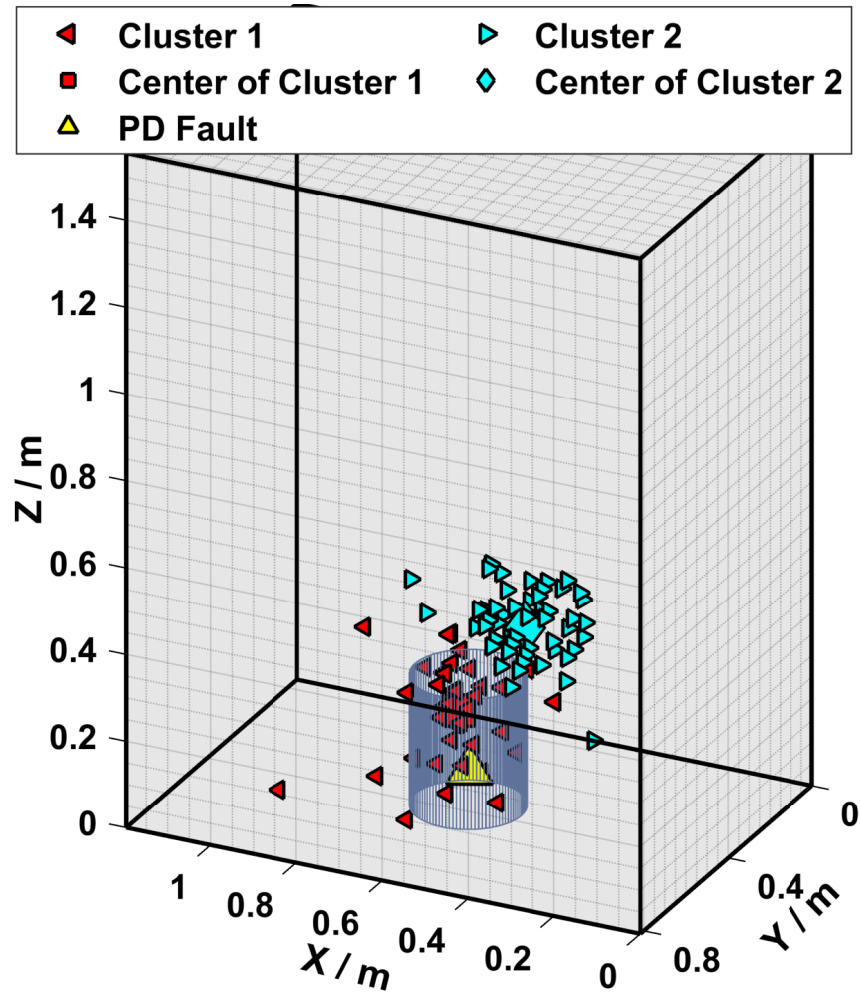


Figure 4.15: 3D schematic of candidate PD coordinates and the barriers around the PD source [163]

determination of the final calculated location for PD, resulting in an increased localization accuracy.

Table 4.5: Localization accuracy for case 2; metal lattice with pressboard barriers; final point obtained by clustering method [163]

Location Number	PD Source Coordinates			Localization Accuracy / mm
	X / mm	Y / mm	Z / mm	
1	400	600	80	130
2	570	250	280	145
3	580	980	280	86

4.7.3 Case 3: Metal Barrier

The experiments in this section are focused with localizing the PD source with a metal cylinder around it (Figure 4.16), which is the worst case scenario. The dimensions of this barrier are identical to the dimensions of the pressboard barrier. As a result, unlike in previous cases, the EM waves emitted from the PD source cannot pass through this barrier. The metal barrier causes greater distortion and a decrease in the power of received signals than the combination of the pressboard and metal lattice barriers, making it the most difficult scenario for localizing the PD source.

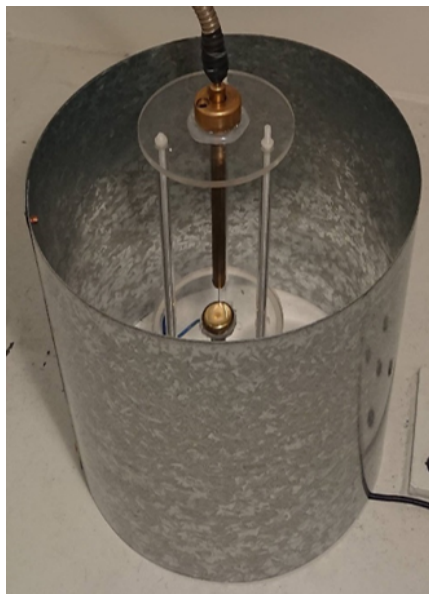


Figure 4.16: Metal barrier

Table 4.6 gives the coordinates of the PD source, as well as the accuracy of the corresponding calculated locations. As anticipated, the accuracy of localization in this case is lower than in cases 1 and 2. It's worth noting that, in addition to the decreased accuracy, the number of signal sets that provided acceptable coordinates is much lower compared to cases 1 and 2.

Table 4.6: Localization accuracy for case 3; metal barrier; final point obtained by clustering method [163]

Location Number	PD Source Coordinates			Localization Accuracy / mm
	X / mm	Y / mm	Z / mm	
1	430	630	80	210
2	570	250	280	115
3	580	980	280	144

This decrease in localization accuracy may be attributed to two key factors. The first reason is that the metal barrier causes distortion in the received signals. Comparing the frequency spectra presented in Figure 4.17 for two signals received by probe 1 and pertained to case 1 (without barrier) and case 3 (with barrier) reveals this phenomenon. For these measurements, the coordinates of the PD source are related with position number 1 in Table 4.6. The metal barrier causes a shift in the primary frequency component as well as other components with notable amplitudes. Wavelet denoising is anticipated to alleviate these impacts by preventing the localization algorithm to include erroneous coordinates for the calculation of the final location of PD.

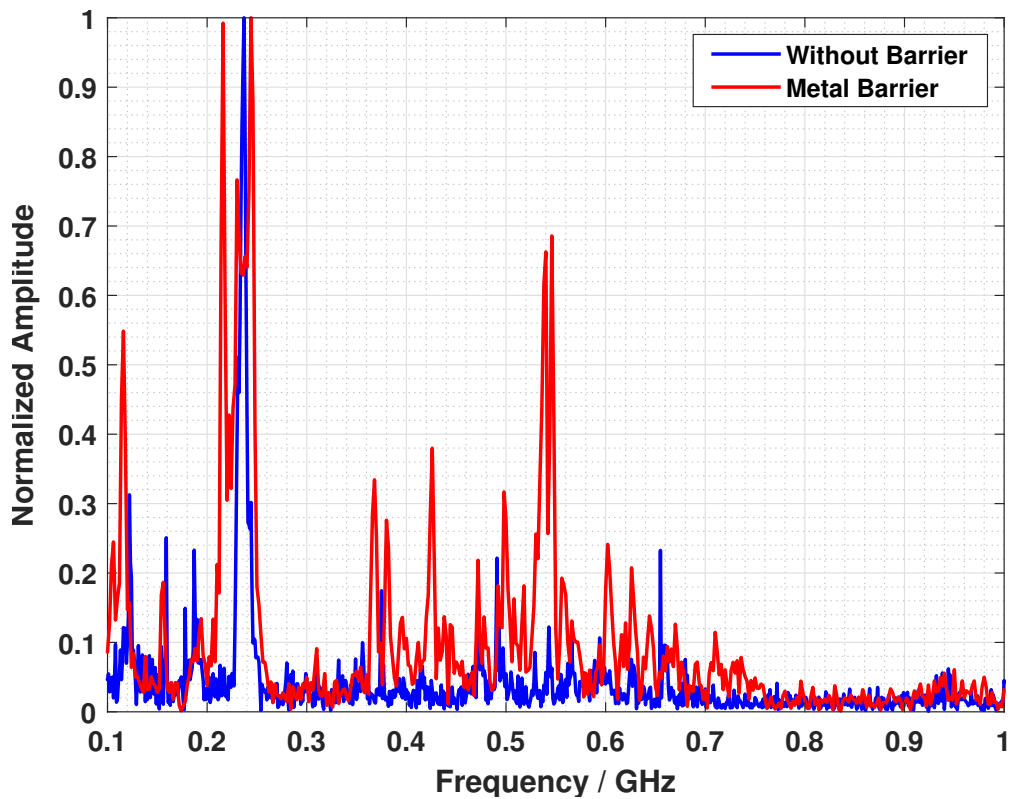


Figure 4.17: Frequency spectra of two signals captured by probe 1 [163]

The attenuation of the signal's power is the second cause for the decline in localization accuracy. When an EM wave reaches a barrier, it loses a percentage of its power owing to reflection, absorption, scattering, and diffraction, depending on the kind of barrier. Path loss and shadowing are two major elements that lead to the signal's power being reduced [171]. The first component corresponds the propagation path's characteristics as well as the power dissipation of the EM wave generated by the PD source. The obstacles between the PD source and the UHF probes are specified in the latter. Because the EM waves only travel a short distance within the transformer

tank, shadowing has a greater impact on power attenuation than path loss. The tank walls and numerous active part features are potential impediments for EM waves on their shortest path to the UHF probes. The downside of the UHF measurement technique is that multiple reflections decrease the signal's power to the point that its AT cannot be determined effectively. The localization algorithm is unable to offer suitable coordinates for the PD location in this scenario. In other words, getting four signals with sufficient power to allow AT identification is a requirement for PD localization.

Based on the preliminary investigation results, the localization algorithm successfully identified the location of the PD fault with an average error less than 20 cm. The approach of using clustering instead of the median of the ATs of the candidate coordinates proves effective as a counter measure. In the subsequent section, the localization algorithm is experimentally verified.

4.8 Experimental Validation

Practical measurements are carried out to evaluate the proposed PD localization algorithm discussed in the previous section. In the following, the measurement test setup and the defined case studies are presented and analyzed. In this section, the resulting location for the PD fault is determined using the discussed clustering method.

4.8.1 Case Study: Transformer Tank Model

Measurement Test Setup

The measurements are performed the transformer tank model in Figure 4.18. Since transformer tanks rarely have oil drain valves at the center of their walls, the DN 80 oil drain valves at the bottom and top on two perpendicular sides are selected for the insertion of UHF probes. A schematic overview of the transformer tank model alongside the UHF probes and axes of a hypothetical spatial Cartesian coordinate system with its origin at the corner of the tank is illustrated in Figure 4.18. The UHF probes have an insertion depth of 9 cm, except for probe 4, which has an insertion depth of 12 cm. The coordinates of the probe tips are given in Table 4.7.

For generation of PD inside the tank, a surface discharge model consisting of a needle on a disc made of polyethylene is used. In order to investigate the influence of prolongation in the AT of the UHF signals caused by the active part of the transformer on the localization accuracy, a grounded cylindrical

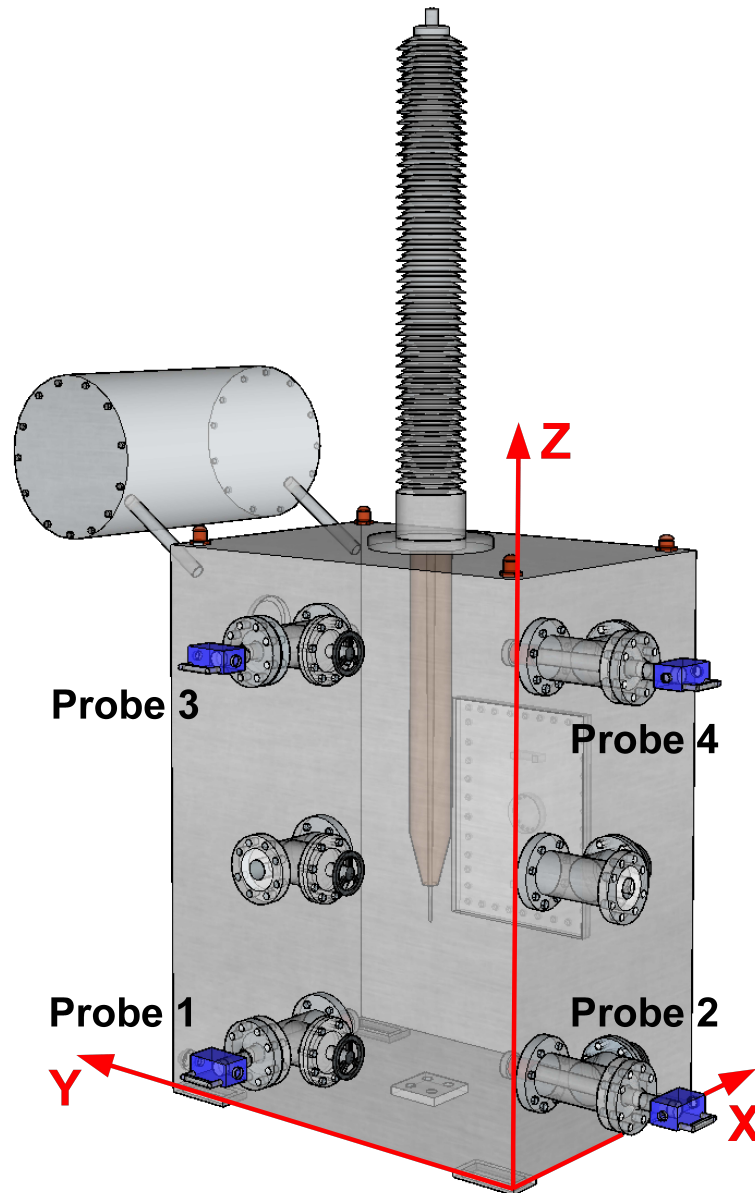


Figure 4.18: Schematic view of the transformer tank model with four probes inserted through the two lowest and the two highest oil drain valves

Table 4.7: Coordinates of the tip of the UHF probes inserted into the tank model

Probe	X / mm	Y / mm	Z / mm
1	90	600	112
2	95	90	112
3	90	600	1373
4	95	120	1373

metal lattice inside a barrier made of paper insulation (Figure 4.14) is placed at the center of the transformer tank model with a radius and a height of 12.4 cm and 30.1 cm, respectively. This barrier represents the winding of the

transformer with its cooling channels and paper insulation. Furthermore, in order to include the effect of the transformer core, a grounded solid aluminum cylinder is positioned at the center of the metal lattice barrier. The PD fault model and the active part model are shown in Figure 4.19.

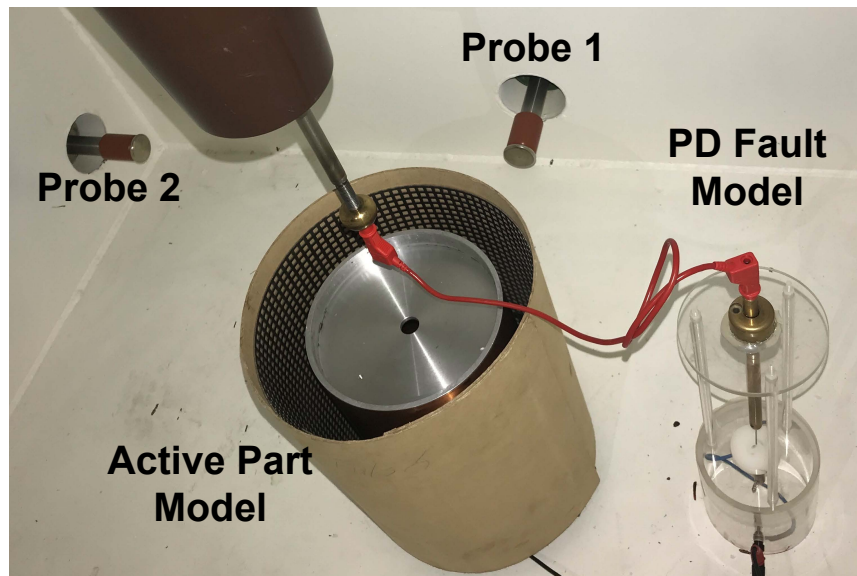


Figure 4.19: View of the surface discharge model next to the active part model inside the tank from its opening

The test circuit shown in Figure 4.20 is utilized for performing the localization measurements. The needle of surface discharge model is placed on high-voltage via the bushing rod. The UHF probes are connected to the DSO with a sampling frequency of 10 GS/s. The intensity of the PD is simultaneously monitored in accordance to IEC 60270 [21] and kept at around 500 pC during the measurements.

Considered Locations for the PD Fault Model

For the evaluation of the localization algorithm, six locations inside the tank are selected. Locations 1 to 3 have the same distance from the tank bottom. The same applies to locations 4 to 6. The considered locations for the PD fault model can be categorized based on the availability of an uninterrupted path between their position and each of the probes. Table 4.8 indicates whether a direct path to each of the probes exists with no interruption by the active part model for the considered locations. For each of the locations, there is an uninterrupted path to at least two of the probes. The coordinates of the considered locations for the PD fault model are listed in Table 4.9. Figure 4.21 shows the tank model alongside the probe tips and the considered locations for the PD fault model in respect to the active part model.

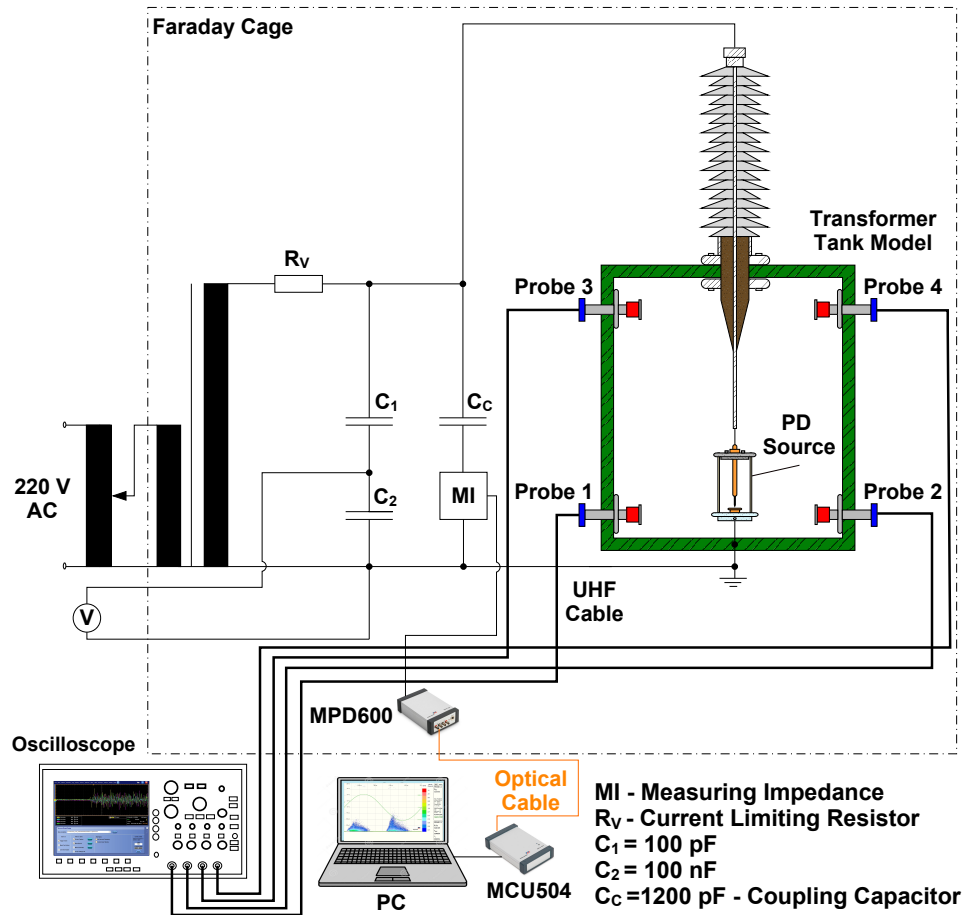


Figure 4.20: Test circuit for performing PD localization measurements using the UHF technique

Table 4.8: Existence of an uninterrupted path between PD fault locations and the probes

Probe	PD Location					
	1	2	3	4	5	6
1	x	x		x	x	
2	x		x	x		x
3	x	x		x	x	x
4	x		x	x	x	x

Result and Discussion

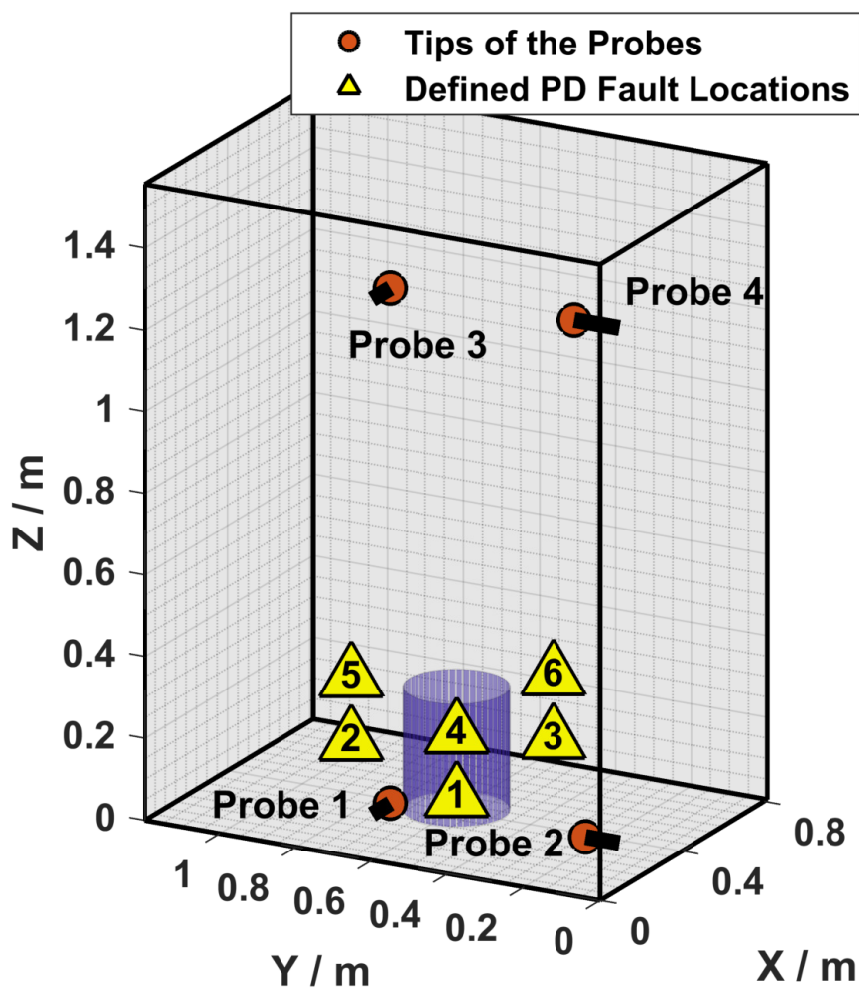
In the following, the localization algorithm is evaluated for different PD locations and scenarios. For this purpose, for each case, a data-set consisting of 1000 signals is considered.

- **In absence of the active part:**

First the ideal case is regarded, i.e. there is an uninterrupted direct path

Table 4.9: Coordinates of the considered locations for the PD fault model inside the tank

Location	X / mm	Y / mm	Z / mm
1	166	465	125
2	400	870	125
3	633	465	125
4	166	465	280
5	400	870	280
6	633	465	280

**Figure 4.21:** Interior of the tank model with the locations considered for the PD fault model in regards to the active part model

to all four probes. For this purpose, the active part model is removed from the tank. The highest localization accuracy is expected for this case. The localization error alongside the determined coordinates of the PD fault are listed in Table 4.10.

Table 4.10: Localization results in absence of the active part model

Location	Distance to PD Source			Localization
	$\Delta X / \text{mm}$	$\Delta Y / \text{mm}$	$\Delta Z / \text{mm}$	Error / mm
1	36.0	9.0	57.0	68.0
2	71.0	36.0	142.0	163.0
3	99.0	54.0	161.0	196.0
4	3.0	74.0	111.0	134.0
5	191.0	2.0	7.0	191.0
6	63.0	92.0	83.0	139.0

- **In presence of the active part:**

The experiments conducted in this section are concerned with localizing the PD source while including the effect of prolongations in the determined AT of UHF signals caused by the active part model in the results. The determined coordinates of the PD fault and the localization error are shown in Table 4.11.

Table 4.11: Localization results in presence of active part model

Location	Distance to PD Source			Localization
	$\Delta X / \text{mm}$	$\Delta Y / \text{mm}$	$\Delta Z / \text{mm}$	Error / mm
1	125.0	88.0	45.0	159.0
2	57.0	70.0	167.0	190.0
3	62.0	92.0	255.0	278.0
4	132.0	58.0	61.0	156.0
5	14.0	194.0	79.0	210.0
6	20.0	273.0	25.0	275.0

Analysis of the Results

According to Table 4.10, the localization error without the active part model is less than 20 cm with an average of 14.85 cm. By placing the active part model in the center of the tank, the average localization error (Table 4.11) is increased by 42 % and in this case is around 21.15 cm with the maximum error for location 3 with 28 cm. A comparison between localization accuracies reported in Table 4.10 and Table 4.11 reveals an overall increase in the localization error. Even for locations 1 and 4, where the direct path is not interrupted by the active part model, the localization accuracy decreases. This is

due to the fact that a portion of the data-sets selected for the final evaluation include reflected signals by the active part model. Due to the proximity between the PD fault model and the active part model, the previously defined selection criteria remain satisfied and hence, signals that have erroneous ATs affect the final outcome of the algorithm. However, in view of the relatively small dimensions of the tank and the fact that the propagation medium in the cases presented is atmospheric air, a maximum error of less than 30 cm is acceptable. Since both of these parameters represent the worst case in the performed investigations concerning the accuracy of the algorithm, an improvement is expected in case of a larger tank filled with insulating oil.

4.8.2 Case Study: Transformer Replica

Measurement Test Setup

In this section, a test setup is designed targeting the determination of the lowest possible localization accuracy under conditions close to the real application. In this regard, the challenges addressed in section 4.1 are in focus. These are on the one hand the high sensitivity or rather the small room for error regarding the AT determination in case of a short run-time between the PD source and the probes, and on the other hand the prolongation of the run-times due to the active part. There are currently no transformers available that are equipped with four antennas for UHF measurements. Hence, in this section a transformer replica is employed for the measurements. For this purpose, a scaled-down model of a three-phase high-voltage transformer is replicated. A metallic enclosure with a length, width and height of 3000 mm, 800 mm, and 1000 mm, respectively, is used as the transformer tank. For the active part, three single phase transformers are placed inside the tank. These transformers are 5 kVA oil-filled single-phase transformers with a cylindrical housing. Through each of the transformer model's walls, a UHF probe is inserted into the tank. Regarding the spatial distribution of the probes, two sensors were placed on the lower edges of each of the end faces, with one sensor centered (probe 1) and the other in a corner (probe 4). The other two sensors (probes 2 and 3) were positioned at the upper edges of each of the longitudinal sides. The reason for this approach is firstly the modeling of a realistic scenario leaning on most recently deployed power transformers already operating in the field, and secondly the consideration of diverse sensor sensitivities. The probes all have a insertion depth of 7 cm, meaning only the tip of the probe is introduced into the tank. For generation of PD inside the

tank, the same fault model as in the previous case study (surface discharge model consisting of a needle on a disc made of polyethylene) is employed. The transformer model is depicted in Figure 4.22. The tank cover is removed to display the active part, the probes and the PD model. The test object is air-filled, which is another factor contributing to the worst-case scenario consideration. The insulating oil would decrease the propagation speed of the EM waves and thus increase the time difference between the received signals, which in turn would have a positive impact on the final localization accuracy that can be achieved.

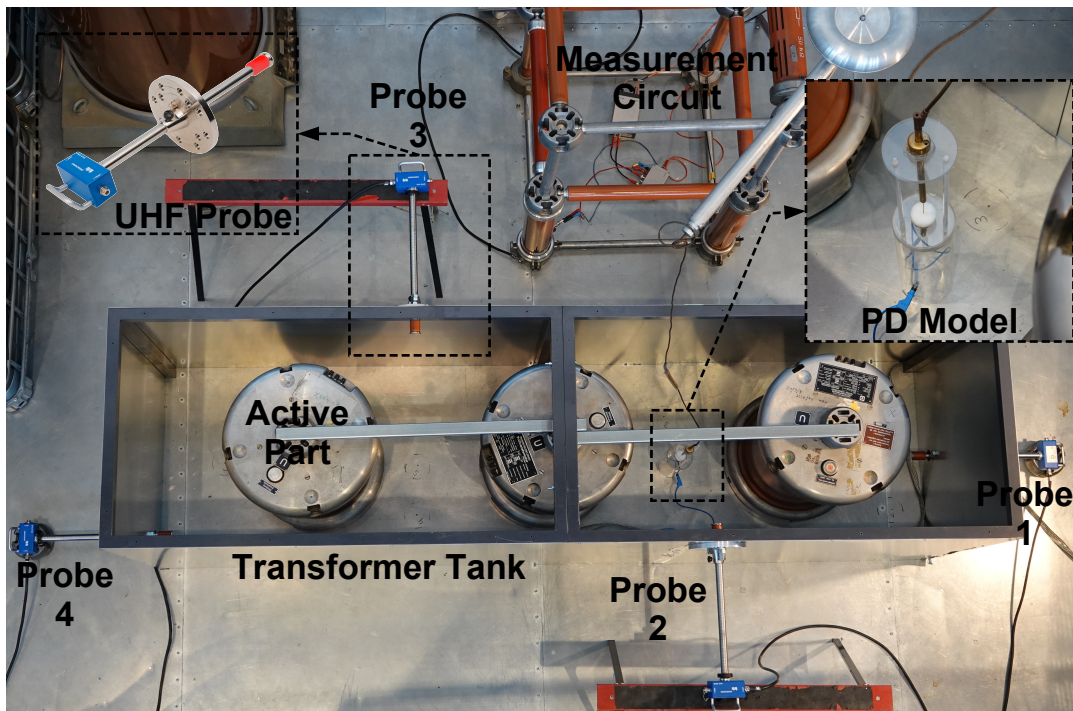


Figure 4.22: Top view of the scaled-down transformer model with cover removed

The test circuit shown in Figure 4.23 is utilized for performing the localization measurements. The needle of the surface discharge model is placed on high-voltage via one of the feed-throughs. The UHF probes are connected to the DSO with a sampling frequency of 10 GS/s. The intensity of the PD is simultaneously monitored in accordance to IEC 60270 [21] and kept at around 500 pC during the measurements. For the evaluation of the algorithm, a database consisting of 1000 data-sets is used.

Considered Locations for the PD Fault Model

A schematic overview of the transformer model alongside the UHF probes and axes of a hypothetical spatial Cartesian coordinate system with its origin

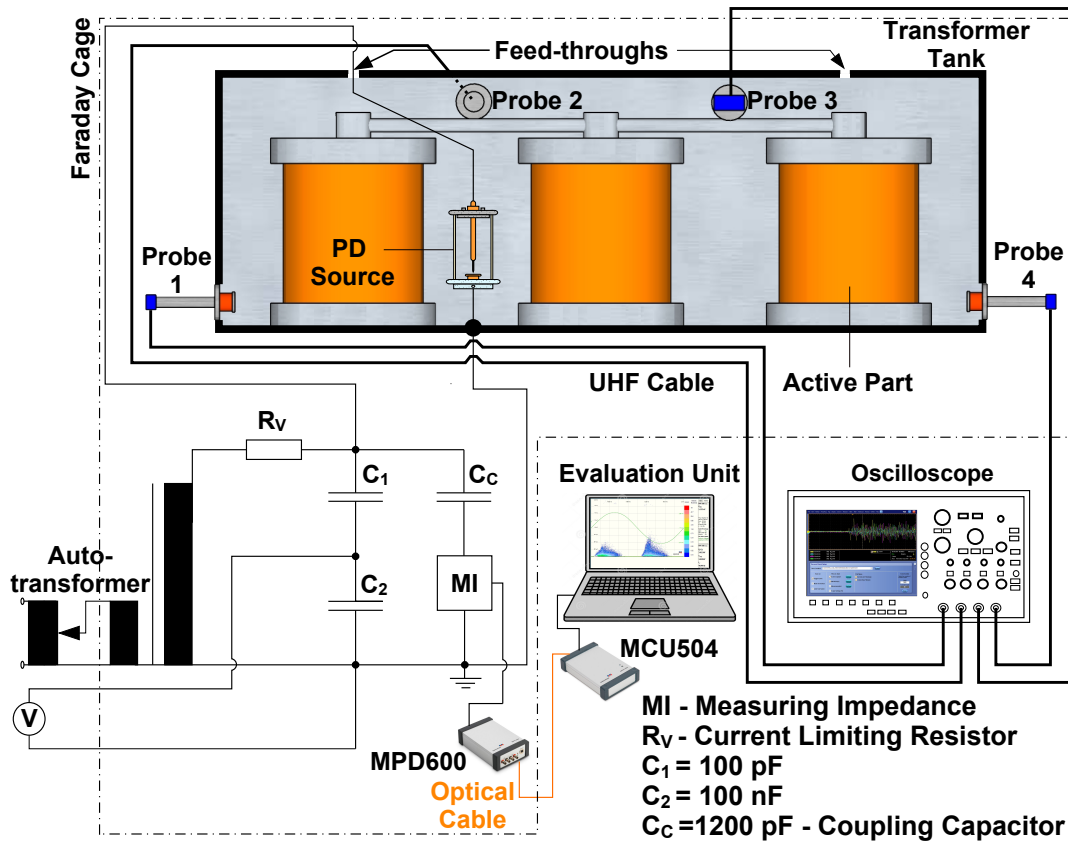


Figure 4.23: Test circuit for performing PD localization measurements using the UHF technique

at the corner of the tank is illustrated in Figure 4.24. For the evaluation of the proposed PD localization algorithm, six locations inside the tank are selected for the positioning of the PD source. These locations are also presented in Figure 4.24. Since the objective of this study is to determine the limits of the proposed algorithm, each selected position for the PD fault grants an uninterrupted propagation path to only one of the probes. The coordinates of the considered locations for the PD fault model are listed in Table 4.12.

Table 4.12: Coordinates of the considered locations for the PD fault model inside the tank

Location	X / mm	Y / mm	Z / mm
1	125	600	280
2	1000	400	280
3	1000	200	280
4	2000	600	280
5	2000	400	280
6	2875	400	280

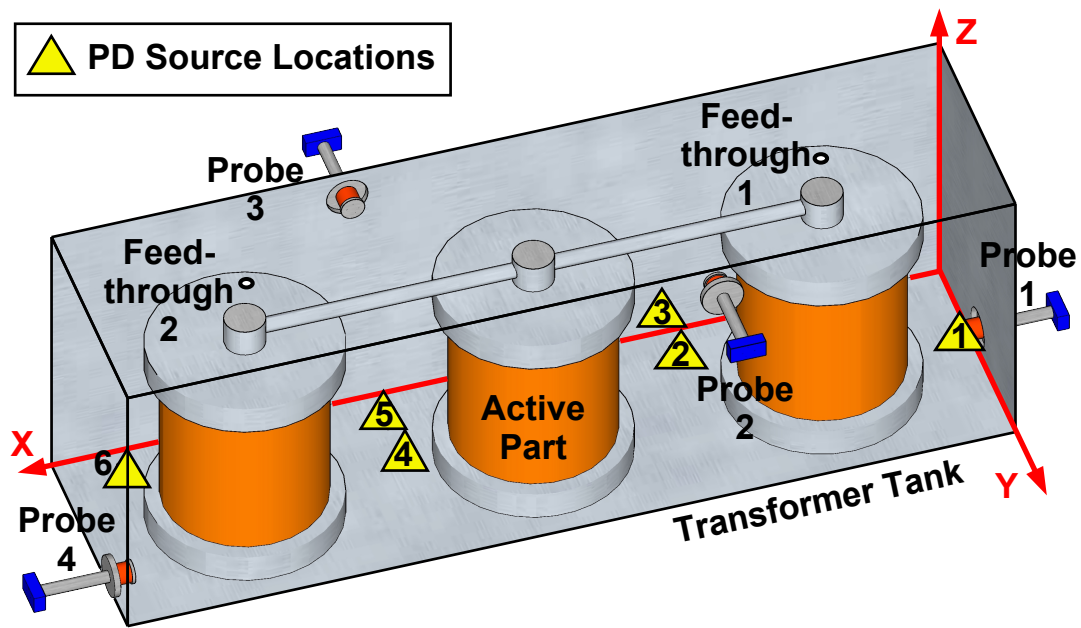


Figure 4.24: Schematic view of the transformer model with the selected positions for the PD model

Results and Discussion

In this section, the results of the performed measurements for the evaluation of the localization algorithm are presented and analyzed. Two scenarios are considered: first, the active part is removed from the tank. This measurement serves the purpose of determining the localization accuracy when no obstacles interfere with the propagation path of the signals and only the reflections generated by the walls of the tank affect the accuracy. In the second step, the measurement is repeated in the presence of the active part. Subsequently, the results are discussed.

- **In absence of the active part:**

First the ideal case is regarded, i.e. there is an uninterrupted direct path to all four probes. For this purpose, the active part is removed from the tank. The highest localization accuracy is expected for this case. The distance between the determined location for the PD fault and the actual location alongside the localization error are listed in Table 4.13.

- **In presence of the active part:**

The experiments conducted in this section are concerned with localizing the PD source while including the effect of prolongations in the determined AT of UHF signals caused by the active part in the results. The distance between the determined location for the PD fault and the actual location, and the localization error are presented in Table 4.14.

Table 4.13: Localization results in absence of the active part

Location	Distance to PD Source			Localization Error / mm
	ΔX / mm	ΔY / mm	ΔZ / mm	
1	133.7	7.8	22.8	135.9
2	56.8	18.5	23.2	64.1
3	72.7	13.4	100.2	124.5
4	106.3	3.2	94.3	142.1
5	97.6	3.0	23.0	100.3
6	103.8	5.3	11.7	104.6

Table 4.14: Localization results in presence of the active part

Location	Distance to PD Source			Localization Error / mm
	ΔX / mm	ΔY / mm	ΔZ / mm	
1	4.9	50.7	231.9	237.4
2	95.7	87.8	104.3	166.6
3	69.8	168.5	71.9	196.1
4	78.9	116.8	86.3	165.3
5	91.0	13.6	162.1	186.4
6	145.9	1.7	56.0	156.3

Analysis of the Results

According to Table 4.13, the localization error in the empty tank is less than 15 cm for all six considered locations with an average of 11.2 cm. By reinstating the active part model in the the tank, the average localization error (Table 4.14) is increased by 65 % and in this case is around 18.5 cm with the maximum error for location 1 with 24 cm. A comparison between localization accuracies reported in Tables 4.13 and 4.14 reveals an overall increase in the localization error with location 2 showing the highest rise with an error of 16.66 cm. In the following, location 2 is in focus. In Figure 4.25, the acquired locations and the final determined coordinates for the PD fault at location 2 are depicted for the two investigated scenarios.

From the database consisting of 1000 signals, only 49 data-sets are selected for the final computation of the PD location in case of the measurement in absence of the active part. This corresponds to about 5 % of the total number of available data-sets. Once the active part is included in the test setup, the number of selected data-sets decreases to 1.7 % of the database. In this regard, a detailed analysis of the relationship between the number of

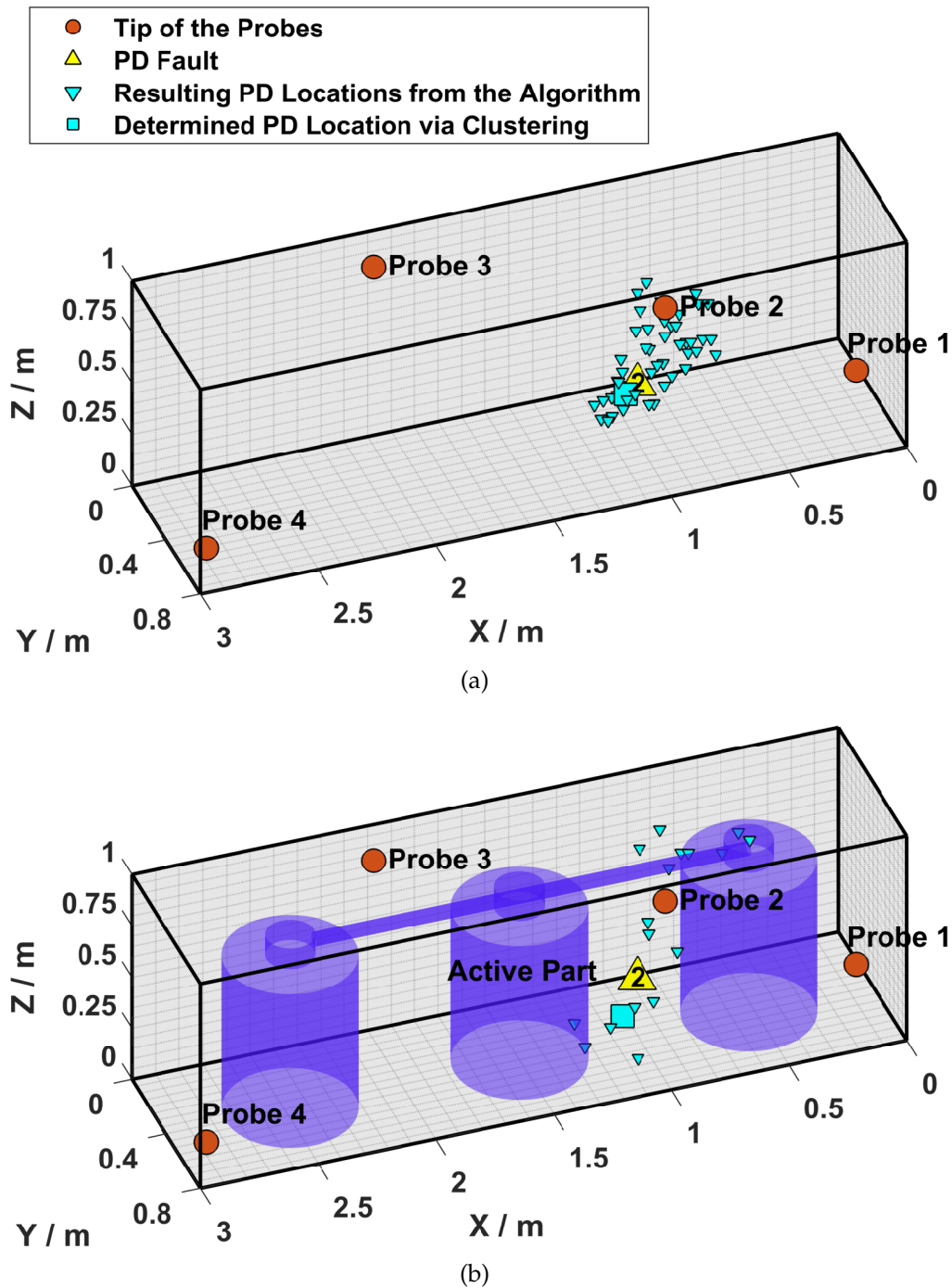


Figure 4.25: Acquired locations and the final determined position for the PD fault in (a) absence, and (b) presence of the active part

input data-sets and localization accuracy is presented. The evaluation was based on the progressive addition of data-sets to the database in increments of 100, starting from an initial database size of 100 data-sets. This process continued until the maximum number of 1000 data-sets was reached. The localization accuracy was then assessed at each stage using the established evaluation metric. By employing this methodology, the relationship between

the number of input data-sets and localization accuracy was investigated in a systematic manner. Focusing on location 2, the results of this investigation for both in absence as well as in presence of the active part are shown in Figure 4.26.

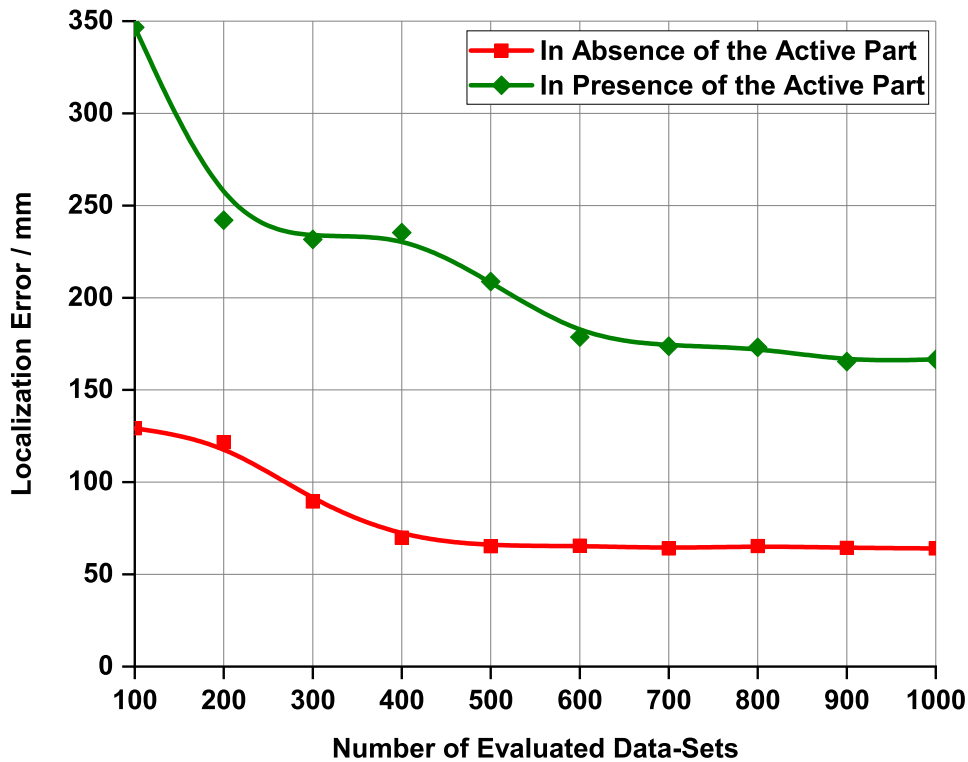


Figure 4.26: Localization accuracy as a function of the number of data-sets considered in absence, and presence of the active part

Initially, with a database size of 100 data-sets, as depicted in Figure 4.26, a relatively high localization error is observed. This can be attributed to the limited amount of data available for accurate localization. Due to the restricted data-set quantity, the algorithm may encounter challenges in capturing the underlying patterns and variations in the signal, leading to higher errors. The insufficient data may result in a less comprehensive representation of the environment and signal patterns.

As the number of data-sets in the database is progressively increased, a consistent and significant trend of decreased localization error is observed. The algorithm greatly benefits from the additional data, as it provides a more extensive and diverse representation of the environment and signal patterns. This expanded data-set allows the algorithm to better discern the relevant information for accurate localization, consequently leading to improved localization accuracy.

It is noteworthy that after reaching a database size between 400 and 600 data-sets, the localization error reaches a relatively stable level. Further increasing the database size beyond this point does not yield significant improvements in accuracy. This observation indicates a diminishing returns effect, wherein the algorithm has already assimilated the essential information necessary for accurate localization from the available data-sets. Therefore, the additional data-sets have diminishing incremental value in reducing the localization error.

Upon reaching the maximum database size of 1000 data-sets, it is observed that the localization error remains relatively constant. The presence of additional data-sets does not have a noticeable impact on further improving the accuracy. This finding suggests that the algorithm has already achieved its optimal performance with the available quantity of data-sets. The plateauing of the localization error indicates that the algorithm has reached a saturation point in terms of its ability to leverage the data-set for localization accuracy.

Moreover, it is important to note that within the database, there exist data-sets that resulted in a location estimate nearly identical to the actual position of the fault location, demonstrating the quality of the proposed method for AT determination. However, in realistic measurements, it is not feasible to single out these specific data-sets from the database. Hence, an assessment based on processing multiple data-sets is a valid and practical approach.

Based on the results, although localization based on 100 data-sets is feasible, increasing the number of data-sets significantly improves the localization accuracy by over 50 %. Therefore, a database with at least 300 data-sets is recommended to achieve a sufficient level of accuracy in localization.

It is also noteworthy that the measurements conducted in this thesis were performed in a scaled-down air-filled replica of a transformer, aiming to determine the lower limit of the achievable localization accuracy. This limitation arises due to the current lack of transformers equipped with sufficient drain valves for probe insertion. Considering the relatively small dimensions of the tank and the atmospheric air as the propagation medium in the presented cases, an error of less than 25 cm is deemed acceptable. However, it is expected that localization accuracy would improve when dealing with larger tanks utilizing oil as the insulating medium, as these two factors (small dimensions and air as propagation medium) have a negative impact on localization accuracy.

4.9 Graphical User Interface and Features of the Localization Algorithm

For the localization algorithm to be suitable for a wide user group of different experience and technical knowledge levels, the developed algorithm was extended with a graphical user interface using the GUI Layout toolbox of *MATLAB*. Hereby, the user is directed through the process, beginning with inputting the necessary initial parameters, such as the size of the tank, the position of the sensors, the permittivity of the insulating medium, the number of signals to be considered, the position of the active part, the signal processing modules to be used, etc. Figure 4.27 shows the corresponding input window of the graphical user interface for inserting the coordinates of the sensors.

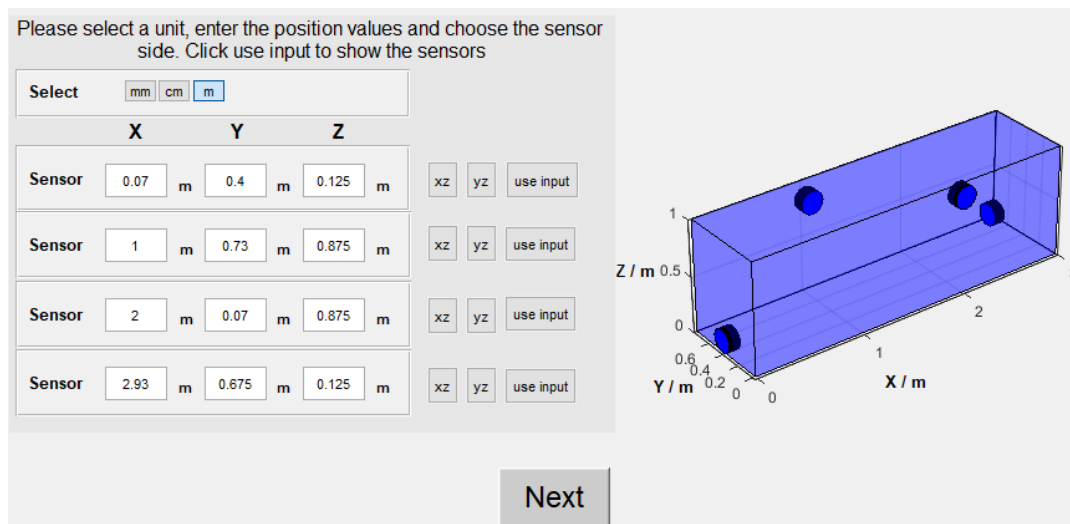


Figure 4.27: Entering window of the coordinates of the sensors via the implemented graphical user interface of the PD localization algorithm

After entering the initial parameters, certain algorithm parameters can be modified for the expert user, while the standard user may proceed with preset features. The user then chooses the folder containing the PD signals and clicks on start the process. Subsequently, the localization begins and the results are shown both visually and as a text file, which contains all the input parameters and the final results. The 3D visualization tool also allows the user to rotate and zoom in and out. An exemplary visualization of the results is depicted in Figure 4.28.

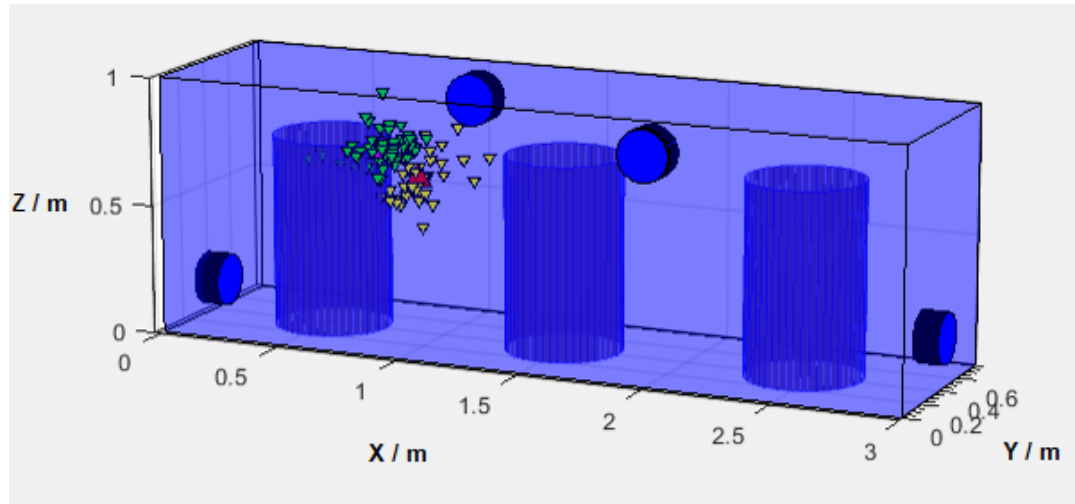


Figure 4.28: Visualized localization results via the implemented graphical user interface of the PD localization algorithm

In this chapter, an algorithm was proposed for the localization of PD using the UHF measurement technique. The algorithm utilizes a multi data-set approach. In order to maximize the efficiency of the algorithm, several rules are applied to only select a portion of the data-sets. Modern methods are employed to pre-process the data-sets. For the determination of the AT of the signals, which is the most critical challenge of this method, the TWCF method is applied. The superiority of the employed AT determination method was demonstrated by means of comparison with other available techniques. The final location of the fault is determined by clustering the candidate PD coordinates.

Measurements were performed in a scaled-down physical model of a transformer with purposely set unfavorable circumstances with the goal of identifying the lowest limit of the localization accuracy achievable with the proposed localization algorithm. It was demonstrated that a localization accuracy of less than 25 cm may be achieved. It is worth noting that a higher localization accuracy is feasible in a genuine oil-filled power transformer due to the lower propagation velocity of electromagnetic waves in insulating oil, which in turn reduces the influence of fluctuations in the determined ATs and leads to better localization results.

Conclusion

The global energy transition towards renewable energy sources has gained significant momentum in recent years. As countries shift away from traditional fossil fuels, the demand for renewable energy technologies, such as wind turbines and solar panels, has grown exponentially. This transition has resulted in the need for a greater number of transformers to step up or step down the voltage of electricity transmitted through power grids. While the deployment of new transformers is necessary to accommodate the increasing demand for energy, it also places a higher stress on the transformers that are already in service. Transformers hold a crucial role in power distribution networks, and any failure or malfunction can result in substantial power outages and significant economic losses. Power transformers are also the most expensive element of the power grid. Their high initial cost is accompanied by a high expectation of service life. A forced outage due to a fault not only affects the reliability of the power grid, but is also associated with high costs for downtime and expensive measures to repair or replace the transformer.

With deteriorating condition of transformers, their risk of failure increases. To minimize costly downtime, transformer maintenance should be planned ahead of time. Therefore, there is a pressing need to develop new methods and approaches for monitoring and diagnostic of transformers. Monitoring and diagnostic techniques are effective tools for determining an asset's state of health, allowing the asset manager to make an informed decision about an appropriate maintenance plan by analyzing the data collected via monitoring and evaluating supplementary diagnostic measurement results. The appropriate condition assessment approach for a transformer depends on its acquisition value and its criticality in the power system. Therefore, the design, technology, and cost of implementing a suitable monitoring system for small transformers significantly differs from larger units. Against this background, two concepts for achieving the above objective were discussed in this work, targeting different types of transformers.

Tracking the concentration of fault gases in the gas cushion of small GSU

transformers employed in wind and photovoltaic farms as the basis for the development of an online monitoring system was the first presented concept in this work. The majority of established and available transformer monitoring systems target the dissolved gases in the transformer oil and are suitable for larger units, however, they are not cost-effective for the small GSUs mentioned above. In case of a fault in a transformer, considerable amounts of fault gases are generated due to the degradation of the insulation system. There is a permanent exchange between the liquid phase and the gas phase of hermetically sealed transformers with gas cushion. Since hydrogen has a low solubility in the liquid phase, and is a common byproduct of different fault types in transformers, it serves as the main target of the developed monitoring system. The monitoring system is exposed to high ambient stress, since in addition to mechanical factors such as the vibrations during the operation of the transformer, it has to cover a large temperature and pressure ranges. Additionally, in case of hermetically sealed transformers with a gas cushion out of nitrogen, it has to operate in a low-oxygen environment. Following a preliminary investigation on available semiconductor-based sensors for the detection of fault gases, a catalytic type sensor was selected following a series of experiments regarding its suitability for the high requirements to be met. Furthermore, auxiliary sensors were integrated to monitor environmental parameters such as temperature, pressure, oxygen level, and humidity. A lab prototype of the monitoring system was developed and subjected to several experimental scenarios. The results indicated that the monitoring system successfully tracked the trend of fault gases in the gas cushion. The developed monitoring system was subsequently industrialized. It features a warning and an alarm function. The warning signal is issued if the sensor system detects a rise in the amount of the fault gases, or the rate of fault gas generation. In this case, the operator can initiate further measures, e.g. analysis of an oil sample via gas chromatography. The monitoring system continues to track the fault gas level, and if the pattern continues, an alarm signal will be issued, allowing the operator to react accordingly.

The second concept covered in this thesis is the UHF measurement technique for PD. In this regard, the electromagnetic (EM) waves emitted in case of PD activity in power transformers are captured by specially designed probes. For several decades, this approach has been widely used for monitoring and diagnostic purposes in the field of gas-insulated substations. For power transformers, due to their intricate inner structure, this is a significantly more demanding challenge.

The conventional PD measurement method in accordance to *IEC 60270* offers the possibility of calibration, detects all PD types, and is considered as reference for PD classification based on so-called PRPD patterns. However, it has also some limitations, e.g. it is susceptible to external interference. Furthermore, its PD localization capabilities is severely limited, since it can only enable a one-dimensional localization. The proposed methods in this thesis provide complementary tools for PD diagnostic measurements in power transformers.

The main disadvantage of the UHF measurement technique is the absence of a calibration procedure comparable to the conventional method, as stated in *IEC TS 62478*. This is due to a variety of factors. Once the probe is inserted into the tank of a transformer, owing to the complex inner structure of the interior of power transformers, specially the active part, a new EM system is established to which general far-field antenna theory is not applicable.

On the topic of PD detection, since the UHF measurement technique features a high resilience against external disturbances due the transformer tank acting as a Faraday cage, it is optimal for measurements with a high background noise, e.g. on-site measurements or online monitoring. A practical technique for PD detection is proposed in this thesis, with the focus on optimal center frequency and bandwidth to obtain patterns with a high correlation to conventional PRPD patterns, allowing the application of existing PD classification know-how to evaluate UHF PRPD patterns. To accomplish this objective, the resonance frequencies of the transformer's tank as a cavity are calculated by considering various factors such as the tank's shape, dimensions, and the material properties of the insulation medium. Subsequently, the center frequencies are ranked in regards to the mode density and depending on the measurement bandwidth. For performing the measurement, the lowest center frequency is selected and a sensitivity check according to *IEC TS 62478* is performed, in order to adjust the gain and the amplification factor of the measurement instrument. The background noise is then evaluated with two possible outcomes: if the background noise is acceptable, measurements for obtaining UHF PRPD patterns are performed. Otherwise, the selected center frequency is removed from the ranking and the described procedure is repeated with the next lowest center frequency. The proposed method was validated through practical measurements, demonstrating remarkable results.

Another aspect of the UHF measurement technique is its capability of localizing PD using the time difference of arrival (TDOA) method. For this

purpose, four probes and consequently four captured EM waves are necessary. The arrival time (AT) of each of the signals is then determined. The distance between the PD source and the respective UHF probe is correlated with the propagation velocity of the EM waves multiplied by their time of flight. The solution to the resulting system of four equations delivers the location of the fault. The effect of deviations in the determined AT of UHF signals on the localization accuracy was analyzed and it was concluded that an algorithm based on only one data-set is not suitable for the complicated problem of PD localization in power transformers due to the high dependency of the localization accuracy on the determined ATs. In this thesis, a PD localization algorithm is proposed, which utilizes a multiple data-set approach. A more exact assessment of the PD location is feasible by using appropriate methods to select only a small portion of the data-sets in combination with modern digital signal processing and clustering for determining the fault location. The proposed algorithm was validated by using a scaled-down physical model of a transformer. It was shown that even in a relatively small transformer tank with evoked reflections through the active part, and air as insulating medium, a localization error of less than 25 cm is achievable. Given the purposefully chosen unfavorable circumstances with the objective of determining the lower limit of the reachable localization accuracy with the proposed localization algorithm, it can be assumed that a significantly higher localization accuracy is achievable in a genuine oil-filled power transformer. This is attributed to the lower propagation velocity of electromagnetic waves in insulating oil, which decreases the effect of deviations in the determined ATs and leads to better localization results.

The instruments and procedures developed and presented in this thesis serve transformer condition diagnosis and monitoring, allowing for a better maintenance and repair strategy and thus improved asset management in terms of operational reliability, availability, cost-effectiveness, and investment planning, all of which contribute to energy efficiency.

Bibliography

- [1] M. J. Heathcote and D. P. Franklin, *The J & P transformer book: A practical technology of the power transformer*, 13th ed. Burlington, MA: Newnes, 2007, ISBN: 9780080551784.
- [2] S. Chakravorti, D. Dey, and B. Chatterjee, *Recent trends in the condition monitoring of transformers: Theory, implementation and analysis*. London: Springer, 2013, ISBN: 9781447155492. DOI: 10 . 1007 / 978 - 1 - 4471 - 5550-8.
- [3] A. E. B. Abu-Elanien and M. M. A. Salama, "Survey on the Transformer Condition Monitoring", in *2007 Large Engineering Systems Conference on Power Engineering*, 2007, pp. 187–191. DOI: 10 . 1109/LESCPE . 2007 . 4437376.
- [4] W. Li, "Evaluating Mean Life of Power System Equipment With Limited End-of-Life Failure Data", *IEEE Transactions on Power Systems*, vol. 19, no. 1, pp. 236–242, 2004, ISSN: 0885-8950. DOI: 10 . 1109/TPWRS . 2003 . 821434.
- [5] A. E. B. Abu-Elanien and M. M. A. Salama, "Asset management techniques for transformers", *Electric Power Systems Research*, vol. 80, no. 4, pp. 456–464, 2010, ISSN: 03787796. DOI: 10 . 1016 / j . epsr . 2009 . 10 . 008.
- [6] M. Ahmed, M. Elkhatib, M. Salama, and K. B. Shaban, "Transformer Health Index estimation using Orthogonal Wavelet Network", in *Electrical Power and Energy Conference (EPEC), 2015 IEEE, IEEE, 2015*, pp. 120–124, ISBN: 978-1-4799-7662-1. DOI: 10 . 1109 / EPEC . 2015 . 7379937.
- [7] P. Jarman, "Transformers and the energy system transition", *Transformers Magazine*, vol. 7, no. 1, pp. 26–33, 2020, ISSN: 1849-3319.
- [8] X. M. López-Fernández, H. B. Ertan, and J. Turowski, *Transformers: Analysis, design, and measurement*. Boca Raton, FL: CRC Press, 2016, ISBN: 1466508248.

- [9] P. Boss, P. Lorin, A. Viscardi, J. W. Harley, and J. Isecke, "Economic aspects and practical experiences of power transformers on-line monitoring", *International Council on Large Electric Systems (CIGRÉ)*, France, 2000.
- [10] S. C. CIGRE, "A2 Transformers, WG 20: Economics of Transformer Management", *ELECTRA*, no. 214, pp. 51–59, 2004.
- [11] T. Gonen, *Electric Power Transmission System Engineering: Analysis and Design*, 3rd. CRC Press, 2018.
- [12] R. Schwarz and M. Muhr, "Diagnostic methods for transformers", in *2008 International Conference on Condition Monitoring and Diagnosis*, 2008, pp. 974–977. DOI: 10.1109/CMD.2008.4580445.
- [13] S. Tenbohlen, F. Vahidi, and J. Jagers, "A worldwide transformer reliability survey", in *VDE High Voltage Technology 2016; ETG-Symposium*, VDE, pp. 1–6, ISBN: 3800743108.
- [14] S. Tenbohlen *et al.*, "Development and Results of a Worldwide Transformer Reliability Survey", *CIGRE SC A2 Colloquium*, 2015. [Online]. Available: <https://bib.irb.hr/prikazi-rad?rad=781670>.
- [15] H. de Faria, J. G. S. Costa, and J. L. M. Olivas, "A review of monitoring methods for predictive maintenance of electric power transformers based on dissolved gas analysis", *Renewable and Sustainable Energy Reviews*, vol. 46, pp. 201–209, 2015, ISSN: 13640321. DOI: 10.1016/j.rser.2015.02.052.
- [16] W. Li, E. Vaahedi, and P. Choudhury, "Power system equipment aging", *IEEE Power and Energy Magazine*, vol. 4, no. 3, pp. 52–58, 2006, ISSN: 1540-7977. DOI: 10.1109/MPAE.2006.1632454.
- [17] A. E. B. Abu-Elanien, "Transformer health assessment and techno-economic end of life evaluation", Ph.D. dissertation, University of Waterloo. [Online]. Available: <https://uwspace.uwaterloo.ca/handle/10012/5993>.
- [18] *IEEE Guide for the Interpretation of Gases Generated in Mineral Oil-Immersed Transformers*, IEEE Std C57.104-2019, 2019.
- [19] CIGRE WG D1.24, "Condition assessment of high voltage insulation in power system equipment", *CIGRE*, no. 703, 2015.
- [20] K. O. Papailiou, *Springer Handbook of Power Systems*. Springer Nature, 2021, ISBN: 9789813299382.

- [21] *High voltage test techniques - Partial discharge measurements*, IEC 60270, 2015.
- [22] A. Müller, M. Jovalekic, and S. Tenbohlen, "Solubility study of different gases in mineral and ester-based transformer oils", in *2012 IEEE International Conference on Condition Monitoring and Diagnosis*, 2012, pp. 937–940. DOI: 10.1109/CMD.2012.6416307.
- [23] J. H. Harlow, *Electric power transformer engineering*. CRC press, 2003.
- [24] R. Kurrer and K. Feser, "The application of ultra-high-frequency partial discharge measurements to gas-insulated substations", *IEEE Transactions on Power Delivery*, vol. 13, no. 3, pp. 777–782, 1998.
- [25] R. Baumgartner, B. Fruth, W. Lanz, and K. Pettersson, "Partial discharge. X. PD in gas-insulated substations-measurement and practical considerations", *IEEE Electrical Insulation Magazine*, vol. 8, no. 1, pp. 16–27, 1992. DOI: 10.1109/57.120634.
- [26] H. Okubo, M. Yoshida, T. Takahashi, T. Hoshino, M. Hikita, and A. Miyazaki, "Partial discharge measurement in a long distance SF/sub 6/ gas insulated transmission line (GIL)", *IEEE Transactions on Power Delivery*, vol. 13, no. 3, pp. 683–690, 1998. DOI: 10.1109/61.686960.
- [27] I. Fofana and Y. Hadjadj, "Electrical-based diagnostic techniques for assessing insulation condition in aged transformers", *Energies*, vol. 9, no. 9, p. 679, 2016. DOI: 10.3390/en9090679.
- [28] C. AJ, M. Salam, Q. Rahman, F. Wen, S. Ang, and W. Voon, "Causes of transformer failures and diagnostic methods – a review", *Renewable and Sustainable Energy Reviews*, vol. 82, pp. 1442–1456, 2018, ISSN: 1364-0321. DOI: <https://doi.org/10.1016/j.rser.2017.05.165>.
- [29] *Mineral oil-filled electrical equipment in service - Guidance on the interpretation of dissolved and free gases analysis*, IEC 60599, 2022.
- [30] *High voltage test techniques - Measurement of partial discharges by electromagnetic and acoustic methods*, IEC TS 62478, 2016.
- [31] A. Gemant and W. Philippoff, "Die Funkenstrecke mit Vorkondensator", *Zeitschrift für technische Physik*, vol. 13, no. 9, pp. 425–430, 1932.
- [32] A. Küchler, *High voltage engineering: Fundamentals - Technology - Applications*. Springer, 2017, ISBN: 9783642119927. DOI: 10.1007/978-3-642-11993-4.

- [33] E. Lemke, "A critical review of partial-discharge models", *IEEE Electrical Insulation Magazine*, vol. 28, no. 6, pp. 11–16, 2012. DOI: 10.1109/MEI.2012.6340519.
- [34] W. Hauschild and E. Lemke, *High-voltage test and measuring techniques*. Heidelberg: Springer, 2014, ISBN: 978-3-642-45352-6.
- [35] H. Illias, G. Chen, and P. L. Lewin, "Modeling of partial discharge activity in spherical cavities within a dielectric material", *IEEE Electrical Insulation Magazine*, vol. 27, no. 1, pp. 38–45, 2011. DOI: 10.1109/MEI.2011.5699446.
- [36] M. Danikas, "The definitions used for partial discharge phenomena", *IEEE Transactions on Electrical Insulation*, vol. 28, no. 6, pp. 1075–1081, 1993. DOI: 10.1109/14.249381.
- [37] A. Cavallini, G. C. Montanari, and M. Tozzi, "Pd apparent charge estimation and calibration: A critical review", *IEEE Transactions on Dielectrics and Electrical Insulation*, vol. 17, no. 1, pp. 198–205, 2010. DOI: 10.1109/TDEI.2010.5412018.
- [38] P. Osvath, E. Carminati, and A. Gandelli, "A contribution on the traceability of partial discharge measurements", *IEEE Transactions on Electrical Insulation*, vol. 27, no. 1, pp. 130–134, 1992. DOI: 10.1109/14.123448.
- [39] *IEEE Guide for the Measurement of Partial Discharges in AC Electric Machinery*, IEEE Std 1434-2014, 2014.
- [40] M. Beyer, W. Boeck, K. Möller, and W. Zaengl, *Hochspannungstechnik: Theoretische und praktische Grundlagen*. Springer Berlin, 2014, ISBN: 9783642648939.
- [41] A. Akbari, P. Werle, H. Borsi, and E. Gockenbach, "Transfer function-based PD localization in power transformers: a feasibility study", *IEEE Electrical Insulation Magazine*, vol. 18, no. 5, pp. 22–32, 2002, ISSN: 0883-7554. DOI: 10.1109/MEI.2002.1044318.
- [42] P. Werle, *Erfassung und Evaluierung von Teilentladungen in Transformatoren mit innovativen Sensoren und adaptierten Verfahren der digitalen Signalverarbeitung*. Cuvillier, 2006, ISBN: 3867270007.
- [43] H. Borsi, P. Werle, and E. Gockenbach, "Various partial discharge measurement and evaluation techniques adapted to different transformer types", in *2013 IEEE International Symposium on Electrical Insulation (ISEI)*, IEEE, 2013, pp. 238–241.

- [44] M. Rahimbakhsh, J. Torres, P. Werle, E. Gockenbach, and M. A. Azirani, "Investigation of Partial Discharge Localization based on Electrical Measurements", in *2018 IEEE 2nd International Conference on Dielectrics (ICD 2018)*, Piscataway, N.J.: IEEE, 2018, pp. 1–4, ISBN: 978-1-5386-6389-9. DOI: 10.1109/ICD.2018.8514629.
- [45] R. Blue, D. Uttamchandani, and O. Farish, "Infrared detection of transformer insulation degradation due to accelerated thermal aging", *IEEE Transactions on Dielectrics and Electrical Insulation*, vol. 5, no. 2, pp. 165–168, 1998. DOI: 10.1109/94.671924.
- [46] S. Degeratu *et al.*, "Condition monitoring of transformer oil using thermal analysis and other techniques", *Journal of thermal analysis and calorimetry*, vol. 119, pp. 1679–1692, 2015.
- [47] A. Marín-Serrano, J. A. Balderas-López, P. A. Calva, and A. Aranda-Pérez, "Thermo-optical properties as complementary parameters for damage assessment of mineral oils aged under controlled conditions used in power transformers", *Thermochimica Acta*, vol. 676, pp. 33–38, 2019, ISSN: 00406031. DOI: 10.1016/j.tca.2019.03.025.
- [48] A. Razzaq, H. Zainuddin, F. Hanaffi, and R. M. Chyad, "Transformer oil diagnostic by using an optical fibre system: a review", *IET Science, Measurement & Technology*, vol. 13, no. 5, pp. 615–621, 2019, ISSN: 1751-8822. DOI: 10.1049/iet-smt.2018.5076.
- [49] L. E. Lundgaard, "Partial discharge. XIII. Acoustic partial discharge detection-fundamental considerations", *IEEE Electrical Insulation Magazine*, vol. 8, no. 4, pp. 25–31, 1992, ISSN: 0883-7554. DOI: 10.1109/57.145095.
- [50] H. D. Ilkhechi and M. H. Samimi, "Applications of the acoustic method in partial discharge measurement: A review", *IEEE Transactions on Dielectrics and Electrical Insulation*, vol. 28, no. 1, pp. 42–51, 2021. DOI: 10.1109/TDEI.2020.008985.
- [51] L. Zhou, J. Cai, J. Hu, G. Lang, L. Guo, and W. Liao, "A Correction-Iteration Method for PD Localization in Transformer based on Acoustic Measurement", *IEEE Transactions on Power Delivery*, p. 1, 2020, ISSN: 0885-8977. DOI: 10.1109/TPWRD.2020.3011455.
- [52] S. A. M. Najafi, E. Gockenbach, P. Werle, and H. Borsi, "Effect of carbonized patterns on oil-impregnated aramid pressboards surface on acoustic emission signals at inhomogeneous electric field",

- IEEE Transactions on Dielectrics and Electrical Insulation*, vol. 25, no. 5, pp. 1644–1650, 2018, ISSN: 1070-9878. DOI: 10.1109/TDEI.2018.006939.
- [53] J. N'cho, I. Fofana, Y. Hadjadj, and A. Beroual, "Review of Physico-chemical-Based Diagnostic Techniques for Assessing Insulation Condition in Aged Transformers", *Energies*, vol. 9, no. 5, p. 367, 2016. DOI: 10.3390/en9050367.
- [54] J. Faiz and M. Soleimani, "Assessment of Computational Intelligence and Conventional Dissolved Gas Analysis Methods for Transformer Fault Diagnosis", *IEEE Transactions on Dielectrics and Electrical Insulation*, vol. 25, no. 5, pp. 1798–1806, 2018, ISSN: 1070-9878. DOI: 10.1109/TDEI.2018.007191.
- [55] S. A. Khan, M. A. Khan, S. A. Wani, and M. D. Equbal, "Performance Enhancement and Extension of DGA-Based Transformer Fault Diagnosis Methods Using Soft-Computing Techniques", in *Soft Computing in Condition Monitoring and Diagnostics of Electrical and Mechanical Systems*, Springer, Singapore, 2020, pp. 287–324. [Online]. Available: https://link.springer.com/chapter/10.1007/978-981-15-1532-3_13.
- [56] T. Piotrowski, P. Rozga, and R. Kozak, "Comparative Analysis of the Results of Diagnostic Measurements with an Internal Inspection of Oil-Filled Power Transformers", *Energies*, vol. 12, no. 11, p. 2155, 2019. DOI: 10.3390/en12112155.
- [57] H. H. Sinaga, "Detection, Identification and Localization of Partial Discharges in Power Transformers using UHF Techniques", *The University of New South Wales Australia. PhD Thesis*, 2012.
- [58] S. Xiao, P. Moore, M. D. Judd, and I. E. Portugues, "An investigation into electromagnetic radiation due to partial discharges in high voltage equipment", in *2007 IEEE Power Engineering Society General Meeting*, 2007, pp. 1–7. DOI: 10.1109/PES.2007.385659.
- [59] I. Choudhury and S. Hashmi, *Encyclopedia of renewable and sustainable materials*. Elsevier, 2020.
- [60] J. A. Kent *et al.*, "Kent and Riegel's handbook of industrial chemistry and biotechnology", 2007.
- [61] I. J. Nagrath and D. P. Kothari, *Power System Engineering*. McGraw-Hill Education, 2012.

- [62] A. B. Norazhar, A. Abu-Siada, and S. Islam, "A review on chemical diagnosis techniques for transformer paper insulation degradation", in *2013 Australasian Universities Power Engineering Conference (AUPEC)*, 2013, pp. 1–6. DOI: 10.1109/AUPEC.2013.6725476.
- [63] J. Faiz and M. Soleimani, "Dissolved Gas Analysis Evaluation in Electric Power Transformers using Conventional Methods, a Review", *IEEE Transactions on Dielectrics and Electrical Insulation*, vol. 24, no. 2, pp. 1239–1248, 2017, ISSN: 1070-9878. DOI: 10.1109/tdei.2017.005959.
- [64] M. H. Zink, *Zustandsbewertung betriebsgealterter Hochspannungstransformatordurchführungen mit Öl-Papier-Dielektrikum mittels dielektrischer Diagnose*. 2013, ISBN: 978-3-86360-067-9. [Online]. Available: https://www.db-thueringen.de/receive/dbt_mods_00022461.
- [65] C. Sun, P. R. Ohodnicki, and E. M. Stewart, "Chemical sensing strategies for real-time monitoring of transformer oil: A review", *IEEE Sensors Journal*, vol. 17, no. 18, pp. 5786–5806, 2017. DOI: 10.1109/JSEN.2017.2735193.
- [66] S. Ferrito, "A comparative study of dissolved gas analysis techniques: The vacuum extraction method versus the direct injection method", *IEEE Transactions on Power Delivery*, vol. 5, no. 1, pp. 20–25, 1990. DOI: 10.1109/61.107324.
- [67] M. Duval, "Dissolved gas analysis: It can save your transformer", *IEEE Electrical Insulation Magazine*, vol. 5, no. 6, pp. 22–27, 1989, ISSN: 0883-7554.
- [68] F. Jakob, "Dissolved Gas Analysis: Past, Present, and Future", *Weidmann ACTI Inc*, 2003.
- [69] J. J. Kelly, "Transformer Fault Diagnosis by Dissolved-Gas Analysis", *IEEE Transactions on Industry Applications*, vol. IA-16, no. 6, pp. 777–782, 1980.
- [70] E. Braesel, E. Brunner, and E. Hartmann, "New tools for the diagnosis of buchholz relay gases", *Elektrizitätswirtschaft*, vol. 98, 1999.
- [71] M. Duval, "A review of faults detectable by gas-in-oil analysis in transformers", *IEEE Electrical Insulation Magazine*, vol. 18, no. 3, pp. 8–17, 2002, ISSN: 0883-7554. DOI: 10.1109/MEI.2002.1014963.
- [72] M. Duval *et al.*, "DGA in Non-Mineral Oils and Load Tap Changers and Improved DGA Diagnosis Criteria", *Working Group D1. 31*, 2010.

- [73] N. Poonnoy, C. Suwanasri, and T. Suwanasri, "Fuzzy logic approach to dissolved gas analysis for power transformer failure index and fault identification", *Energies*, vol. 14, no. 1, 2021, ISSN: 1996-1073. DOI: 10.3390/en14010036. [Online]. Available: <https://www.mdpi.com/1996-1073/14/1/36>.
- [74] H.-C. Sun, Y.-C. Huang, and C.-M. Huang, "A review of dissolved gas analysis in power transformers", *Energy Procedia*, vol. 14, pp. 1220–1225, 2012, 2011 2nd International Conference on Advances in Energy Engineering (ICAEE), ISSN: 1876-6102. DOI: <https://doi.org/10.1016/j.egypro.2011.12.1079>.
- [75] U. M. Rao, I. Fofana, K. N. V. P. S. Rajesh, and P. Picher, "Identification and application of machine learning algorithms for transformer dissolved gas analysis", *IEEE Transactions on Dielectrics and Electrical Insulation*, vol. 28, no. 5, pp. 1828–1835, 2021. DOI: 10.1109/TDEI.2021.009770.
- [76] S. A. Wani, A. S. Rana, S. Sohail, O. Rahman, S. Parveen, and S. A. Khan, "Advances in dga based condition monitoring of transformers: A review", *Renewable and Sustainable Energy Reviews*, vol. 149, p. 111347, 2021, ISSN: 1364-0321. DOI: <https://doi.org/10.1016/j.rser.2021.111347>.
- [77] M. Duval, "The duval triangle for load tap changers, non-mineral oils and low temperature faults in transformers", *IEEE Electrical Insulation Magazine*, vol. 24, no. 6, pp. 22–29, 2008, ISSN: 0883-7554. DOI: 10.1109/MEI.2008.4665347.
- [78] J. Faiz and M. Soleimani, "Dissolved gas analysis evaluation in electric power transformers using conventional methods a review", *IEEE Transactions on Dielectrics and Electrical Insulation*, vol. 24, no. 2, pp. 1239–1248, 2017. DOI: 10.1109/TDEI.2017.005959.
- [79] J. Schneider *et al.*, "Asset management techniques", *International Journal of Electrical Power & Energy Systems*, vol. 28, no. 9, pp. 643–654, 2006.
- [80] M. K. Pradhan and T. S. Ramu, "Diagnostic testing of oil-impregnated paper insulation in prorated power transformers under accelerated stress", in *Conference record of the 2004 IEEE international symposium on electrical insulation*, IEEE, 2004, pp. 66–69, ISBN: 0-7803-8447-4. DOI: 10.1109/ELINSL.2004.1380452.

- [81] M. K. Pradhan, "Assessment of the Status of Insulation During Thermal Stress Accelerated Experiments on Transformer Prototypes", *IEEE Transactions on Dielectrics and Electrical Insulation*, vol. 13, no. 1, pp. 227–237, 2006, ISSN: 1070-9878. DOI: 10.1109/tdei.2006.1593420.
- [82] M. T. Imani, M. Farahani, M. Kuhnke, K. Homeier, and P. Werle, "Measuring methods for solubility of gases in insulation liquids", in *2017 IEEE 19th International Conference on Dielectric Liquids (ICDL)*, 2017, pp. 1–4.
- [83] A. Krätge, S. Hoek, M. Koch, and W. Koltunowicz, "Robust measurement, monitoring and analysis of partial discharges in transformers and other hv apparatus", *IEEE Transactions on Dielectrics and Electrical Insulation*, vol. 20, no. 6, pp. 2043–2051, 2013. DOI: 10.1109/TDEI.2013.6678852.
- [84] G. V. R. Xavier, H. S. Silva, E. G. da Costa, A. J. R. Serres, N. B. Carvalho, and A. S. R. Oliveira, "Detection, classification and location of sources of partial discharges using the radiometric method: Trends, challenges and open issues", *IEEE Access*, vol. 9, pp. 110787–110810, 2021. DOI: 10.1109/ACCESS.2021.3102888.
- [85] J. Fuhr, "Procedure for identification and localization of dangerous PD sources in power transformers", *IEEE Transactions on Dielectrics and Electrical Insulation*, vol. 12, no. 5, pp. 1005–1014, 2005, ISSN: 1070-9878.
- [86] P. Werle and M. A. Azirani, "UHF Teilentladungsmessungen an Leistungstransformatoren: Grundlagen, Möglichkeiten und Grenzen", in *1st Oberlausitzer Energiesymposium (OLES)*, 2017.
- [87] H. Jahangir, A. Akbari, P. Werle, M. Farahani, J. Szczechowski, and M. A. Azirani, "UHF PD Measurements on Power Transformers - Sensitivity Investigations", *VDE Fachtagung, Hochspannungstechnik*, 2016.
- [88] H. Jahangir, A. Akbari, P. Werle, M. A. Azirani, and J. Szczechowski, "UHF characteristics of different types of PD sources in power transformers", in *2017 Iranian Conference on Electrical Engineering (ICEE)*, pp. 1242–1247. DOI: 10.1109/IranianCEE.2017.7985232.
- [89] D. M. Pozar, *Microwave Engineering*, 4th Edition. Hoboken: Wiley, 2012, ISBN: 9780470-631553.

- [90] M. Hartje, P. Werle, M. Huntke, M. A. Azirani, and S. Peik, "Simulation and Measurement of PD in the UHF Frequency Range - Studies in Time and Frequency Domain", in *20th International Symposium on High Voltage Engineering (ISH)*, 2017.
- [91] A. Akbari, H. Jahangir, P. Werle, M. A. Azirani, and J. Szczechowski, "A Study on Relationship between PD Waveforms in HF and UHF Bands", in *20th International Symposium on High Voltage Engineering (ISH)*, 2017.
- [92] H. R. Hassani, A. Akbari, H. Jahangir, M. A. Azirani, and P. Werle, "Novel particle-based model of negative corona in oxygen for investigation on emission of electromagnetic waves", *IEEE Transactions on Dielectrics and Electrical Insulation*, vol. 27, no. 3, pp. 857–865, 2020, ISSN: 1070-9878. DOI: 10.1109/TDEI.2020.008762.
- [93] C. A. Balanis, *Antenna theory: Analysis and design*, 4th ed. Hoboken, NJ: Wiley, 2016, ISBN: 9781118642061.
- [94] M. Siegel, M. Beltle, S. Tenbohlen, and S. Coenen, "Application of UHF sensors for PD measurement at power transformers", *IEEE Transactions on Dielectrics and Electrical Insulation*, vol. 24, pp. 331–339, 2017, ISSN: 1070-9878. DOI: 10.1109/TDEI.2016.005913.
- [95] M. Siegel *et al.*, "Calibration Proposal for UHF Partial Discharge Measurements at Power Transformers", *Energies*, vol. 12, no. 16, p. 3058, 2019.
- [96] E. L. Bronaugh and J. Osburn, "Measuring antenna parameters in a GHz transverse electromagnetic (GTEM) cell", in *IEEE Antennas and Propagation Society International Symposium*, Piscataway, NJ: IEEE Service Center, 1992, pp. 2064–2066, ISBN: 0-7803-0730-5.
- [97] G. J. Behrmann, D. Gross, and S. Neuhold, "Limitations of Attempting Calibration of Partial Discharge Measurements in VHF and UHF Ranges", in *2020 IEEE Conference on Electrical Insulation and Dielectric Phenomena (CEIDP)*, pp. 155–159. DOI: 10.1109/CEIDP49254.2020.9437476.
- [98] M. A. Azirani, P. Werle, and A. Akbari, "Effect of Surroundings of UHF Partial Discharge Probes on the Captured Pulses in Power Transformers", in *IEEE 2nd International Conference on Dielectrics (ICD 2018)*, Piscataway, N.J.: IEEE, 2018, pp. 1–5, ISBN: 978-1-5386-6389-9. DOI: 10.1109/ICD.2018.8514737.

- [99] H. Jahangir, A. Akbari, P. Werle, and J. Szczechowski, "Possibility of PD calibration on power transformers using UHF probes", *IEEE Transactions on Dielectrics and Electrical Insulation*, vol. 24, no. 5, pp. 2968–2976, 2017, ISSN: 1070-9878.
- [100] R. M. Herkert, J. K. Daher, K. P. Ray, and B. Subbarao, "Measurement and modeling of near- and far-field antenna factor", in *IEEE International Symposium on Electromagnetic Compatibility*, IEEE, 1994, pp. 237–241, ISBN: 0-7803-1398-4.
- [101] R. E. Collin, *Field theory of guided waves* (The IEEE series on electromagnetic wave theory), 2. ed. New York, NY: IEEE, 1991, ISBN: 9780879422370.
- [102] D. A. Hill, *Electromagnetic fields in cavities: Deterministic and statistical theories*. John Wiley & Sons, 2009, ISBN: 9780470465905.
- [103] D. K. Cheng, *Fundamentals of engineering electromagnetics*. Addison-Wesley, 1993, ISBN: 0201566117.
- [104] M. D. Judd, L. Yang, and I. Hunter, "Partial discharge monitoring of power transformers using UHF sensors. Part I: sensors and signal interpretation", *IEEE Electrical Insulation Magazine*, vol. 21, no. 2, pp. 5–14, 2005, ISSN: 0883-7554. DOI: 10.1109/mei.2005.1412214.
- [105] L. Yang and M. D. Judd, "Propagation characteristics of UHF signals in transformers for locating partial discharge sources", *13th International Symposium on High Voltage Engineering*, 2003.
- [106] H. H. Sinaga, B. T. Phung, and T. R. Blackburn, "PD localization in transformers using UHF method", *IEEE Transactions on Dielectrics and Electrical Insulation*, vol. 19, no. 6, pp. 1891–1900, 2012, ISSN: 1070-9878. DOI: 10.1109/TDEI.2012.6396945.
- [107] S. Markalous, T. Strehl, C. Herold, and T. Leibfried, "Enhanced signal processing for conventional and unconventional PD measuring methods: Wavelet denoising, automatic detection algorithms and averaging for arrival time-based PD location in transformers and power cables", in *2008 international conference on condition monitoring and diagnosis*, I. O. E. Engineers and Electronics, Eds., Beijing, China: John Wiley, 2009, pp. 1115–1118, ISBN: 978-1-4244-1621-9. DOI: 10.1109/CMD.2008.4580479.

- [108] H. R. Mirzaei, A. Akbari, E. Gockenbach, M. Zanjani, and K. Miralikhani, "A novel method for ultra-high-frequency partial discharge localization in power transformers using the particle swarm optimization algorithm", *IEEE Electrical Insulation Magazine*, vol. 29, no. 2, pp. 26–39, 2013, ISSN: 0883-7554. DOI: 10.1109/MEI.2013.6457597.
- [109] *Algorithms for automated arrival time estimation of partial discharge signals in power cables*, 2007.
- [110] X. Song, M. Judd, and C. Zhou, "An optimal algorithm for applying wavelet transform in identifying the arrival time of pd pulse in a uhf detection system", in *2007 42nd International Universities Power Engineering Conference*, IEEE, 2007. DOI: 10.1109/upec.2007.4468997.
- [111] H. Jahangir, A. Akbari, P. Werle, H. R. Mirzaei, and E. Hajipour, "Time-to-arrival estimation of UHF PD signals based on dynamic cumulative sum of likelihood ratio", in *19th International Symposium on High Voltage Engineering (ISH)*, cigre, 2015, pp. 1–6.
- [112] M. Lavielle, "Using penalized contrasts for the change-point problem", *Signal Processing*, vol. 85, no. 8, pp. 1501–1510, 2005, ISSN: 0165-1684. DOI: 10.1016/j.sigpro.2005.01.012.
- [113] D. Herres, *Oscilloscopes: A manual for students, engineers, and scientists*. Cham, Switzerland: Springer, 2020, ISBN: 9783030538842. DOI: 10.1007/978-3-030-53885-9.
- [114] A. Ferrero, Ed., *Modern measurements: Fundamentals and applications*. Wiley, 2015, ISBN: 9781119021315. DOI: 10.1002/9781119021315.
- [115] A. Reid, M. Judd, and C. Johnstone, "Development of uhf transformer probe sensors for on-line partial discharge measurement", in *2009 44th International Universities Power Engineering Conference (UPEC)*, 2009, pp. 1–4.
- [116] S. Coenen, S. Tenbohlen, T. Strehl, and S. Markalous, "Fundamental characteristics of UHF PD probes and the radiation behavior of PD sources in power transformers", in *2009 International Symposium on High Voltage Engineering (ISH)*.
- [117] *UVS 610*. [Online]. Available: <https://www.omicronenergy.com/en/products/uv-610/> (visited on Apr. 11, 2022).
- [118] *TVS 2*. [Online]. Available: <https://www.pdix.com/products/pd-accessories/pd-sensors.html> (visited on Apr. 11, 2022).

- [119] *UHF 50/80*. [Online]. Available: www.bss-hochspannungstechnik.de/en/products/uhrsensors/uhf-dn5080 (visited on Apr. 11, 2022).
- [120] S. S. Sandler and R. King, "Compact conical antennas for wide-band coverage", *IEEE Transactions on Antennas and Propagation*, vol. 42, no. 3, pp. 436–439, 1994, ISSN: 0018-926X. DOI: 10.1109/8.280735.
- [121] *UHT 1*. [Online]. Available: <https://www.omicronenergy.com/en/products/uht1/> (visited on Apr. 11, 2022).
- [122] *UHF PD Plate Sensor*. [Online]. Available: <https://www.doble.com/product/pd-accessories/> (visited on Apr. 11, 2022).
- [123] *UHF-PS1*. [Online]. Available: www.bss-hochspannungstechnik.de/en/products/uhrsensors/uhf-ps1 (visited on Apr. 11, 2022).
- [124] M. A. Azirani, P. Werle, A. Akbari, H. Jahangir, and J. Szczechowski, "An investigation on PRPD patterns generated by the UHF measurement technique for power transformers", in *2017 Iranian Conference on Electrical Engineering (ICEE)*, pp. 1144–1147. DOI: 10.1109/IranianCEE.2017.7985213.
- [125] H. Jahangir, A. Akbari, M. A. Azirani, P. Werle, and J. Szczechowski, "Turret-Electrode Antenna for UHF PD Measurement in Power Transformers - Part I: Introduction and Design", *IEEE Transactions on Dielectrics and Electrical Insulation*, vol. 27, no. 6, pp. 2113–2121, 2020, ISSN: 1070-9878. DOI: 10.1109/TDEI.2020.008874.
- [126] W. Sikorski, C. Szymczak, K. Siodła, and F. Polak, "Hilbert curve fractal antenna for detection and on-line monitoring of partial discharges in power transformers", *Eksploracja i Niezawodność - Maintenance and Reliability*, vol. 20, no. 3, pp. 343–351, 2018, ISSN: 15072711. DOI: 10.17531/ein.2018.3.1.
- [127] T. Pinpart and M. D. Judd, "Experimental comparison of UHF sensor types for PD location applications", in *IEEE Electrical Insulation Conference, 2009. EIC 2009*, IEEE / Institute of Electrical and Electronics Engineers Incorporated, 2009, pp. 26–30, ISBN: 978-1-4244-3915-7. DOI: 10.1109/EIC.2009.5166319.
- [128] H. Jahangir, A. Akbari, M. A. Azirani, P. Werle, and J. Szczechowski, "Turret-Electrode Antenna for UHF PD Measurement in Power Transformers – Part II: Performance Investigation", *IEEE Transactions on Dielectrics and Electrical Insulation*, vol. 27, no. 6, pp. 2122–2129, 2020, ISSN: 1070-9878. DOI: 10.1109/TDEI.2020.008882.

- [129] H. R. Mirzaei, A. Akbari, M. Zanjani, K. Miralikhani, E. Gockenbach, and H. Borsi, "Investigating suitable positions in power transformers for installing UHF antennas for partial discharge localization", in *IEEE CMD2012*, Piscataway, N.J.: IEEE, 2012, pp. 625–628, ISBN: 978-1-4673-1020-8. DOI: 10.1109/CMD.2012.6416223.
- [130] H. Jahangir, A. Akbari, P. Werle, and J. Szczechowski, "UHF PD measurements on power transformers-advantages and limitations", *IEEE Transactions on Dielectrics and Electrical Insulation*, vol. 24, no. 6, pp. 3933–3940, 2017, ISSN: 1070-9878.
- [131] C. P. Beura, M. Beltle, and S. Tenbohlen, "Study of the Influence of Winding and Sensor Design on Ultra-High Frequency Partial Discharge Signals in Power Transformers", *Sensors*, vol. 20, no. 18, 2020. DOI: 10.3390/s20185113.
- [132] C. P. Beura, M. Beltle, P. Wenger, and S. Tenbohlen, "Experimental Analysis of Ultra-High-Frequency Signal Propagation Paths in Power Transformers", *Energies*, vol. 15, no. 8, p. 2766, 2022. DOI: 10.3390/en15082766.
- [133] M. A. Azirani, M. Ariannik, P. Werle, and A. Akbari, "Optimal Frequency Selection for Detection of Partial Discharges in Power Transformers using the UHF Measurement Technique", *Measurement*, vol. 172, 2021, ISSN: 0263-2241. DOI: 10.1016/j.measurement.2020.108895.
- [134] Omicron electronics GmbH, *MPD 600 Product Manual: High-end Partial Discharge Measurement and Analysis System*, 2019. [Online]. Available: www.omicronenergy.com/.
- [135] *DPO7000C*. [Online]. Available: <https://www.tek.com/en/products/oscilloscopes/dpo7000-digital-phosphor-oscilloscope> (visited on May 3, 2022).
- [136] *LMR-400-UF*. [Online]. Available: <https://timesmicrowave.com/> (visited on May 1, 2022).
- [137] A. V. Oppenheim, A. S. Willsky, and S. H. Nawab, *Signals and Systems* (Prentice-Hall signal processing series), 2nd ed. Upper Saddle River: Prentice Hall and London : Prentice-Hall International, 1997, ISBN: 0138147574.
- [138] E. O. Brigham, *The Fast Fourier Transform and its Applications*. Englewood Cliffs, N.J.: Prentice Hall, 1988, ISBN: 0133075052.

- [139] ZVA8. [Online]. Available: https://www.rohde-schwarz.com/us/products/test-and-measurement/network-analyzers/rs-zva-vector-network-analyzer_63493-9660.html (visited on May 3, 2022).
- [140] J. Kuffel and E. Kuffel, *High voltage engineering fundamentals*. Elsevier, 2000.
- [141] *IEEE Guide for Loading Mineral-Oil-Immersed Transformers and Step-Voltage Regulators*, IEEE Std C57.91-2011, 2012.
- [142] *Power transformers - Part 7: Loading guide for mineral-oil-immersed power transformers*, IEC 60076-7, 2018.
- [143] M. A. Azirani, M. Kuhnke, P. Werle, and W. Sorgatz, "New DGA Sensor for Power Transformers Sealed by Gas Cushion", in *20th International Symposium on High Voltage Engineering (ISH)*, 2017.
- [144] M. A. Azirani, M. Kuhnke, P. Werle, and W. Sorgatz, "Online Fault Gas Monitoring System for Hermetically Sealed Power Transformers", in *2018 Condition Monitoring and Diagnosis (CMD)*, pp. 1–5. DOI: 10.1109/CMD.2018.8535777.
- [145] "Arduino mega 2560", 2023. [Online]. Available: <https://www.arduino.cc/>.
- [146] *Power transformers - Part 1: General*, IEC 60076-1, 2011.
- [147] S. V. Kulkarni and S. A. Khaparde, *Transformer engineering: design, technology, and diagnostics*. CRC Press, 2017.
- [148] J. L. Volakis, Ed., *Antenna engineering handbook*, 4. ed. New York NY u.a.: McGraw-Hill, 2007, ISBN: 0-07-147574-5.
- [149] C. A. Balanis, *Advanced engineering electromagnetics*, 2nd ed. Hoboken, N.J.: John Wiley & Sons, 2012, ISBN: 9780470589489. [Online]. Available: <http://www.loc.gov/catdir/enhancements/fy1210/2011029122-d.html>.
- [150] M. A. Azirani, M. Ariannik, P. Werle, and A. Akbari, "Electromagnetic wave radiation due to partial discharges inside power transformers in the frequency domain", in *Proceedings of the 21st International Symposium on High Voltage Engineering*, B. Németh, Ed., Cham: Springer International Publishing, 2020, pp. 838–849, ISBN: 978-3-030-31676-1.

- [151] S. A. Schelkunoff, "On Representation of Electromagnetic Fields in Cavities in Terms of Natural Modes of Oscillation", *Journal of Applied Physics*, vol. 26, no. 10, pp. 1231–1234, 1955, ISSN: 0021-8979. DOI: 10.1063/1.1721880.
- [152] M. A. Azirani, P. Werle, A. Akbari, H. Jahangir, and J. Szczechowski, "An Investigation on the Relation Between PRPD Patterns Acquired by Conventional and UHF Nonconventional PD Measuring Technique for Power Transformers", in *20th International Symposium on High Voltage Engineering (ISH)*, 2017.
- [153] K. Yee, "Numerical solution of initial boundary value problems involving maxwell's equations in isotropic media", *IEEE Transactions on Antennas and Propagation*, vol. 14, no. 3, pp. 302–307, 1966, ISSN: 0018-926X. DOI: 10.1109/TAP.1966.1138693.
- [154] A. Taflove and S. C. Hagness, *Computational electrodynamics: the finite-difference time-domain method; 3rd ed* (Artech House antennas and propagation library). Boston, MA: Artech House, 2005.
- [155] W. Yu, *Electromagnetic simulation techniques based on the FDTD method* (Wiley series in microwave and optical engineering). Oxford: Wiley-Blackwell, 2009, ISBN: 0470502037.
- [156] M. Zanjani, A. Akbari, H. R. Mirzaei, N. Shirdel, E. Gockenbach, and H. Borsi, "Investigating partial discharge UHF electromagnetic waves propagation in transformers using FDTD technique and 3D simulation", in *Proceedings of 2012 IEEE International Conference on Condition Monitoring and Diagnosis: Bali-Indonesia, September 23-27, 2012*, Piscataway, NJ: IEEE, 2012, pp. 497–500, ISBN: 978-1-4673-1019-2. DOI: 10.1109/CMD.2012.6416187.
- [157] T. Brosche, W. Hiller, E. Fauser, and W. Pfeiffer, "Novel characterization of PD signals by real-time measurement of pulse parameters", *IEEE Transactions on Dielectrics and Electrical Insulation*, vol. 6, no. 1, pp. 51–59, 1999, ISSN: 1070-9878. DOI: 10.1109/94.752009.
- [158] Z. Tang, C. Li, W. Wang, H. Wang, L. Wang, and Y. Ding, "The propagation characteristics of electromagnetic wave generated from partial discharges in power transformer by fdfd simulation", in *2007 Annual Report - Conference on Electrical Insulation and Dielectric Phenomena*, 2007, pp. 200–203. DOI: 10.1109/CEIDP.2007.4451613.

- [159] M. A. Azirani, M. Ariannik, P. Werle, and A. Akbari, "Enhancing the Accuracy of Partial Discharge Localization in Power Transformers Using the UHF Measurement Technique", in *2019 IEEE Electrical Insulation Conference (EIC)*, pp. 58–62. DOI: 10.1109/EIC43217.2019.9046629.
- [160] I. Daubechies, *Ten Lectures on Wavelets*. Society for Industrial and Applied Mathematics, 1992.
- [161] D. L. Donoho and I. M. Johnstone, "Ideal spatial adaptation via wavelet shrinkage", *Biometrika*, vol. 81, no. 3, pp. 425–455, 1994.
- [162] M. A. Azirani, M. Ariannik, P. Werle, and A. Akbari, "Optimized Arrival Time Determination of UHF Pulses for Localization of Partial Discharges in Power Transformers", in *2018 IEEE Conference on Electrical (CEIDP)*, pp. 522–526. DOI: 10.1109/CEIDP.2018.8544757.
- [163] M. Ariannik, M. A. Azirani, P. Werle, and A. Akbari, "UHF Measurement in Power Transformers: An Algorithm to Optimize Accuracy of Arrival Time Detection and PD Localization", *IEEE Transactions on Power Delivery*, vol. 34, no. 4, pp. 1530–1539, 2019, ISSN: 0885-8977.
- [164] M. Ariannik, M. A. Azirani, P. Werle, and A. Akbari, "A Novel Algorithm for UHF-Based Partial Discharge Localization in Power Transformers", in *VDE-Fachtagung Hochspannungstechnik, IEEE*, 2018, pp. 1–6.
- [165] J. C. Bezdek, Ed., *Pattern Recognition with Fuzzy Objective Function Algorithms* (Advanced Applications in Pattern Recognition). Boston, MA: Springer US, 1981, ISBN: 978-1-4757-0452-5. DOI: 10.1007/978-1-4757-0450-1.
- [166] G. Strang, *Introduction to Linear Algebra*, 5th. Wellesley, MA: Wellesley-Cambridge Press, 2016, pp. 314–319.
- [167] X. Ma, C. Zhou, and I. J. Kemp, "Automated wavelet selection and thresholding for PD detection", *IEEE Electrical Insulation Magazine*, vol. 18, no. 2, pp. 37–45, 2002, ISSN: 0883-7554. DOI: 10.1109/57.995398.
- [168] S. M. Markalous, S. Tenbohlen, and K. Feser, "Detection and location of partial discharges in power transformers using acoustic and electromagnetic signals", *IEEE Transactions on Dielectrics and Electrical Insulation*, vol. 15, no. 6, pp. 1576–1583, 2008, ISSN: 1070-9878. DOI: 10.1109/TDEI.2008.4712660.

-
- [169] C. J. Bennoch and M. D. Judd, "A UHF system for characterising individual PD sources within a multi-source environment", *13th International Symposium on High Voltage Engineering (ISH)*, 2003. [Online]. Available: <https://strathprints.strath.ac.uk/38903/>.
- [170] J. C. Bezdek, *Pattern Recognition with Fuzzy Objective Function Algorithms*. Springer Science & Business Media, 2013, ISBN: 9781475704501.
- [171] A. Goldsmith, *Wireless communications*. Cambridge: Cambridge University Press, 2005, ISBN: 9780521837163.



Mohammad Akbari Azirani

School Education

1995 - 2000, Salehin School, Tehran

Elementary School

2000 - 2002, Geschwister-Jacobs-Schule, Hanover

Orientation Level

2002 - 2006, Salam II School, Tehran

High School

University Education

2007 - 2012, K. N. Toosi University of Technology, Tehran

B.Sc. in Electrical Engineering

2012 - 2015, Leibniz Universität Hannover

M.Sc. in Electrical Engineering

Professional Experience

August 2020 - present, PFISTERER Kontaktsysteme GmbH

Team leader - HV Cable Systems

April 2016 - July 2020, Institute of Electric Power Systems, High Voltage Technology and Asset Management Section (Schering-Institute), Leibniz Universität Hannover

Research Assistant and PhD Candidate

Core Competencies

- **Leadership:** Inspiring and motivating team members, setting clear goals, providing guidance, and making effective decisions.
- **Technical Knowledge:** Proficiency in relevant technical skills and knowledge specific to the projects being managed.
- **Communication:** Strong verbal and written communication skills, facilitating collaboration with stakeholders and ensuring smooth project communication.
- **Project Management:** Proficiency in methodologies, tools, and techniques for planning, executing, monitoring, and controlling projects.
- **Team Management:** Experience in resource allocation, task delegation, performance evaluation, and fostering a positive environment.
- **Stakeholder Management:** Effective management of relationships with clients, team members, executives, and external partners.
- **Risk Management:** Identifying and mitigating risks, creating risk management plans, and minimizing project disruptions.
- **Financial Management:** Knowledge of budgeting principles, cost estimation, tracking project finances, and delivering within allocated budgets.
- **Time Management:** Strong organizational skills for prioritizing tasks, meeting deadlines, and optimizing project schedules.
- **Conflict Resolution:** Handling conflicts and disagreements with effective negotiation and diplomacy skills.

Contact Information

mohammad.azirani
@ifes.uni-hannover.de

ResearchGate

LinkedIn

ORCID

Born

July 19, 1989, in
Esfahan

Family Status

Married

